University of Antwerp

Faculty of Science
Department of Physics

When electrocatalysis meets electron paramagnetic resonance - gaining insight into electrochemical reactions

Thesis submitted in fulfilment of the requirements for the degree of
Doctor in Science: Physics
at the University of Antwerp to be defended by

Mohammad Samanipour

Promotor: Prof. dr . Sabine Van Doorslaer
Co-promotor: Dr. H. Y. Vincent Ching

Antwerp 2022

Members of the jury

Internal doctoral committee

Chair	**Prof. dr Sofie Cambré** University of Antwerp, Antwerp, Belgium
Promotor	**Prof. dr . Sabine Van Doorslaer** University of Antwerp, Antwerp, Belgium
Co-promotor	**Dr. H. Y. Vincent Ching** University of Antwerp, Belgium
Member	**Prof. dr. Dirk Lamoen** University of Antwerp, Antwerp, Belgium

External jury members

Prof. dr. Alexander Schnegg
Max Planck Institute for Chemical Energy Conversion,
Mülheim an der Ruhr, Germany

Prof. dr Ange Mouithys-Mickalad
University of Liège, Liège, Belgium

Summary

The interest in environmentally friendly production of chemical products has increased in recent years. Electrocatalysis provides a clean and inexpensive method for chemical synthesis, which can play its role in green chemistry if it is employed at optimum conditions. Decreasing the energy cost is the crucial challenge in performing electrosynthesis in large-scale industrial productions. To this end, an in-depth understanding of what exactly happens during the reaction is necessary, and it requires the identification of the short-lived intermediates. These intermediates are formed due to electron transfer in the electrochemical process, so they often are paramagnetic species such as organic radicals and transition-metal complexes in their specific oxidation states. Electron paramagnetic resonance (EPR) spectroscopy is used to detect paramagnetic species. Using different EPR techniques, one can identify the molecular structures. The combination of electrochemistry and EPR (SEC-EPR) can help to detect the paramagnetic intermediates and unravel the reaction mechanisms, which eventually leads to overcoming the energy cost challenge. Despite its benefits and long history, the SEC-EPR field has not received a lot of attention due to its challenges. As mentioned above, the intermediates are often short-lived, so the conventional *ex-situ* SEC-EPR experiments are not practical in many cases. Hence, in many cases, *in-situ* experiments need to be performed to get real-time information from the reaction. Performing *in-situ* experiments are challenging due to the lack of commercial SEC-EPR cells. Other methods for stabilising the intermediates, such as spin trapping and freeze-quenching, can be combined with *in-situ* and *ex-situ* experiments. This thesis focuses on both *in-situ* and *ex-situ* experiments, introducing novel SEC-EPR cells and the challenges of designing them and investigating the electrochemical reactions. Spin-trap and direct EPR techniques are employed depending on the requirements for each case study. Moreover, the freeze-quenching of an SEC-EPR cell to trap intermediates is tested. DFT computations completed the EPR data in the identification of paramagnetic species.

This thesis is divided in four main parts:

Part I (Introduction and methodology) consists of three chapters: **Chapter 1 (General introduction)** gives a short introduction to the main goals of this thesis. **Chapter 2 (Experimental and Computational Methods)** focuses on the theoretical background of the experimental and computational methods used in this thesis. **Chapter 3 (State of art in EPR spectro-electrochemistry)** gives explanations about the challenges of performing SEC-EPR methods and a review of prior works in this field.

Part II (Pitfalls of spin-trap EPR) focuses on the non-innocent role of 5,5-dimethylpyrroline-N-oxide (DMPO) used for trapping radicals formed in a homogeneous copper-catalysed reaction. In **Chapter 4 (The non-innocent role of spin traps),** the reactivity of DMPO with Cu(II) complexes is investigated. Different EPR techniques are used to provide in-depth information about the copper ligands. DFT computations were performed for the identification of the intermediates.

Part III (EPR-spectroelectrochemistry and spin trapping) contains four chapters focusing on combining spin trapping with SEC-EPR studies. *In-situ* experiments and DFT computations are used to unravel the reaction mechanism by detecting and identifying the radical intermediates for the electrochemical cyclisation of allyl 2-bromobenzyl in **Chapter 5 (Reductive intramolecular cyclisation of allyl 2-bromobenzyl ether)** and electrochemical aldol condensation of acetone in **Chapter 6 (Re-evaluating the electrochemical self-condensation of acetone by EPR and DFT)**. Detailed information about the reaction mechanism and the structure of the trapped intermediates are given. In the same way, the *ex-situ* EPR experiments and DFT computations helped in ecstasy detection in **Chapter 7 (How EPR can help in developing a screening strategy for ecstasy)**. **Chapter 8 (Reactive oxygen species formation at Pt nanoparticles)** is a small chapter in which the electrochemical formation of the oxygen radical species on Pt nanoparticles is studied by detection and quantification of radical species using different spin traps.

Part IV (Direct EPR spectroelectrochemistry) focuses on the direct detection of paramagnetic species. In **Chapter 9 (*In-situ* SEC-EPR cells, design and validation)**, I introduced two different *in-situ* setups designed by collaborators. The first setup, which is a static cell, focuses on the efficiency of ITO as a working electrode in the presence of different electrodeposited catalytic nanoparticles (Ag and NiO). The second cell is a flow cell that enables us to take advantage of controlling hydrodynamical flow and increase reproducibility, thus improving the efficiency of electrochemistry experiments. Both setups were validated by me for direct detection of electroreduction of methyl viologen and benzoquinone. **Chapter 10 (Identifying reaction intermediates in carbon-halogen bond electroreduction)** is an ongoing work which focuses on carbon-halogen electroreduction. In this chapter, electroreduction of 1- and 2-bromonaphthalene are investigated in which the reaction mechanisms have been already proposed previously on the basis of other techniques. The *in-situ* EPR data show the presence of radical intermediates. The DFT computations were employed to corroborate the interpretation of the EPR data. The results of the DFT computation of the radical intermediates proposed in the reaction mechanisms seem to contradict the EPR data. **Chapter 11 (SEC-EPR study of the catalytic activity of Mo-Cu complexes in CO_2 reduction)** is the final research chapter that focuses on the EPR detection of Mo-Cu complexes employed as catalysts for CO_2 reduction. The results of both *ex-situ* and *quasi-in-situ* methods are reported. In the *ex-situ* experiments, a freeze-quenching setup is designed for sample collection. A quasi-*in-situ* setup is developed and validated for performing electrochemistry inside an EPR tube. Different EPR techniques and DFT computations are used for data analysis.

Samenvatting

De belangstelling voor milieuvriendelijke productie van chemische producten is de laatste jaren sterk toegenomen. Elektrokatalyse biedt een schone en goedkope methode voor chemische synthese, die een rol kan spelen in de transitie naar groene chemie als zij onder optimale omstandigheden wordt toegepast. Bij de uitvoering van elektrosynthese tijdens grootschalige industriële processen blijkt het verlagen van de energiekosten een cruciale uitdaging te zijn. Daartoe is een grondig begrip nodig van wat er precies gebeurt tijdens de chemische reactie, en dat vereist de identificatie van de kortlevende tussenproducten. Deze tussenproducten worden gevormd als gevolg van elektronenoverdracht in het elektrochemische proces, en vaak zijn dit paramagnetische systemen, zoals organische radicalen en overgangsmetaalcomplexen in specifieke oxidatietoestanden. Elektronen paramagnetische resonantie (EPR) spectroscopie wordt gebruikt om paramagnetische species op te sporen. Met behulp van verschillende EPR-technieken kan men de moleculaire structuren identificeren. De combinatie van elektrochemie en EPR (SEC-EPR) kan helpen om de paramagnetische tussenproducten op te sporen en de reactiemechanismen te ontrafelen. Ondanks het feit dat SEC-EPR veel voordelen heeft en reeds lang gekend is, maken verschillende uitdagingen dat SEC-EPR nog steeds niet veel aandacht krijgt. Zoals gezegd zijn de tussenproducten vaak van korte duur, zodat de conventionele *ex-situ* SEC-EPR experimenten in veel gevallen niet praktisch zijn. Daarom moeten geregeld *in-situ*-experimenten worden uitgevoerd om *real-time* informatie van de reactie te bekomen. Het uitvoeren van *in-situ*-experimenten is een uitdaging wegens het gebrek aan commerciële SEC-EPR-cellen die generiek toepasbaar zijn. Andere methoden om de tussenproducten te stabiliseren, zoals *spin trapping* en *freeze-quenching*, kunnen dan worden gecombineerd met *in-situ* en *ex-situ* experimenten. Dit proefschrift richt zich op zowel *in-situ* als *ex-situ* experimenten. Het introduceert nieuwe SEC-EPR cellen, bespreekt de uitdagingen van het ontwerpen ervan en past de cellen toe in het onderzoek van specifieke elektrochemische reacties. *Spin-trap* en directe EPR technieken worden gebruikt afhankelijk van de vereisten voor elke casestudy. Bovendien wordt de mogelijkheid van *freeze-quenching* van een SEC-EPR cel onderzocht om kortlevende tussenproducten te vangen en onderzoeken. DFT-berekeningen ondersteunen de analyse van de EPR parameters, wat uiteindelijk een identificatie van paramagnetische soorten toelaat.
Dit proefschrift bestaat uit vier delen:

Deel I (Inleiding en methodologie) bestaat uit drie hoofdstukken: **Hoofdstuk 1 (Algemene inleiding)** geeft een korte inleiding op de belangrijkste doelstellingen van dit proefschrift. **Hoofdstuk 2 (Experimentele en computationele methoden)** richt zich op de theoretische achtergrond van de experimentele en computationele methoden die in dit proefschrift worden gebruikt. **Hoofdstuk 3 (State of art in EPR spectro-elektrochemie)** geeft uitleg over de uitdagingen van het uitvoeren van SEC-EPR methoden en een overzicht van eerdere werken op dit gebied.

Deel II (Valkuilen van spin-trap EPR) richt zich op de rol van 5,5-dimethylpyrroline-N-oxide (DMPO) voor het vangen van radicalen gevormd in een homogene koper-gekatalyseerde reactie. In **hoofdstuk 4 (De niet-onschuldige rol van spin-traps)** wordt de reactiviteit van DMPO met Cu(II)-complexen onderzocht. Verschillende EPR-technieken worden gebruikt om diepgaande informatie over de koperliganden te verkrijgen. DFT berekeningen werden uitgevoerd voor de identificatie van de tussenproducten.

Deel III (EPR-spectroelectrochemie en spin trapping) bevat vier hoofdstukken die gericht zijn op het combineren van *spin trapping* met SEC-EPR studies. *In-situ* experimenten en DFT berekeningen worden gebruikt om het reactiemechanisme te ontrafelen door het detecteren en identificeren van de radicalaire tussenproducten voor de elektrochemische cyclisatie van allyl 2-bromobenzyl in **hoofdstuk 5 (Reductieve intramoleculaire cyclisatie van allyl 2-bromobenzyl ether)** en elektrochemische aldolcondensatie van aceton in **hoofdstuk 6 (Herevaluatie van de elektrochemische zelfcondensatie van aceton door EPR en DFT).** Er wordt gedetailleerde informatie over het reactiemechanisme en de structuur van de gevangen tussenproducten gegeven. Op dezelfde manier hielpen de *ex-situ* EPR-experimenten en DFT-berekeningen bij de detectie van ecstasy in **hoofdstuk 7 (Hoe EPR kan helpen bij de ontwikkeling van een screeningstrategie voor ecstasy). Hoofdstuk 8 (Reactieve vorming van zuurstofsoorten op Pt-nanopartikels)** is een klein hoofdstuk waarin de elektrochemische vorming van de zuurstofradicale soorten op Pt-nanopartikels wordt bestudeerd door detectie en kwantificering van radicalen met behulp van verschillende spin-traps.

Deel IV (Directe EPR-spectroelectrochemie) richt zich op de directe detectie van paramagnetische verbindingen. In **hoofdstuk 9 (*In-situ* SEC-EPR-cellen, ontwerp en validatie)** introduceerde ik twee verschillende *in-situ* opstellingen die door medewerkers zijn ontworpen. De eerste opstelling, een statische cel, richt zich op de efficiëntie van ITO als werkelektrode in aanwezigheid van verschillende elektrolytische nanodeeltjes (Ag en NiO). De tweede cel is een doorstroomcel die ons in staat stelt te profiteren van een gecontroleerde hydrodynamische stroming en verhoogde reproduceerbaarheid om de efficiëntie van elektrochemische experimenten te verbeteren. Beide opstellingen werden door mij gevalideerd voor de directe detectie van de elektroreductie van methylviolet en benzoquinon. **Hoofdstuk 10 (Identificatie van reactie-intermediairen in de elektroreductie van koolstof-halogeenverbindingen)** is een lopend werk dat zich richt op de elektroreductie van koolstof-halogeenverbindingen. In dit hoofdstuk worden elektroreducties van 1- en 2-broomftaleen onderzocht waarbij de reactiemechanismen reeds eerder zijn voorgesteld op basis van andere technieken. De *in-situ* EPR gegevens tonen de aanwezigheid van radicalaire tussenproducten. De DFT-berekeningen werden gebruikt om de interpretatie van de EPR-gegevens te bevestigen. De resultaten van de DFT-berekening van de in de reactiemechanismen voorgestelde radicalaire tussenproducten lijken de EPR gegevens tegen te spreken. **Hoofdstuk 11 (SEC-EPR studie van de katalytische activiteit van Mo-Cu complexen bij CO_2 reductie)** is het laatste onderzoekshoofdstuk dat zich richt op de EPR detectie van Mo-Cu complexen die worden gebruikt als katalysatoren voor CO_2 reductie. De resultaten van zowel *ex-situ* als *quasi-in-situ* methoden worden gerapporteerd. In de *ex-situ* experimenten is een *freeze-quenching* opstelling ontworpen voor het verzamelen van monsters. Een *quasi-in-situ* opstelling is ontwikkeld en

gevalideerd voor het uitvoeren van elektrochemie in een EPR-buis. Verschillende EPR-technieken en DFT-berekeningen worden gebruikt voor gegevensanalyse.

Table of Contents

List of abbreviations

ABBE	Allyl 2-bromobenzyl ether
ACAC	Acetylacetonate
ACN	Acetonitrile
AMP	Amphetamine
ATC	Amphetamine-type stimulants
BN	Bromonaphthalene
AZO	Aluminum Zinc Oxide
BQ	1,4-Benzoquinone
BZX	1,3-Benzodioxole
CE	Counter Electrode
COSMO	Conductor-like screening model
CPE	Constant Phase Element
CV	Cyclic Voltammetry
C-X	Carbon-halogen
CW	Continuous Wave
DAA	Diacetone Alcohol
DEPMPO	5-(diethoxyphosphoryl)-5-methyl-1-pyrroline-N-oxide
DET	Dissociative electron transfer)
DFT	Density Functional Theory
DI	Double integral
DMF	Dimethylformamide
DMPO	5,5-dimethyl-2-hydroxyl-pyrrolin-1-yl
DMSO	Dimethylsulfoxide
DXM	Dextromethorphan
EASA	Electrochemical active surface area
EC	Electron coherence
	Electrochemical
EFG	Electric field gradient

EGB	Electrogenerated Base
ENDOR	Electron-nuclear double resonance
EP	Electron polarization
	Electrochemical profile
EPR	Electron Paramagnetic Resonance (spectroscopy)
EPRoC	EPR-on-a-chip
ESR	Electron spin resonance (spectroscopy)
ESEEM	Electron spin echo envelope modulation (spectroscopy)
EZ	Electron Zeeman
FCF	Flexible carbon fibre
FSEcho	Field sweep echo-detected (EPR)
G	Gibbs free energies
GC	Glassy Carbon
	Gas Chromatography
GGA	Generalized gradient approximation
HAT	Hydrogen atom transfer
HYSCORE	Hyperfine sublevel correlation (spectroscopy)
HF	Hyperfine
IR	Infrared
ITO	Indium Tin Oxide
KS	Kohn Sham
LC	Liquid Chromatography
LDA	Local density approximation
LEA	Law enforcement agencie
LSV	linear sweep voltammetry
MDBD	3,4-methylenedioxy-N-methyl-α-ethylphenylethylamine
MDMA	3,4-methylenedioxymethamphetamine
MDEA	3,4-methylenedioxy-N-ethylamphetamine
MS	Mass Spectrometry
MV	1,1'-dimethyl-4,4'-bipyridinium dichloride
MW	Microwave
N	Naphthalene
NC	Nuclear coherence
NMR	Nuclear Magnetic Resonance (spectroscopy)
NP	Nuclear polarization
	Nano particle
NQ	Nuclear quadrupole
NZ	Nuclear Zeeman
ORR	Oxygen reduction reaction
PBN	N-tert-butyl-α-phenylnitrone
PBS	Phosphate-buffered saline
PEEK	Polyether Ether Ketone
PET	Polyethylene terephthalate
PFA	Polyfluoroalkane
POM	Polyoxymethylene
PMA	Para-methoxyamphetamine
PMMA	Poly(methyl methacrylate)

List of abbreviations

PY	Pyridine
Q-factor	Quality factor
RDE	Rotating Disc Electrode
RE	Reference Electrode
RF	Radio frequency
ROS	Reactive oxygen species
SEC	Spectroelectrochemical
SCF	Self-consistent field
SHE	Standard hydrogen electrode
S/N	Signal-to-noise
SO	Spin-Orbit
SMD	Solvation model based on density
SWV	Square wave voltammetry
TBAP	Tetrabutylammonium Perchlorate
TBAB	Tetrabutylammonium Bromide
TBAFP	Tetrabutylammonium Hexafluorophosphate
TCO	Transparent Conductive Oxides
TEMPO	(2,2,6,6-tetramethylpiperidin-1-yl)oxyl
TFE	2,2,2-trifluoroethanol
TMI	Transition-metal ions
UV-VIS	Ultraviolet-Visible (spectroscopy)
WE	Working Electrode
XTC	Esctasy
ZFS	Zero-field splitting

Part I
Introduction and Methodology

CHAPTER 1

General introduction

In the search for clean and green industrial ways of making chemical products, electrosynthesis has many advantages. The main advantages are that (1) you do not need many starting materials and (2) the redox reactions tend to happen in a 'cleaner' way (less side products). The big drawback is the high electric energy cost. Electrocatalysis circumvents this disadvantage. Electrocatalytic synthesis uses electrodes covered with catalysts that will facilitate the reaction and lower the energy barrier, making the electrosynthesis procedure less costly. However, little is known at present about the mechanisms driving electrocatalytic synthesis, and this hampers advancements in the field. There is in fact need for dedicated characterization tools that allow unravelling these mechanisms. This chapter gives an introduction to the challenges of green chemistry and electrocatalysis. It specifies the potential of spectroelectrochemistry and the goals of the current thesis.

1.1 The importance of green chemistry

Anthropogenic activities are putting a large strain on our planet. On the one hand, human activities have generated a massive quantity of contaminants and hazards in the natural environment. On the other hand, the increase in greenhouse gases due to the usage of fossil resources (coal, oil, gas) as energy sources has caused global warming and massive climate change. According to the International Energy Agency, the vast majority (80%) of the energy needed for transportation, generation of electricity, powering manufacturing, industry, and other aspects that influence our daily life stems from fossil fuels [1]. Due to the growing world population and expanding industrialization, the global energy demand has increased to 18 TW and is predicted to be up to 26 TW in 2040 [1], which correspondingly increases enormously the amount of CO_2 production. Thus, one of the most crucial challenges has become the lowering of consumption of fossil fuels in order to decrease the production of CO_2. Different options to create global-scale sustainable energy systems such as solar energy, wind energy, and hydroelectric power are currently considered [2–4]

The energy demand of the chemical industry was reported in 2010 to be 8% of global energy demand, and almost all of it was driven by fossil fuels [5]. Developing clean and non-toxic methods to produce industrial chemicals that use renewable energy sources will play a vital role in our attempts to decrease CO_2 emissions and hazardous materials.
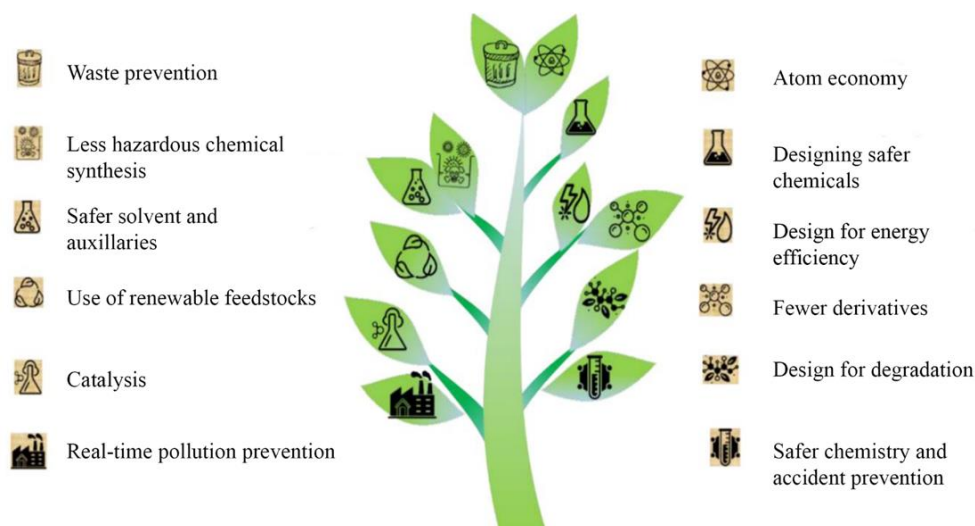
Figure 1.1 Principles of green chemistry. The figure is taken from [6].

Green chemistry introduces the design of chemical products and processes that remove or reduce the use of hazardous materials [7,8]. Anastas and Warner suggested the twelve principles of green chemistry in 1998 [9], shown in Figure 1.1. They form a guiding framework for the design of new chemical products and processes across all steps of the process life-cycle, from the raw materials used to the efficiency and safety of the transformation, the toxicity and biodegradability of products, and reagents used [10]. Research programs focusing on green chemistry have a broad scope and

include a wide variety of topics such as polymers, solvents, catalysis, biobased renewables, analytical method development, synthetic methodology development, and the design of safer chemicals [8].

1.2 Catalysis

Catalysis, as one of the principles of green chemistry, is a process in which the rate of a chemical reaction increases by lowering the required energy barrier by adding non-sacrificial agents, known as catalysts. Catalysts react with the reactants and form intermediates leading to the final products of the reaction. They are not consumed in the reaction and thus remain unchanged after it. Figure 1.2 schematically shows the different energy behaviours for a catalyzed and uncatalyzed process. Catalytic reactions can be classified into three different classes. In homogeneous catalysis, the reactants and the catalysts are in the same phase, while in heterogeneous catalysis, the catalyst and the reactants are not. Biocatalysis involving enzymes and other biomolecules is often considered as a third category.
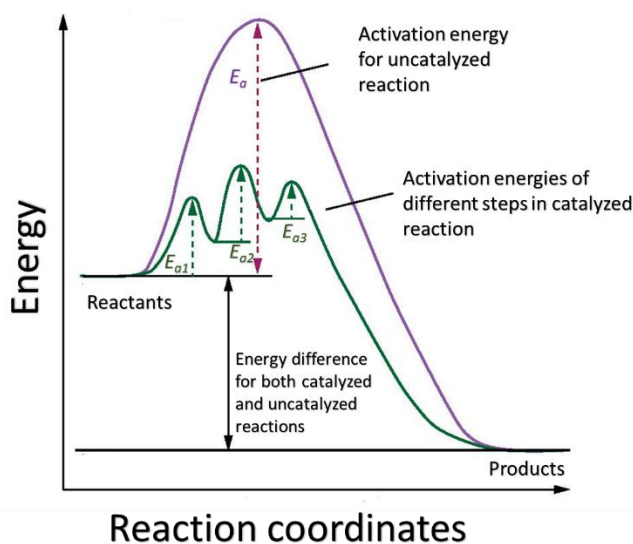
Figure 1.2 Schematic of variation of the energy in the absence (purple) and presence (green) of catalysts.

Catalysis plays an essential role in chemistry. In 90% of all commercially manufactured chemical compounds such as medicines, fine chemicals, polymers, fibres, fuels, paints, and lubricants, catalysts are estimated to be used at some point during the manufacturing process. [11,12]. As evidence of the importance of catalysis, I like to stress that Nobel Prizes in Chemistry were recently awarded in 2021 (B. List and D. W.C. MacMillan) for the development of asymmetric organocatalysis [13], in 2010 (R.F. Heck, E. Negishi, and A. Suzuki) for palladium-catalyzed cross couplings in organic synthesis [14], and in 2005(Y. Chauvin, R.H. Grubbs, and R.R. Schrock) for the development of the metathesis method in organic synthesis [15].

By using catalysts, it is possible to reduce the temperature of the chemical reactions, and for the highly selective reactions, one can also reduce the waste and unwanted side reactions, leading to a greener technology [12,16]. Despite the advantages, standard catalysis also has some dark sides. In the case of homogeneous catalysis, the catalysts should be separated from the product after the reaction. This separation phase is often very expensive [17]. Moreover, the use of homogeneous catalysts is temperature limited since some catalysts are active at temperatures at which the reactants can degrade. Nowadays, the chemical industry relies on heterogeneous catalysis because of the advantage that catalysts can easily be removed from the reaction mixture [18]. Even though catalysts decrease the activation energy, the reaction still needs to receive enough energy to occur. This is often provided by increasing the temperature and pressure, which is not a green process. In electrochemistry, electrical energy provides the activation energy. So the reaction can happen at the ambient condition (room temperature and atmospheric pressure). In the next section, I will introduce the advantages of electrochemistry and the benefits of combining it with catalysis.

1.3 Electrocatalysis

Electrosynthesis consists of producing chemical compounds using electrochemistry, in which the electron transfer occurs on the surface of an electrode in an electrochemical cell. An applied potential provides the required energy for the reaction to take place. Electrochemistry has the potential to be utilized in the development of innovative ecologically friendly methods. [19]. Some of the advantages are listed below.

1) Electrochemistry allows the electrosynthesis of products, hence, redox reactions can be done with fewer side products.
2) The applied potential allows controlling the reaction selectivity and the reaction rate.
3) The reaction conditions are typically mild since electrochemistry is performed at ambient conditions (room temperature and atmospheric pressure), which is important in terms of energy saving.
4) One can avoid using toxic materials such as reducing agents or volatile solvents, leading to safer operating conditions.
5) The electrochemical process can be monitored in real time. In contrast with the classical analysis during an electrochemistry process, one can receive rapid feedback from the chemistry that is happening simultaneously [20,21]. Hence the minimization of the errors will be more feasible.

Moreover, electrochemistry plays a role in battery development [22]

Despite the mentioned advantages, the biggest challenge that one should deal with is the high energy costs of the electrochemical process. Electrocatalysis is a method that combines the best of both worlds of electrochemistry and catalysis, which keeps the advantages of electrochemistry plus lowering the activation energy for the experiment due to using catalysts. The advantages of electrocatalysis cover nine of the twelve principles of green chemistry [19].
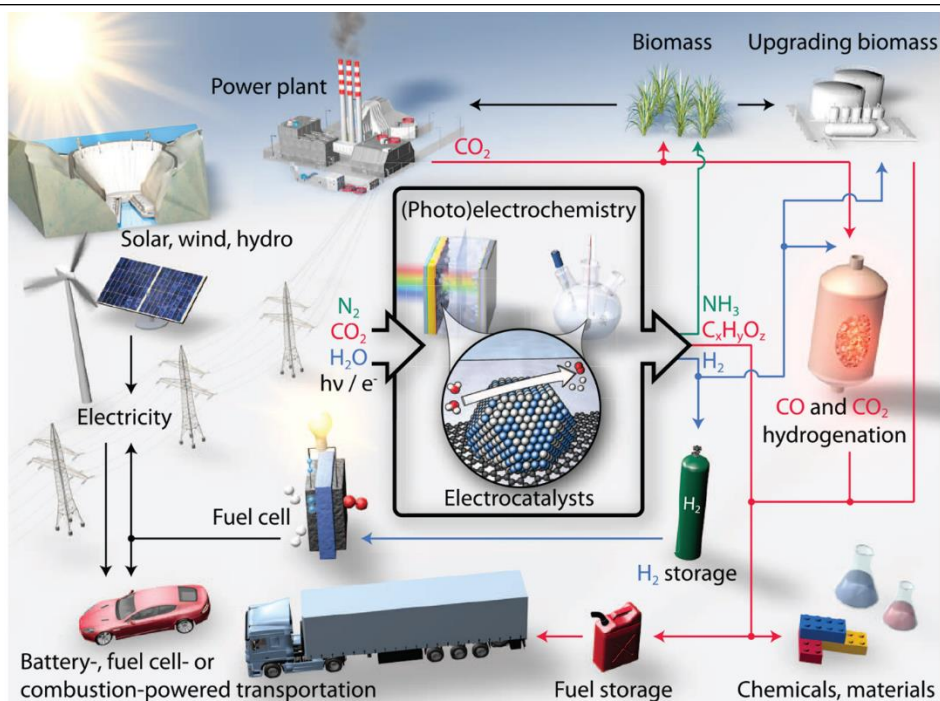
Figure 1.3 Sustainable energy future. Schematic representation of a sustainable energy landscape based on electrocatalysis. Figure taken from [23]*.*

Electrocatalysis allows using sustainable resources in nature (Figure 1.3). For instance, by developing good electrocatalysts, renewable sources in the Earth's atmosphere such as water, carbon dioxide, and N_2 can be converted to essential industrial chemical products via an electrochemical process [24–26]. Electrocatalysis can facilitate the water-splitting process as a sustainable source of hydrogen [27,28]. Hydrogen peroxide, which has application in the pulp- and water-bleaching, can be derived via electrochemical H_2O reduction reactions [29]. Carbon dioxide might be used as a feedstock for fuels, commercial chemicals, fine chemicals, and polymer and plastic precursors via electroreduction [30]. Similarly, the electroreduction of N_2 to ammonia would enable the sustainable synthesis of fertilizers at the desired concentration, avoiding energy expenses caused by the commonly used Haber-Bosch process [31]. To make those applications possible, the design of effective electrocatalysts with acceptable efficiency and selectivity is necessary. In general, many performance characteristics should be considered while developing the electrocatalysts, which are different for each particular application [28]. When developing electrochemical reactions, one should have a profound understanding of what exactly happens in the reaction. For example, identifying the intermediates that may be created during a stepwise reaction is necessary to understand the reaction mechanism, leading to the evaluation and design of the most optimized electrocatalyst. Moreover, one should consider that the catalyst can change depending on the operation condition, and these changes can affect its efficiency and selectivity. Developing *in-situ* characterisation methods can enable us to gather real-time information on the chemical characteristics of species participating in the reaction mechanism [8,23,28,32].

1.4 Spectroelectrochemistry

Although electrochemical methods provide much information about the reactions, extra information may be needed to study a chemical reaction. Spectroscopy provides the possibility of monitoring the reactions in order to obtain extra information. The easiest way to combine spectroscopy and electrochemistry is by taking aliquots of the reaction mixture and investigate them spectroscopically *ex-situ*. *In-situ* spectroelectrochemistry, i.e. *in-situ* spectroscopy during the electrochemical process, is however more preferred. In addition to an electrochemically observed redox process, it provides details about the mechanism to control the chemical reaction. Several optical spectroscopy techniques such as UV-Vis, Raman, and FT-IR spectroscopy are often used in spectroelectrochemistry studies [33–36]. Also, magnetic resonance techniques, i.e. nuclear magnetic resonance (NMR) and electron paramagnetic resonance (EPR), are combined with electrochemistry. EPR is a technique to detect systems containing unpaired electrons or paramagnetic centres. Many catalytic materials or reaction intermediates involve paramagnetic centres such as transition-metal ions (TMI) and free radicals, making EPR spectroscopy a powerful tool to investigate their characteristics and roles in the electrocatalytic process [12,37]. The EPR parameters of the paramagnetic species are directly and sensitively connected to their geometry and electronic structures, which characterize their reactivity. Using EPR, the presence of paramagnetic centres may confirm radical reaction mechanisms or reveal the oxidation states of the TMI, their coordination geometry, and the neighbouring ligands [37]. Spectroelectrochemical EPR (SEC-EPR) allows real-time monitoring of the TMI and radicals during electrocatalytic activity. However, the use of SEC-EPR still poses challenges, including the need for a design of novel and easy-to-use setups, trapping and fast detection of paramagnetic intermediates and unambiguous interpretation of EPR data.

1.5 The goal of this thesis

The research in this thesis is performed in the framework of an FWO research project, "Towards a targeted optimization of electrocatalysis by combining electrosynthesis with *in-situ* electron paramagnetic resonance", a collaboration between the UAntwerp research groups BIMEF (PI S. Van Doorslaer) and ELCAT (PI T. Breugelmans) and the VUB research group SURF (PI A. Hubin). While the ELCAT group focused on the development of new cells for SEC-EPR and the SURF group studied the oxygen reduction reaction, my research focused on the use of EPR spectroscopy and corroboration of EPR analysis with density functional theory (DFT) in electrocatalysis. The thesis is divided in four main parts.

Part I (Introduction and methodology) consists of three chapters, including the general introduction given here in chapter 1.

Chapter 2 contains a detailed description of the theoretical background, experimental and computational methods used in this thesis. This includes an introduction into EPR, basics of electrochemistry and DFT computations.

In **chapter 3,** the state of art in SEC-EPR is discussed, including a review of prior efforts in combining electrocatalysis with EPR.

Part II (Pitfalls of spin-trap EPR) focuses on the combination of EPR with the spin traps. Spin-trapping is a technique in which the reactive radical species are converted to stable radicals that are detectable by EPR. Spin-trap EPR is sometimes used in electrochemistry (see also part (III)) however, use of spin traps may lead to unwanted side reactions. In **chapter 4,** these non-innocent side reactions are investigated for a specific case in homogeneous catalysis. The reactivity of 5,5-dimethylpyrroline-N-oxide (DMPO) with Cu(II) complexes is considered as the case study. Different EPR techniques provided extensive information on the ligands that coordinate to the Cu(II) paramagnetic centre. DFT computation results are used in order to identify the molecular structures of the complexes and learn about the unwanted reactions.

Part III (EPR-spectroelectrochemistry and spin-trapping) consists of four chapters that focus on the analysis of electrochemical reactions using *in-situ* and *ex-situ* EPR in which spin traps are used.

Chapter 5 studies the *in-situ* electrochemical cyclisation mechanism of allyl 2-bromobenzyl ether. An electrochemical setup to perform *in-situ* EPR experiments designed in the ELCAT group of the University of Antwerp was employed in order to validate the proposed cyclization mechanism of 2-bromobenzyl ether. This work shows the application of *in-situ* EPR experiments and spin-trapping to detect the reactive radical intermediates. DFT computations are included to support the experimental data.

In **chapter 6**, a spectro-electrochemistry setup using wire electrodes is used to study the electrochemical self-condensation of acetone. A combination of *in-situ* EPR, use of spin traps, and DFT is employed to understand the reaction mechanism

Chapters 7 and 8 focus on *ex-situ* EPR experiments using spin traps to elucidate electrochemical processes.

In **chapter 7**, collaborative work with the A-Sense lab (University of Antwerp) is discussed. The chapter highlights how spin-trap EPR and DFT allow the identification of radical cation intermediates generated during the detection of ecstasy with an electrochemical setup.

Chapter 8 briefly highlights the collaboration with the SURF group (VUB) on the oxygen reduction reaction with Pt nanoparticles as the catalyst on electrodes.

Part IV (Direct EPR spectroelectrochemistry**)** focuses on the direct detecting of paramagnetic intermediates with EPR.

Chapter 9 is a short chapter in which I will introduce two different *in-situ* setups that were designed by the ELCAT group. The SEC-EPR validation occurred through the electrochemical reduction of methyl viologen and benzoquinone in which the generated radicals can be directly observed with EPR,

Chapter 10 will focus on the carbon-halogen (C-X) electrochemical reduction. In this chapter, the electrochemical reduction of 1- and 2-bromonaphthalene species is studied. *In-situ* EPR experiments at room temperature are performed to detect the radical intermediates.

Finally, **chapter 11** focuses on Mo-Cu complexes employed as catalysts for CO_2 reduction. A reaction mechanism was proposed earlier [38], and a preliminary EPR study of intermediate states in the mechanism is given. Electrolysis has been carried out in two different electrochemical cells with different sampling methods. In the first setup,

electrolysis was performed in bulk and transferred afterwards to the EPR tube. In the second method, electrolysis was performed in an EPR tube ($\emptyset$ $4\ mm$). The sample was freeze-quenched during electrolysis

1.6 References

[1]   *World Energy Outlook 2015" (International Energy Agency, 2015)*,
        https://www.iea.org/reports/world-energy-outlook-2015.
[2]   S. Venkata Mohan and A. Pandey, *Sustainable Hydrogen Production*, in
        Biohydrogen, Vol. 305 (Elsevier, 2019), pp. 1–23.
[3]   S. Chu and A. Majumdar, *Opportunities and Challenges for a Sustainable
        Energy Future*, Nature **488**, 294 (2012).
[4]   N. S. Lewis and D. G. Nocera, *Powering the Planet: Chemical Challenges in
        Solar Energy Utilization*, Proc. Natl. Acad. Sci. U. S. A. **103**, 15729 (2006).
[5]   R. Gardner, *The Outlook for Energy: A View to 2040*, in *2015 EDI Proceedings*
        (ASEE Conferences, 2015).
[6]   S. Rashmi Pradhan, R. F. Colmenares-Quintero, and J. C. Colmenares
        Quintero, *Designing Microflowreactors for Photocatalysis Using
        Sonochemistry: A Systematic Review Article*, Molecules **24**, 3315 (2019).
[7]   P. T. Anastas, L. G. Heine, and T. C. Williamson, *Green Chemical Syntheses
        and Processes* (ACS Publications, 2000).
[8]   P. T. Anastas and M. M. Kirchhoff, *Origins, Current Status, and Future
        Challenges of Green Chemistry*, Acc. Chem. Res. **35**, 686 (2002).
[9]   P. T. Anastas and J. Warner, *Green Chemistry : Theory and Practice* (Oxford
        University Press, New York, 1998).
[10]   P. Anastas and N. Eghbali, *Green Chemistry: Principles and Practice*, Chem.
        Soc. Rev. **39**, 301 (2010).
[11]   V. Polshettiwar and R. S. Varma, *Green Chemistry by Nano-Catalysis*, Green
        Chem. **12**, 743 (2010).
[12]   B. C. Gates, *Catalytic Chemistry* (John Wiley and Sons Inc, New York, 1991).
[13]   *The Nobel Prize in Chemistry 2021*,
        https://www.nobelprize.org/prizes/chemistry/2021/summary.
[14]   *The Nobel Prize in Chemistry 2010*,
        http://nobelprize.org/nobel_prizes/chemistry/laureates/2010/.
[15]   *The Nobel Prize in Chemistry 2005*,
        http://nobelprize.org/nobel_prizes/chemistry/laureates/2005/].
[16]   S. Van Doorslaer and D. M. Murphy, *EPR Spectroscopy in Catalysis*, EPR
        Spectrosc. **321**, 1 (2011).
[17]   R. Agrawal, *Separations: Perspective of a Process Developer/Designer*,
        AIChE J. **47**, 967 (2001).
[18]   G. Rothenberg, *Catalysis : Concepts and Green Applications* (Wiley-VHC,
        Weinheim, 2008).
[19]   B. A. Frontana-Uribe, R. D. Little, J. G. Ibanez, A. Palma, and R. Vasquez-
        Medrano, *Organic Electrosynthesis: A Promising Green Methodology in
        Organic Chemistry*, Green Chem. **12**, 2099 (2010).
[20]   J. Tanko, *Encyclopedia of Electrochemistry. Volume 8: Organic
        Electrochemistry* (ACS Publications, 2005).
[21]   O. Hammerich and B. Speiser, *Organic Electrochemistry* (CRC Press Boca
        Raton, FL, New York, 2016).
[22]   M. Albert, *Introduction to Green Chemistry* (CRC Press, New York, 2001).

[23] Z. W. Seh, J. Kibsgaard, C. F. Dickens, I. Chorkendorff, J. K. Nørskov, and T. F. Jaramillo, *Combining Theory and Experiment in Electrocatalysis: Insights into Materials Design*, Science. **355**, 141 (2017).

[24] G. A. Olah, A. Goeppert, and G. K. S. Prakash, *Beyond Oil and Gas: The Methanol Economy* (Wiley. VCH Verlag GmbH and Co. KGaA, Weinheim, 2018).

[25] J. M. Campos-Martin, G. Blanco-Brieva, and J. L. G. Fierro, *Hydrogen Peroxide Synthesis: An Outlook beyond the Anthraquinone Process*, Angew. Chemie Int. Ed. **45**, 6962 (2006).

[26] *Mineral Commodity Summaries*, https://pubs.er.usgs.gov/publication/70140094.

[27] Y. Jiao, Y. Zheng, M. Jaroniec, and S. Z. Qiao, *Design of Electrocatalysts for Oxygen- and Hydrogen-Involving Energy Conversion Reactions*, Chem. Soc. Rev. **44**, 2060 (2015).

[28] J. D. Benck, T. R. Hellstern, J. Kibsgaard, P. Chakthranont, and T. F. Jaramillo, *Catalyzing the Hydrogen Evolution Reaction (HER) with Molybdenum Sulfide Nanomaterials*, ACS Catal. **4**, 3957 (2014).

[29] S. Siahrostami, A. Verdaguer-Casadevall, M. Karamad, D. Deiana, P. Malacrida, B. Wickman, M. Escudero-Escribano, E. A. Paoli, R. Frydendal, T. W. Hansen, I. Chorkendorff, I. E. L. Stephens, and J. Rossmeisl, *Enabling Direct H_2O_2 Production through Rational Electrocatalyst Design*, Nat. Mater. **12**, 1137 (2013).

[30] D. T. Whipple and P. J. A. Kenis, *Prospects of CO_2 Utilization via Direct Heterogeneous Electrochemical Reduction*, J. Phys. Chem. Lett. **1**, 3451 (2010).

[31] C. J. M. van der Ham, M. T. M. Koper, and D. G. H. Hetterscheid, *Challenges in Reduction of Dinitrogen by Proton and Electron Transfer*, Chem. Soc. Rev. **43**, 5183 (2014).

[32] E. Santos and W. Schmickler, *Catalysis in Electrochemistry: From Fundamental Aspects to Strategies for Fuel Cell Development* (John Wiley and Sons, New Jersey, 2011).

[33] J. C. Dong, X. G. Zhang, V. Briega-Martos, X. Jin, J. Yang, S. Chen, Z. L. Yang, D. Y. Wu, J. M. Feliu, C. T. Williams, Z. Q. Tian, and J. F. Li, *In Situ Raman Spectroscopic Evidence for Oxygen Reduction Reaction Intermediates at Platinum Single-Crystal Surfaces*, Nat. Energy **4**, 60 (2019).

[34] J. Sun, L. Gong, W. Wang, Z. Gong, D. Wang, and M. Fan, *Surface-enhanced Raman Spectroscopy for On-site Analysis: A Review of Recent Developments*, Luminescence **35**, 808 (2020).

[35] J.-Y. Ye, Y.-X. Jiang, T. Sheng, and S.-G. Sun, *In-Situ FTIR Spectroscopic Studies of Electrocatalytic Reactions and Processes*, Nano Energy **29**, 414 (2016).

[36] L. Dunsch, *Recent Advances in in Situ Multi-Spectroelectrochemistry*, J. Solid State Electrochem. **15**, 1631 (2011).

[37] K. Dyrek and M. Che, *EPR as a Tool to Investigate the Transition Metal Chemistry on Oxide Surfaces*, Chem. Rev. **97**, 305 (1997).

[38] A. Mouchfiq, T. K. Todorova, S. Dey, M. Fontecave, and V. Mougel, *A Bioinspired Molybdenum–Copper Molecular Catalyst for CO_2*

Electroreduction, Chem. Sci. **11**, 5503 (2020).

CHAPTER 2

Experimental and Computational Methods

In this chapter, I introduce the main methods that have been used during this thesis.

In the first part, the focus lies on the theoretical and experimental aspects of electron paramagnetic resonance (EPR) spectroscopy. First, a brief explanation of the theory behind EPR spectroscopy will be given. Next, I will introduce different terms of the spin Hamiltonian of a paramagnetic system. Then I will focus on different EPR techniques such as continuous-wave (CW) and pulse EPR methods.

In the next section, I explain some basic electrochemistry methods that are employed in the experiments of this thesis.

The last section contains a short introduction in the density functional theory (DFT) and its use to compute EPR parameters.

2.1 Electron paramagnetic resonance spectroscopy

EPR spectroscopy is a magnetic resonance technique that can only be applied to study systems containing unpaired electrons called paramagnetic systems. Fortunately, there are plenty of categories of paramagnetic systems, such as (in)organic radicals or transition metals in particular oxidation states. Due to the unpaired electron(s) in their electronic structure, paramagnetic species have non-zero total electron spins ($S > 0$). A free electron contains an inherent magnetic moment given by $\hat{\boldsymbol{\mu}} = -g_e \mu_B \hat{\boldsymbol{S}}$, with $g_e \approx 2.0023$ the free electron g-factor and $\mu_B = \frac{e\hbar}{2m_e}$ the Bohr magneton ($9.274 \times 10^{-24} J\,T^{-1}$), with $e = 1.602 \times 10^{-19}\,C$ the electron charge, $\hbar = \frac{h}{2\pi}$ and $h = 6.626 \times 10^{-34}\,J\,Hz^{-1}$ the Planck constant, and $m_e = 9.11 \times 10^{-31}\,kg$ the electron mass.

The EPR technique is based on the interaction of electromagnetic waves and the inherent magnetic moments of electron spin in an external magnetic field. Let us describe this for a free electron. The presence of an external magnetic field $\boldsymbol{B_0}$ lifts the degeneracy of the spin states and splits them. This phenomenon is called the Zeeman effect. The Hamiltonian of such a system, considering $\boldsymbol{B_0} \parallel \boldsymbol{Z}$, is given by:

$$\hat{H} = -\hat{\boldsymbol{\mu}}.\,\boldsymbol{B_0} = g_e \mu_B B_0 \hat{S}_z \qquad (2.1)$$

with the corresponding energy eigenvalues of :

$$E_{\alpha,\beta} = g_e \mu_B B_0 m_s = \pm \frac{1}{2} g_e \mu_B B_0 \qquad (2.2)$$

where the $E_{\alpha,\beta}$ represents the energy eigenvalues of the electron spin states $|\alpha>$ and $|\beta>$, corresponding to the electron spin number $m_s = +1/2$ and $m_s = -1/2$, respectively.

In an EPR experiment, a paramagnetic system in the magnetic field is irradiated by electromagnetic waves (usually microwaves (MW)). If the energy difference between the two spin states becomes equal to the energy of a single photon, the electron can change its spin state by absorbing the photon. EPR records this spin transition. The condition that fulfils the transition is called the resonance condition, which can be written as:

$$\Delta E = h\nu = g_e \mu_B B_0 \qquad (2.3)$$

In real-life systems, the unpaired electron is localized in molecular orbitals. Hence the orbital angular momentum $\hat{\boldsymbol{L}}$ and its related magnetic moment will play a role. For a non-degenerated electronic ground state, the orbital angular momentum is quenched ($L = 0$). Although this is the case for many organic radical systems, the interaction between the ground state and excited state can couple the spin and orbital angular momentum by admixing the angular momentum from the excited states into the ground states. The Spin-Orbit (SO) interaction causes a deviation from the principal g-value of the free electron (g_e).

$$hv = (g_e + \Delta g)\mu_B B_0 = g\mu_B B_0 \qquad (2.4)$$

This deviation Δg is a local effect on the paramagnetic centre, so the g-factor is a fingerprint for the corresponding paramagnetic centre. The environment of the unpaired electron is most often non-isotropic. Hence, $\boldsymbol{g}$, in general, is a tensor represented by a 3×3 matrix. In its eigenspace, the $\boldsymbol{g}$-tensor is diagonal with principal values g_x, g_y, and g_z.

$$\boldsymbol{g} = \begin{pmatrix} g_{xx} & g_{xy} & g_{xz} \\ g_{yx} & g_{yy} & g_{yz} \\ g_{zx} & g_{zy} & g_{zz} \end{pmatrix} \Rightarrow \boldsymbol{g}_{diagonal} = \begin{pmatrix} g_x & 0 & 0 \\ 0 & g_y & 0 \\ 0 & 0 & g_z \end{pmatrix} \qquad (2.5)$$

In case $g_x = g_y = g_z$, this reduces to an isotropic scalar for higher than cubic symmetry systems. In case there is local axial symmetry, we have $g_x = g_y \neq g_z$, and for a rhombic symmetry or lower, the principal g-values will be $g_x \neq g_y \neq g_z$.

In a non-viscous liquid sample, due to the fast rotation of the molecules, the anisotropy contribution of $\boldsymbol{g}$ is averaged to zero, and there is only the isotropic contribution of $\boldsymbol{g}$-tensor [1–3].

$$g_{iso} = \frac{g_x + g_y + g_z}{3} \qquad (2.6)$$

2.1.1 The spin Hamiltonian

So far, we have only considered the interaction of an unpaired electron and the external magnetic field. In a paramagnetic molecule, the unpaired electron may additionally experience several interactions depending on the molecular environment. These interactions are caused by surrounding magnetic nuclei or/and surrounding electron spins. The terms of the spin Hamiltonian that are of interest in this study are:

$$\hat{H} = \hat{H}_{EZ} + \hat{H}_{NZ} + \hat{H}_{HF} + \hat{H}_{NQ} + \hat{H}_{ZFS} \qquad (2.7)$$

with $\hat{H}_{EZ}$ the electron Zeeman interaction, $\hat{H}_{NZ}$ the nuclear Zeeman interaction, $\hat{H}_{HF}$ the hyperfine interaction, $\hat{H}_{NQ}$ the nuclear-quadrupole interaction, and $\hat{H}_{ZFS}$ the zero-field splitting interaction. In the following subsections, I briefly describe these interactions and their origins.

2.1.1.1 Electron Zeeman interaction

I already introduced the electron Zeeman (EZ) interaction describing the interaction between the unpaired electron spin and the external magnetic field. As mentioned earlier, $\hat{L}$ plays an important role, and in the most general case, the Hamiltonian is a sum of EZ and SO coupling:

$$\hat{H} = \mu_B \, \boldsymbol{B_0}\big(g_e\hat{S} + \hat{L}\big) + \lambda\hat{L}\,.\hat{S} \tag{2.8}$$

with λ the SO coupling constant. By considering an effective spin operator $\hat{S}'$ and a non-isotropic effective $\boldsymbol{g}$-tensor, the electron Zeeman spin Hamiltonian interaction can be written as:

$$\hat{H}_{EZ} = \mu_B\boldsymbol{B_0}\boldsymbol{g}\hat{S}' \tag{2.9}$$

Using second-order perturbation theory the $\boldsymbol{g}$-tensor can be defined as the sum of an isotropic term and a non-isotropic term resulting from SO coupling.

$$\boldsymbol{g} = \boldsymbol{1}g_e + 2\lambda\boldsymbol{\Lambda} \tag{2.10}$$

with $\boldsymbol{\Lambda}$ a symmetric tensor with matrix elements:

$$\Lambda_{\mu,\nu} = \sum_{n\neq0} \frac{\langle\Psi_0|\hat{L}_\mu|\Psi_n\rangle\langle\Psi_n|\hat{L}_\nu|\Psi_0\rangle}{\epsilon_0 - \epsilon_n} \tag{2.11}$$

where $\hat{L}_\mu$ are the angular momentum operators along the $\mu = x, y, z$ axes and $n = 1, 2, 3, ...$ represents the quantum number of the excited states Ψ_n with eigenvalue ϵ_n. In the following, the effective spin operator will be indicated as $\hat{S}$.

2.1.1.2 Nuclear Zeeman interaction

The nuclear Zeeman (NZ) interaction appears when there are nuclei with non-zero spin in the system that is studied. This interaction describes the Zeeman interaction between nuclear spins and the external magnetic field.

$$\hat{H}_{NZ} = \mu_n \sum_k \boldsymbol{B_0}g_{n,k}\,\hat{I}_k = \mu_n \sum_k B_0 g_{n,k}\,\hat{I}_{k,z} \tag{2.12}$$

where μ_n is the nuclear magneton, $\boldsymbol{B_0}$ is the external magnetic field, g_n is the nuclear g-factor and $\hat{I}_k$ is the nuclear spin operator. Moreover, the corresponding energy values are given by:

$$E = \mu_n B_0 g_n m_I \tag{2.13}$$

where m_I is the magnetic quantum number of the nuclei [1,3].

2.1.1.3 Hyperfine interaction

The hyperfine (HF) interaction describes the interaction between the electron spin and the nuclear spins ($I_k > 0$). This term is given by:

$$\widehat{H}_{HF} = \sum_k \widehat{\mathbf{S}} \cdot \mathbf{A}_k \cdot \widehat{\mathbf{I}}_k \tag{2.14}$$

where $\widehat{\mathbf{S}}$ represents the electron spin operator and $\mathbf{A}_k$ the hyperfine interaction tensor and $\widehat{\mathbf{I}}_k$ the nuclear spin operator of the kth nucleus
The hyperfine interaction tensor consists of two different parts:

$$\mathbf{A} = a_{iso}\mathbf{1} + \mathbf{T} \tag{2.15}$$

The first term is the Fermi contact or isotropic hyperfine coupling, which occurs due to the non-zero electron spin density at the nucleus with the isotropic hyperfine coupling coefficient a_{iso} being

$$a_{iso} = \frac{2\mu_0}{3} g_e \mu_B \, g_n \mu_N \rho_N^{\alpha-\beta} \tag{2.16}$$

$\rho_N^{\alpha-\beta}$ represents the spin density at nucleus N, which gives the difference between the expectation value of the number of electrons in α and β spin states. Moreover, $\mathbf{1}$ is the 3×3 unit matrix.
The second term is the anisotropic part, which stems from the magnetic dipole-dipole interaction of the electron and nuclear spin given by:

$$T_{ij} = \frac{\mu_0}{4\pi} g_e \mu_B \, g_n \mu_N \left\langle \psi_0 \left| \left[\frac{3r_i r_j}{r^5} - \frac{\delta_{ij}}{r^3} \right] \right| \psi_0 \right\rangle \tag{2.17}$$

where $|\psi_0\rangle$ is the ground-state wave function of the electron, and r_i represent the coordinates of the electron spin ($i = x, y, z$) with respect to the nuclear spin.
The hyperfine coupling interaction is often considerably smaller than 10^3 MHz [1,3]. We will see typical examples in later chapters.

2.1.1.4 Nuclear-quadrupole interaction

The nuclear-quadrupole (NQ) interaction describes the interaction between the electric quadrupole moment of the nucleus and the electric field gradient (EFG) due to all charges around the nucleus. This EFG is described as a 3×3 matrix, expressing the second derivative of the electrostatic potential $V(\mathbf{r})$ at the nucleus, due to charge e at position $\mathbf{r}$.

$$eq = \begin{pmatrix} V_{xx} & V_{xy} & V_{xz} \\ V_{yx} & V_{yy} & V_{yz} \\ V_{zx} & V_{zy} & V_{zz} \end{pmatrix} = \frac{\partial^2 V(\boldsymbol{r})}{\partial i \partial j} \qquad (2.18)$$

with $i, j = x, y, z,$ and e is the elementary charge. This matrix is traceless and symmetric and can be diagonalized to

$$eq = \begin{pmatrix} V_x & 0 & 0 \\ 0 & V_y & 0 \\ 0 & 0 & V_z \end{pmatrix} \qquad (2.19)$$

Nuclei with spin $I > \frac{1}{2}$ have non-spherical charge distribution. The deviation from the spherical distribution causes an electric quadrupole moment Q.
Equation (2.20) describes the nuclear-quadrupole interaction resulting from the interaction between the EFG and the quadrupole moment.

$$\hat{H}_{NQ} = \hat{\boldsymbol{I}}.\boldsymbol{P}.\hat{\boldsymbol{I}} \qquad (2.20)$$

$\boldsymbol{P}$ is the nuclear-quadrupole tensor, a 3×3 symmetric, and traceless matrix which is diagonal in the eigenframe.

$$\begin{pmatrix} P_x & 0 & 0 \\ 0 & P_y & 0 \\ 0 & 0 & P_z \end{pmatrix} = \begin{pmatrix} K(-1+\eta) & 0 & 0 \\ 0 & K(-1-\eta) & 0 \\ 0 & 0 & 2K \end{pmatrix} \qquad (2.21)$$

with K determined by:

$$K = \frac{e^2 qQ/h}{4I(2I-1)} = \frac{P_z}{2} \qquad (2.22)$$

and eq is the V_z.
Furthermore, η is obtained by:

$$\eta = \frac{P_x - P_y}{P_z} \qquad (2.23)$$

The principal values P_x, P_y, P_z of the nuclear-quadrupole matrix are labeled as: $|P_x| \leq |P_y| \leq |P_z|$ and $0 \leq \eta \leq 1$. The magnitude of nuclear quadrupole interaction is typically in the range of $10^{-1} - 10^1 MHz$. [1,3]. We will see examples in chapter 4.

2.1.1.5 Zero-field splitting

The zero-field splitting interaction arises when there is more than one unpaired electron ($S>1/2$) in the system. Zero-field splitting spin Hamiltonian is described by:

$$\hat{H}_{ZFS} = \widehat{S}.D.\widehat{S} \qquad (2.24)$$

In which D is the zero-field interaction tensor. The origins of this interaction are i) spin-spin coupling, which is due to the magnetic dipole interaction between the unpaired electrons, and ii) spin-orbit coupling [1,3].
None of the systems that we have investigated in this thesis are high spin.

2.1.2 Continuous-wave EPR

The continuous-wave (CW) EPR experiment was introduced by Zavoisky in 1944 [4]. In this experiment, a paramagnetic sample is continuously irradiated with MW with a constant frequency. A sweepable magnetic field is simultaneously applied to the sample. The paramagnetic sample absorbs the MW species at the resonance condition (Equations (2.3), Figure 2.1 *a*). In the CW-EPR experiment, the MW absorption is detected as a function of magnetic field, and the spectrum reflects the EPR parameters (Figure 2.1 *b)*. The sweep range of the magnetic field should cover the specific magnetic field in which the resonance condition is satisfied. It is advantageous in a CW-EPR experiment to record the spectrum via amplitude modulation as the first derivative of the absorption spectrum (Figure 2.1 c). The main advantage is the noise reduction.
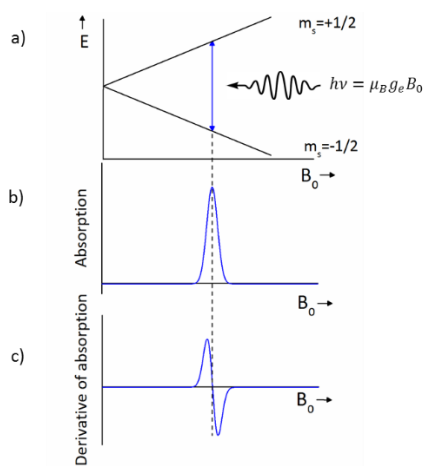

Figure 2.1 Illustration of a CW-EPR experiment on free electrons. a) The resonance condition of a free electron ($S = \frac{1}{2}$) in the magnetic field; b) The MW absorption signal for this system; c) The EPR signal via amplitude modulation leading to the first derivative signal.

Since in a general case, $\boldsymbol{g}$ is a tensor with a fixed orientation versus the molecule frame, the molecule's orientation in the magnetic field will change the magnetic field at which the EPR signal is observed. For powders or frozen samples of systems with anisotropic $\boldsymbol{g}$-tensor, the overall spectrum will reflect the g-anisotropy. In those cases, all $\boldsymbol{g}$-tensor orientations versus the magnetic field are observed simultaneously since all orientations of the molecule versus the magnetic field occur. The resonance condition is different for each orientation of the molecule versus the magnetic field. The final spectrum will be the sum of the EPR signals for all the orientations weighted with their relative occurrence. Figure 2.2 shows the EPR spectra of different symmetries of the $\boldsymbol{g}$-tensor for an $S = \frac{1}{2}$ system. A system characterized by an isotropic g-value gives rise to a signal peak at a magnetic field position corresponding to g_{iso}. In the case of axial symmetry ($e.g.$ $g_\perp = g_y = g_z \neq g_x = g_\parallel$) we discern the two different principal g-values and for the rhombic case $g_y \neq g_z \neq g_x$ we recognize the principal g-values at three magnetic field values (Figure 2.2).
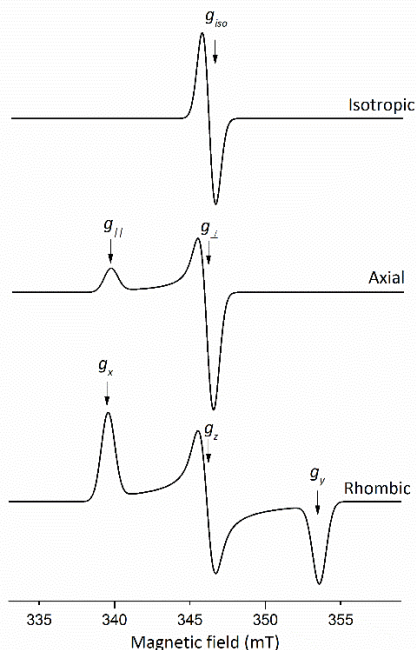
Figure 2.2. Examples of CW-EPR spectra corresponding to different g-tensor symmetries for an $S = \frac{1}{2}$ system

For an $S = \frac{1}{2}$ and $I > 0$ system, the hyperfine interaction and nuclear Zeeman interaction will also affect the EPR spectrum, leading to further splitting of the EPR lines.

Figure 2.3a) shows the energy-level diagram of a system with $S = \frac{1}{2}$ and $I = \frac{1}{2}$ values (two-spins system) in the presence of a fixed external magnetic field where the nuclear Zeeman interaction is larger than hyperfine interaction. We assume for simplicity that g and hyperfine coupling are isotropic. As explained in sections 2.1.1.2 and 2.1.1.3, the

M.Samanipour

nuclear spin interacts with both the external magnetic field (NZ) and the electron spin (HF). Taking into account only the EZ, NZ, and HF interactions, the energy at a given external field B_0 is

$$E = g_{iso}\mu_B B_0 m_s - g_N \mu_N B_0 m_I + a_{iso} m_s m_I \qquad (2.25)$$

where $m_s = \pm\frac{1}{2}$ represents the electron magnetic spin quantum state and $m_I = \pm\frac{1}{2}$ represents the nuclear magnetic spin quantum state. Equation (2.25) thus gives four different energy levels. After the energy splitting caused by the EZ interaction, further splittings occur due to the NZ interaction. Finally, the HF interaction shifts the energy levels with $\frac{1}{4}a_{iso}$ up and down according to the third term of equation (2.25). In a CW-EPR experiment, a spin transition should only change the electron spin state ($\Delta m_s = \pm 1$ and $\Delta m_I = 0$), which are the allowed transitions. For an $S = \frac{1}{2}$, $I = \frac{1}{2}$ system, there are two allowed EPR transitions with the energy quanta EPR I and EPR II(Figure 2.3a). By sweeping the magnetic field under MW irradiation, the resonance condition will be reached consecutively for the two transitions. Figure 2.3.b) shows the corresponding CW-EPR spectrum for the two-spin system that was described above. The spectrum consists of two signals (a doublet). The magnitude of the separation between the EPR signals is proportional to the isotropic hyperfine coupling constant a_{iso}:

$$B_0(EPR\ II) - B_0(EPR\ I) = \frac{a_{iso}}{\mu_B\ g_{iso}} \qquad (2.26)$$
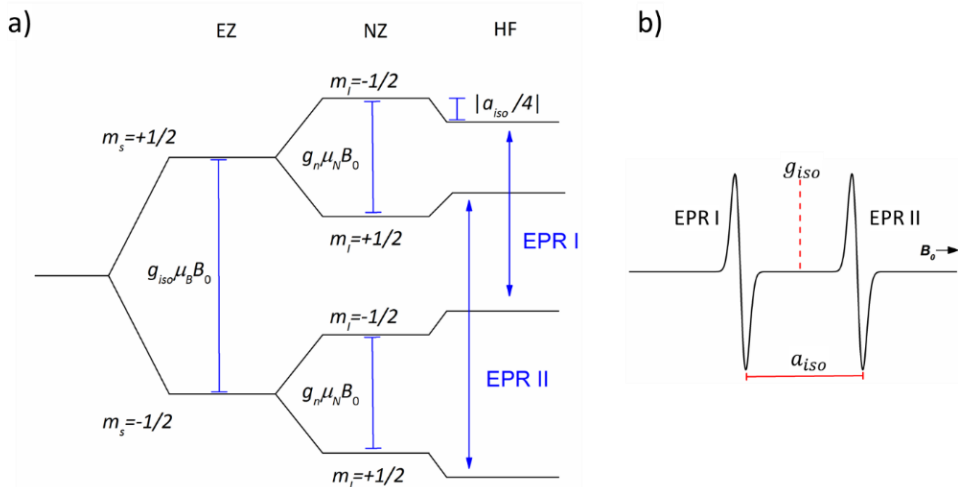
Figure 2.3. a)The energy-level diagram of an S=1/2 and I =1/2 spin system in a fixed external magnetic field with isotropic g and hyperfine values. Where g_N and a_{iso} are positive and $\frac{a_{iso}}{2} < g_N \mu_N B_0$ and b)the corresponding CW-EPR spectrum.

The number of lines in an EPR spectrum is related to the nuclear spin number. The relation between the number of lines and the nuclear spin follows a general rule which is given by:

$$N = 2nI + 1 \qquad (2.27)$$

where n is the number of the magnetically equivalent nuclei in terms of nuclear spin and hyperfine coupling, and I is the nuclear spin.

Figure 2.4.a demonstrates the EPR spectra of a water solution of 2,2,6,6-tetramethyl-1-piperidinyloxyl (TEMPO). Because of the rapid motion of TEMPO in water, only the isotropic part of the g-tensor and hyperfine tensor contribute to the spectrum. As the free electron in TEMPO is localized on the NO fraction, and ^{14}N has $I = 1$, the electron spin energy levels are split into three levels corresponding to $m_I = 0, \pm 1$ leading to three EPR transitions. Therefore a triplet appears in the EPR spectrum. In Figure 2.4b, the EPR spectrum of a frozen solution of CuI in dimethyl sulfoxide (DMSO) in the presence of O_2 is shown. Cu(I) is diamagnetic, and thus EPR silent. It becomes oxidized by O_2 to Cu(II), and Cu(II) forms a square pyramidal complex with DMSO. The g-tensor symmetry is axial. Since $^{63,\,65}Cu$ has a nuclear spin $I = \frac{3}{2}$ four EPR lines at each principal g-value direction are expected. In the low magnetic field are, a clear splitting in four lines is indeed observed for the $g_{\parallel}$ signal. The $A_{\parallel}$ hyperfine coupling value is large ($A_{\parallel} = 375\ MHz$) in the magnetic field area reflecting $g_{\perp}$ and $A_{\perp}$, a broad singnal is observed. Here, $A_{\perp}$ is small and the hyperfine splitting in unresolved.

Figure 2.4 The experimental X-band CW-EPR spectrum of a) 0.5 mM solution of TEMPO at room temperature, b) frozen solution of 50 mM CuI in DMSO under the air/O_2 measured at 100 K.

M.Samanipour

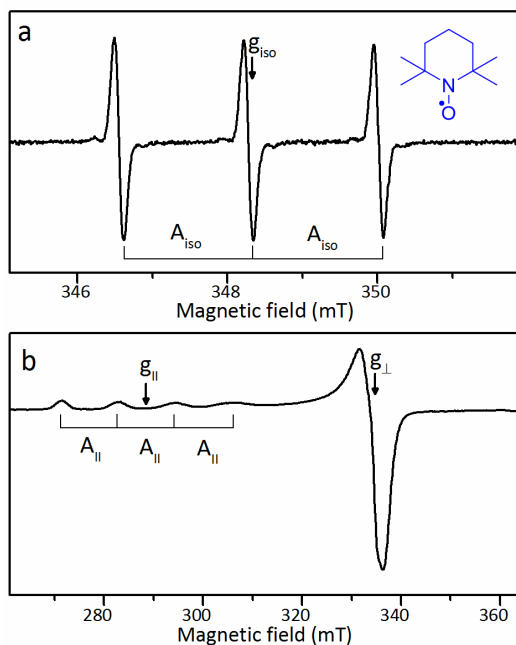In the CW-EPR spectrum in Figure 2.4b, the signals are broad. The broadening can be due to several reasons, such as unresolved hyperfine structures, g and A strain effects or dipolar broadening. The line broadening can be homogeneous or inhomogeneous, leading to Lorentzian and Gaussian line shapes, respectively. In many real systems, none of the line shapes is the case, but a convolution of both profiles (Voigtian shape) contributes to the CW-EPR spectrum. Depending on the system, the line broadening can be isotropic or anisotropic.

2.1.2.1   Rotational diffusion (molecular tumbling)

As explained before, in a non-viscous solvent, the anisotropic interactions are completely averaged due to the rapid molecular tumbling. In many systems, the molecular tumbling is not fast enough to produce fully isotropic spectra. In these cases, the effect of rotational diffusion should be considered. The rotational correlation time coefficient τ_c characterises this effect. In order to completely average out the anisotropy, the molecular tumbling rate should be much faster than the difference in the resonant condition of different molecular orientations. For example, in nitroxides with a hyperfine anisotropy ($A_{zz} - A_{xx}$ (A_{yy})) of 3 mT (84 MHz = 8.4×10^7 s^{-1}), the rotational correlation time should be much shorter than 10^{-9} s (in practice, below 10^{-11} s). Such small τ_c-values are the case for small objects in solutions with low viscosity but not for large systems or viscose solvents. Insufficiently fast rotational diffusion leads to broadening in CW-EPR lines, and this broadening of spectra falls into two categories of fast and slow motion. Fast motion is observed when $\frac{1}{\tau_c}$ is larger than the resonance frequencies of different molecular orientations ($\tau_c < 10^{-9}$ s for nitroxides) but still short enough to observe the line broadenings on the CW-EPR spectra. The rotational diffusion can be isotropic or anisotropic.

Slow motion is observed when $\frac{1}{\tau_c}$ is similar to or smaller than the difference in resonance frequencies for different molecular orientations. Slow motion is often observed in viscous solvents or when a radical is attached to a large molecular assembly. The shape of the EPR spectra in slow motion is more complicated than the fast motion effect, considering local motions on top of the tumbling of the whole system. Despite the presence of several models, simulation of the slow motion effect is not straightforward.

The effect of rotational diffusion on the spectra is illustrated in chapters 4 (Figure 4.7) and 10 (Figure 10.6) [2].

A CW-EPR experiment can be performed at different microwave frequencies and, as a consequence, different magnetic field ranges. In this thesis, we use X-band CW-EPR for all the measurements. In this kind of experiment, the microwave frequency value is around 9.7 GHz. [2,3].

2.1.3 Spin-trapping

Radical species have unpaired electrons in their electronic structure, making them detectable by EPR. Some radicals, such as organic radicals in solution, are very reactive and therefore have a short lifetime, making them difficult to be detected by EPR. Spin traps are species that react rapidly with the unstable radical species to form a more stable radical. The more stable radical, formed by trapping the unstable spin adduct by the spin trap, lives long enough to be detectable by EPR. Nitrones and nitroso compounds form two main families of spin traps. The first category is used more often due to the stability of their spin adduct. There are generally two families of nitrone spin traps, the cyclic nitrones such as 5,5-dimethyl-1-pyroline *N*-oxide (DMPO) and the acyclic nitrones such as *N*-tert-Butyl-α-phenylnitrone (PBN), which are the most widely used ones. The cyclic and acyclic spin traps are also called DMPO-type and PBN-type nitrones, respectively [5–7].

Moreover, there are several analogues for both of them, such as 5-*tert*-butoxycarbonyl 5-methyl-1-pyrroline *N*-oxide (BMPO) [8], 5-carbamoyl-5-methyl-1-pyrroline *N*-oxide (AMPO) [7], 5-Diethoxyphosphoryl-5-methyl-I-pyrroline N-Oxide (DEPMPO) [9] and 5-di-isopropoxy phosphoryl-5-methyl-1-pyrroline *N*-oxide (DIPPMPO) [10] for DMPO and α-(4-Pyridyl *N*-oxide)-*N-tert*-butylnitrone (4-POBN) [11] for PBN, which is more soluble in water. In general, selection of a particular spin-trap depends on the chemical nature of the radical adduct and the solvent. In this thesis, DMPO and PBN were mainly used due to their efficiency in trapping carbon-centred and oxygen-centred radicals. Moreover, they are electrochemically inert in the potential window that is required.

If needed, other spin traps were used, e.g. DEPMPO.

2.1.4 Simulating CW-EPR spectra

In order to extract information such as electronic and geometry structures from the EPR spectra, the magnetic parameters such as *g* and HF values should be determined. It requires simulation of the EPR spectra. In this thesis, all EPR spectra were simulated using EasySpin [12], which is a package running in MATLAB software which allows the simulation and fitting of the EPR spectrum. Almost any paramagnetic species in a solid state and liquid state can be simulated using Easyspin. The simulation process starts with an educated guess of the EPR parameters based on the experiment, which will then be improved. This improvement can be made either manually by manipulating the EPR parameters by the Easyspin user (which is the case in most parts of this thesis) or using the automatic fitting of Easyspin (esfit). Both methods are very sensitive to the initial values. Therefore the initial guess is important and needs knowledge about investigating spin systems (which should be obtained from the literature) and about the influence of each EPR parameter on the EPR spectrum. For instance, in an isotropic spectrum, the *g*-value can be determined from the central field position of the EPR spectrum and equation (2.3) (see Figure 2.4.a). HF couplings can be determined by the peak distance of a particular splitting on the spectrum (see Figure 2.4.a).

Other important parameters are line width values to simulate the line broadening. Choice of Lorentzian, Gaussian, or Voigtian line broadening can be obtained from the

experimental spectrum. As a result of homogeneous line broadening, Lorentzian lines have very broad wings compared with Gaussian lines, and Gaussian lines are the results of inhomogeneous line broadening. [2]. The starting value of linewidth for simulation can be obtained by measuring the distance between the maximum and minimum of a single line (peak-to-peak linewidth) on the experimental CW-EPR spectrum. Despite similar rules, the simulation process in the presence of anisotropy is more complicated.) because the amount of parameters increases (principle values of the g and HF tensors and the relative orientation of the tensors).

2.1.5 Pulse EPR

As explained above, CW-EPR is a powerful tool to detect EZ interactions and strong hyperfine interactions. Nevertheless, many of the terms in the spin Hamiltonian, such as small HF interactions, NZ interactions, and NQ interactions, are not detectable in a CW-EPR. Pulse EPR brings us enough sensitivity to observe these small interactions.

Despite sharing the same physical basics with CW-EPR, pulse EPR is different in several aspects. Instead of continuously sending low-power MW (≤ 0.2 W at 9-10 GHz) to the sample, short high-power MW pulses (1kW at 9-10 GHz) are used in the pulse EPR experiment. The spectrometer in the pulse EPR experiments records the evolution of the electron magnetization vector $\boldsymbol{M}$ after excitation due to the short MW pulses as opposed to the detection of MW absorption in CW-EPR. In pulse EPR experiments, different parameters of the pulse sequences, such as time delays, pulse lengths, and MW frequency, as well as the magnetic field can be swept. The application of pulse EPR methods that are used in this thesis will be explained later (see 2.1.4.2).

2.1.5.1 Classical picture

A paramagnetic sample in a magnetic field consists of spins with different related spin resonance frequencies due to the different molecular orientations, strain effects, and different quantum states. Paramagnetic centres with approximately the same resonance condition make a spin packet.

In the presence of an external magnetic field $\boldsymbol{B_0}$, the spin packets are aligned along the magnetic field direction in the thermal equilibrium. Hence, the total magnetization vector $\boldsymbol{M} = \frac{1}{V}\sum_i \boldsymbol{\mu_i}$, is aligned with the magnetic field. As before, we choose the z-axis of the laboratory frame along the direction of the magnetic field. If an external force tilts $\boldsymbol{M}$ away from the equilibrium, the magnetic field applies a torque on it, and consequently, the magnetization vector starts to precess counter-clockwise around the z-axis with the precessing frequency (Larmor frequency) of the electrons in the spin packet ω_L, defined below.

$$\omega_L = \gamma B_0 = \frac{g\mu_B B_0}{\hbar} \qquad (2.28)$$

In a pulse EPR experiment, the applied MW pulse induces the tilting of the total magnetization vector $\boldsymbol{M}$ from the z-axis. The rotation frequency is proportional to the

magnitude of the magnetic field B_1 component of the MW pulse. What we measure in a pulse EPR experiment is the precessing of the M vector. The evolution of the M vector is obtained by

$$\frac{d}{dt}M = -\gamma(B_0 + B_1(t)) \times M \qquad (2.29)$$

$B_1(t)$ lies along the x-axis of the laboratory frame. We can decompose $B_1(t)$ in two different counter-rotating components $B_1(t) = B_{1+}(t) + B_{1-}(t)$, which are rotating with the MW frequency. $B_{1+}(t)$ rotates counter-clockwise, and $B_{1-}(t)$ rotates clockwise. Only $B_{1+}(t)$ precesses in resonance with the spins and, as a consequence, interacts effectively with them.
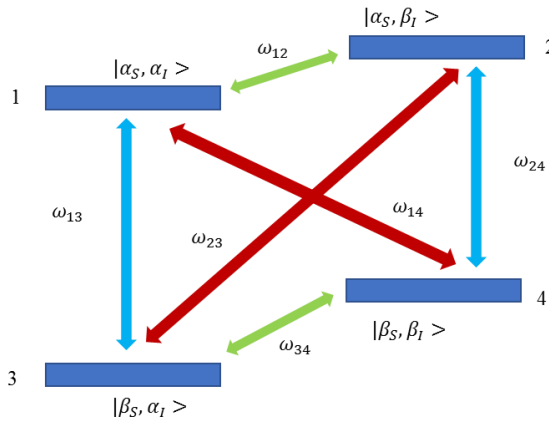
Figure 2.5 The energy level and possible transitions of a system with $S = \frac{1}{2}$ and $I = \frac{1}{2}$. ω_{12} and ω_{34} indicate the nuclear frequencies, which represent the ($|\Delta m_s| = 0$ and $|\Delta m_I| = 1$) transition (green arrows), The blue arrows show the allowed EPR transitions ($|\Delta m_s| = 1$ and $|\Delta m_I| = 0$) and the forbidden EPR transitions ($|\Delta m_s| = 1$ and $|\Delta m_I| = 1$) are in red.

For simplicity, we move to a frame rotating with the MW frequency. In this rotating frame B_{1+} is time-independent. From now on, we call this B_1 instead of B_{1+}. B_1 induces the magnetization to turn from the z-axis to the x,y plane. For rectangular pulses, the flip angle θ is then given by:

$$\theta = \omega_1 t_p = \gamma B_1 t_p \qquad (2.30)$$

in which t_p is the pulse length. A pulse is characterized by its flip angle, *i.e.* a π pulse inverts the direction of the magnetization.

Depending on the parameters one wants to measure, different sequences of pulses with varying flip angles are used. π and $\frac{\pi}{2}$ pulses are often used in common pulse EPR experiments.

M.Samanipour

In the next sections, we will discuss different sequences and their applications. The techniques will be described assuming an $S = \frac{1}{2}$, $I = \frac{1}{2}$ system. For simplicity, the energy scheme in Figure 2.3 is rearranged to the scheme in Figure 2.5.

2.1.5.2 Hyperfine spectroscopy

Hyperfine spectroscopy methods such as electron spin echo envelope modulation (ESEEM) [13] and pulse electron nuclear double resonance (ENDOR) are the pulse EPR techniques that are widely used to probe small transitions that are not resolved in a CW EPR measurement. These transitions can be nuclear Zeeman interactions identifying the nuclei, hyperfine interactions between an electron spin and weakly coupled neighbouring nuclei that are up to 0.8 nm away and the quadrupole interactions of $I > \frac{1}{2}$ nuclei [1,14]. Contributions of these interactions to the spin Hamiltonian have been explained in sections 2.1.1.3 and 2.1.1.4. Detecting small couplings leads us to identify more neighbouring nuclei, which subsequently gives a clearer perspective of the structure of molecules. This, in turn, provides more evidence to characterise the intermediates generated during the (electro)chemical reaction. However, it should be noted that as powerful as pulse EPR can be, most measurements need to be performed in the solid state at low temperature (e.g. frozen solutions or immobilized molecules) because, with the exception of particular spin systems in organic solvents, the spin relaxation times of paramagnetic species at ambient temperatures are too short for the application of pulse sequences and subsequent detection which are normally in the 100 ns to 10 μs timescale. Here we will very briefly describe ESEEM and pulse ENDOR, and I again refer the reader to the literature [3,15] for a more in-depth explanation.

2.1.5.3 ESEEM experiments

Electron spin echo envelope modulation (ESEEM) spectroscopy is a method to detect nuclear frequencies in a paramagnetic system. In all ESEEM experiments, one needs a sequence of MW pulses with a constant frequency which can be subdivided into different building blocks. The sequence starts with the preparation period consisting of one or more pulses to take the electron spins to a coherent or polarized state. Then during an evolution time, the system evolves under the influence of the spin Hamiltonian. The following step is the mixing period in which one induces, by applying a particular MW pulse sequence mixing of electron coherence (EC), electron polarization (EP), nuclear coherence (NC), and nuclear polarization (NP). Finally, in the detection part, a pulse sequence creates detectable EC. In an ESEEM experiment, this last step creates a spin echo, and the intensity of the echo is recorded versus time. The time signal is Fourier transformed to the frequency domain. By simulation of the frequency spectrum, the hyperfine tensor $\boldsymbol{A}$ and quadrupole tensor $\boldsymbol{P}$ of magnetic nuclei in the neighbourhood of unpaired electrons can be determined. The ESEEM experiments are utilized to detect the small nuclear frequencies of the paramagnetic centre ($< 30\ MHz$) [1,3,17,18] (*e.g.* couplings of nuclei in the second coordination sphere of the electron spin).

ESEEM experiments need to be performed at different magnetic field positions to reconstruct the full hyperfine and quadrupole tensors.

In this section, I introduce the ESEEM sequences which are used in the thesis.

2.1.5.3.1 Two-Pulse ESEEM

The two-pulse ESEEM (2P-ESEEM) experiment is the most straightforward experiment among all ESEEM experiments. In this experiment, the Hahn echo sequence $\frac{\pi}{2} - \tau - \pi - \tau - echo$ (Figure 2.6a) is used. In this sequence, the first $\frac{\pi}{2}$ pulse creates EC that evolves during time interval τ before applying the π pulse. The π pulse mixes the ECs, and generates the echo after the second evolution time τ. In a 2P-ESEEM experiment, the intensity of the echo is measured as a function of τ. The echo intensity decreases with τ because of dephasing of the electron spins in the *xy* plane. The time scale in which the magnetic moments precessing in the xy plane within a spin packet lose their phase coherency and cannot refocus to make the echo is described by a quantity called transverse relaxation time (T_2). Besides this, the decaying time signal is modulated with the nuclear frequencies. The echo modulation for an $S = \frac{1}{2}, I = \frac{1}{2}$ system with ideal pulses is given by:

$$V_{2p}(\tau) = 1 - \frac{k}{4}[2 - 2\cos(\omega_{12}\tau) - 2\cos(\omega_{34}\tau) + \cos(\omega_-\tau) + \cos(\omega_+\tau)] \tag{2.31}$$

where k represents the modulation depth and $\omega_\pm$ sum and difference between ω_{12} and ω_{34}. Although the 2P-ESEEM is advantageous in identifying the nuclei coupled to the unpaired electron, it has many disadvantages. In the frequency domain, we see peaks at $\omega_\pm$ which are easily distinguishable for a simple $S = \frac{1}{2}, I = \frac{1}{2}$ system, but in a system with more nuclei, it causes many difficulties to deconvolute the spectrum.

Because of the short T_2 relaxation time of the electron spins, the modulation has to be measured in a short time, consequently causing a broadening of the spectrum in the frequency domain [1,3]. Despite its downsides, 2P-ESEEM is a fast and straightforward method compared with other ESEEM techniques and is often used as a preliminary experiment which provides information to set up more complex experiments such as ENDOR, 3P-ESEEM and HYSCORE.

2.1.5.3.2 Three-pulse ESEEM

The three pulse ESEEM (3P-ESEEM) experiment is based on the stimulated echo from the sequence $\frac{\pi}{2} - \tau - \frac{\pi}{2} - T - \frac{\pi}{2} - \tau - echo$, which is shown in Figure 2.6b. The first two $\frac{\pi}{2}$-pulses, applied with the time difference τ induce the NCs. The NC evolves during time T. The time T is the time that is varied during the experiment. The third $\frac{\pi}{2}$-pulse creates ECs. The modulation of the echo during a 3P-ESEEM experiment is given for an $S = \frac{1}{2}, I = \frac{1}{2}$ system by:

$$V_{3p}(\tau) = \frac{1}{2}\left\{\left[1 - \frac{k}{2}[1 - \cos(\omega_{34}\tau)][1 - \cos(\omega_{12}(T + \tau))]\right]\right.$$

$$\left. + \left[1 - \frac{k}{2}[1 - \cos(\omega_{12}\tau)]\big[1 - \cos\big(\omega_{34}(T + \tau)\big)\big]\right]\right\}$$

(2.32)

As we see in equation (2.32), the combination frequencies $\omega_\pm$ no longer contribute and we only have the basic nuclear frequencies. In contrast with 2P-ESEEM, we have fewer detected frequencies, which makes it a preferred method over 2P-ESEEM.

In a 3P-ESEEM, due to inducing NCs, the nuclear spin-spin relaxation time determines the time domain limitation. The nuclear spin-spin relaxation time is of the order of electron spin-lattice relaxation time T_1. The longer relaxation time solves the earlier mentioned broadening problem in the frequency domain that occurs in the two-pulse ESEEM experiment.

The echo-modulation in the 3P-ESEEM experiment depends on the τ-value, leading to blind spots for some specific τ-value. Hence the experiment should be repeated at different τ-values, which is time-consuming. Another issue with the 3P-ESEEM is that it creates undesirable extra echoes. A phase cycling procedure needs to be applied to exclude those echoes. [1,3,19]

2.1.5.4 HYSCORE

Since the 2P-ESEEM and 3P-ESEEM are one-dimensional experiments, signal overlaps may hamper spectral analysis. Hyperfine Sublevel Correlation Spectroscopy (HYSCORE) is a two-dimensional four-pulse method that can solve this drawback. The MW pulse sequence $\frac{\pi}{2} - \tau - \frac{\pi}{2} - t_1 - \pi - t_2 - \frac{\pi}{2} - \tau - echo$ (Figure 2.6c) is used in this experiment. The first two $\frac{\pi}{2}$-pulses with an evolution time τ create NC. After a time t_1 the π-pulse mixes NC. After the second free-evolution time t_2, a $\frac{\pi}{2}$-pulse transfers the NC to detectable EC. In the experiments, the free-evolution times t_1 and t_2 are varied independently, and the intensity of echo is recorded for each pair of (t_1, t_2). A two-dimensional Fourier transform converts the time signals to the frequency domain (ν_1, ν_2). The frequency domain can be divided into four quadrants based on the sign of the frequencies. We only depict (+,+) and (-,+) quadrants because the others contain the same information. In case of weak coupling ($|\frac{A}{2}| < |\nu_N|$, ν_N is the NZ frequency), the cross-peaks appear in (+,+) quadrant, and in case of strong coupling ($|\frac{A}{2}| > |\nu_N|$), we observe them in the (-,+) quadrant. The nature of the coupled nuclei can be identified by the position of the peaks spectrum. For instance, weakly coupled ^1H and ^{14}N nuclei are centred around the corresponding Larmor frequency. Moreover, the appearance of cross peaks of weakly coupled and strongly coupled nuclei in different quadrants decreases the difficulty of data interpretation which, together with its two-dimensionality, also makes HYSCORE the desired experiment when there are various nuclei contributing to the spin hamiltonian.

HYSCORE is a time-consuming experiment due to the independent variation of t_1 and t_2. Besides, similar as in 3P-ESEEM, the experiment needs to be performed for different τ values, and phase cycling needs to be used. Moreover, ESEEM experiments generally can not be used for low-viscosity solutions at room temperature since no modulation can be detected with the rapid tumbling of molecules. [1,3,20].

HYSCORE will be extensively used in chapters 4 and 11.
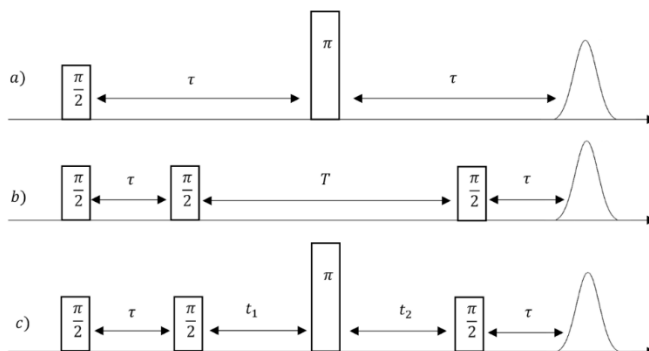
Figure 2.6. Microwave pulse sequences of the ESEEM experiments used in this thesis: a) 2P-ESEEM, b) 3P-ESEEM, and c) HYSCORE

2.1.5.5   ENDOR

The next set of techniques that are often used to study nuclear frequencies is Electron Nuclear DOuble Resonance or ENDOR. In this technique, both MW and radio frequency (RF) simultaneously irradiate the spin system. Similarly to the ESEEM, ENDOR is a high-resolution technique for hyperfine spectroscopy in order to identify nuclei in the vicinity of the paramagnetic centre, which can not be obtained from the CW-EPR experiment. ESEEM and ENDOR methods are complementary methods.

I here discuss two pulsed ENDOR techniques

2.1.5.5.1   Davies ENDOR

This   experiment   involves   the   MW   pulse   sequence $\pi - T - \frac{\pi}{2} - \tau - \pi - \tau - echo$ (Figure 2.7a). This pulse sequence starts with a selective preparation MW π-pulse, which inverts the polarization of a particular EPR transition. A selective radiofrequency (RF) π-pulse with varying frequency is applied, which inverts the nuclear polarisation whenever the RF agrees with a nuclear transition and affects the electron polarisation. At the end of the sequence, a standard Hahn echo is used to read out the signal. The Davies ENDOR experiment is suitable for the detection of strongly coupled nuclei [1,3,21] and is used in chapter 4 for the detection of strongly coupled ^{14}N of pyridine to Cu(II).

2.1.5.5.2 Mims ENDOR

Mims ENDOR uses the stimulated echo pulse sequence $\frac{\pi}{2} - \tau - \frac{\pi}{2} - T - \frac{\pi}{2} - \tau - echo$ similar as in 3P-ESEEM (Figure 2.7b). The first two MW $\frac{\pi}{2}$-pulses make the nuclear coherences; then, during the time T a selective RF π-pulse changes the polarization of NMR transitions whenever the RF equals a nuclear frequency. The final $\frac{\pi}{2}$-pulse creates the detectable EC. Since this experiment uses the stimulated echo, it needs to be performed at different τ values and summed to avoid blind spots. The Mims ENDOR experiment is suitable for detecting weakly coupled nuclei [1,3,22] and is used in chapter 11 to detect weakly coupled protons to Mo(V) centres.
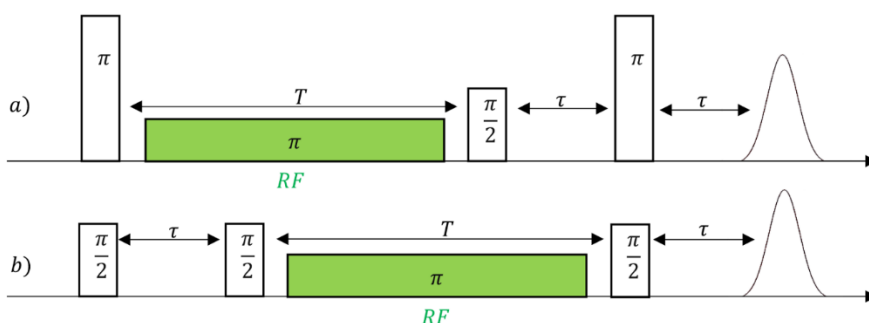

Figure 2.7 The pulse sequences of a) Davies ENDOR and b) Mims ENDOR

2.2 Electrochemical methods

In this section, I will introduce the electrochemical techniques that are used in this thesis. Further details on electrochemistry can be found in [23,24]

2.2.1 Introduction

Electrochemical reactions involve redox reactions when a charge transfer occurs on the electrode surface. A general equation describes those reactions:

$$O + ne^- \rightleftharpoons R \qquad (2.33)$$

in which O refers to the oxidized species, R refers to the reduced species, and n is the number of electrons transferred.
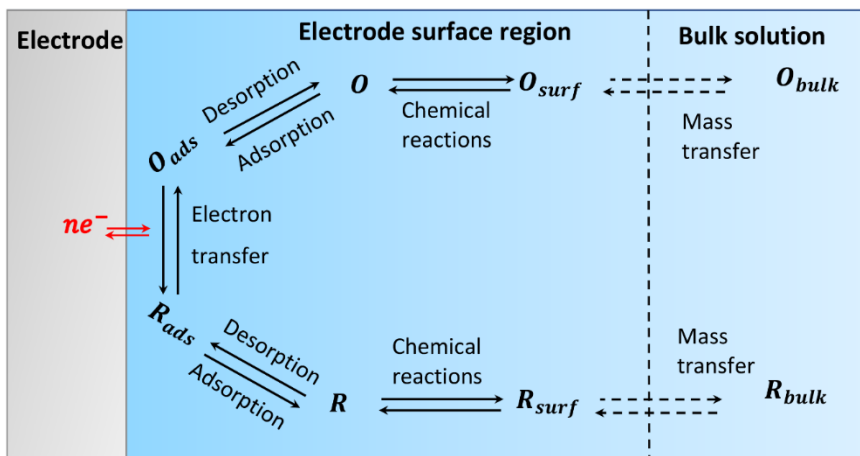
Figure 2.8. Possible reaction steps during a general electrochemical reaction. O and R indicates oxidation and reduction reactions, respectively. Ads and surf stand for adsorption and surface, respectively. The figure is redrawn from [23]

In an electrochemical cell, two electrodes are minimally required in which each one of them is responsible for a half-reaction. On one of the electrodes, the species lose their electron(s) (oxidation), and on the other one, they gain the electron(s) (reduction). An electrolyte connects these electrodes in order to let the electrical current flow. In order to have current, one needs to apply a sufficiently high potential difference between two electrodes. The speed of the reaction is controlled by this potential difference, as well as the concentration of the reagents and thermodynamics. In an electrochemical cell, a potentiostat provides the required energy for the potential difference. To control the applied potential, a reference electrode (RE) is added to the two-electrode system. In a three-electrode cell, the electrode at which the desired half-reaction is happening is called the working electrode (WE), and the other electrode is called the counter electrode (CE).

2.2.2 Complexity of the electrochemical process

In an electrochemical cell, the reaction occurs on the electrode by transferring an electron from a molecule to the electrode or vice versa. In order to transfer electrons, the molecules should move from the bulk of the solution (O_{bulk} or R_{bulk}) to the electrode surface (O_{surf} or R_{surf}). The charge transfer occurs as soon as the molecules are close enough to the electrode. Then the product moves to the bulk of the solution. It is also possible that after the charge transfer, other chemical reactions occur, which can be a second charge transfer or a chemical reaction. Figure 2.8 shows the possible steps in an electrochemical reaction, although not all will occur in a specific setup. The movement of the species from the bulk solution to the electrode surface and vice versa is called mass transfer. For an electrochemical reaction to occur, there must be the adsorption of reactants to the surface in order for charge transfer to take place. Moreover, the desorption of the products is necessary to make space for the new reactant to come towards the surface.

In the following sections, I will introduce the electrochemical techniques that will be used in this thesis.

2.2.3 Cyclic voltammetry

Cyclic voltammetry (CV) is one of the electrochemical techniques that has many applications. It is often used for preliminary study of a system to identify the electrochemical behaviour of a reactant. In this experiment, the applied potential to the WE is scanned linearly in a triangular waveform between two potential values. The current values for each potential value are measured. As the outcome, the measured current (I) is plotted versus the potential values (E) to give a cyclic voltammogram (Figure 2.9).
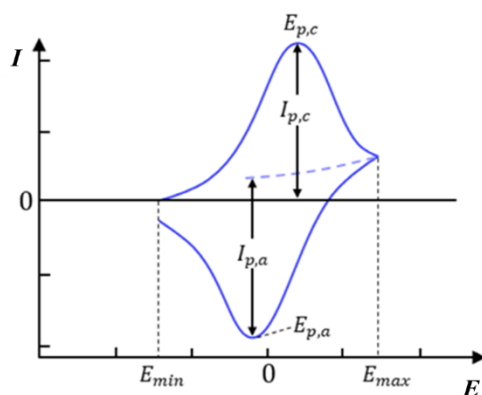
Figure 2.9. Cyclic voltammogram of a reversible system. The current peaks in the cathodic sweep at $E_{p,c}$, indicating the reduction half-reaction. Conversely, $E_{p,a}$, indicates the oxidation half-reaction. $I_{p,c}$ and $I_{p,a}$ are the corresponding peak currents.

The shape of the curve contains information about the reaction. On reaching a potential where the oxidation reaction at the electrode begins, the current rises until it reaches a

maximum value (the peak current). Then because of consumption of the electroactive species, the current decreases due to the shortage of reactants at the electrode surface. During the reversed cathodic sweep, the oxidation reactants are again reduced, leading to a decrease in the current. The difference in potential between the oxidation and reduction peak is a measure for the reversibility of the electrochemical process.

2.2.4 Chronoamperometry

Chronoamperometry (CA) is a technique in which the potential of the WE varies stepwise, and the resulting current versus time is measured (Figure 2.10). Analysis of the data from these experiments gives information about the reactions happening on the electrode and their rates. The charge that flows through the cell during electrolysis may be quantified to the theoretical amount of the reacted material based on Faraday's law of electrolysis:

$$n = \frac{Q}{zF}$$

(2.34)

where n is the amount of product that can be made theoretically in mol, Q is the charge that passes in the cell, z in the number of electrons transfer per molecule and, F is the Faraday constant ($96485\ C\ mol^{-1}$). The charge Q can be obtained by integrating the current response over time in the CA experiment. One can calculate the current efficiency ϕ_i of a product i using the amount of the product at the end of the experiment n_i over the theoretical amount n.

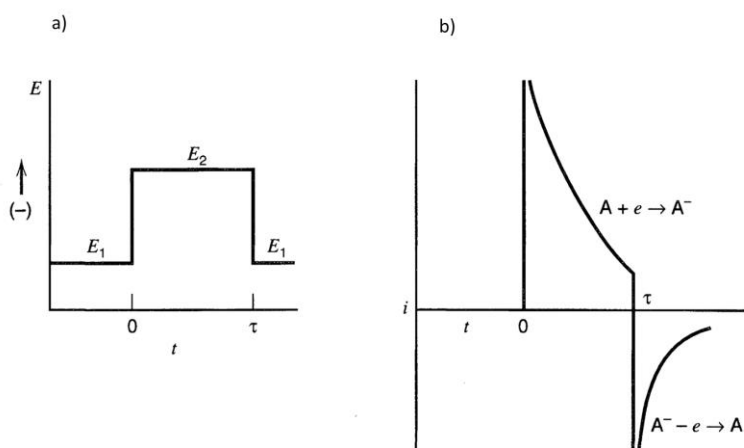$$\phi_i = \frac{n_i}{n}$$

(2.35)

Figure 2.10. Double step (CA) a) typical waveform and b) current response. Figure taken from [24]

Current efficiencies equal to unity for a particular product i represent that all charges in the reaction were consumed to make the product i. ϕ_i smaller than one is the evidence of the presence of side products.

2.3 Density functional theory (DFT)

2.3.1 Basics of DFT

Density functional theory (DFT) is a computational method to investigate molecular properties based on quantum mechanics. DFT deals with solving the time-independent Schrödinger equation for a many-body system.

$$\hat{H}\Psi(\mathbf{r_1}, \mathbf{r_2}, \dots) = E\Psi(\mathbf{r_1}, \mathbf{r_2}, \dots) \qquad (2.36)$$

According to the Born-Oppenheimer approximation, the evolution of the electrons and nuclei can be considered separately

$$\Psi = \Psi_{\mathbf{el}}\,\Psi_{\mathbf{nuc}} \qquad (2..$$

We focus here on the electronic equation. For a system consisting of N electrons, the electronic Hamiltonian operation in atomic units is given by:

$$\hat{H}_{\mathrm{el}} = -\frac{1}{2}\sum_i \nabla_i^2 + \frac{1}{2}\sum_{i \neq j} \mathbf{r}_{ij}^{-1} - \sum_{I,i} Z_I r_{Ii}^{-1} \qquad (2.38)$$

with i and j label the electrons and I the nuclei coordinates. Z_I is the charge of nucleus I , r_{Ii} is the distance between i'th electron and I'th nucleus and r_{ij} is the distance between electrons i and j. The last term of the equation (2.38) defines an external potential $V_{ext} = \sum_i v_{ext}(r_i)$. The first and second terms are kinetic energy and the electron repulsion energy, respectively. Hence,

$$\hat{H}_{\mathrm{el}} = \hat{T} + \hat{V}_{\mathrm{ee}} + \hat{V}_{\mathrm{ext}} \qquad (2.39)$$

However, the equation (2.36) does not have a solution in a closed form for a system consisting of more than one electron. Hence, the solution needs to be approximated. DFT is one of the methods that provides a suitable approximation. The DFT method maps the many-body problem to a three-dimensional problem in terms of electron density $\rho(r)$ [25]. For this, Kohn and Hohenberg worked out the necessary theorems:

1) The external potential $\hat{V}_{\mathrm{ext}}$ and, hence the total energy is a unique (but unknown) functional of the electron density $\hat{V}_{ext} = \hat{V}_{ext}[\rho]$ and $E = E[\rho]$.
2) The electron density that returns the minimum value of the energy functional for a given external potential represents the ground-state density.

$$E[\rho] \geq E_0 = E[\rho_0] \tag{2.40}$$

All the terms contributing to the energy are a functional of ρ, since E itself is a functional of ρ

$$E[\rho] = T[\rho] + E_{ee}[\rho] + E_{ext}[\rho] \tag{2.41}$$

Although the Hohenberg-Kohn theorem converts a 3N-dimensional problem to a 3-dimensional equation, it does not provide a partial solution because the energy functional still has unknown terms in the equation (2.41).

$$E_{ext}[\rho(\boldsymbol{r})] = \int \rho(\boldsymbol{r}) \; v_{ext}(\boldsymbol{r})d\boldsymbol{r} \tag{2.42}$$

and,

$$E_{ee}[\rho(\boldsymbol{r})] = \frac{1}{2}\int \rho(\boldsymbol{r}) \; v_c(\boldsymbol{r})d\boldsymbol{r} + E_{ncl}[\rho(\boldsymbol{r})] \tag{2.43}$$

In the latter, the first term is the classical Coulomb interaction, and the second part is the non-classical part containing the exchange and electron-correlation terms. The functionals of $T[\rho]$ and $E_{ncl}[\rho]$ are unknown.

Kohn and Sham introduced an approach to find a solution to approximate the kinetic energy [26]. For this, they use a fictitious system of non-interacting particles.

For such a non-interactive system with the Hamiltonian

$$\widehat{H}_{\mathrm{ni}} = -\frac{1}{2}\sum_i \nabla_i^2 + \sum_i v_{\mathrm{KS}}(\boldsymbol{r}_i) \tag{2.44}$$

the problem reduces to solving the one-electron equation.

$$\hat{h}_{\mathrm{KS}}\phi_i(\boldsymbol{r}) = \epsilon_i\phi_i \tag{2.45}$$

with

$$\hat{h}_{\mathrm{KS}} = -\frac{1}{2}\nabla^2 + v_{KS}(\boldsymbol{r}) \tag{2.46}$$

Kohn and Sham assumed that the electron density ρ_{ni} of the fictitious non-interacting system is the same as for the real system.

$$\rho_{ni}(\boldsymbol{r}) = \sum_i \sum_S |\phi_i(r, S)|^2 = \rho(\boldsymbol{r}) \tag{2.47}$$

The total energy of the real system can then be rewritten as

$$E[\rho(\mathbf{r})] = T_{ni}[\rho(\mathbf{r})] + \int \rho(\mathbf{r})\ v_{ks}(\mathbf{r})d\mathbf{r}$$

(2.48)

with:

$$v_{ks}(\mathbf{r}) = \frac{\delta T[\rho(\mathbf{r})] - \delta T_{ni}[\rho(\mathbf{r})]}{\delta \rho(\mathbf{r})} + v_{ext}(\mathbf{r}) + v_c(\mathbf{r}) + \frac{\delta E_{ncl}}{\delta \rho(\mathbf{r})}$$

(2.49)

We define:

$$\hat{v}_{XC}(\mathbf{r}) = \frac{\delta E_{XC}}{\delta \rho(\mathbf{r})} = \frac{\delta T[\rho(\mathbf{r})] - \delta T_{ni}[\rho(\mathbf{r})]}{\delta \rho(\mathbf{r})} + \frac{\delta E_{ncl}}{\delta \rho(\mathbf{r})}$$

(2.50)

So for a real system:

$$\left[-\frac{1}{2}\nabla^2 + v_{ext}(\mathbf{r}) + v_c[\rho(\mathbf{r})] + v_{XC}[\rho(\mathbf{r})] \right]\phi_i = \epsilon_i\phi_i$$

(2.51)

In equation (2.51), the exchange-correlation term $\hat{v}_{XC}[\rho(\mathbf{r})]$ is unknown so the Kohn-Sham method still does not allow calculating the exact energies but already reduces the part of the energies for which the functionals need to be guessed significantly. There is a wide variety of functionals to approximate the exchange-correlation interaction. Local density approximation (LDA) functionals (*e.g.*, LDA, VWN3,…) have a huge application in solid-state physics. Generalized gradient approximation (GGA) functionals, considering the terms depending on the density gradient, are popular in chemistry calculations. BP86, PBE, and BLYP functionals are the most popular functionals from this category. Hybrid functionals were introduced by Becke in 1993. Becke gained a significant improvement in the energy by mixing the LDA and/or GGA functionals with a portion of the exchange interaction from Hartree-Fock theory. B3LYP is the most favoured among the hybrid functionals as well as PBE0. In equation (2.51), the last two terms on the left-hand side depend on the density. Hence initial values for the density and the iterative method, *i.e.* self-consistent-field (SCF), should be employed in order to solve the equation. Selecting the initial Kohn-Sham orbitals ϕ_i leads us to provide the initial electron density for the starting point of the calculations.

The Kohn-Sham orbitals are built as a linear combination of basis sets.

$$\phi_i(\mathbf{r}) = \sum_j c_{ij}\psi_i(\mathbf{r})$$

(2.52)

Depending on the atoms existing in the structure, different types of basis sets can be chosen, *e.g.* Gaussian functions or plane waves. [3]

2.3.2 Calculating EPR parameters with DFT

In order to calculate the EPR parameters for a given molecular structure, one first needs to optimize the geometry. The coordinates of the optimized geometry are used to calculate the EPR parameters in a single-point computation. The **g**-tensor and hyperfine couplings are calculated via a second-order perturbation approach. In this approach, the **g**-tensor components are given by:

$$g_{\mu\nu} = \frac{2}{\alpha} \frac{\partial^2 \langle \psi_0 | \hat{H} | \psi_0 \rangle}{\partial B_\mu \partial S_\nu} \bigg|_{B=S=0} \qquad (2.53)$$

Here $|\psi_0\rangle$ is the wave function of the ground state, and $\alpha = \frac{1}{137}$ is the fine-structure constant. The perturbation operators need to be considered in the Hamiltonian $\hat{H}$ via the Hellmann-Feynman theorem [27].

$$g_{\mu\nu} = \frac{2}{\alpha} \frac{\partial}{\partial B_\mu} \left(\left\langle \psi_{B_\mu} \left| \frac{\partial \hat{H}}{\partial S_\nu} \right|_{S=0} \right| \psi_{B_\mu} \right\rangle \right) \bigg|_{B=0} \qquad (2.54)$$

in which $\left| \psi_{B_\mu} \right\rangle$ is the eigenfunction of Hamiltonian in the presence of the external magnetic field along the x-axis. Only the first-order correction of the magnetic field is needed. Since we calculate the **g**-tensor components at $B = 0, S = 0$, in perturbation contributions, only the linear terms of the spin component and the order of 0 and 1 of the magnetic field component are effective. As mentioned earlier, the major interactions in **g**-tensor come from the EZ and SO couplings. These contributions are given by:

$$\hat{H}_{EZ} = \frac{\alpha}{2} \sum_i g_e \hat{\mathbf{s}}_i . \mathbf{B}(\mathbf{r}) \qquad (2.55)$$

$$\hat{H}_{SO} = \frac{\alpha^2 (g_e - 1)}{2} \sum_{i,I} Z_I \, \hat{\mathbf{s}}_i . \frac{\mathbf{r}_{iI} \times \hat{\mathbf{p}}_i}{|\mathbf{r}_{iI}|^3} \qquad (2.56)$$

in which r_{iI} is the distance between I^{th} nucleus and i^{th} electron, and $\hat{\mathbf{p}}_i$ is the momentum operator of electron i.
The hyperfine tensor **A** is calculated in a similar way,

$$A_{\mu\nu} = \frac{\partial}{\partial I_\mu} \left(\left\langle \psi_{I_\mu} \left| \frac{\partial \hat{H}}{\partial S_\nu} \right|_{S=0} \right| \psi_{I_\mu} \right\rangle \right) \bigg|_{I=0} \qquad (2.57)$$

All the DFT computations for EPR parameters and geometry optimisation in this thesis have been performed using ORCA 3.2. [28].

2.3.3 Gibbs Energy calculations

In order to calculate the vibrational frequency, calculations were performed using ORCA 4.1 [28]. After computing the vibrational frequencies and the normal modes of the system, for a given temperature and pressure (ambient conditions in this thesis), the thermodynamic functions such as enthalpy (H), entropy (S), and Gibbs free energy (G) are determined, assuming a gas-phase molecule and using statistical mechanics. The first function is the inner energy (U), is composed of

$$U = E_{el} + E_{ZPE} + E_{vib} + E_{rot} + E_{trans} \qquad (2.58)$$

in which E_{el} is the total energy from the single point calculation, E_{ZPE} is the zero-point energy, E_{vib} is the finite temperature correction to E_{ZPE}, E_{rot} is the rotational thermal energy and E_{trans} is the translational thermal energy. Enthalpy is given by,

$$H = U + k_B T \qquad (2.59)$$

in which U is the inner energy and k_B is Boltzmann's constant, and T is the temperature. By adding the entropy (S) to the enthalpy, Gibbs free energy value are obtained, which is given by

$$G = H + TS \qquad (2.60)$$

2.4 References

[1]   A. Schweiger and G. Jeschke, *Principles of Pulse Electron Paramagnetic Resonance* (Oxford University Press Inc, New York, 2001).

[2]   V. Chechick, E. Carter, and Damien Murphy, *Electron Paramagnetic Resonance,* (Oxford University Press, Cardif, 2015).

[3]   D. Goldfarb and S. Stoll, *EPR Spectroscopy: Fundamentals and Methods* (JOHN WILEY & SONS, Chichester, 2017).

[4]   E. K. Zavoisky, *Paramagnetic Relaxation of Liquid Solutions for Parallel Fields*, J. Phys. **8**, 377 (1944).

[5]   A. Alberti and D. Macciantelli, *Electron Paramagnetic Resonance: A Practitioner's Toolkit* (John Wiley & Sons Inc., New Jersey, 2009).

[6]   C. L. Hawkins and M. J. Davies, *Detection and Characterisation of Radicals in Biological Materials Using EPR Methodology*, Biochim. Biophys. Acta - Gen. Subj. **1840**, 708 (2014).

[7]   F. A. Villamena, A. Rockenbauer, J. Gallucci, M. Velayutham, C. M. Hadad, and J. L. Zweier, *Spin Trapping by 5-Carbamoyl-5-Methyl-1-Pyrroline N -Oxide (AMPO): Theoretical and Experimental Studies*, J. Org. Chem. **69**, 7994 (2004).

[8]   H. Zhao, J. Joseph, H. Zhang, H. Karoui, and B. Kalyanaraman, *Synthesis and Biochemical Applications of a Solid Cyclic Nitrone Spin Trap: A Relatively Superior Trap for Detecting Superoxide Anions and Glutathiyl Radicals*, Free Radic. Biol. Med. **31**, 599 (2001).

[9]   C. Frejaville, H. Karoui, B. Tuccio, F. le Moigne, M. Culcasi, S. Pietri, R. Lauricella, and P. Tordo, *5-Diethoxyphosphoryl-5-Methyl-1-Pyrroline N-Oxide (DEPMPO): A New Phosphorylated Nitrone for the Efficient In Vitro and In Vivo Spin Trapping of Oxygen-Centred Radicals*, J. Chem. Soc. Chem. Commun. 1793 (1994).

[10]   F. Chalier and P. Tordo, *5-Diisopropoxyphosphoryl-5-Methyl-1-Pyrroline N-Oxide, DIPPMPO, a Crystalline Analog of the Nitrone DEPMPO: Synthesis and Spin Trapping PropertiesElectronic Supplementary Information (ESI) Available: Tables of Crystallographic Data. See Http://Www.Rsc.Org*, J. Chem. Soc. Perkin Trans. 2 2110 (2002).

[11]   E. G. Janzen, Y. Y. Wang, and R. V. Shetty, *Spin Trapping with .Alpha.-Pyridyl 1-Oxide N-Tert-Butyl Nitrones in Aqueous Solutions. A Unique Electron Spin Resonance Spectrum for the Hydroxyl Radical Adduct*, J. Am. Chem. Soc. **100**, 2923 (1978).

[12]   S. Stoll and A. Schweiger, *EasySpin, a Comprehensive Software Package for Spectral Simulation and Analysis in EPR*, J. Magn. Reson. **178**, 42 (2006).

[13]   S. Van Doorslaer, *Hyperfine Spectroscopy - ESEEM*, in *EPR Spectroscopy: Fundamentals and Methods*, edited by D. Goldfarb and S. Stoll, 1st ed. (Wiley, 2018), pp. 377–400.

[14]   S. Stoll, *Pulse EPR*, in *EMagRes*, Vol. 6 (John Wiley & Sons, Ltd, Chichester, UK, 2017), pp. 23–38.

[15]   A. Schweiger and G. Jeschke, *Principles of Pulse Electron Paramagnetic Resonance* (Oxford University Press, 2001).

[16] J. R. Harmer, *Hyperfine Spectroscopy - ENDOR*, in *EPR Spectroscopy: Fundamentals and Methods*, edited by D. Goldfarb and S. Stoll, 1st ed. (Wiley, 2018), pp. 331–357.

[17] L. G. Rowan, E. L. Hahn, and W. B. Mims, *Electron-Spin-Echo Envelope Modulation*, Phys. Rev. **137**, A61 (1965).

[18] W. B. Mims, *Envelope Modulation in Spin-Echo Experiments*, Phys. Rev. B **5**, 2409 (1972).

[19] J. M. Fauth, A. Schweiger, L. Braunschweiler, J. Forrer, and R. R. Ernst, *Elimination of Unwanted Echoes and Reduction of Dead Time in Three-Pulse Electron Spin-Echo Spectroscopy*, J. Magn. Reson. **66**, 74 (1986).

[20] M. M. Roessler and E. Salvadori, *Principles and Applications of EPR Spectroscopy in the Chemical Sciences*, Chem. Soc. Rev. **47**, 2534 (2018).

[21] E. R. Davies, *A New Pulse Endor Technique*, Phys. Lett. A **47**, 1 (1974).

[22] W. B. Mims, *Pulsed Endor Experiments*, Proc. R. Soc. London. Ser. A. Math. Phys. Sci. **283**, 452 (1965).

[23] C. M. A. Brett and A. M. O. Brett, *ELECTROCHEMISTRY Principles, Methods, and Applications* (Oxford University Press Inc, New Yourk, 1993).

[24] A. J. Brad and L. R. Faulkner, *ELECTROCHEMICAL METHODS Fundamentals and Applications*, Vol. 1 (JOHN WILEY & SONS, INC., New York, 2000).

[25] P. Hohenberg and W. Kohn, *Inhomogeneous Electron Gas*, Phys. Rev. **136**, B864 (1964).

[26] W. Kohn and L. J. Sham, *Self-Consistent Equations Including Exchange and Correlation Effects*, Phys. Rev. **140**, A1133 (1965).

[27] S. Epstein, *The Variation Method in Quantum Chemistry* (Academic Press, New York, New York, 1974).

[28] F. Neese, *The ORCA Program System*, Wiley Interdiscip. Rev. Comput. Mol. Sci. **2**, 73 (2012).

State of art in EPR spectro-electrochemistry

EPR spectroscopy is not usually considered a standard technique within the electrochemist's toolkit. It was used more frequently in electrocatalysis research from the 1960's until the 1990's to identify paramagnetic reaction intermediates and elucidate reaction mechanisms, but is less used nowadays. Since the 1990's however, technological progress has made advanced EPR methods more readily available, which has allowed for more sensitive measurements and better identification of intermediate species. Furthermore, developments in additive manufacturing have made it easier and cheaper to construct specialised electrochemical cells for EPR research. This chapter aims to provide an overview of contemporary research combining electrocatalysis and EPR, and this offers a starting point for the research discussed in this work. Firstly, the chapter covers the challenges involved with *in-situ* cell design and gives an overview of recent cell designs. Next, a number of contemporary mechanistic and quantitative studies are discussed to explore the possibilities of CW-EPR spectroscopy. Finally, it covers advanced pulse EPR techniques and their (so far) limited use in electrocatalytic research.

3.1   Introduction

The fields of electrocatalysis and EPR spectroscopy have a shared history that goes back further than one might expect from the relatively low number of contemporary studies. As mentioned in chapter 1, research in electrocatalysis is mainly concerned with what happens to the electrode surface and on the electrode-electrolyte interface. Chapter 2 highlighted that while electrochemical techniques probe the surface processes but provide no direct information about what may happen subsequently in the solution, EPR can monitor certain paramagnetic species on the surface but is also able to detect electrochemical reaction intermediates in solution after desorption.

As explained in chapter 2, EPR is a technique for the detection of paramagnetic species. Although this causes limitations on the number of species observable by EPR in comparison to other spectroscopy techniques, a wide variety of catalytic systems still contain paramagnetic centres. Hence, *in-situ* EPR techniques can provide valuable information on structure–reactivity relationships. Selected examples of such paramagnetic systems include:

1) Transition-metal ions (TMI) in paramagnetic oxidation states: These species play an essential role in catalytic and electrocatalytic synthesis [1–3]. The vast majority of *in-situ* EPR studies focus on analysing their changes in different temperatures and atmospheres. Reviews in ref [4–6] are partly and reviews in ref [7,8] are entirely dedicated to this topic. Table 3.1 shows selected paramagnetic TMI that can be used in catalysis. Due to the short electron relaxation times, it is not always straightforward to detect all of them with EPR at room-temperature. Freezing to temperatures below 77 K is then required, which can impose some restrictions for *in-situ* studies under realistic reaction conditions. However, EPR on freeze-quenched samples can still provide essential information on redox and catalytic behaviour [5].

Table 3.1 Selected TMI relevant for heterogeneous catalysis with corresponding electron structure of the outer subshell. Table taken from [5]*.*

d^1	d^2	d^3	d^4	d^5	d^6	d^7	d^8	d^9
V^{4+}	V^{3+}	Mn^{4+}	Mn^{3+}	Mn^{2+}		Ni^{3+}	Ni^{2+}	Ni^+
Mo^{5+}	Mo^{4+}	Mo^{3+}	Cr^{2+}	Fe^{3+}	Fe^{2+}	Rh^{2+}	Rh^+	Rh^0
Cr^{5+}		Cr^{3+}		Ru^{3+}	Ru^{2+}		Pt^{2+}	Pt^+
Ti^{3+}				Os^{3+}	Os^{2+}	Pd^{3+}	Pd^{2+}	Pd^+
Zr^{3+}				Ir^{4+}	Co^{3+}	Co^{2+}	Co^+	Ag^{2+}
								Au^{2+}
								Cu^{2+}

2) Radical species, such as $O_2^{\bullet-}$ or $OH^{\bullet-}$, can be formed in solution or on the surface of a solid. Related defect centres such as O^- can be formed in the bulk of solids like metal oxides [9]. Radical species can be formed in many chemical reactions, such as electrocatalytic reactions. This thesis focuses on the latter.

The term *in-situ* EPR is in catalysis not always clearly defined and may refer to:

 (A) *Quasi-in-situ* studies, in which the catalysts are pretreated at high temperatures and special atmospheres in line with real reaction conditions, and then cooled down for EPR experiment purposes without contact with ambient atmosphere.
 (B) Real *in-situ* EPR: Recording the EPR spectra under the reaction condition simultaneously with the progress of the chemical reaction.

The works on case (B) are less numerous than case (A) because of (i) the lack of commercially available experimental tools and the challenges to make them; (ii) at the higher temperatures in which the catalysts are active, the EPR signals for the TMI are not detectable due to the short relaxation times. The articles that will be introduced in the following sections will contain both categories mentioned above [5].

From the 1960's until the late 1990's, spectroelectrochemical EPR (SEC-EPR) was much more common in electrocatalysis research than it is now and was typically used to identify radical species generated during the electrode reaction to elucidate reaction mechanisms and kinetic parameters. Early works did much to push SEC-EPR forward through studies on the oxidation and reduction pathways of various molecules such as nitriles, hydrocarbons and amines [10–12]. Several different SEC-EPR cells were developed during this time, upon which new contemporary designs are based as discussed in the section '*in-situ* setup design' of this review. Nowadays, studies combining electrochemistry and EPR often use EPR as a tool to identify structural changes or defects in materials, or the redox behaviour of enzymes and metal-ligand complexes [13–18]. In fact, the potential of SEC-EPR in electrocatalysis is currently under-utilised since it can yield valuable information about paramagnetic intermediate species that cannot be obtained with combining electrochemistry with other characterisation techniques. FTIR, UV-VIS and Raman are often favoured for studies of electrode interfaces because of their versatility and ease of use [19–22]. However, EPR has its own advantages: it is very sensitive, and a conventional setup can readily detect concentrations in the μM range, and can detect paramagnetic intermediates directly. SEC-EPR combines the dynamic character of electrochemical experiments with the specific requirements of EPR measurements but is complicated by the conflicting requirements of the two disciplines (see further). Nevertheless, with careful experimental design, many of the challenges and sources of error can be overcome or avoided to yield precise information about the identity and quantity of paramagnetic intermediates and, ultimately, the reaction mechanism.

3.2   Setup designs and related challenges

The requirements for successful EPR detection contradict the common practices of analytical electrochemistry. In a conventional EPR spectrometer, a sample is placed in a resonance cavity (MW resonator) that is situated between the poles of an electromagnet, which generate the external magnetic field. Figure 3.1 shows the different parts of an X-band CW-EPR.

The sample is placed in the resonance cavity, with sample holders being typically cylindrical quartz tubes or flat cells. The resonance cavity containing the sample is tuned so that the MW frequency matches the cavity's resonance frequency, and standing waves are formed. The quality factor (Q-factor) describes the efficiency with which a

cavity stores the MWs. Higher Q-factors result in more sensitive CW-EPR measurements. The Q-factor is maximised by critically coupling the cavity with the detector, meaning that the amount of MWs reflected to the detector is minimised. When the resonance condition is fulfilled during an EPR measurement, the sample absorbs the MWs, and the coupling condition is disturbed, causing MWs to reflect back to the detector. In combination with the amplitude modulation detection discussed in chapter 2, this results in the typical CW-EPR signal.

1: Microwave source
2: Signal arm attenuator
3: Bias attenuator
4: Phase shifter
5: Circulator
6: Detector diode
7: Load
8: Wave guide
9: Magnets
10: Cavity
11: Sample position
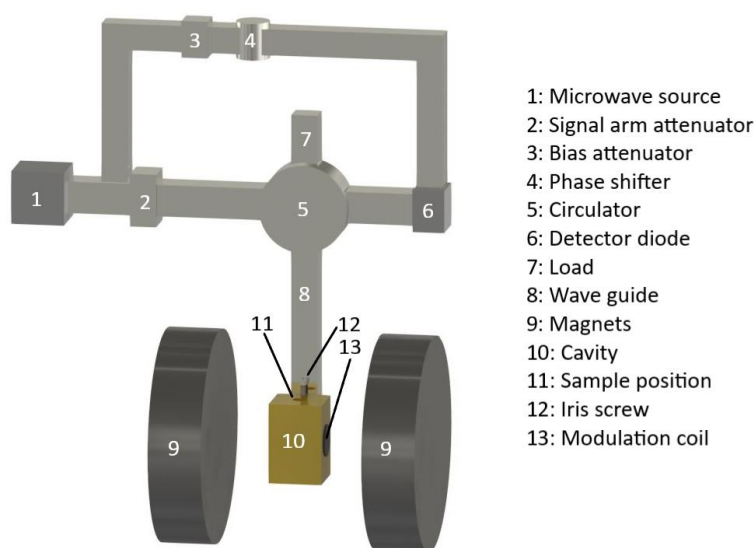12: Iris screw
13: Modulation coil

Figure 3.1 Schematic drawing of an X-band CW-EPR spectrometer

As a result of this instrumental setup, there should be minimal MW absorption by any materials within the cavity that are not the species of interest. Additionally, these materials should preferably have a low relative permittivity. The electric field strength varies across the inside of the cavity with local minima and maxima. MWs are absorbed by materials in an electric field, with higher absorption taking place at higher relative permittivity (*i.e.* lossy samples) and/or higher electric field strength. The placement of material at the electric field minimum therefore becomes more crucial the higher its relative permittivity is, for instance, for the polar solvents.

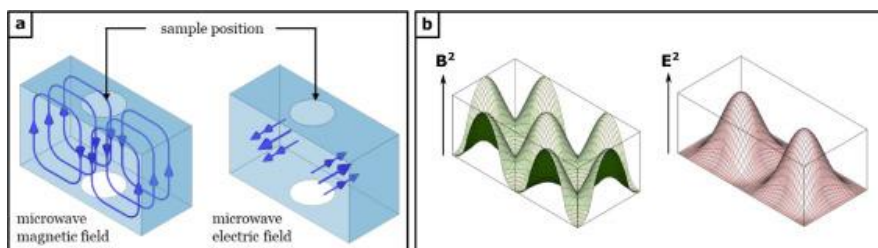Figure 3.2: (a) The magnetic field vector (left) and electric field vector (right) inside a TE_{102} cavity when standing waves are formed. (b) The resulting magnetic field intensity (left) and electric field intensity (right). Adapted from ref [23].

In TE_{102} resonance cavities typically used for X-band CW-EPR experiments, the local minima and maxima are well-documented (Figure 3.2), and the optimal minimum of the electric field is a thin line in the middle of the cavity, parallel to the electric field vector in which the magnetic field component magnitude is maximum. EPR sample holders for lossy samples are therefore very thin (≤ 1 mm). Two types of commercial reaction vessels are available to date for the room temperature experiments in polar solvents: capillaries and flat cells with a flat section sample gap of 0.3 or 0.5 mm from Wilmad. The aforementioned aspects need to be taken into consideration when designing a combined SEC-EPR setup, and options need to be carefully weighed off. Ideally, EPR requires the use of non-absorptive materials for cavity tuning and subsequent measurement of samples. If absorptive materials are unavoidable, their volume should be reduced to a minimum. Additionally, cell materials with paramagnetic centres will complicate spectra when the g-values are similar to the paramagnetic species of interest due to spectral overlap, *e.g.* radical signals in polymers that are synthesised through a radical polymerisation reaction or the E-centre in quartz. In some cases, the background signal can be eliminated by a pretreatment, *e.g.* heating, but in most cases, it is better to avoid these materials. In all cases, blank experiments with just the cell should be performed as a control. Next, the electrolytes used in electrochemistry typically have a high relative permittivity, and the electrolyte volume inside the cavity should therefore also be minimised and precisely placed in the electric field minimum. Special care should also be taken with the electrical components such as connecting wires and electrodes. Bulk metal electrodes can be reflective, and electrode support materials may also reflect or absorb the MWs. Their volumes should therefore also be minimised by using thin wires or ultrathin sheets if they are placed inside the cavity. Finally, the dimensions of the cavity place strict size limitations on electrochemical cell design. The high relative permittivity of electrolytes means that as little volume as possible should be placed outside the electric field minimum. The dimensions of the TE_{102} rectangular cavity in X-band CW-EPR are already discussed. Other cavities, such as the TM_{110} or TE_{011} cylindrical cavities, can also be used. These cavities have different (size) requirements than the TE_{102} cavity, but the principles are the same. EPR can also be performed at higher frequency ranges, such as Q-band (35 GHz) and W-band (95 GHz), leading to higher spectral resolution [23]. However, this comes at a price: the maximum diameter of samples for Q- and W-band cavities are 3 mm and 0.8 mm, respectively, restricting the degrees of freedom in cell design for the electrochemist tremendously. The small sizes of the sample holder restrict the types of electrodes that can be used: bulk electrodes do not fit, and thus wires or thin electrodes are used that are far from ideal to do analytical electrochemistry ([24] for X- and [25] for Q/W-band).

When investigating a catalyst/reaction combination, the initial characterisation is done by electrochemical means only, i.e. cyclic voltammetry (CV). It is important that one can draw parallels between these measurements and *in-situ* EPR experiments to be confident that the observed phenomenon corresponds to the desired one. Some general considerations should be made when interpreting SEC-EPR results. Firstly, due to the dimension restrictions, the *in-situ* electrochemical behaviour may deviate from the bulk. Secondly, the electrode surface should be reproducible in order to obtain similar EPR signal intensity and electrochemical behaviour between experiments. Thirdly, the positioning of the reference electrode (RE) should be carefully determined to avoid the introduction of uncompensated ohmic resistance. Finally, the distance between the

working (WE) and counter electrode (CE) should be small enough so that the compliance voltage of the potentiostat is not exceeded and large enough so that radicals generated at the counter electrode do not diffuse within the sensitive part of the cavity. Some of these aspects will be mentioned in later chapters.

The majority of the SEC-EPR related studies in the last decade up to the current work were performed in commercial flat cells. Examples of electrochemical EPR cells for different applications are listed in Table 3.2 and Table 3.3. Most designed setups are based on the cells that were published earlier and were listed by Wadhawan and Compton in the section *EPR Spectroscopy in Electrochemistry* from the *Encyclopedia of Electrochemistry* [26]. Some have been adapted for specific applications.

Table 3.2. SEC-EPR studies in which in-situ generated organic radicals were detected

Nature	Cell	WE	CE	RE	Stabilisation	Solvent	Freq.	Ref.	Year
Quinones, diimines, transition metal radical anions, enzymes	Silica tube	Pt wire	Pt wire	Ag wire	None, low temperature	DMF	W, Q	[25]	2011
Various conjugated organic molecules	'Spectroelectrochemical cell'	Pt wire	Pt helical wire	Ag wire	None	Unspecified	X	[27]	2018
(5-etoxycarbonylmethylidene-4-oxothiazolidine-2-ylidene)-N-phenylethanone	No info	No info	No info	No info	None, low temperature	DMSO	X	[28]	2011
Selenadiazoloquinolones	Flat cell	Pt mesh	Pt wire	Ag wire	Temperature	DMSO	X	[18]	2012
Nitroquinolones	Flat cell	Pt mesh	Pt wire	Ag wire	Nitrosodurene	DMSO, MeOH, CD$_3$OD, DMSO-d$_6$	X	[29]	2013
Guanine oxidation through Ru(II) complex	Flat cell	Pt wire	Pt wire	Ag wire	PBN	H$_2$O	X	[30]	2014
2,2-dinitroethene-1,1-diaine	Flat cell	Au mesh	Pt wire	Ag/AgCl wire	None	ACN, DMF	X	[31]	2015
Phenazine-di-N-oxide with IPA	Custom	Au and Pt helical wire	Pt rod	Ag wire	None	ACN	X	[32]	2014
β-cyclodextrin with ferrocene	'Spectroelectrochemical quartz cell'	Pt mesh	No info	Ag/Ag$^+$	None	DMSO	X	[33]	2014
Shikonin and isovalerylshikonin	Flat cell	Pt mesh	Pt	Ag/Ag$^+$	None	ACN	X	[14]	2015
Methyl viologen	Custom LGR	Pt wire, Ag wire	Pt wire, Ag wire	Ag wire, AgCl wire	None	ACN, H$_2$O	X	[34]	2015
Ketoconazole oxidation	Silica tube	Cu, Ag, Pt, graphite	Ag/AgCl wire	CE	None	H$_2$O	X	[24]	2015

Nature	Cell	WE	CE	RE	Stabilisation	Solvent	Freq.	Ref.	Year
Benzoquinone	Custom LGR	Pt wire, Ag wire	Pt wire, Ag wire	Ag wire, AgCl wire	None	ACN	X	[35]	2016
Oxidation of flavonolignan silybin	Flat cell	Pt mesh	Pt wire	Ag wire	BMPO	ACN	X	[36]	2016
Fluorinated/chlorinated 2,1,3-benzothia/selenadiazoles	'Electrochemical cell for EPR'	Pt	No info	No info	None	DMF	X	[37]	2017
Sandmeyer reaction	Flat cell	Pt wire	Pt wire	None	PBN	DMF, ACN, MeOH	X	[38]	2018
N-hydroxyl-phthalimide	Flat cell	Pt plate	Pt wire	Ag wire	None	ACN	X	[39]	2018
Trithiatetrazocinyl radical anions	Flat cell	Au mesh	2 Pt wires	Ag/AgCl wire	None	CH_2Cl_2	X	[40]	2018
Quinones, perylene-diimide, pyrene, flavin, tryptophan, tyrosine	Flat cell	Pt wire	Pt wire	Ag/AgCl ref, Ag/Ag$^+$	None	ACN	X	[41]	2019

Table 3.3 SEC-EPR studies in which in-situ generated paramagnetic metal complexes were detected.

Nature	Cell	WE	CE	RE	Stabilisation	Solvent	Freq.	Ref.	Year
[Mo(CO)$_4$L] complexes	Silica tube	Pt	Pt	None	None	CH$_2$Cl$_2$	X	[42]	2011
Ru(II) complex	Silica tube	Pt wire	Pt wire	Ag wire	Temperature	CH$_2$Cl$_2$	X	[43]	2017
Cr(bpy)$_3$ complexes	Silica tube	Au helical wire	Pt wire	Ag wire	None	DMF	X	[44]	2015
[(dpp-bian)Re(CO)$_3$Br]	Silica tube	Au helical wire	Pt wire	Ag/Ag$^+$	None	DMF, ACN	X	[13]	2018
FcP(O)(OC$_2$H$_5$)$_2$	Silica tube	Au helical wire	Pt wire	Ag/Ag$^+$	Temperature	DMF	X	[45]	2016
Tris('2,2'-bipyridine)Zn(II) diperchlorate	Silica tube	Au helical wire	Pt wire	No info	None	DMF	X	[46]	2013
Ni, Cu and Co with ligands: benzene-1,2-dithiolate or 3,6-dichlorobenzene-1,2-dithiolate	Flat cell	Pt mesh	Pt wire	Ag wire	Temperature	DMF, CH$_2$Cl$_2$	X	[47]	2014

3.3   Applications

Due to the specific possibility of paramagnetic intermediate detection offered by the combination of electrochemistry and EPR, it appeals to scientists acquainted with different subdivisions of the electrochemical science such as batteries, complexes, polymers, supercapacitors, organic electrochemistry, etc. In all cases the EPR spectrum is simulated to confirm the identity of the paramagnetic intermediate, and a mechanism is postulated based on this information. EPR data can also be used for quantitative studies. As previously stated, these experiments can be performed *in-situ* under reaction conditions or quasi-*in-situ* following by quench-freezing after or during electrolysis for EPR measurements. Here, some examples are discussed in a non-exhaustive exemplary way.

3.3.1   *In-situ* CW-EPR experiments

A study by Tamski *et al.* shows that radical species generated by an electrocatalytic reaction in a custom setup can be precisely quantified using a combined SEC-EPR approach [35]. Tamski *et al.* found that with careful design of the SEC-EPR setup, specifically the cell and the resonating chamber, reliable quantification up to µM concentrations is possible. Their work does highlight an additional challenge for SEC-EPR measurements: quantification is not a routine exercise and requires more careful planning and thought than other techniques such as UV-VIS or Raman. Important to note is that this study was performed on a radical species with a relatively simple EPR spectrum and a long lifetime ($t_{1/2} \approx 20$ s).

In some cases, a deeper understanding of the reaction mechanism can be obtained by the introduction of radical traps and scavengers. Radical scavengers are molecules that react with radical intermediates and therefore block the reaction from proceeding further. Radical traps convert short-living radicals in long-living radicals (see also part II and part III of this thesis). Depending on the radical species, different scavengers and traps can be used. In a study on electrochemical ammonia degradation by Liu *et al.*, the authors proposed a reaction mechanism that included several radical species that they could detect by SEC-EPR [48]. The production of ˙Cl and ˙OH was determined by EPR using 5,5-dimethyl-1-pyrroline N-oxide (DMPO) as the spin trap. In order to determine the dominant active species, they added nitrobenzene (NB) as an ˙OH scavenger and *tert*-butanol (*t*BuOH) as a ˙Cl and ˙OH scavenger and found that the major contributor to ammonia conversion is likely ˙Cl. While spin traps and scavengers can give useful information about competing species in a reaction mechanism, their addition may complicate or influence the (electro)chemistry of the system. Therefore their use, should be considered carefully. This will be discussed in more detail in chapter 4.

Functionalisation of the working electrode offers possibilities to probe biochemical redox reactions electrochemically. Ali *et al.* used a combined EPR and electrochemical setup to provide evidence for an electrocatalytic mechanism for the oxidation of NADH to NAD^+ [49]. They grafted carbon electrodes with quinone molecules with two different methods. The first method uses an electrochemical process to introduce anthraquinone on flexible carbon fibre (FCF) to make the electrodes named (FCF-AQ). The second methodology modifies the FCF by quinone groups using a one-pot chemical

reaction using $KMnO_4$, FCF, and quinones. The electrodes made by the second methodology are named (FCF-O). CV experiments showed drastically different redox behaviour for the functionalised electrodes in the presence of the NADH compared to the absence of NADH. Ali *et al.* then looked at the NAD^+ regeneration from NADH by the functionalised electrodes through *in-operando* EPR spectroscopy. They recorded EPR spectra of the electrodes while running chronoamperometric experiments. In the absence of NADH, a baseline EPR spectrum was obtained for each of the functionalised electrodes. When the experiments were repeated in the presence of NADH, the intensity of the EPR signal increased for both FCF-AQ and FCF-O, which is consistent with an increase in the concentration of unpaired electrons in the sample. The difference in intensity increase in presence of NADH between FCF-AQ and FCF-O agrees with the ratio of surface concentration of the quinone functional groups of FCF-AQ and FCF-O. Ali *et al.* found that the increase in spin concentration shows Butler-Volmer behavior consistent with electrocatalysts. From this, they proposed a new mechanism for the electro-oxidation of NADH by the quinone groups.

3.3.2 Quasi *in-situ* CW-EPR experiments

EPR detection of TMIs usually requires low temperatures with the electrochemical cell immersed in the liquid nitrogen during the quasi *in-situ* experiment. Quench-freezing stops the electrolysis and isolates the active states. At low temperatures, the polar solvent (such as water and acetonitrile) no longer strongly absorb MWs, so the standard 4 mm EPR tubes can be used, which allows using electrodes with higher surface areas [15,50]. Freezing also provides the advantage of stability for the reactive species. A nice example of a well-suited SEC-EPR system can be found in a study by Mondal *et al.* on water oxidation by tris(5,10,15-pentafluorophenyl)-2,3,7,8,12,13,17,18-octabromocobalt corrole ($CoBr_8$) [51]. Water can be oxidised via a $2e^-/2H^+$ pathway to H_2O_2, or via a $4e^-/4H^+$ pathway to O_2. CV experiments in acetonitrile under homogeneous conditions show two oxidation peaks at 0.95 V and 1.4 V vs NHE corresponding to the processes [cor-Co(III)-OH_2/ cor$^{\bullet+}$-Co(III)-OH] and [cor$^{\bullet+}$-Co(III)-OH/ cor$^{\bullet+}$-Co(III)-OH$^{\bullet-}$]. Upon freezing of the sample after half an hour of electrolysis at 1.3 V, a signal is observed in EPR (Figure 3.4A). The EPR data with and without water (Figure 3.4A green and red, respectively) show a signal at $g = 1.98$, which is characteristic of an organic radical. Literature and DFT calculations suggest that this signal corresponds to the Co(III) corrole radical cation. Electrolysis upon addition of a base shows a new rhombic EPR signal (Figure 3.4A blue) around $g = 2.01$ with the g anisotropy smaller than the EPR spectrum of Co(II) corrole. Previous results on the oxygenation of Co(II) corrole and porphyrins show that the obtained signal corresponds to [Co(III)-$O_2^{\bullet-}$]. EPR spin quantification shows $15 \pm 5\%$ of this species in the solution. The fast decay rate (half-life around 60 s) of the EPR signal proves the nonstability of the product resulting from O_2 binding to Co(II) species. The quantification results indicate that [Co(III)-$O_2^{\bullet-}$] is the precursor to the evolved O_2.
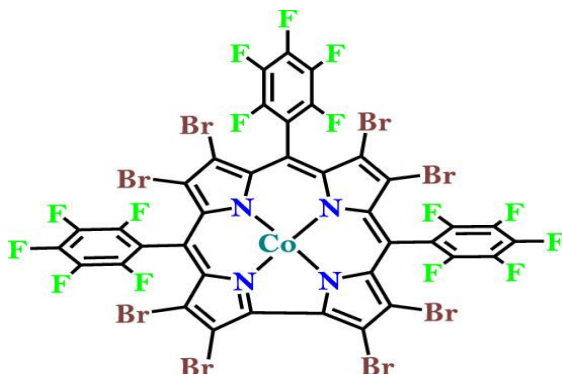
Figure 3.3 Chemical structure of the investigated cobalt(III) corrole complex (CoBr$_8$).
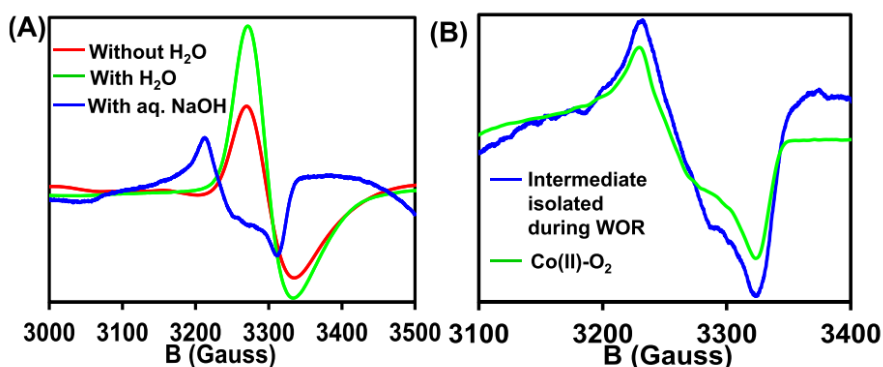

Figure 3.4. CW-EPR of cobalt(III)–superoxide intermediate involved in water oxidation recorded at 77 K. EPR spectra of (A) the oxidised CoBr$_8$ produced by electrochemical oxidation in degassed acetonitrile (red), in water:acetonitrile mixture (green), in aqueous-base:acetonitrile mixed solvent (blue), and (B) Co(III) superoxo corrole as obtained by oxygenation of the reduced Co(II) corrole (green) and after electrochemical oxidation in degassed aqueous-base:acetonitrile solvent mixture (blue). Reprinted (adapted) with permission from Mondal et al. [51].

A setup using a gold WE and silver pseudo-reference wire and Pt CE in a standard EPR tube designed by Kutin *et.al* [50] can be used for homogeneous and heterogeneous catalytic reactions. Kutin *et al.* showed that they could follow the electrochemical film formation of a cobalt oxide from a Co(NO$_3$)$_2$ solution using EPR spectroscopy [50]. Such films have the potential for use in large-scale water splitting applications. They followed the EPR intensity of Co(II) in both the electrolyte and the cobalt/phosphate derivative film and were able to distinguish between the two due to the difference in EPR relaxation times. The authors studied the effect of potential on the deposition mechanism through the use of EPR at low temperature. At high potentials, they detected an increase in Co(IV) formation instead of Co(II), which signifies the presence of Co(IV) under catalytic potentials.

Quasi *in-situ* pulse EPR Experiments

Up until this point, we have only discussed CW-EPR studies. As explained in section 2.1.3, ESEEM and ENDOR techniques offer more detailed information and are used to address the small nuclear transitions which are not detectable by CW-EPR. They require, however, low temperatures and thus freeze-quenching experiments.
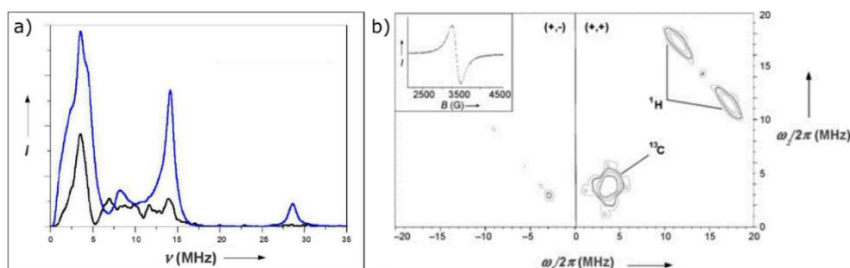

Figure 3.5 a) 2P-ESEEM spectrum of Mn(II) complex intermediate with $^{13}CO_2$ bubbling before (black) and after (blue) adding water. b) HYSCORE spectrum of the frozen solution of [Mn-(dmbpy)(CO)$_3$]$_2$ 0.45 mM MeCN + 0.1 M TBAP + $^{13}CO_2$ + 5% H_2O. Adapted from Bourrez et al. [53].

Bourrez *et al.* [52,53] studied the CO_2 electrocatalytic reduction by Mn complexes which are precursors for electrocatalysis of CO_2 to CO in hydro-organic electrolytes. They proposed the following catalytic cycle. The reaction begins with the reduction of $[Mn^I(L)(CO)_3]^-$ (L = bpy(2,2'-bipyridine)), followed by a dimerization reaction. The dimer then reacts with CO_2 and a proton. In this step, a low-spin Mn(II) complex intermediate is made, which is detectable by EPR. At the end, the Mn(II) species is reduced to the initial Mn(I) complex. The electrochemical experiments were performed *ex-situ* in a standard one-compartment three-electrode electrochemical cell with a vitreous carbon WE, Ag/AgNO$_3$ RE and a Pt plate CE. In order to identify the intermediate, EPR measurements were performed on a frozen sample taken after electrolysis containing $[Mn^0(dmbpy)(CO)_3]_2$ bubbled with $^{13}CO_2$ before and after the addition of 5% water in CH$_3$CN. Since ^{12}C has no nuclear spin, $^{13}CO_2$ is necessary in order to be observable in EPR. The CW-EPR spectrum showed a broad signal at $g_{iso} = 2.001$ with a linewidth around 100 mT, which does not reveal much information about the coupled nuclei. The significant amount of water used in the electrocatalytic process makes analysis by IR spectroscopy challenging. In contrast, pulse EPR methods at the frozen solution provided direct evidence about the nuclei coupled to the Mn(II). The 2*P*-ESEEM spectrum showed peaks at 3.50 and 6.9 MHz, which correspond with the Larmor frequency (and its combination line) of ^{13}C from $^{13}CO_2$; and another peak at 14.10 MHz, which correspond with the Larmor frequency of ^1H. By adding water, the ESEEM signal from protons became more dominant, which corroborates the interaction of water protons with the electron spin (Figure 3.5a). Using HYSCORE measurements, they found relatively isotropic weak hyperfine coupling of 6.4 MHz for ^1H and dipolar interaction of 1.2 MHz for ^{13}C (Figure 3.5b). The results show the direct coordination of ^{13}C nuclei to the Mn^{II} ion and the protons further from the metal centre, thus demonstrating an experimental method to find the oxidation state of the metal and the bond characteristics of CO_2 in the CO_2-adduct intermediate in the electrocatalytic cycle.

He *et al.* [54] studied the electrochemical nitrate reduction to NO_2 on 1T-MoS_2 distributed onto a carbon paper substrate. The 1T phase of MoS_2 (*i.e.* phase with octahedral coordination) exhibits metallic behaviour. 1T-MoS_2 is used for phase engineering in electrocatalysis to increase the catalytic activity [55,56]. It is used for CO_2 reduction [57–60], denitrification [61–63], and electrosynthesis of functional molecules [64–67]. He *et al.* performed their electrolysis experiments in nitrite, citric acid and phosphate buffers with pH values ranging between 4 and 7 in a two-compartment electrochemical cell separated by a Nafion perfluorinated membrane. The WE consisted of a 1T-MoS_2 powder/nafion ink suspension on a carbon paper substrate, with an Ag/AgCl RE and Pt wire CE. The reduction of CO_2 by the metal complex was performed *in-situ* in a standard EPR tube for the CW-EPR experiments. Using [1]H Davies ENDOR experiments, they detected the proton hyperfine couplings to confirm the protons' locations versus the electrochemically active Mo(V) of 1T-MoS_2 [54]. The hyperfine coupling of the proton binding to the Mo centre was obtained, with the isotropic contribution value (A_{iso} = 1.2 MHz) and electron-nucleus dipolar contribution ($\mathbf{A_{dip}}$ = [-4.6, 3.3, 1.3] MHz). From these values, the distance between Mo(V) and the proton is estimated to be around 3.26 Å and the angle O-Mo-H is ~ 115°.

Gerlach *et al.* reported electrocatalytic oxidation of water using 6,6′-dihydroxybipyridine (6,6′-dhbp)/copper complexes as the catalyst [68]. 6,6′-dhbp/copper complexes are capable of electrocatalytic water oxidation in an aqueous base which can be used to make a sustainable energy source. CV experiments were performed using a vitreous carbon WE, Ag/AgCl RE and Pt disk CE. The EPR experiments were performed *in-situ*; it is not mentioned what cells were used. The various oxidation forms of complex **1** are shown in Figure 3.6. CW-EPR spectra showed that 6,6′-dhbp ligands coordinate to copper at pH 5.7 - 12.6, but do not bind to Cu^{2+} at pH 3.5 and 13.3. Between pH 5.7 – 10, only species **1a** exists, which disappears between pH 10 – 12 as **1b** and **1c** appear. HYSCORE experiments were performed for further identification of species **1a**, **1b** and **1c**. HYSCORE is able to detect water protons up to 0.7 nm and ^{13}C atoms of the ligands up to 0.44 nm away from the paramagnetic centre. HYSCORE spectra of complex **1** show the ligated water protons between pH 10 - 12.5, and show the ^{13}C atoms of 6,6′-dhbp ligand between pH 10 - 12.5.
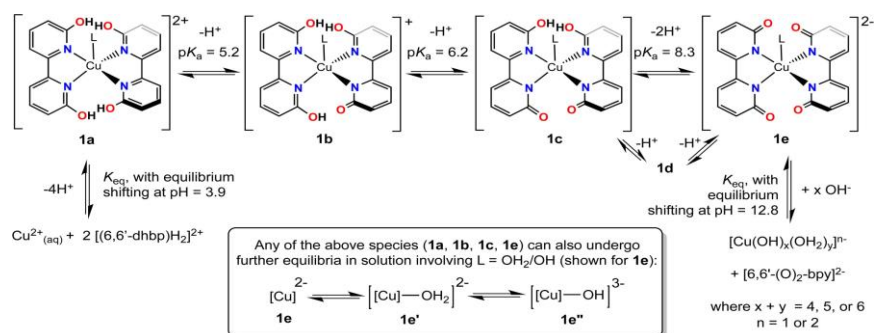

*Figure 3.6 Complex Hydrogen Ion Interrelationships of [(6,6′-dhbp)₂Cu]ⁿ (where n = charge) Complexes (**1**) in water (L = OH₂/OH). Adapted from Gerlach et al.* [68]*.*

3.4   Outlook

In general, the use of SEC-EPR as a mainstream technique is at the moment limited by the fact that most EPR spectrometers are large and expensive instruments that are often only accessible in specialised laboratories. This is especially so for high-frequency instruments working at W-band and higher frequencies. As an example, Belgium only has one high-field EPR spectrometer housed at the University of Antwerp. However, most SEC-EPR setups use X-band CW-EPR spectrometers. Moreover, the development of the inexpensive (10-fold cheaper) table-top X-band CW-EPR instruments opens the use of SEC-EPR to non-specialists [69].

Potentially, the use of EPR can be even more boosted by combination with the miniaturisation of EPR instruments. In recent years an EPR Mobile Universal Surface Explorer (EPR-MOUSE) was introduced that allows low-frequency EPR at surfaces [70]. A pulsed EPR 'dipstick' spectrometer is another evolved device containing an EPR sensor with a diameter of 2 mm and length of 3.6 mm at a frequency of 2.6 GHz. This device is suitable for catalytic studies since it can be immersed in a liquid sample [71]. This builds on the EPR-on-a-chip (EPRoC) devices, in which all the different parts of the EPR instrument, such as microwave detections, electromagnets and the resonator, are mounted on a millimetre-sized chip [72,73]. The surface resonator in EPRoC relaxes the limitation of inserting the sample in the resonator. Instead, due to the tiny size of the instrument, one may immerse the sensor in the solution or place the sample on the sensor to measure the EPR data. The new microwave technology extremely decreases the instrumental costs.

An important future evolution points to the use of rapid-scan EPR techniques in SEC-EPR [23,74,75]. This technique decreases the acquisition time down to milliseconds. The short sweep time in this technique enables us to detect short-lived radicals. It also allows using MW powers higher than conventional CW-EPR, leading to a larger S/N ratio [75–78]. The earlier-mentioned EPRoC allows for rapid-scan EPR [79].

The future progress in SEC-EPR focuses on pulse EPR techniques and higher frequencies than X-band to use the advantages of these techniques for *in-situ* experiments. High-field EPR spectrometers using a nonresonant sample holder instead of a cavity [80,81]. This can decrease the restrictions caused by the space limitations in the cavities, which provides the possibility of performing very high-frequency *in-situ* SEC-EPR experiments in the future with a larger S/N ratio and better separation of overlapping signals compared with the X-band EPR experiments. The ability to perform higher frequency experiments using EPRoC [82] will enable us decreasing the limitation of Q-band and W-band experiments which offers another way to tackle the size problem.

3.5   References

[1]   C. Ma, P. Fang, and T. S. Mei, *Recent Advances in C-H Functionalization Using Electrochemical Transition Metal Catalysis*, ACS Catal. **8**, 7179 (2018).

[2]   K. Tammeveski and J. H. Zagal, *Electrocatalytic Oxygen Reduction on Transition Metal Macrocyclic Complexes for Anion Exchange Membrane Fuel Cell Application*, Curr. Opin. Electrochem. **9**, 207 (2018).

[3]   A. L. Balch and K. Winkler, *Electrochemistry of Fullerene/Transition Metal Complexes: Three Decades of Progress*, Coord. Chem. Rev. **438**, 213623 (2021).

[4]   A. Brückner, *In-Situ Spectroscopy of Catalysts* (American Scientific Publishers, California, 2004).

[5]   A. Brückner, *In Situ Electron Paramagnetic Resonance: A Unique Tool for Analysing Structure–Reactivity Relationships in Heterogeneous Catalysis*, Chem. Soc. Rev. **39**, 4673 (2010).

[6]   A. Brückner, *Looking on Heterogeneous Catalytic Systems from Different Perspectives: Multitechnique Approaches as a New Challenge for In Situ Studies*, Catal. Rev. **45**, 97 (2003).

[7]   M. Labanowska, *EPR Monitoring of Redox Processes in Transition Metal Oxide Catalysts*, ChemPhysChem **2**, 712 (2001).

[8]   K. Dyrek and M. Che, *EPR as a Tool To Investigate the Transition Metal Chemistry on Oxide Surfaces*, Chem. Rev. **97**, 305 (1997).

[9]   M. Chiesa, E. Giamello, and M. Che, *EPR Characterization and Reactivity of Surface-Localized Inorganic Radicals and Radical Ions*, Chem. Rev. **110**, 1320 (2010).

[10]   P. H. Rieger, I. Bernal, W. H. Reinmuth, and G. K. Fraenkel, *Electron Spin Resonance of Electrolytically Generated Nitrile Radicals*, J. Am. Chem. Soc. **85**, 683 (1963).

[11]   R. G. Compton, B. A. Coles, and M. J. Day, *The Oxidation of Triphenylacetic Acid in Acetonitrile*, J. Electroanal. Chem. **200**, 205 (1986).

[12]   R. N. Adams, *Anodic Oxidation Pathways of Aromatic Hydrocarbons and Amines*, Acc. Chem. Res. **2**, 175 (1969).

[13]   P. A. Abramov, A. A. Dmitriev, K. V. Kholin, N. P. Gritsan, M. K. Kadirov, A. L. Gushchin, and M. N. Sokolov, *Mechanistic Study of the [(Dpp-Bian)Re(CO)₃Br] Electrochemical Reduction Using in Situ EPR Spectroscopy and Computational Chemistry*, Electrochim. Acta **270**, 526 (2018).

[14]   G. Armendáriz-Vidales and C. Frontana, *Insights into Dissociative Electron Transfer in Esterified Shikonin Semiquinones by in Situ ESR/UV-Vis Spectroelectrochemistry*, Phys. Chem. Chem. Phys. **17**, 29299 (2015).

[15]   K. Abdiaziz, E. Salvadori, K. P. Sokol, E. Reisner, and M. M. Roessler, *Protein Film Electrochemical EPR Spectroscopy as a Technique to Investigate Redox Reactions in Biomolecules*, Chem. Commun. **55**, 8840 (2019).

[16]   S. L. J. Tan and R. D. Webster, *Electrochemically Induced Chemically Reversible Proton-Coupled Electron Transfer Reactions of Riboflavin (Vitamin B 2)*, J. Am. Chem. Soc. **134**, 5954 (2012).

[17]   F. Zhang and S. Mu, *Influence of Potential and Temperature on the ESR*

Spectra of Polyaniline Synthesized Using the Interface Polymerization, J. Phys. Chem. B **114**, 16687 (2010).

[18]   A. Staško, K. Lušpai, Z. Barbieriková, J. Rimarčík, A. Vagánek, V. Lukeš, M. Bella, V. Milata, M. Zalibera, P. Rapta, and V. Brezová, *Stable Radical Trianions from Reversibly Formed Sigma-Dimers of Selenadiazoloquinolones Studied by in Situ EPR/UV-Vis Spectroelectrochemistry and Quantum Chemical Calculations*, J. Phys. Chem. A **116**, 9919 (2012).

[19]   J. C. Dong, X. G. Zhang, V. Briega-Martos, X. Jin, J. Yang, S. Chen, Z. L. Yang, D. Y. Wu, J. M. Feliu, C. T. Williams, Z. Q. Tian, and J. F. Li, *In Situ Raman Spectroscopic Evidence for Oxygen Reduction Reaction Intermediates at Platinum Single-Crystal Surfaces*, Nat. Energy **4**, 60 (2019).

[20]   J. Sun, L. Gong, W. Wang, Z. Gong, D. Wang, and M. Fan, *Surface-Enhanced Raman Spectroscopy for on-Site Analysis: A Review of Recent Developments*, Luminescence **35**, 808 (2020).

[21]   J. Y. Ye, Y. X. Jiang, T. Sheng, and S. G. Sun, *In-Situ FTIR Spectroscopic Studies of Electrocatalytic Reactions and Processes*, Nano Energy **29**, 414 (2016).

[22]   L. Dunsch, *Recent Advances in in Situ Multi-Spectroelectrochemistry*, J. Solid State Electrochem. **15**, 1631 (2011).

[23]   D. Goldfarb and S. Stoll, *EPR Spectroscopy: Fundamentals and Methods* (JOHN WILEY & SONS, Chichester, 2017).

[24]   M. A. Morsy and A. N. M. Kawde, *Electron Paramagnetic Resonance Monitoring for On-Demand Electrochemically-Generated Radicals*, Electrochim. Acta **160**, 22 (2015).

[25]   P. R. Murray, D. Collison, S. Daff, N. Austin, R. Edge, B. W. Flynn, L. Jack, F. Leroux, E. J. L. McInnes, A. F. Murray, D. Sells, T. Stevenson, J. Wolowska, and L. J. Yellowlees, *An in Situ Electrochemical Cell for Q- and W-Band EPR Spectroscopy*, J. Magn. Reson. **213**, 206 (2011).

[26]   J. D. Wadhawan and R. G. Compton, *EPR Spectroscopy in Electrochemistry*, in *Encyclopedia of Electrochemistry:*, edited by A. J. Bard (Wiley, 2007).

[27]   S. Pluczyk, M. Vasylieva, and P. Data, *Using Cyclic Voltammetry, UV-Vis-NIR, and EPR Spectroelectrochemistry to Analyse Organic Compounds*, J. Vis. Exp. 1 (2018).

[28]   I. Cekić-Lasković, R. Marković, D. M. Minić, and E. Volanschi, *Electrochemical Reduction of (5-Etoxycarbonylmethylidene-4-Oxothiazolidine-2-Ylidene)-N-Phenylethanone in Aprotic Medium: A Spectroelectrochemical Approach*, J. Electroanal. Chem. **651**, 50 (2011).

[29]   K. Luspai, Z. Barbieriková, M. Malcek, L. Bucinsky, A. Stasko, M. Bella, V. Milata, P. Rapta, and V. Brezová, *Cathodic and Photocatalytic Reduction of Nitroquinolones Investigated by In Situ EPR/UV-Vis Spectroelectrochemistry and EPR Spectroscopy*, Curr. Org. Chem. **17**, 2427 (2013).

[30]   C. Ribaut, G. Bordeau, P. Perio, K. Reybier, V. Sartor, O. Reynes, P. L. Fabre, and N. Chouini-Lalanne, *EPR Spectroelectrochemical Investigation of Guanine Radical Formation and Environment Effects*, J. Phys. Chem. B **118**, 2360 (2014).

[31]   L. Šimková, E. Dmitrieva, J. Klíma, L. Dunsch, and J. Ludvík, *(Spectro) Electrochemical Investigation of Reduction Mechanism of a New Energetic*

Molecule 2,2-Dinitroethene-1,1-Diamine (FOX-7) in Aprotic Solvents, J. Solid State Electrochem. **19**, 103 (2015).

[32] S. I. Kulakovskaya, A. V. Kulikov, L. N. Sviridova, and E. V. Stenina, *Electrochemical and Electron Paramagnetic Resonance Study of the Mechanism of Oxidation of Phenazine-Di-n-Oxide in the Presence of Isopropyl Alcohol at Glassy Carbon and Single-Walled Carbon Nanotube Electrodes*, Electrochim. Acta **146**, 798 (2014).

[33] L. S. Hernández-Muñoz, C. Frontana, and F. J. González, *Covalent Modification of Carbon Surfaces with Cyclodextrins by Mediated Oxidation of β-Cyclodextrin Monoanions*, Electrochim. Acta **138**, 22 (2014).

[34] M. A. Tamski, J. V. MacPherson, P. R. Unwin, and M. E. Newton, *Electrochemical Electron Paramagnetic Resonance Utilizing Loop Gap Resonators and Micro-Electrochemical Cells*, Phys. Chem. Chem. Phys. **17**, 23438 (2015).

[35] M. A. Tamski, M. W. Dale, B. G. Breeze, J. V. Macpherson, P. R. Unwin, and M. E. Newton, *Quantitative Measurements in Electrochemical Electron Paramagnetic Resonance*, Electrochim. Acta **213**, 802 (2016).

[36] R. Sokolová, J. Tarábek, B. Papoušková, J. Kocábová, J. Fiedler, J. Vacek, P. Marhol, E. Vavříková, and V. Křen, *Oxidation of the Flavonolignan Silybin. in Situ EPR Evidence of the Spin-Trapped Silybin Radical*, Electrochim. Acta **205**, 118 (2016).

[37] Y. Makarov, A. V. Zibarev, L. A. Shundrin, I. G. Irtegova, P. A. Avrorov, T. F. Mikhailovskaya, A. G. A. Y. Makarov, A. G. A. Y. Makarov, and A. V. Zibarev, *Electrochemical Reduction, Radical Anions, and Dehalogenation of Fluorinated/Chlorinated 2,1,3-Benzothia/Selenadiazoles*, Arkivoc **2017**, 166 (2017).

[38] Q. Liu, B. Sun, Z. Liu, Y. Kao, B. W. Dong, S. Da Jiang, F. Li, G. Liu, Y. Yang, and F. Mo, *A General Electrochemical Strategy for the Sandmeyer Reaction*, Chem. Sci. **9**, 8731 (2018).

[39] M. A. Buckingham, W. Cunningham, S. D. Bull, A. Buchard, A. Folli, D. M. Murphy, and F. Marken, *Electrochemically Driven C−H Hydrogen Abstraction Processes with the Tetrachloro-Phthalimido-N-Oxyl (Cl$_4$PINO) Catalyst*, Electroanalysis **30**, 1698 (2018).

[40] X. Yu, T. L. Roemmele, and R. T. Boeré, *Synthesis, Electronic Structures, and Electrochemistry of 3-Triarylphosphoraniminato-1,3,5-Trithia-2,4,6,8-Tetrazocines: Detection of Trithiatetrazocinyl Radical Anions*, ChemElectroChem **5**, 968 (2018).

[41] M. Toybenshlak and R. Carmieli, *A New and Robust Method for In-Situ EPR Electrochemistry*, Isr. J. Chem. **59**, 1 (2019).

[42] E. Bulak, T. Varnali, B. Schwederski, D. Bubrin, J. Fiedler, and W. Kaim, *Separation of Metal Binding and Electron Transfer Sites as a Strategy to Stabilise the Ligand-Reduced and Metal-Oxidized Form of [Mo(CO)$_4$L]*, Organometallics **30**, 6441 (2011).

[43] M. Dürr, J. Klein, A. Kahnt, S. Becker, R. Puchta, B. Sarkar, and I. Ivanović-Burmazović, *Redox Behavior of a Dinuclear Ruthenium(II) Complex Bearing an Uncommon Bridging Ligand: Insights from High-Pressure Electrochemistry*, Inorg. Chem. **56**, 14912 (2017).

[44] K. Kholin, M. Valitov, V. Burilov, E. Tselischeva, S. Strekalova, A. Mustafina, Y. Budnikova, and M. Kadirov, *Spectroelectrochemistry: ESR of Paramagnetic Intermediates in the Electron Transfer Series [Cr(Bpy)₃]n (n = 3+, 2+, 1+, 0, 1-)*, Electrochim. Acta **182**, 212 (2015).

[45] M. Khrizanforov, S. Strekalova, K. Kholin, V. Khrizanforova, V. Grinenko, T. Gryaznova, and Y. Budnikova, *One-Stage Synthesis of FcP(O)(OC₂H₅)₂ from Ferrocene and α-Hydroxyethylphosphonate*, RSC Adv. **6**, 42701 (2016).

[46] M. K. Kadirov, K. V. Kholin, E. Y. Tselishcheva, V. A. Burilov, and A. R. Mustafina, *Cyclic Voltammetry of Tris (2 , 2 ´ Bipyridine) Zinc (II) Diperchlorate*, Russ. Chem. Bull. **62**, 1327 (2013).

[47] P. Machata, P. Herich, K. Lušpai, L. Bucinsky, S. Šoralová, M. Breza, J. Kozisek, and P. Rapta, *Redox Reactions of Nickel, Copper, and Cobalt Complexes with "Noninnocent" Dithiolate Ligands: Combined in Situ Spectroelectrochemical and Theoretical Study*, Organometallics **33**, 4846 (2014).

[48] Y. Liu, J. Mei, C. Shen, M. Huang, M. Yang, Z. Wang, W. Sand, and F. Li, *Rapid and Selective Electrochemical Transformation of Ammonia to N₂ by Substoichiometric TiO₂-Based Electrochemical System*, RSC Adv. **10**, 1219 (2020).

[49] M. A. Ali, A. Hassan, G. C. Sedenho, R. V. Gonçalves, D. R. Cardoso, and F. N. Crespilho, *Operando Electron Paramagnetic Resonance for Elucidating the Electron Transfer Mechanism of Coenzymes*, J. Phys. Chem. C **123**, 16058 (2019).

[50] Y. Kutin, N. Cox, W. Lubitz, A. Schnegg, and O. Rüdiger, *In Situ EPR Characterization of a Cobalt Oxide Water Oxidation Catalyst at Neutral PH*, Catalysts **9**, (2019).

[51] B. Mondal, S. Chattopadhyay, S. Dey, A. Mahammed, K. Mittra, A. Rana, Z. Gross, and A. Dey, *Elucidation of Factors That Govern the 2e-/2H+vs 4e-/4H+Selectivity of Water Oxidation by a Cobalt Corrole*, J. Am. Chem. Soc. (2020).

[52] M. Bourrez, F. Molton, S. Chardon-Noblat, and A. Deronzier, *[Mn(Bipyridyl)(CO)₃Br]: An Abundant Metal Carbonyl Complex as Efficient Electrocatalyst for CO₂ Reduction*, Angew. Chemie **123**, 10077 (2011).

[53] M. Bourrez, M. Orio, F. Molton, H. Vezin, C. Duboc, A. Deronzier, and S. Chardon-Noblat, *Pulsed-EPR Evidence of a Manganese(II) Hydroxycarbonyl Intermediate in the Electrocatalytic Reduction of Carbon Dioxide by a Manganese Bipyridyl Derivative*, Angew. Chemie Int. Ed. **53**, 240 (2014).

[54] D. He, H. Ooka, Y. Kim, Y. Li, F. Jin, S. H. Kim, and R. Nakamura, *Atomic-Scale Evidence for Highly Selective Electrocatalytic N−N Coupling on Metallic MoS₂*, Proc. Natl. Acad. Sci. **117**, 31631 (2020).

[55] Y. Huang, Y. Sun, X. Zheng, T. Aoki, B. Pattengale, J. Huang, X. He, W. Bian, S. Younan, N. Williams, J. Hu, J. Ge, N. Pu, X. Yan, X. Pan, L. Zhang, Y. Wei, and J. Gu, *Atomically Engineering Activation Sites onto Metallic 1T-MoS2 Catalysts for Enhanced Electrochemical Hydrogen Evolution*, Nat. Commun. **10**, 982 (2019).

[56] M. A. Lukowski, A. S. Daniel, F. Meng, A. Forticaux, L. Li, and S. Jin, *Enhanced Hydrogen Evolution Catalysis from Chemically Exfoliated Metallic*

MoS₂ Nanosheets, J. Am. Chem. Soc. **135**, 10274 (2013).

[57]   R. Kortlever, J. Shen, K. J. P. Schouten, F. Calle-Vallejo, and M. T. M. Koper, *Catalysts and Reaction Pathways for the Electrochemical Reduction of Carbon Dioxide*, J. Phys. Chem. Lett. **6**, 4073 (2015).

[58]   M. B. Ross, P. De Luna, Y. Li, C.-T. Dinh, D. Kim, P. Yang, and E. H. Sargent, *Designing Materials for Electrochemical Carbon Dioxide Recycling*, Nat. Catal. **2**, 648 (2019).

[59]   Y. Lum and J. W. Ager, *Sequential Catalysis Controls Selectivity in Electrochemical CO₂ Reduction on Cu*, Energy Environ. Sci. **11**, 2935 (2018).

[60]   K. D. Yang, W. R. Ko, J. H. Lee, S. J. Kim, H. Lee, M. H. Lee, and K. T. Nam, *Morphology-Directed Selective Production of Ethylene or Ethane from CO₂ on a Cu Mesopore Electrode*, Angew. Chemie Int. Ed. **56**, 796 (2017).

[61]   M. Duca and M. T. M. Koper, *Powering Denitrification: The Perspectives of Electrocatalytic Nitrate Reduction*, Energy Environ. Sci. **5**, 9726 (2012).

[62]   V. Rosca, M. Duca, M. T. de Groot, and M. T. M. Koper, *Nitrogen Cycle Electrocatalysis*, Chem. Rev. **109**, 2209 (2009).

[63]   K. Kamiya, T. Tatebe, S. Yamamura, K. Iwase, T. Harada, and S. Nakanishi, *Selective Reduction of Nitrate by a Local Cell Catalyst Composed of Metal-Doped Covalent Triazine Frameworks*, ACS Catal. **8**, 2693 (2018).

[64]   M. D. Kärkäs, *Electrochemical Strategies for C–H Functionalization and C–N Bond Formation*, Chem. Soc. Rev. **47**, 5786 (2018).

[65]   M. Jouny, J. J. Lv, T. Cheng, B. H. Ko, J. J. Zhu, W. A. Goddard, and F. Jiao, *Formation of Carbon–Nitrogen Bonds in Carbon Monoxide Electrolysis*, Nat. Chem. **11**, 846 (2019).

[66]   V. R. Pattabiraman and J. W. Bode, *Rethinking Amide Bond Synthesis*, Nature **480**, 471 (2011).

[67]   T. Wang, J. Ibañez, K. Wang, L. Fang, M. Sabbe, C. Michel, S. Paul, M. Pera-Titus, and P. Sautet, *Rational Design of Selective Metal Catalysts for Alcohol Amination with Ammonia*, Nat. Catal. **2**, 773 (2019).

[68]   D. L. Gerlach, S. Bhagan, A. A. Cruce, D. B. Burks, I. Nieto, H. T. Truong, S. P. Kelley, C. J. Herbst-Gervasoni, K. L. Jernigan, M. K. Bowman, S. Pan, M. Zeller, and E. T. Papish, *Studies of the Pathways Open to Copper Water Oxidation Catalysts Containing Proximal Hydroxy Groups During Basic Electrocatalysis*, Inorg. Chem. **53**, 12689 (2014).

[69]   S. A. Bonke, T. Risse, A. Schnegg, and A. Brückner, *In Situ Electron Paramagnetic Resonance Spectroscopy for Catalysis*, Nat. Rev. Methods Prim. **1**, 33 (2021).

[70]   L. E. Switala, B. E. Black, C. A. Mercovich, A. Seshadri, and J. P. Hornak, *An Electron Paramagnetic Resonance Mobile Universal Surface Explorer*, J. Magn. Reson. **285**, 18 (2017).

[71]   O. Zgadzai, Y. Twig, H. Wolfson, R. Ahmad, P. Kuppusamy, and A. Blank, *Electron-Spin-Resonance Dipstick*, Anal. Chem. **90**, 7830 (2018).

[72]   J. Anders, A. Angerhofer, and G. Boero, *K-Band Single-Chip Electron Spin Resonance Detector*, J. Magn. Reson. **217**, 19 (2012).

[73]   J. Anders and K. Lips, *MR to Go*, J. Magn. Reson. **306**, 118 (2019).

[74]   D. G. Mitchell, M. Tseitlin, R. W. Quine, V. Meyer, M. E. Newton, A. Schnegg, B. George, S. S. Eaton, and G. R. Eaton, *X-Band Rapid-Scan EPR of*

Samples with Long Electron Spin Relaxation Times: A Comparison of Continuous Wave, Pulse and Rapid-Scan EPR, Mol. Phys. **111**, 2664 (2013).

[75]   R. W. Quine, G. A. Rinard, S. S. Eaton, and G. R. Eaton, *Quantitative Rapid Scan EPR Spectroscopy at 258MHz*, J. Magn. Reson. **205**, 23 (2010).

[76]   D. G. Mitchell, G. M. Rosen, M. Tseitlin, B. Symmes, S. S. Eaton, and G. R. Eaton, *Use of Rapid-Scan EPR to Improve Detection Sensitivity for Spin-Trapped Radicals*, Biophys. J. **105**, 338 (2013).

[77]   Z. Yu, R. W. Quine, G. A. Rinard, M. Tseitlin, H. Elajaili, V. Kathirvelu, L. J. Clouston, P. J. Boratyński, A. Rajca, R. Stein, H. Mchaourab, S. S. Eaton, and G. R. Eaton, *Rapid-Scan EPR of Immobilized Nitroxides*, J. Magn. Reson. **247**, 67 (2014).

[78]   Z. Yu, T. Liu, H. Elajaili, G. A. Rinard, S. S. Eaton, and G. R. Eaton, *Field-Stepped Direct Detection Electron Paramagnetic Resonance*, J. Magn. Reson. **258**, 58 (2015).

[79]   S. Künstner, A. Chu, K.-P. Dinse, A. Schnegg, J. E. McPeak, B. Naydenov, J. Anders, and K. Lips, *Rapid-Scan Electron Paramagnetic Resonance Using an EPR-on-a-Chip Sensor*, Magn. Reson. **2**, 673 (2021).

[80]   P. A. S. Cruickshank, D. R. Bolton, D. A. Robertson, R. I. Hunter, R. J. Wylde, and G. M. Smith, *A Kilowatt Pulsed 94 GHz Electron Paramagnetic Resonance Spectrometer with High Concentration Sensitivity, High Instantaneous Bandwidth, and Low Dead Time*, Rev. Sci. Instrum. **80**, (2009).

[81]   S. Un, P. Dorlet and A. W. Rutherford, *A High-Field EPR Tour of Radicals in Photosystems I and II,* Appl. Magn. Reson., **21**, 341, (2001).

[82]   A. V. Matheoud, G. Gualco, M. Jeong, I. Zivkovic, J. Brugger, H. M. Rønnow, J. Anders, and G. Boero, *Single-Chip Electron Spin Resonance Detectors Operating at 50 GHz, 92 GHz, and 146 GHz*, J. Magn. Reson. **278**, 113 (2017).

Part II
Pitfalls of spin trap EPR

CHAPTER 4

The non-innocent role of spin traps

Spin traps, like 5,5-dimethyl-1-pyroline *N*-oxide (DMPO) are commonly used to identify radicals formed in numerous chemical and biological systems, many of which contain metal-ion complexes. In this chapter, continuous wave electron paramagnetic resonance and hyperfine spectroscopy are used to prove the equatorial ligation of DMPO(-derived) molecules to Cu(II), even in the presence of competing nitrogen bases. The experimental data are corroborated with density functional theory calculations. It is shown that ^{14}N HYSCORE can be used as a fingerprint method to reveal the coordination of DMPO(-derived) molecules to Cu(II), an interaction that might influence the outcome of spin-trapping experiments and consequently the conclusion drawn on the mechanism under study.

4.1 Introduction

Copper is one of the most abundant transition metals on earth, with relatively low toxicity [1]. Its rich redox chemistry is exploited both by nature and by synthetic chemists to functionalize organic molecules [2–5]. The efficient way in which Cu-containing enzymes can activate O_2 to perform selective oxidase and oxygenase reactions has inspired chemists in their search of Cu/O_2 systems for selective oxidation of organic molecules [2–4]. In many of the copper-catalyzed synthesis pathways of organic molecules, the formation of highly reactive, short-living radical intermediates, such as reactive oxygen species (ROS, e.g. $O_2^{\bullet-}$, $^{\bullet}OH$, …) and carbon-centered radicals, are hypothesized to play a crucial role [2–4]. Electron paramagnetic resonance is by far the most used analytical technique to study (intermediate) radical formation and to investigate paramagnetic redox states of transition metals, such as Cu(II) [6]. The detection of very reactive radicals with EPR can, in some cases, be done directly after rapid freezing of the sample but is mostly performed indirectly *via* spin trap EPR [7–9] Spin trapping exploits the rapid reaction of very short-living radicals with diamagnetic spin trap molecules to form a more stable radical that can be easily detected by EPR. In most cases, nitrones, *N*-oxides and nitroso compounds are used as spin traps that will lead to a stable nitroxide radical after reaction with the short-living radical, as is demonstrated in Figure 4.1 for the very common spin trap DMPO (5,5-dimethyl-1-pyroline *N*-oxide, **1**) [7,8].
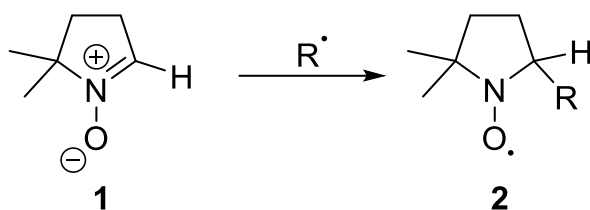

Figure 4.1 The spin trapping reaction illustrated for the reaction of a short-living radical R• with DMPO (1) to form the EPR-detectable adduct (2).

Not surprisingly, spin trap EPR has been abundantly used to support radical mechanisms in copper-catalyzed synthetic and biological reactions (selected examples: [10–16]) and very often the spin trap is added in very large excess, up to the 10^3 range in equivalence compared to the copper catalyst. Many studies have, however, pointed out considerable pitfalls in the use of spin trap EPR, such as unwanted side reactions and follow-up reactions that may lead to serious misinterpretations [8]. It was reported that nucleophilic addition of water to DMPO can lead to the formation of a DMPO/$^{\bullet}OH$ radical adduct in the presence of iron or copper ions [17,18]. Similarly, Fe(II) and Cu(II) ions favor superoxide formation in dimethyl sulfoxide (DMSO) in the presence of NaOH under aerobic circumstances [19]. Observation of a spin trapped radical is therefore not always a proof of radical pathways in the reaction under study. Addition of transition-metal chelators to the reaction mixture can considerably hamper this unwanted formation of radical adducts, albeit in a way that is strongly dependent on the type of chelator and transition-metal ion [18,19].

Despite the attention given to the potential pitfalls of spin trap EPR in terms of radical formation [7,8], surprisingly little attention has been paid to the possibility that transition-metal ions may form a complex with the spin traps or that the spin traps can strongly alter the reaction mechanism under study. Mason and co-workers suggested that Cu(II) can form a complex with DMPO, since the EPR spectra of the Cu(II) component in frozen aqueous solutions of $CuSO_4$ and of $CuSO_4$:DMPO mixtures strongly differ [17]. However, the large spectral difference reported in [17] is entirely due to freezing effects (bad glass formation in the $CuSO_4$/water case leading to exchange narrowing) and in principle not a proof of DMPO ligation. Betley and co-workers showed that a dipyrromethene $Cu(O_2)$ complex can react with DMPO to form a very unusual Cu(O-DMPO) adduct, showing an alarming non-innocent effect of the spin trap [20].

In the current work, we unravel the interaction of the spin trap DMPO with Cu(II) ions. The methods of choice are advanced continuous-wave (CW) and pulsed EPR techniques. Pulsed EPR, and especially hyperfine techniques, allow mapping out the interactions between the unpaired electrons of paramagnetic molecules - the unpaired electron of the Cu(II) ion - and the magnetic nuclei surrounding this electron [21,22]. This facilitates the identification of the complexing ligands. We first focus on the copper-catalyzed aerobic oxygenation of benzylpyridine *N*-oxides developed in the ORSY group (Dept. of Chemistry, University of Antwerp) [23] and show that the addition of DMPO to trap free radicals considerably alters the copper complexes involved in the reaction. In order to understand the intricate effect of DMPO on Cu(II)-containing systems, the Cu(II)-DMPO interaction is then monitored in the absence and presence of potentially competing strong nitrogen bases and chelators. Furthermore, the dependence of the complex formation on the starting oxidation state of the copper ions is tested. Density functional theory (DFT) computations are performed to corroborate the experimental data.

4.2 Materials and methods

4.2.1 Sample preparation

DMPO (5,5-dimethyl-1-pyrroline *N*-oxide) (>97%), pyridine, 2,2'-bipyridine, copper(II) chloride and copper(I) iodide were purchased from Sigma-Aldrich. Dimethyl sulfoxide (99.9 %) was purchased from Fisher Scientific. Copper(II) acetylacetonate (99%), was purchased from Arcos Organics and, 2-benzylpyridine *N*-oxide was prepared as described previously [23].

4.2.2 Magnetic resonance spectroscopy

X-band continuous wave (CW) and pulsed EPR measurements were performed on a Bruker ElexSys E580 spectrometer (microwave frequency 9.73 GHz) equipped with a liquid-helium cryostat (Oxford Inc). The low temperature CW-EPR measurements were performed at 100 K using a modulation amplitude of 0.5 mT, a modulation frequency of 100 kHz and a microwave power of 0.437 mW. The room-temperature CW-EPR

measurements of the Cu(II) complexes were performed using a modulation amplitude of 0.5 mT, a modulation frequency of 100 kHz and a microwave power of 30 mW. For the corresponding spectra of the DMPO-trapped radicals, a modulation amplitude of 0.1 mT and a microwave power of 0.75 mW was used.

The standard HYSCORE (hyperfine sublevel correlation spectroscopy) [24] experiments were performed with a $\pi/2$-τ-$\pi/2$-t_1-π-t_2-$\pi/2$-τ-$echo$ pulse sequence. The pulse lengths were $t_{\pi/2}$=16 ns and t_π=32 ns. The times t_1 and t_2 were varied from 96 to 3984 ns with the time step of 16 ns. The HYSCORE spectra are the sum of spectra taken at different τ-values (see figure captions).

Davies ENDOR (electron nuclear double resonance) experiments [25] have been performed using the π-T-$\pi/2$-τ-π-τ-$echo$ microwave pulse sequence with a 16 μs radio-frequency (rf) π-pulse applied during time T(=20 μs). A shot repetition time of 5 ms was used. Lengths of the microwave pulses are given in the figure captions. The rf frequency was swept from 1 MHz to 31 MHz in steps of 100kHz. An ENI A-300 amplifier was used.

The EPR, ENDOR and HYSCORE spectra were simulated using EasySpin v5.2.28 [26], a MATLAB toolbox developed for EPR simulations. All data were processed and simulated using the MATLAB R2020a version (The MathWorks, Inc., Natrick, MA). All HYSCORE time traces were baseline-corrected with a third order polynomial, apodized with a Hamming window and zero-filled. After two-dimensional Fourier transformation, the absolute-value spectra were computed and spectra recorded for different τ-values were added together to avoid blind-spot effects.

4.2.3 Computational methods

Spin-unrestricted density functional theory (DFT) calculations were performed using the ORCA package [27–30]. To mimic the solvent effect for all samples the COSMO model was used [31]. For the geometry optimizations of the Cu(II) complexes under study, the Becke-Perdew density functional (BP86) [32–34] was used. The Ahlrichs split-valence plus polarization (SVP) basis set was used for all atoms except copper [35]. The Ahlrich (2df,2pd) polarization functions were obtained from the TurboMole basis set library as implemented in ORCA. For the copper atoms the doubly polarized triple-zeta (TZVPP) (Ahlrichs, unpublished) basis set was used. The energy was converged to 1×10^{-8} Hartree (E_h) and the tolerances of convergence in the geometry optimization were 3×10^{-4} E_h/Bohr for the gradient and 5×10^{-6} E_h for the total energy. The coordinates of the optimized structures are given in the Supplementary Information (4.6.2.1)). For the single point calculations of the EPR parameters of the Cu(II) complexes, different combinations of density functionals and basis sets were investigated. As functionals, the B3LYP functional [36], BHandHLYP functional [37] and the PBE0 functional [38] were evaluated. These were tested in combination with either the 6-31+G** basis set [39,40] or EPR-II [41] for all light atoms. For the copper atom the triply polarized Core Properties basis set (CP(PPP)) was used as implemented in ORCA. The detailed comparison is given in the supplementary information (4.6.2.1).

4.3 Results and discussion

4.3.1 Influence of DMPO on copper-catalyzed aerobic oxygenation of benzylpyridine N-oxides

In recent work, researchers from the ORSY group (University of Antwerp) reported a copper-catalyzed aerobic oxygenation reaction of benzylpyridine *N*-oxides [23]. Facile oxidation of 2-benzylpyridine *N*-oxide (**3**) to the related benzoyl product **4** is obtained when CuI is used as a catalyst in DMSO at 100 °C under O_2 (reaction scheme in Figure 4.2). To test whether radical intermediates are formed during this reaction, the reaction mixture was quenched in a solution of DMPO in DMSO after 1 hour of reaction (reaction conditions, see legend in Figure 4.3). Although organic radicals were trapped, the room-temperature and low-temperature EPR spectra also revealed significant changes to the spectral features (and thus the nature) of the Cu(II) complexes that are formed by oxidation of Cu(I) during this reaction (Figure 4.3). Cu(II) ions are formed through oxidation of the Cu(I) centers in the presence of O_2.
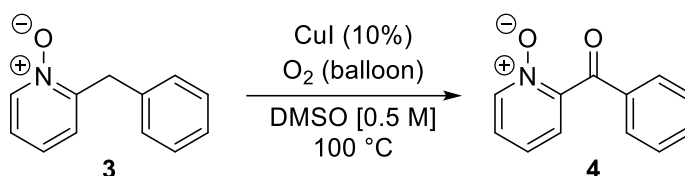

Figure 4.2. Oxidation reaction of 2-benzylpyridine N-oxide 3 using the approach described in [23]
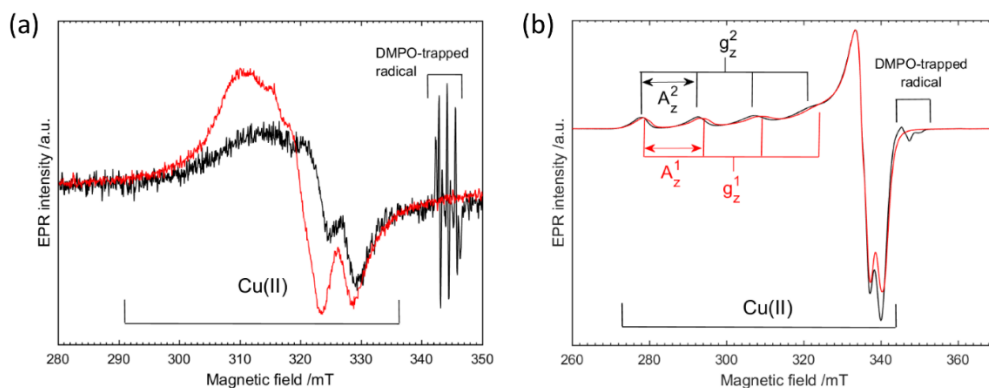

*Figure 4.3. EPR evidence of the influence of DMPO on the oxidation of **3** via reaction scheme 2. (a) Room-temperature and (b) low-temperature (100 K) X-band CW-EPR spectra of reaction mixture before (red) and after (black) quenching in DMPO solution. Reaction conditions: 0.5 M **3**, 50 mM CuI, DMSO (10 mL), O_2 (balloon), 100 °C, 1 h. Quenching of 1 mL reaction mixture in 1 mL 0.5 M DMPO in DMSO.*

Without DMPO, the low-temperature CW-EPR spectrum taken after 1 h of reaction (Figure 4.3b, red trace, EPR parameters marked with superscript 1) shows the formation of a Cu(II) complex with EPR features typical of a square pyramidal or octahedral

mononuclear copper(II) complex. With the addition of DMPO (Figure 4.3b, black trace, EPR parameters marked with superscript 2), these EPR features are altered and the *g*-values and ^{63,65}Cu hyperfine coupling (*A*) of the two samples are clearly different. The same is reflected in the room-temperature CW-EPR spectrum (Figure 4.3a). This points to an involvement of DMPO (or a DMPO-derived product) in the ligation of the Cu^{2+} ions.

4.3.2 DMPO ligation to copper(II) ions in different model systems

In order to investigate in more detail, the interaction of *in situ* generated Cu(II) species with DMPO at the high concentrations used for spin trapping, CW-EPR spectra of aerated CuI/DMSO solutions with increasing concentrations of DMPO were recorded (Figure 4.4). EPR-active Cu(II) was generated from the EPR-silent Cu(I) starting material during preparation of the EPR sample in air. The EPR parameters of the CuI/DMSO solution (Table 4.1, complex I) are typical of $CuBr_2.2H_2O$ in DMSO [42] and of CuI in aerobic DMSO [43]. Upon addition of DMPO, the contribution of a new Cu(II) species (Table 4.1, complex II) is observed in the EPR spectrum. The weight of this component is growing with increasing DMPO concentration (see inset Figure 4.4 and Table 4.2). The spectral change is also observed at room temperature (Figure 4.5A). The *g*- and Cu hyperfine values of complex II resemble those of frozen methanol solutions of $Cu(ClO_4)_2.2H_2O$ and pyridine *N*-oxide ($g_{x,y}$=2.08, g_z=2.320, $A_{x,y}$=26 MHz, A_z=448 MHz) and of $Cu(ClO_4)_2.2H_2O$ and β-picoline *N*-oxide ($g_{x,y}$=2.082, g_z=2.300, $A_{x,y}$=44 MHz, A_z=482 MHz) [44].

Table 4.1: Principal g and copper hyperfine values obtained by simulation of the low-temperature CW-EPR spectra of the different Cu(II) complexes under study and the composition.

Complex	Copper salt	DMPO	py[a]	g_x ±0.002	g_y ±0.002	g_z ±0.002	A_x /MHz ±15	A_y /MHz ±15	A_z /MHz ±5
I	CuI	-	-	2.080	2.084	2.408	20	20	-380
II	CuI	+	-	2.069	2.079	2.339	10	10	-470
III	CuI [b]	-	+	2.060	2.060	2.269	37	37	-545
IV	CuI [b]	+	+	2.063	2.063	2.276	36	36	-537
V	[Cu(acac)$_2$][c]	-	-	2.066	2.054	2.291	-39	20	-512
V'	[Cu(acac)$_2$]	+	-	2.066	2.054	2.291	-39	20	-512

All samples were measured in DMSO under air. The hyperfine values for ^{63}Cu are given. The simulated spectra are shown in Figure S4.1 (supplementary information) and in Figure 4.6. The sign of the hyperfine principal was determined using the room-temperature spectra and assuming the largest copper hyperfine value to be negative.[a]py is pyridine. [b] simulation includes the hyperfine coupling to four ^{14}N nuclei of the pyridine ligands (A(^{14}N)=(33 42.8 33) MHz), [c] acac = acetylacetonate
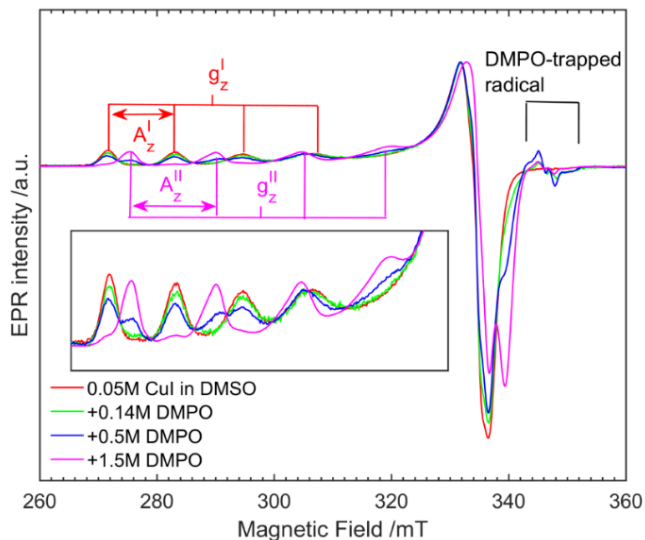
Figure 4.4. X-band CW-EPR spectra of frozen solutions of 0.05 M CuI in DMSO in air with increasing concentration of DMPO, recorded at 100 K. DMPO concentration: 0 M (red), 0.14 M (green), 0.5 M (blue) and 1.5 M (magenta). Each spectrum has been normalized to the double integral i.e. total number of observed spins. The inset shows an enlargement of the low-field area. The individual spectra are shown in Figure S4.1 (supplementary information)

Furthermore, a weak contribution of a DMPO-trapped radical is observed. Room-temperature CW-EPR confirmed the formation of DMPO/radical adducts, known to occur through the nucleophilic attack of water (present in the DMSO here) to DMPO in the presence of Cu(II) ions [17] (Figure 4.5B). The large differences in the g and copper hyperfine values of the EPR signature of complexes I and II (Table 4.1) indicate an involvement of DMPO(-derived) molecule(s) in the coordination sphere of Cu(II).

Table 4.2 Relative contribution of the two components in the simulations of the CW-EPR spectra of aerated CuI/DMSO with different concentrations of DMPO. Compound I: no DMPO involvement in Cu(II) complex, Compound II: Involvement of DMPO in Cu(II) complex. For simulations , see supplementary information, Figure S4.1.

[DMPO] (M)	% compound I	% compound II
0	100	0
0.14	86	14
0.5	65	35
1.5	8	92

Since DMSO is expected to be a weak competitor to DMPO as a ligand for Cu(II), the effect of DMPO in the presence of strong nitrogen bases or bidentate chelators was tested. Figure 4.6a shows the EPR spectrum of a frozen DMSO solution of 0.05 M CuI

in the presence of 0.2 M pyridine (py) prepared in air. The EPR parameters (Table 4.1, complex III) are typical of the square-planar $[Cu(py)_4]^{2+}$ complex [45,46]. Addition of 1.5 M DMPO to the solution results in the formation of a DMPO-trapped radical as well as very subtle changes in the EPR spectrum of the Cu(II) complexes (Figure 4.6b, Table 4.1, complex IV). Figure 4.6c shows the EPR spectrum of a frozen solution of 2 mM copper(II) bis-acetylacetonate ($[Cu(acac)_2]$) in DMSO. The corresponding EPR parameters (complex V, Table 4.1) differ from the ones of $[Cu(acac)_2]$ in a non-coordinating solvent (toluene:CHCl$_3$, g=[2.048, 2.052, 2.252], A(^{63}Cu)=[81 58 572] MHz), but resemble more those of adducts of $[Cu(acac)_2]$ formed with different bases or coordinating solvents [47–49].This indicates that axial coordination of DMSO (or water present in the DMSO) is occurring. Apart from the formation of small amounts of DMPO-trapped radicals, no clear effect of addition of DMPO to EPR spectrum of the $[Cu(acac)_2]$/DMSO solution is observed (Figure 4.6d, Table 4.1). The effects are confirmed in the room-temperature EPR data (Figure 4.7). The room-temperature CW-EPR spectrum of a mixture 0.05 M CuI and 0.2 M pyridine in DMSO points to the presence of different Cu(II) complexes with varying number of pyridine ligands, while only complex III is observed at 100 K, which is consistent with the known Cu(II)-pyridine temperature-dependent equilibria in solution [49].
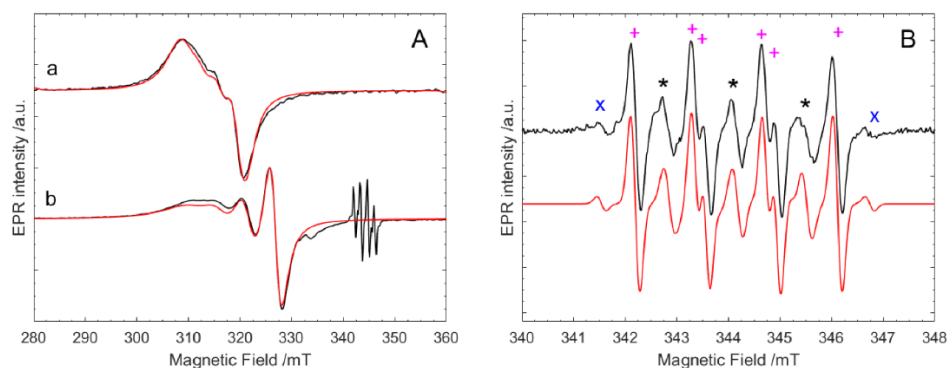

*Figure 4.5.**(A)** Experimental room-temperature (black) and simulated (red) X-band CW-EPR spectra of aerated solutions of 50 mM CuI in DMSO with (a) 0, (b) 1.5 M DMPO. The simulations of the contributions of the Cu(II) centers were done using the principal g and copper hyperfine values given in Table 4.1. A rotational correlation time of (a) 17 ps and (b) 70 ps was used. **(B)** Zoom into the EPR signal of the radical component in Figure 4.5 A(b). These signals stem from radicals trapped by DMPO. The spectrum can be simulated assuming three contributions: (+) g_{iso} = 2.0066, A^N= 1.375 mT, A^H= 1.18 mT (74%, DMPO-OOH) [50], (x) g_{iso} = 2.0067, A^N= 1.48 mT, A^H= 2.25 mT (6%, DMPO-alkyl [7,50]) and (*) g_{iso} = , A^N= 1.34 mT (20%, DMPOX, a degradation product of DMPO [51]). The spectra were recorded with a microwave power of (A) 30 mW and (b) 0.75 mW.*
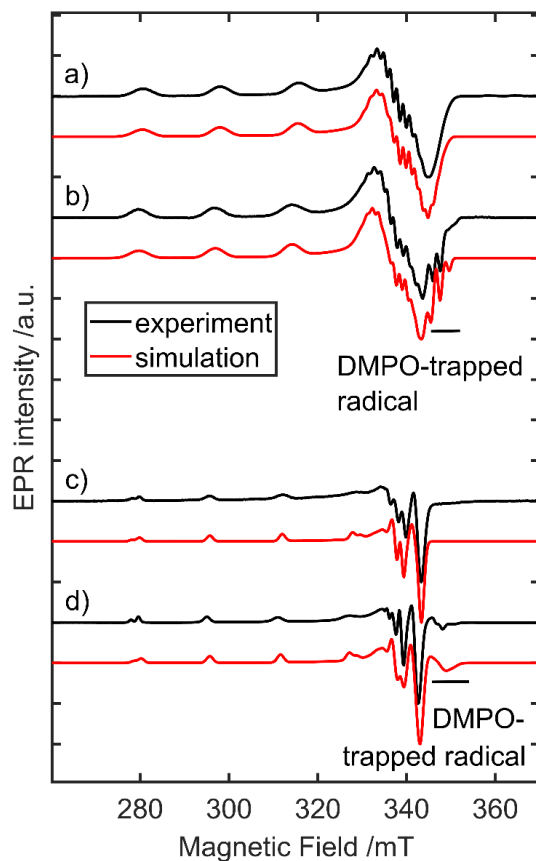
*Figure 4.6. X-band experimental and simulated CW-EPR spectra of frozen solutions of 0.05 M CuI and 0.2 M pyridine without (a) and with (b) 1.5 M DMPO and 2 mM [Cu(acac)$_2$] without (c) and with (d) 1.5 M DMPO. All solutions are in DMSO, prepared in air. All spectra were recorded at 100 K. The contributions of the Cu(II) complexes are simulated using the parameters in Table 4.1 and Table 4.3. To mimic the spectral contribution of a radical in (b) and (d), the following values were used for the simulation: **g**=[2.0022, 2.0060, 2.0088], **A**(^{14}N)=[13, 14, 79] MHz, and **A**(^{1}H)=[52 44 57] MHz. These parameters are in the order of what is expected for DMPO-trapped radicals* [7].
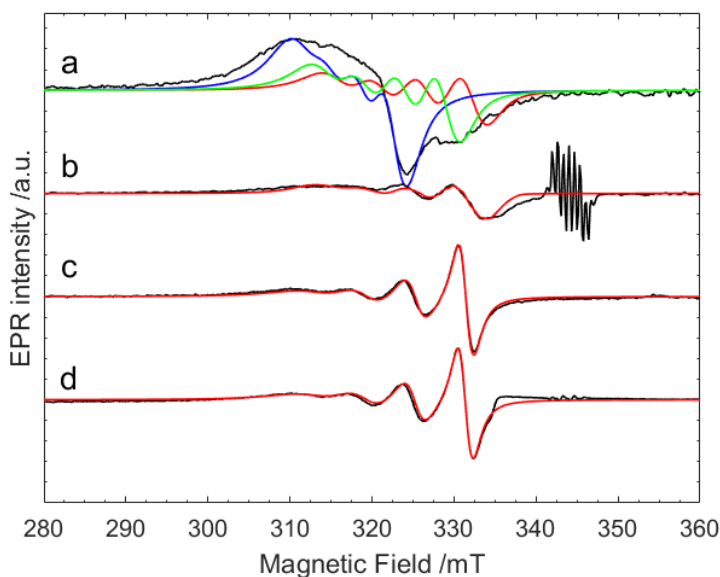
Figure 4.7. Experimental room-temperature (black) X-band CW-EPR spectra of aerated solutions of 50 mM CuI in DMSO with (a) 200 mM pyridine, (b) 200 mM pyridine and 1.5 M DMPO, and of 2 mM Cu(acac)$_2$ in DMSO with (c) 0 or (d) 1.5 M DMPO. The experimental spectra are recorded with a microwave power of 30 mW. The red spectra show the simulations using the parameters for (a) complex III, (b) complex IV, (c,d) complex V with the parameters that appear in Table 4.1. Blue spectrum: simulation assuming g=[2.078 2.078 2.37], and A^{Cu} = [30 30 -383] MHz; green spectrum: simulation assuming g=[2.066 2.066 2.303], and A^{Cu} = [35 35 -491] MHz. The EPR parameters of the latter two are obtained from complex I and III using a very crude assumption that each equatorial pyridine or DMSO ligand contributes g$_i$/4 of A^{Cu}$_i$/4 (i=x,y,z) of resp. complex III and complex I to the total principal g or hyperfine value. The simulation in blue represents a complex with one pyridine and 3 DMSO ligands, while the simulation in green represents a complex with three pyridine and 1 DMSO. This is of course only a crude estimate of the EPR parameters, but it illustrates that the complex spectrum observed at room temperature is due to the presence of Cu(II) complexes with varying amounts of pyridine ligands. The rotational correlation times used for the simulation are (a) 17.7 ps, (b) 35 ps and (c,d) 70 ps.

In order to unravel further the effect of DMPO on the different Cu(II) complexes, HYSCORE (hyperfine sublevel correlation spectroscopy) experiments were performed. This two-dimensional pulsed EPR technique allows detecting the interactions of the unpaired electron of the Cu(II) ion with the magnetic nuclei of its ligands and is thus a helpful tool to map out the ligation to the copper ion. Figure 4.8 shows a comparison of the HYSCORE spectra of CuI/DMSO with and without DMPO taken at different magnetic field settings. While the HYSCORE spectra of the DMPO-free complex I (Figure 4.8a,c) reveal only the hyperfine interaction of the unpaired electron with surrounding ^{1}H nuclei (see below), HYSCORE cross peaks due to interactions with ^{14}N nuclei are visible after addition of DMPO (Figure 4.8b,d). The corresponding ^{14}N hyperfine and nuclear quadrupole couplings are given in Table 4.3 with the simulations shown in Figure 4.9(a,b). Ligands that coordinate equatorially to Cu(II) via the nitrogen

M.Samanipour

atom are known to exhibit ^{14}N hyperfine values in the order of 30-50 MHz [45]. The small ^{14}N hyperfine couplings observed for Complex II are in line with those of remote nitrogen atoms (*i.e.* nitrogen atoms of the ligand that are not directly bound to the Cu(II) ion) [52,53] or those of axially bound nitrogen bases (weak coordination to Cu(II) *via* nitrogen atom) [54,55] (see also DFT computations). Since DMPO is the only ^{14}N-bearing compound in the solution, this confirms DMPO-ligation to the *in situ* generated Cu(II) ion. The same coupling is found when a Cu(II) salt is used from the start, and the observed effect is thus not induced by the oxidation reaction of Cu(I) to Cu(II) (Figure 4.9(c,d)).
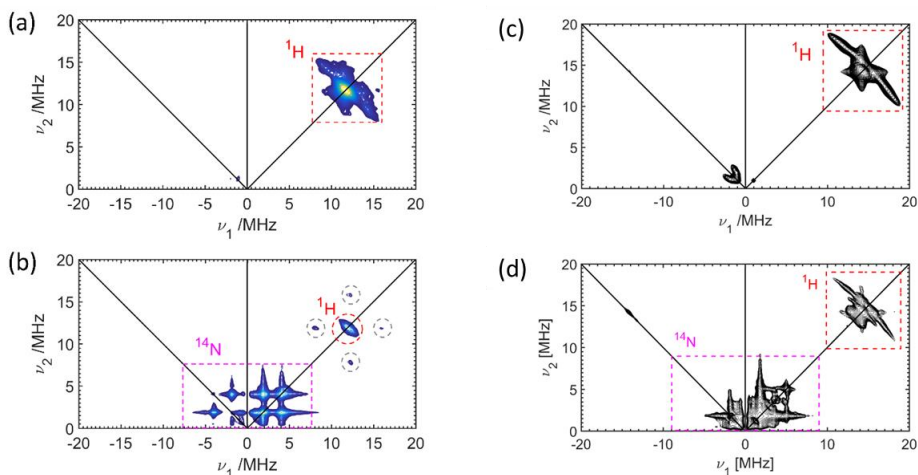

Figure 4.8. X-band HYSCORE spectra of (a,c) Complex I (0.05 M CuI in DMSO under air) and (b,d) Complex II (0.05 M CuI and 1.5 M DMPO in DMSO) recorded at 10 K. The related simulations are shown in Figure 4.9(a,b), Figure 4.10. The simulation parameters are given in Table 4.3. The relevant signal areas corresponding with cross peaks of the ^{1}H and ^{14}N hyperfine interactions are marked in red and magenta, respectively. The cross peaks marked with grey circles are due to combination frequencies between the ^{1}H and ^{14}N nuclear frequencies. The spectra are taken at magnetic-field positions agreeing with g_z, $m_I=3/2$, i.e. (a) 274 mT and (b) 277 mT and at magnetic-field positions agreeing with $g_{x,y}$, i.e. (c) 334.5 mT and (d) 335 mT . All spectra are summed over different τ-values: (a,c) 124, 150 and 174 ns, and (b,d) 150, 200, 224 and 250 ns.

The observed HYSCORE spectrum can be simulated assuming the interaction with one ^{14}N nucleus and the absence of combination frequencies between two ^{14}N frequencies indicate that only one DMPO(-derived) molecule is binding. The only combination frequencies that are observed are between ^{1}H and ^{14}N nuclear frequencies (marked with circles in Figure 4.8b). For the DMPO/Cu ratio used for the EPR experiments, the ligation of one DMPO molecule is corroborated by optical absorption spectra in the near infrared, while multiple DMPO start to ligate to Cu(II) at very high DMPO/Cu(II) ratio (Figure S4.5).

Table 4.3. Principal ^{14}N hyperfine (A) and quadrupole (P) couplings found in this work

Complex	Source	$\|A_x^N\|$ /MHz ±0.1	$\|A_y^N\|$ /MHz ±0.1	$\|A_z^N\|$ /MHz ±0.1	$\alpha^A, \beta^A,$ $\gamma^A/°$ ±10	P_x^N /MHz ±0.10	P_y^N /MHz ±0.10	P_z^N /MHz ±0.10	$\alpha^P, \beta^P,$ $\gamma^P/°$ ±10
II,IV, (V')	DMPO	1.4	1.4	2.1	0, 0,0	1.8	-0.05	-1.75	60, 60, 70
III	py	33.0	33.4	42.8	0,90,0	0.68	0.69	-1.37	0,90,0
IV	py	31.2	31.8	40.4	0,90,0	0.50	0.60	-1.10	0,90,0

*The Euler angles of the **A** and **P** tensors in the **g** tensor frame as defined in EasySpin [26] are also given. The corresponding simulations are shown in Figure 4.9 (HYSCORE) and Figure 4.13 (ENDOR). The signs of the quadrupole principal values are taken from DFT computations(see supplementary information).*
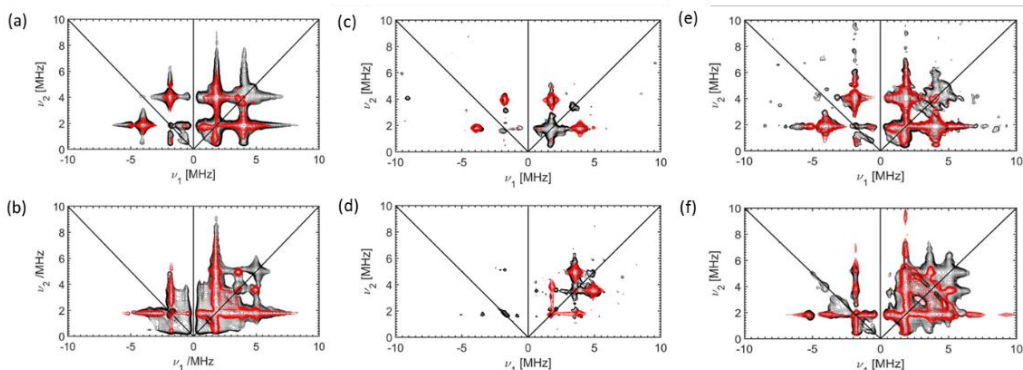

Figure 4.9: Experimental (black) and simulated (red) X-band ^{14}N-HYSCORE spectra of (a,b) Complex II (0.05 M CuI and 1.5 M DMPO), (c,d) Complex II (2 mM CuCl$_2$ in 1.5 M DMPO) and (e,f) Complex IV (0.05 M CuI, 0.2 M pyridine and 1.5 M DMPO) in DMSO under air. recorded at 10 K. Spectra taken at magnetic-field settings (a) 277 mT, (b) 335 mT,(c) 283 mT, (d) 337.2 mT, (e) 282.8 mT, and (f) 336.9 mT. The simulations are done using the ^{14}N parameters given in Table 4.3 for all of the spectra. And ^{13}C contribution of [-2 -2 4] MHz was added to high-light the presence of ^{13}C contributions (in natural abundance) in this frequency area for (e) and (f). Spectra are summed over different τ-values: (a,b): τ = 150, 200, 224 and 250 ns, (c,d): τ = 104 and 120 ns and (e,f) τ = 150 and 200 ns. Note the extreme effect of the τ-values at which the experiments are performed on the spectral signature for (c,d) when comparing to (a,b).
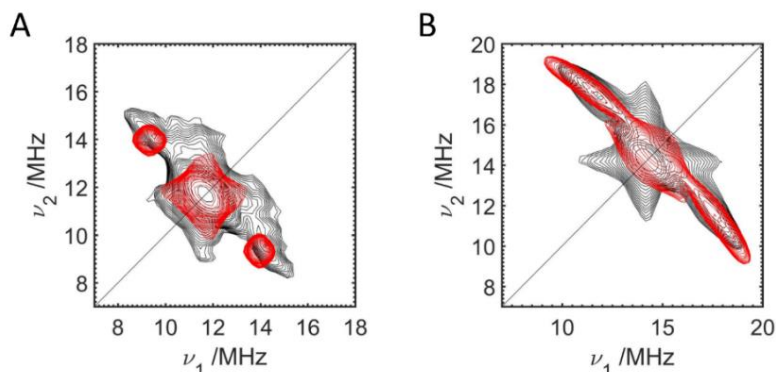
Figure 4.10. Experimental (black) X-band HYSCORE spectra of complex I (0.05 M CuI in DMSO under air) taken at 10 K at observer positions (A) 274.0 mT and (B) 334.5 mT. The simulations (red) are done with ^1H hyperfine values of a magnitude characteristic of equatorially bound water ($\textbf{A}$=[10.5 -4.9 -0.9] MHz, $(\alpha^A, \beta^A, \gamma^A)$=(0,15,90)°) and of axially bound water ($\textbf{A}$=[-2.28 -2.98 5.07] MHz, $(\alpha^A, \beta^A, \gamma^A)$=(0,10,0)°). This indicates that water ligation is likely happening to the copper ion, since much smaller proton hyperfine couplings are expected for the DMSO protons.
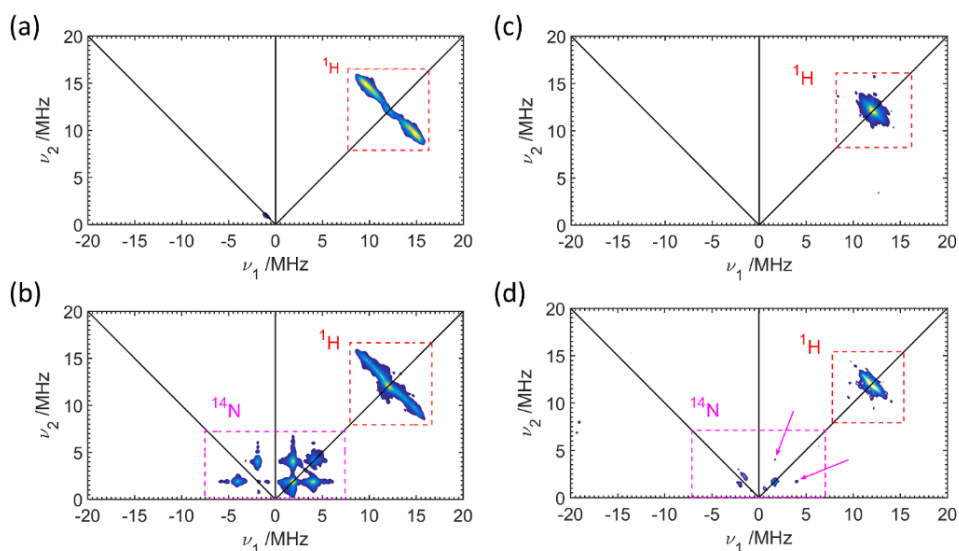

Figure 4.11. X-band HYSCORE spectra of (a) Complex III (0.05 M CuI and 0.2 M pyridine in DMSO under air), (b) Complex IV (0.05 M CuI, 0.2 M pyridine and 1.5 M DMPO in DMSO under air), (c) Complex V (0.02 M [Cu(acac)$_2$] in DMSO under air) and (d) Complex V' (0.02 M [Cu(acac)$_2$] and 1.5 M DMPO in DMSO under air) recorded at 10 K. The related simulations are shown in Figure 4.9(c,d). The simulation parameters are given in Table 4.3. The relevant signal areas corresponding with cross peaks of the ^1H and ^{14}N hyperfine interactions are marked in red and magenta, respectively. The spectra are taken at magnetic-field positions agreeing with g_z, m_I=3/2, i.e. (a) 274 mT, (b) 282.8 mT, (c) 283.4 mT and (d) 279.5 mT. The spectra are summed over different τ-values: (a) 124, 150, 174 and 200 ns, (b) 150 and 200 ns, (c) 120 and 150 ns, and (d) 150 and 180 ns. The arrows indicate the weak cross peaks due to the ^{14}N contributions.
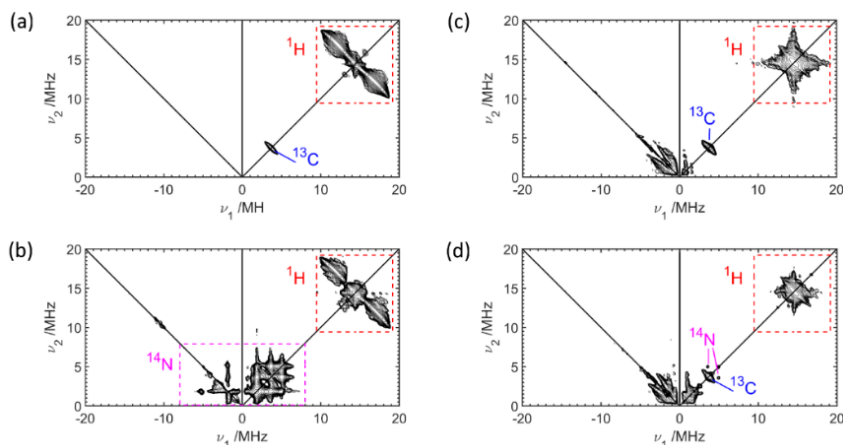
Figure 4.12 : X-band HYSCORE spectra of (a) Complex III (0.05 M CuI and 0.2 M pyridine in DMSO under air), (b) Complex IV (0.05 M CuI, 0.2 M pyridine and 1.5 M DMPO in DMSO under air), (c) Complex V (0.02 M Cu(acac)$_2$ in DMSO under air) and (d) Complex V' (0.02 M Cu(acac)$_2$ and 1.5 M DMPO in DMSO under air) recorded at 10 K. The relevant signal areas corresponding with cross peaks of the ^{1}H, ^{13}C and ^{14}N hyperfine interactions are marked in red and magenta, respectively. The spectra are taken at magnetic-field positions agreeing with $g_{x,y}$, i.e. (a) 336.9 mT, (b) 336.9 mT, (c) 341.9 mT and (d) 341.4 mT. The spectra are summed over different τ values: (a,b) 150 and 200 ns, (c,d) 120 and 150 ns. The ^{13}C interactions observed here, are due to the pyridine and acetylacetonate ligands. The ^{13}C signal is also visible in Figure 4.12b, where it is hidden in the contributions of the ^{14}N(DMPO) ligand (see also simulations in Figure 4.9 (e,f))
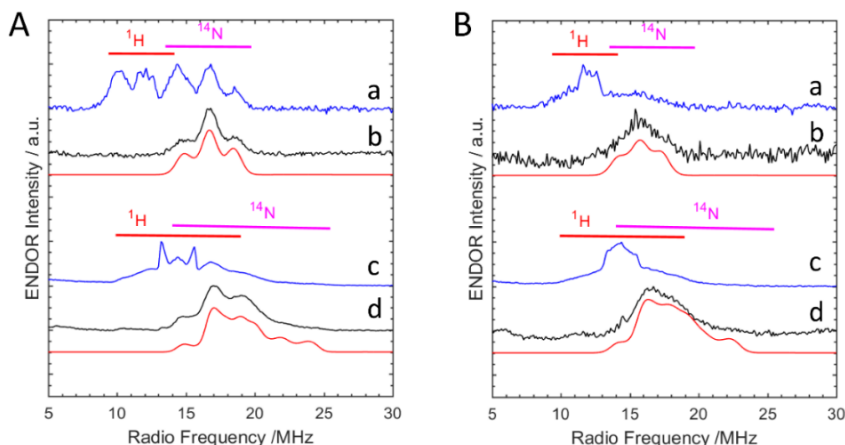

Figure 4.13. Davies ENDOR spectra of a frozen DMSO solution of 50 mM CuI and 200 mM pyridine with (A) 0 M and (B) 1.5 M DMPO. The magnetic field settings are A,B(a,b) 282.8 mT, A,B(c,d) 336.9 mT. The spectra are recorded with weak microwave pulses (traces in blue, $t_{\pi/2}$=100 ns, t_π=200 ns) or hard pulses (traces in black, $t_{\pi/2}$=20 ns, t_π=40 ns, except Ab: $t_{\pi/2}$=12 ns, t_π=24 ns). In Davies ENDOR with hard pulses the contributions of weakly coupled nuclei (^{1}H contributions in this case) is suppressed. Red spectra show the simulations of the ^{14}N contribution using the parameters given in Table 4.3.

Furthermore, a similar effect is found when comparing the HYSCORE spectra of frozen oxygenated DMSO solutions of CuI/pyridine without and with DMPO (Figure 4.11(a,b), Figure 4.12(a,b)). The ^{14}N-HYSCORE contributions in the CuI/py/DMPO mixture can be simulated with the same parameters as those found for the mixtures without DMPO (Table 4.3,Figure 4.9(e,f)). Note, that the hyperfine couplings to the ^{14}N nuclei of the pyridine ligands are considerably larger and only visible in the Davies ENDOR spectra (Figure 4.13 and Table 4.3). A slight shift in the hyperfine values is observed upon addition of DMPO, in line with the slight shifts in the *g* and copper hyperfine values (Table 4.1).

When DMPO is added to a DMSO solution of [Cu(acac)$_2$], the CW-EPR spectra did not change markedly (Figure 4.6 (c,d) and Table 4.1). Although the effect on the HYSCORE spectra is also minimal, weak ^{14}N cross peaks can be observed in the HYSCORE spectra (Figure 4.11d, Figure 4.12d) that agree with the cross peaks found after addition of DMPO to the other copper complexes studied here. This indicates that DMPO ligation is occurring also in the [Cu(acac)$_2$] case, although to a far lower extend, as is clear from the low overall intensity of these cross peaks. It does show that HYSCORE spectroscopy may help to reveal a ligation mode that is not directly clear from the corresponding CW-EPR data.

All HYSCORE and Davies ENDOR spectra show interactions with the nearby protons. The ^{1}H hyperfine couplings spectrum of the [Cu(py)$_4$]$^{2+}$ and [Cu(acac)$_2$] complexes have been extensively studied before [46,47] and will not be discussed here. Surprisingly, the ^{1}H HYSCORE spectra of complex I show a broad ridge centred around the proton Larmor frequency (Figure 4.8a,c). The extended ridge can be simulated using principal hyperfine values of a magnitude characteristic for water ligation (Figure 4.10, [56]). Presence of water cannot be excluded, because of the sample handling in air. Similar ^{1}H couplings are observed after addition of DMPO (Figure 4.8d), indicating that DMPO ligation does not replace the water ligand. Note that the ^{1}H HYSCORE contribution in Figure 4.8b is slightly suppressed by the strong modulations due to ^{14}N couplings (the so-called cross suppression effect [57]).

4.4 Understanding the DMPO ligation

The above experimental results clearly show that DMPO is affecting the complexation of Cu(II) ions. Since the same ^{14}N hyperfine and quadrupole signature is found starting from Cu(II) salts or Cu(I) salts that oxidize *in situ*, the observed ligation is not linked to the oxidation of the Cu(I) salts. In order to elucidate the ligation of a DMPO(-derived) molecule to Cu(II), density functional theory calculations were performed for [Cu(py)$_4$]$^{2+}$, [Cu(py)$_3$(DMPO)]$^{2+}$ and [Cu(py)$_4$(DMPO)]$^{2+}$ complexes using different functional/basis set combinations (section 4.6.2 in Supplementary Information). The combination in which the BHandHLYP functional is used together with the EPR-II basis set for the light elements and CP(PPP) for the Cu atom led to the best match between the theoretical and experimental ^{14}N hyperfine and quadrupole values for [Cu(py)$_4$]$^{2+}$ (Table S4.2, DFT-computed parameters: A^N = [34.47 36.17 44.95] MHz and P^N=[0.59 0.81 -1.40] MHz – values averaged for the 4 pyridine ligands). The same functional/basis sets combination predicts a slight decrease in the ^{14}N hyperfine values of the pyridine ligands in [Cu(py)$_3$(DMPO)]$^{2+}$ (Table S4.4, DFT-computed parameters:

A^N = [31.35 32.99 41.25] MHz – values averaged for the 3 pyridine ligands), fully in line with what is observed experimentally for Complex IV (Table 4.3). A similar trend is, however, also observed for $[Cu(py)_4(DMPO)]^{2+}$ (Table S4.6, DFT-computed parameters: A^N = [31.70 33.36 41.04] MHz – values averaged for the 4 pyridine ligands). In the latter square pyramidal complex, the DMPO ligand is at an axial position (Figure S4.4). The computed magnitude of the ^{14}N hyperfine of the DMPO ligand is, however, considerably smaller for $[Cu(py)_4(DMPO)]^{2+}$ (Table S4.6, A^N = [0.10 -0.24 -0.28] MHz) than for $[Cu(py)_3(DMPO)]^{2+}$ (Table S4.4, A^N = [0.59 -0.6 -2.11] MHz). The latter matches better the experiment (Table 4.3). A similar trend is found for all other functional/basis set combinations (Table S4.2, Table S4.4, Table S4.6). This strongly suggests that the DMPO ligation occurs in an equatorial position and not in an axial position.

Although the theoretical ^{14}N hyperfine values of the $[Cu(py)_3(DMPO)]^{2+}$ model agree fairly well with the experiment, the quadrupole values of the DMPO ^{14}N nucleus do not match so well. Interestingly, the experimentally observed ^{14}N quadrupole value $|\frac{e^2qQ}{h}|$ (i.e., twice the maximal principal component of the P tensor) is very high (3.6 MHz). While nitroxide spin probes have been reported to have quadrupole values of the same magnitude [58], nuclear quadrupole resonance of pyridine N-oxide and derivatives reveal much smaller nuclear quadrupole values ($|\frac{e^2qQ}{h}|$ values between 1.114 and 1.598 MHz [59]). This reflects the different hybridization of the nitrogen orbitals. Depending on the choice of the functional and basis set, $|\frac{e^2qQ}{h}|_{DFT}$ lies between 1.92 and 2.28 MHz for 14N of DMPO in $[Cu(py)_3(DMPO)]^{2+}$. Although these values are well above the value computed for free DMPO (Table S4.6), they are below the value observed experimentally. Even assuming a correction factor based on the difference between the experimental and computed quadrupole values for pyridine N-oxide, the $|\frac{e^2qQ}{h}|_{DFT}$ values for ^{14}N(DMPO) in $[Cu(py)_3(DMPO)]^{2+}$ remain below the experimental ones. This could point to the fact that a DMPO-derived molecule and not DMPO is ligating, although it is most likely due to the short-comings of the model (high degree of rotation freedom of both DMPO and pyridine ligands around the Cu-O or Cu-N bond, potential additional ligation of DMSO (solvent) molecules or counter ions). Indeed, given that the same equatorial binding mode was found experimentally for all complexes studied here, it points to a single ligation mechanism. If this would involve a DMPO-derived molecule, the same formation mechanism in the presence of either Cu(I) or Cu(II) would be required, and the DMPO-derivative should be formed in high concentration. DMPO-trapped radicals are observed in the EPR spectra of the Cu(II) complexes in the presence of DMPO (Figure 4.4-4.7), but the ligation of a nitroxide radical to the Cu(II) center can be excluded on the basis of the CW-EPR spectra because if the two paramagnetic centers are in such close proximity (< 1 nm), one would expect to see dipolar and exchange coupling effects such as broadening or splitting of the EPR lines.

Even though DMPO can easily ligate copper in the presence of a nitrogen base, such as pyridine, and is also a ligation competitor to 2-benzylpyridine *N*-oxide in the reaction given in the scheme of Figure 4.2, only a limited effect of addition of DMPO to $[Cu(acac)_2]$ is seen. The DMPO ligation observed for a minor fraction probably involves loss or monodentate ligation of one of the acetylacetonate ligands, since the DMPO is

again equatorially coordinating. Evidence of displacement of the axial ligand (DMSO or water) by DMPO was not observed, although the expected small interaction with the DMPO ^{14}N nucleus may be hard to observe experimentally. The different competition behavior in [Cu(acac)$_2$], is undoubtedly related to the stable bidentate ligation mode as well as the charge of the acetylacetonate ligand. Strong bases, such as imidazole, are found to bind axially to the [Cu(acac)$_2$] complex, but not replace the equatorial acetylacetonate ligands [55].

4.5 Conclusion

Through a combination of CW EPR and hyperfine spectroscopy, the non-innocent role of the spin trap DMPO in the monitoring of radical formation in copper-catalyzed reactions was revealed. Using the example of an aerobic oxidation reaction of 2-benzylpyridine N-oxide as test case, the present work shows that the spin trap DMPO may interfere with the reaction mechanism under study. It is shown that the observation of fingerprint ^{14}N HYSCORE cross peaks can unambiguously determine the ligation of a DMPO(-derived) molecule to Cu(II). DMPO is found to be able to ligate to Cu(II) also in the presence of competing nitrogen bases or typical ligands, such as pyridine. The same equatorial ligation mode occurs when starting from a Cu(II) salt or a Cu(I) salt that is in situ oxidized, indicating that the ligation is not linked to the oxidation reaction. DMPO is less able to replace the acetylacetonate ligand in [Cu(acac)$_2$], both due to the negative charge of the acetylacetonate ligand and its bidentate binding mode.

Overall, this study shows that one should be very cautious when using spin trap EPR in the presence of Cu(II) salts, bases and ligands. The validity of the spin trap method can be easily evaluated by exploiting both changes in the CW EPR spectrum of the Cu(II) complex and the fingerprint ^{14}N HYSCORE peaks that reveal ligation of the spin trap to the metal ion and thus highlight the possible interference of the spin trap in the reaction mechanism. Similar approaches should be extended to other metal ions, when using spin traps to investigate the mechanism of metal-catalyzed reactions. The study also shows that we should be careful when using spin traps in systems whereby metal ions can be generated in redox processes, as may occur in certain electrochemical experiments.

4.6 Supplementary information

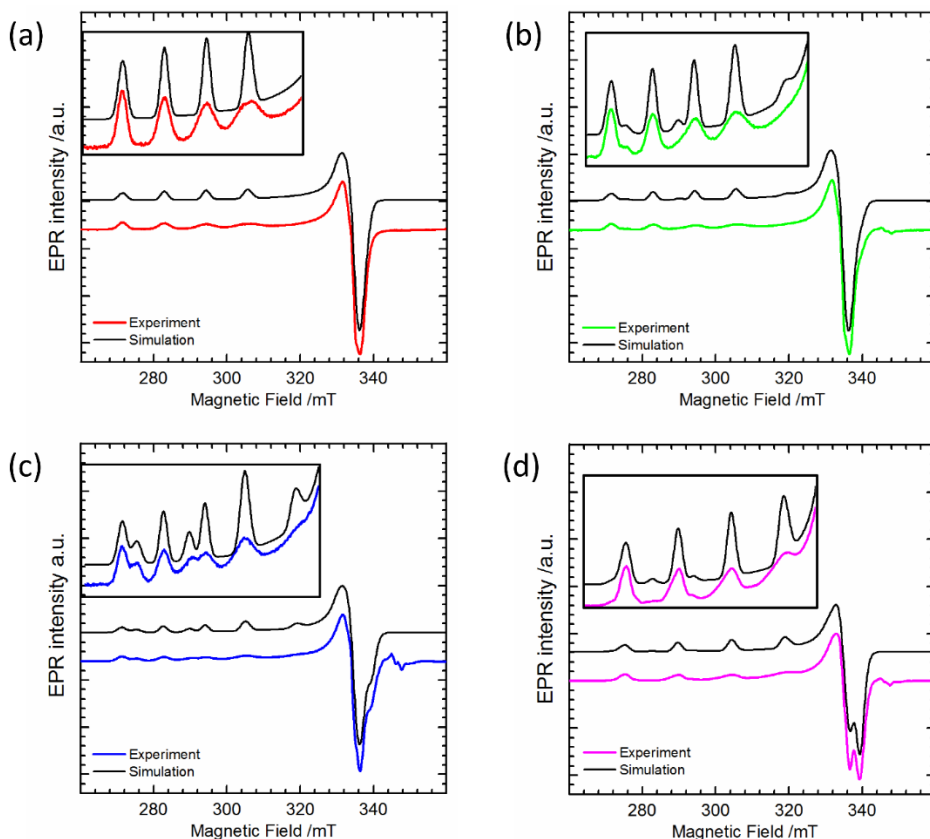## 4.6.1 CW-EPR spectra of DMSO solutions of CuI with and without DMPO

Figure S4.1 Experimental low-temperature and simulated CW-EPR spectra of aerated solutions of CuI in DMSO with (a) 0, (b) 0.14 M, (c) 0.5 M and (d) 1.5 M DMPO. A contribution of a second Cu(II) species is observed with increasing concentration of DMPO (relative amount, see Table 4.2). See also Figure 4.4 main text. The simulations were done using the principal g and copper hyperfine values given in Table 4.1.

M.Samanipour

4.6.2 Density functional theory (DFT) computations

4.6.2.1 DFT computations of Cu(II) model complexes

The following section contains an overview of the computed ^{14}N hyperfine and nuclear quadrupole principal values for the $[Cu(py)_4]^{2+}$, $[Cu(py)_3(DMPO)]^{2+}$ and $[Cu(py)_4(DMPO)]^{2+}$ complexes using different functional/basis set combinations as explained in the Materials and Methods section. The geometry-optimized structure is also given (see Materials and Methods

A. $[Cu(py)_4]^{2+}$

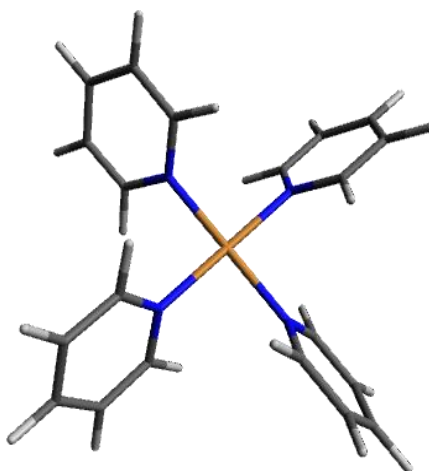*Figure S4.2 Geometry-optimized configuration of $[Cu(py)_4]^{2+}$. The coordinates of the atoms are reported in Table S 1.*

Table S4.1.The coordinates (in Å) of the geometry-optimized $[Cu(py)_4]^{2+}$ complex.

C	4.233119	-1.273600	-4.283894
C	4.977832	-0.084080	-4.241821
C	4.512790	0.979154	-3.458814
C	3.041438	-1.356279	-3.545837
C	2.629185	-0.246706	-2.798330
N	3.357235	0.895359	-2.756162
H	4.577853	-2.127714	-4.885780
H	5.916079	0.028094	-4.803240
H	5.075887	1.922034	-3.387642
H	2.426044	-2.266977	-3.546297
H	1.693712	-0.267097	-2.218913
Cu	2.717369	2.471000	-1.645988
N	4.454365	2.437411	-0.595674

N	0.989785	2.518906	-2.710243
N	2.070442	4.033796	-0.522474
C	1.024473	2.687140	-4.054387
C	-0.145386	2.733459	-4.821941
C	-1.385291	2.583847	-4.180262
C	-1.412893	2.401195	-2.788366
C	-0.203709	2.382394	-2.083250
C	5.246712	3.535985	-0.556985
C	6.455416	3.548493	0.149210
C	6.845274	2.395521	0.849338
C	6.014773	1.263896	0.811886
C	4.828448	1.318408	0.070745
C	1.740950	5.207344	-1.114397
C	1.303235	6.310145	-0.371341
C	1.187780	6.187639	1.022638
C	1.522792	4.965803	1.627987
C	1.969372	3.911001	0.823160
H	2.015771	2.784921	-4.522317
H	-0.073322	2.880120	-5.908848
H	-2.320592	2.609422	-4.759152
H	-2.358934	2.278492	-2.242465
H	-0.184324	2.256491	-0.990152
H	4.899261	4.424715	-1.105339
H	7.072999	4.457697	0.147876
H	7.786834	2.378892	1.418358
H	6.277363	0.339196	1.344847
H	4.158578	0.447757	0.004404
H	1.830265	5.259335	-2.210112
H	1.053872	7.246830	-0.889557
H	0.840250	7.035791	1.631273
H	1.447074	4.821914	2.715024
H	2.255822	2.942857	1.261233

M.Samanipour

Table S4.2 Single-point DFT-computed ^{14}N hyperfine and quadrupole couplings of the pyridine ligands in $[Cu(py)_4]^{2+}$ The computations were performed using different combinations of functional and basis sets for the light elements. In all cases, CP(PPP) was used as basis set for the copper atom. To mimic the solvent effect (DMSO) the COSMO model was used. All values are in MHz. The best agreement with the experiment is highlighted.

Atom	A_x	A_y	A_z	P_x	P_y	P_z
Functional/basis sets: B3LYP/6-31+G**						
^{14}N(py)	36.80	38.22	50.30	0.48	0.64	-1.12
^{14}N(py)	36.80	38.22	50.29	0.49	0.63	-1.12
^{14}N(py)	36.77	38.18	50.24	0.49	0.63	-1.12
^{14}N(py)	36.85	38.27	50.35	0.49	0.63	-1.12
Functional/basis sets : BHandHLYP/6-31+G**						
^{14}N(py)	29.51	31.09	39.42	0.60	0.69	-1.29
^{14}N(py)	29.51	31.09	39.42	0.60	0.68	-1.28
^{14}N(py)	29.49	31.07	39.39	0.60	0.68	-1.28
^{14}N(py)	29.55	31.13	39.47	0.60	0.69	-1.29
Functional/basis sets : PBE0/6-31+G**						
^{14}N(py)	35.64	37.07	48.30	0.47	0.62	-1.09
^{14}N(py)	35.56	36.99	48.19	0.47	0.62	-1.09
^{14}N(py)	35.59	37.03	48.24	0.47	0.62	-1.09
^{14}N(py)	35.59	37.02	48.24	0.47	0.62	-1.09
Functional/basis sets : B3LYP/EPR-II						
^{14}N(py)	41.03	42.54	55.27	0.48	0.74	-1.22
^{14}N(py)	41.03	42.54	55.26	0.48	0.74	-1.22
^{14}N(py)	40.99	42.50	55.21	0.48	0.74	-1.22
^{14}N(py)	41.06	42.60	55.34	0.48	0.74	-1.22
Functional/basis sets : BHandHLYP /EPR-II						
^{14}N(py)	34.47	36.17	44.94	0.59	0.81	-1.40
^{14}N(py)	34.47	36.17	44.94	0.59	0.81	-1.40
^{14}N(py)	34.44	36.14	44.91	0.59	0.81	-1.40
^{14}N(py)	34.51	36.21	44.99	0.59	0.81	-1.40
Functional/basis sets : PBE0 /EPR-II						
^{14}N(py)	39.79	41.33	53.16	0.45	0.75	-1.20
^{14}N(py)	39.70	41.24	53.5	0.45	0.75	-1.20
^{14}N(py)	39.74	41.28	53.09	0.45	0.75	-1.20
^{14}N(py)	39.74	41.27	53.10	0.45	0.75	-1.20

B. [Cu(py)₃(DMPO)]²⁺
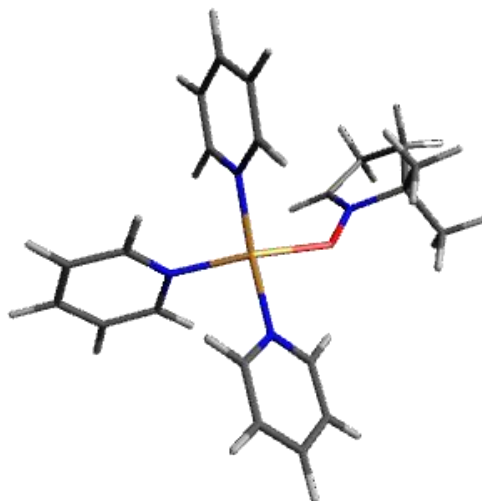
Figure S4.3 Geometry-optimized configuration of [Cu(py)₃(DMPO)]²⁺. The coordinates of the atoms are reported inTable S4.3.

Table S4.3 The coordinates (in Å) of the geometry-optimized [Cu(py)₃(DMPO)]²⁺ complex.

Cu	2.365392	2.183717	-1.879680
N	0.499935	2.136361	-2.610022
N	2.806145	0.321509	-2.538847
N	3.906219	2.167801	-0.578938
C	3.988619	0.124404	-3.171097
C	4.361229	-1.132323	-3.662781
C	3.491549	-2.218953	-3.477452
C	2.273687	-2.009357	-2.810793
C	1.960501	-0.721892	-2.359088
C	-0.521178	2.378628	-1.750840
C	-1.857855	2.349777	-2.167542
C	-2.143623	2.073350	-3.514277
C	-1.081082	1.824997	-4.398289
C	0.229935	1.858199	-3.909183
C	4.823988	3.163083	-0.573945
C	5.873231	3.192773	0.352973
C	5.966387	2.168581	1.308443
C	5.007644	1.142578	1.300466
C	3.995114	1.170889	0.334662
H	4.649519	0.997493	-3.283407
H	5.325361	-1.247291	-4.177871
H	3.760951	-3.219614	-3.847210
H	1.562725	-2.829869	-2.639321
H	1.012824	-0.515426	-1.839831

M.Samanipour

H	-0.253783	2.594408	-0.705173
H	-2.656775	2.543482	-1.438019
H	-3.184251	2.048705	-3.870592
H	-1.256316	1.601333	-5.459985
H	1.087592	1.651594	-4.567333
H	4.694684	3.952044	-1.328328
H	6.602399	4.014621	0.318272
H	6.778574	2.168629	2.050893
H	5.036922	0.320693	2.029699
H	3.232377	0.378851	0.289730
O	2.334598	4.162561	-1.632438
N	1.804049	5.032263	-2.455485
C	1.813155	5.015282	-3.762375
C	1.222385	6.326635	-1.866847
C	0.516298	6.908204	-3.118661
C	1.190898	6.237270	-4.340495
C	2.416324	7.171940	-1.393575
C	0.276111	5.987561	-0.716627
H	2.297875	4.190690	-4.305834
H	0.589039	8.011129	-3.145246
H	-0.559257	6.643020	-3.095343
H	0.484909	5.993474	-5.160247
H	1.988722	6.862078	-4.803427
H	3.096473	7.420559	-2.232652
H	2.038228	8.118662	-0.961010
H	2.991339	6.636848	-0.613036
H	0.814961	5.484681	0.109169
H	-0.160442	6.927561	-0.325575
H	-0.557304	5.340809	-1.055591

Table S4.4 Single-point DFT-computed ^{14}N hyperfine and quadrupole couplings of the pyridine and DMPO ligands in [Cu(py)$_3$(DMPO)]$^{2+}$. The computations were performed using different combinations of functional and basis sets for the light elements. In all cases, CP(PPP) was used as basis set for the copper atom. To mimic the solvent effect (DMSO) the COSMO model was used. All values are in MHz. The best agreement with the experiment is highlighted.

Atom	A_x	A_y	A_z	P_x	P_y	P_z
Single point: B3LYP/6-31+G**						
^{14}N(py)	30.25	31.53	42.20	0.48	0.63	-1.11
^{14}N(py)	35.88	37.27	49.49	0.49	0.62	-1.11
^{14}N(py)	30.03	31.23	42.03	0.49	0.62	-1.11
^{14}N(DMPO)	0.34	-0.95	-2.50	-0.44	-0.60	1.04
Single point: BHandHLYP /6-31+G**						
^{14}N(py)	24.31	25.80	33.02	0.59	0.69	-1.28
^{14}N(py)	28.19	29.78	37.87	0.60	0.68	-1.28
^{14}N(py)	24.34	25.75	33.11	0.59	0.68	-1.27
^{14}N(DMPO)	0.46	-0.68	-2.13	-0.39	-0.57	-0.96
Single point: PBE0/6-31+G**						
^{14}N(py)	29.42	30.74	40.66	0.46	0.63	-1.09
^{14}N(py)	34.58	36.00	47.27	0.46	0.62	-1.08
^{14}N(py)	29.11	30.34	40.35	0.47	0.61	-1.08
^{14}N(DMPO)	0.29	-0.97	-2.63	-0.42	-0.60	1.02
Single point: B3LYP/EPR-II						
^{14}N(py)	33.46	34.83	46.04	0.47	0.75	-1.22
^{14}N(py)	39.80	41.29	54.13	0.48	0.73	-1.21
^{14}N(py)	33.29	34.57	45.92	0.49	0.73	-1.22
^{14}N(DMPO)	0.455	-0.88	-2.51	-0.46	-0.68	1.14
Single point: BHandHLYP /EPR-II						
^{14}N(py)	32.84	34.55	43.07	0.59	0.81	-1.39
^{14}N(py)	32.84	34.55	43.07	0.59	0.81	-1.39
^{14}N(py)	28.37	29.88	37.61	0.58	0.80	-1.39
^{14}N(DMPO)	0.59	-0.60	-2.11	-0.44	-0.60	1.04
Single point: PBE0/EPR-II						
^{14}N(py)	32.59	34.00	44.44	0.44	0.45	-1.19
^{14}N(py)	38.43	39.95	51.82	0.44	0.74	-1.18
^{14}N(py)	32.35	33.66	44.21	0.42	0.68	-1.10
^{14}N(DMPO)	0.44	-0.87	-2.61	-0.42	-0.68	1.10

C. [Cu(py)₄(DMPO)]²⁺
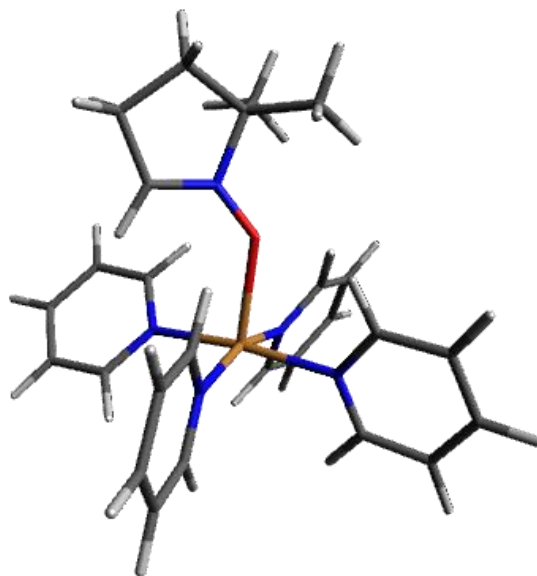
Figure S4.4 Geometry-optimized configuration of [Cu(py)₄(DMPO)]²⁺. The coordinates of the atoms are reported in Table S 4.5.

Table S 4.5 The coordinates (in Å) of the geometry-optimized [Cu(py)₄(DMPO)]²⁺ complex.

Cu	3.132043	1.854884	-0.497845
N	4.562809	1.622014	-1.951776
N	1.646039	1.513573	0.879907
N	4.498886	1.973025	1.043668
N	1.745822	1.439346	-1.967041
O	2.759923	4.086257	-0.675928
C	4.233713	2.850690	2.042416
C	5.076972	3.000293	3.149158
C	6.234692	2.209413	3.232250
C	6.505140	1.298948	2.199670
C	5.615057	1.212129	1.120704
C	4.937295	2.674958	-2.713562
C	5.850316	2.542801	-3.767621
C	6.387636	1.276045	-4.045454
C	5.985220	0.182681	-3.261852
C	5.067487	0.395294	-2.225273
C	1.281568	2.424390	-2.768944
C	1.330265	0.166754	-2.160837
C	0.428288	-0.169937	-3.178151
C	-0.058814	0.846652	-4.015657
C	0.374191	2.165337	-3.805044
C	0.594714	2.362981	0.952441
C	-0.480953	2.135539	1.820074

C	-0.469382	0.988191	2.630020
C	0.622956	0.109890	2.547561
C	1.666019	0.408938	1.661341
N	3.433733	5.168176	-0.446736
C	2.679358	6.507834	-0.348267
C	3.857375	7.509135	-0.420239
C	5.108733	6.719024	0.033810
C	4.718912	5.300933	-0.217233
C	1.698390	6.620416	-1.514321
C	1.957735	6.523700	1.008458
H	3.311058	3.441554	1.942461
H	4.820249	3.726057	3.933819
H	6.915377	2.301283	4.091795
H	7.395942	0.655288	2.217939
H	5.804729	0.510688	0.295766
H	4.474736	3.643170	-2.471536
H	6.127249	3.427596	-4.358224
H	7.106913	1.141003	-4.867107
H	6.369800	-0.830457	-3.445592
H	4.719686	-0.442855	-1.601268
H	1.653111	3.437501	-2.549040
H	1.728151	-0.602163	-1.480353
H	0.117034	-1.216863	-3.302379
H	-0.769160	0.613084	-4.822971
H	0.017555	2.993375	-4.434105
H	0.638297	3.245823	0.296380
H	-1.314024	2.852021	1.852080
H	-1.302717	0.780938	3.318079
H	0.677472	-0.800068	3.161823
H	2.544386	-0.249295	1.575903
H	3.667539	8.404365	0.200970
H	3.992174	7.846474	-1.467151
H	5.345517	6.865171	1.112449
H	6.026537	6.997283	-0.522954
H	5.374350	4.419595	-0.199664
H	0.904093	5.852426	-1.445751
H	1.216868	7.617901	-1.483934
H	2.217196	6.517768	-2.488293
H	2.673800	6.467056	1.852992
H	1.385381	7.466851	1.107059
H	1.244566	5.680127	1.088109

Table S4.6 Single-point DFT-computed ^{14}N hyperfine and quadrupole couplings of the py and DMPO ligands in $[Cu(py)_4(DMPO)]^{2+}$ for different functional/basis set combinations for the light elements. CP(PPP) was used as basis sets for Cu. To mimic the solvent effect, the COSMO model was used. All values are in MHz.

Atom	A_x	A_y	A_z	P_x	P_y	P_z
Single point: B3LYP/6-31+G**						
$^{14}N(py)$	34.07	35.40	46.22	0.61	0.64	-1.25
$^{14}N(py)$	34.57	35.93	47.05	0.60	0.64	-1.24
$^{14}N(py)$	34.09	35.34	45.94	0.59	0.63	-1.22
$^{14}N(py)$	39.07	40.57	52.97	0.60	0.64	-1.24
$^{14}N(DMPO)$	0.079	-0.23	-0.26	-0.34	-0.51	0.85
Single point: BHandHLYP/6-31+G**						
$^{14}N(py)$	26.04	27.57	34.65	0.68	0.73	-1.41
$^{14}N(py)$	26.46	28.01	35.28	0.68	0.73	-1.41
$^{14}N(py)$	26.24	27.69	34.75	0.66	0.72	-1.38
$^{14}N(py)$	29.40	31.09	38.98	0.68	0.75	-1.43
$^{14}N(DMPO)$	0.13	-0.22	-0.25	-0.22	-0.54	0.76
Single point: PBE0/6-31+G**						
$^{14}N(py)$	32.66	34.01	43.96	0.58	0.63	-1.21
$^{14}N(py)$	33.16	34.53	44.77	0.58	0.63	-1.21
$^{14}N(py)$	32.76	34.03	43.82	0.57	0.63	-1.20
$^{14}N(py)$	37.29	38.81	50.15	0.58	0.62	-1.20
$^{14}N(DMPO)$	0.09	-0.23	-0.26	-0.33	-0.50	0.83
Single point: B3LYP/EPR-II						
$^{14}N(py)$	38.16	39.58	50.92	0.60	0.75	-1.35
$^{14}N(py)$	38.62	40.07	51.74	0.60	0.75	-1.35
$^{14}N(py)$	38.22	39.56	50.66	0.59	0.74	-1.33
$^{14}N(py)$	43.76	45.36	58.37	0.60	0.74	-1.34
$^{14}N(DMPO)$	0.045	-0.269	-0.297	-0.39	-0.55	0.94
Single point: BHandHLYP/EPR-II						
$^{14}N(py)$	30.52	32.16	39.58	0.72	0.82	-1.54
$^{14}N(py)$	30.98	32.64	40.25	0.72	0.82	-1.54
$^{14}N(py)$	30.81	32.36	39.74	0.70	0.81	-1.51
$^{14}N(py)$	34.49	36.30	44.58	0.74	0.81	-1.56
$^{14}N(DMPO)$	0.10	-0.24	-0.28	-0.29	-0.54	0.83
Single point: PBE0 /EPR-II						
$^{14}N(py)$	36.60	38.05	48.49	0.57	0.75	-1.32
$^{14}N(py)$	37.09	38.56	49.30	0.57	0.75	-1.32
$^{14}N(py)$	36.76	38.13	48.39	0.55	0.75	-1.30
$^{14}N(py)$	41.82	43.43	55.35	0.57	0.74	-1.31
$^{14}N(DMPO)$	0.0575	-0.26	-0.30	-0.37	-0.53	0.910

4.6.2.2 Effect of coordination on ^{14}N quadrupole coupling of DMPO

The $\frac{e^2qQ}{h}$- values measured experimentally in complexes II and IV are much higher than those expected for a free *N*-oxides. We, therefore, computed the nuclear quadrupole values for pyridine *N*-oxide, for which experimental values exist (1.188 MHz [59]) and used these values to derive a correction factor for all other DFT-computed $\frac{e^2qQ}{h}$- values, *i.e.*

$$\lambda = |\frac{e^2qQ}{h}|_{exp}/|\frac{e^2qQ}{h}|_{DFT} = 1.244$$

Although this correction factor is only approximatively correct, it gives a means to evaluate the experimentally observed trends.

The computations of the *N*-oxides, pyridine *N*-oxide and DMPO, were done using restricted Kohn-Sham with B3LYP functional and EPR-II basis sets. For the Cu(II) complex unrestricted KS was used, with the same functional and same basis set for the light elements. For further details on [Cu(py)$_3$(DMPO)]$^{2+}$ see Table S4.4. The same trends were found for other functional/basis sets combinations.

Table S4.7 DFT-computed and corrected ^{14}N nuclear quadrupole value of the N-oxide/nitroxide. Values are given in MHz.

	$(\frac{e^2qQ}{h})_{DFT}$	$(\frac{e^2qQ}{h})_{corrected} = \lambda(\frac{e^2qQ}{h})_{DFT}$
Pyridine *N*-oxide	0.955	1.188
DMPO	1.399	1.740
[Cu(py)$_3$(DMPO)]$^{2+}$	2.28	2.836

4.6.3 UV-vis spectroscopy

To estimate the equilibrium constant (K) for the DMPO-Cu(II) complex, UV-vis spectrophotometric titrations were performed. In Figure S4.5, the band centered at 926 nm corresponds to the *d-d* transition of Cu(II) in DMSO. Upon the addition of DMPO the intensity of this band decreases, but not to zero, as DMPO(-derivatives) and the DMPO-ligated Cu(II) complexes also absorb at this wavelength range. Note, at lower wavelengths the spectra become saturated by the absorption of DMPO at these very high concentrations.
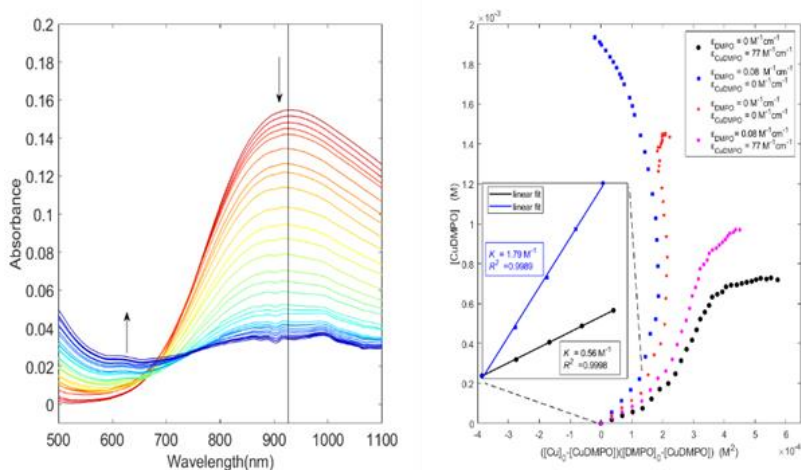
Figure S4.5: left UV-vis spectra of a 2 mM CuCl₂ DMSO solution with increasing amounts of DMPO (0 to 58 µL, 0 to 490 mM) recorded on a Cary 5000 UV-Vis-NIR (Agilent). The vertical line marks 926 nm. right plot of $[CuDMPO]$ vs $([Cu]_0 - [CuDMPO])([DMPO]_0 - [CuDMPO])$ based on the absorbance at 926 nm, see text for more details.

From the EPR studies, it was determined that predominantly only one DMPO(-derivative) is ligated to the Cu(II) center up to $\frac{[DMPO]}{[Cu(I/II)]} = 30$. In the below derivation, Cu stands for Cu(II), DMPO stands for both DMPO or a DMPO-derivative and CuDMPO stands for Cu(II) ligating to one DMPO ligand in addition to solvent ligands.

$$Cu + DMPO \rightleftharpoons CuDMPO \tag{1}$$

$$K_1 = \frac{[CuDMPO]}{[Cu][DMPO]} \tag{2}$$

$$A_{926\,nm} = \varepsilon_{Cu}[Cu] + \varepsilon_{DMPO}[DMPO] + \varepsilon_{CuDMPO}[CuDMPO] \tag{3}$$

$$[Cu]_0 = [Cu] + [CuDMPO] \tag{4}$$

$$[DMPO]_0 = [DMPO] + [CuDMPO] \tag{5}$$

where $[X]$ is the concentration at equilibrium, $[X]_0$ is the total concentration of in the sample, ε_X is the extinction coefficient at 926 nm.
Hence,

$$[CuDMPO] = \frac{\varepsilon_{Cu}[Cu]_0 + \varepsilon_{DMPO}[DMPO]_0 - A_{926\,nm}}{\varepsilon_{Cu} + \varepsilon_{DMPO} - \varepsilon_{CuDMPO}} \tag{6}$$

$$[CuDMPO] = K_1([Cu]_0 - [CuDMPO])([DMPO]_0 - [CuDMPO]) \tag{7}$$

ε_{Cu} at 926 nm was determined from the pure CuCl₂ in DMSO sample to be 77 M⁻¹cm⁻¹. ε_{DMPO} at 926 nm was approximated to be $0 \leq \varepsilon_{DMPO} \leq 0.079$. The upper limit was estimated from the spectra with 441 mM DMPO. ε_{CuDMPO} at 926 nm was approximated

to be $0 \leq \varepsilon_{CuDMPO} \leq 77$. ε_{Cu} was taken as the upper limit. Using these limits, $[CuDMPO]$ vs. $([Cu]_0 - [CuDMPO])([DMPO]_0 - [CuDMPO])$ were plotted (Figure S4.5 right). Clearly the data does not follow the linearity as defined by (7). This is because at the high concentration of DMPO, more than one DMPO molecule may ligate to Cu(II) (see the absence of a clear isosbestic point). Nevertheless, there is some linearity at the lower $\frac{[DMPO]}{[Cu]}$ molar ratios, up to ~ 35 which was also close to the highest concentration used in the EPR measurements where only CuDMPO was observed. Linear fitting of the two extreme cases in Figure S4.5 right gave an estimation of K_1 to be $0.56 \leq K_1 \leq 1.79$ M^{-1}.

4.7 References

[1] K. S. Egorova and V. P. Ananikov, *Toxicity of Metal Compounds: Knowledge and Myths*, Organometallics **36**, 4071 (2017).

[2] H. Sterckx, B. Morel, and B. U. W. Maes, *Catalytic Aerobic Oxidation of C(Sp3)−H Bonds*, Angew. Chemie - Int. Ed. **58**, 7946 (2019).

[3] R. Trammell, K. Rajabimoghadam, and I. Garcia-Bosch, *Copper-Promoted Functionalization of Organic Molecules: From Biologically Relevant Cu/O 2 Model Systems to Organometallic Transformations*, Chem. Rev. **119**, 2954 (2019).

[4] S. D. McCann and S. S. Stahl, *Copper-Catalyzed Aerobic Oxidations of Organic Molecules: Pathways for Two-Electron Oxidation with a Four-Electron Oxidant and a One-Electron Redox-Active Catalyst*, Acc. Chem. Res. **48**, 1756 (2015).

[5] K. W. Shimkin and D. A. Watson, *Recent Developments in Copper-Catalyzed Radical Alkylations of Electron-Rich Tt-Systems*, Beilstein J. Org. Chem. **11**, 2278 (2015).

[6] M. M. Roessler and E. Salvadori, *Principles and Applications of EPR Spectroscopy in the Chemical Sciences*, Chem. Soc. Rev. **47**, 2534 (2018).

[7] A. Alberti and D. Macciantelli, *Electron Paramagnetic Resonance: A Practitioner's Toolkit* (John Wiley & Sons Inc., New Jersey, 2009).

[8] C. L. Hawkins and M. J. Davies, *Detection and Characterisation of Radicals in Biological Materials Using EPR Methodology*, Biochim. Biophys. Acta - Gen. Subj. **1840**, 708 (2014).

[9] D. Dvoranová, Z. Barbieriková, and V. Brezová, *Radical Intermediates in Photoinduced Reactions on TiO₂ (An EPR Spin Trapping Study)*, Molecules **19**, 17279 (2014).

[10] B. Lu, Y. Cheng, L.-Y. Chen, J.-R. Chen, and W.-J. Xiao, *Photoinduced Copper-Catalyzed Radical Aminocarbonylation of Cycloketone Oxime Esters*, ACS Catal. **9**, 8159 (2019).

[11] Y. Feng, P.-H. Lee, D. Wu, Z. Zhou, H. Li, and K. Shih, *Degradation of Contaminants by Cu^+ Activated Molecular Oxygen in Aqueous Solutions: Evidence for Cupryl Species (Cu^{3+})*, J. Hazard. Mater. **331**, 81 (2017).

[12] M. A. Bizeto, W. A. Alves, C. A. S. Barbosa, A. M. D. C. Ferreira, and V. R. L. Constantino, *Evaluation of Hexaniobate Nanoscrolls as Support for Immobilization of a Copper Complex Catalyst*, Inorg. Chem. **45**, 6214 (2006).

[13] M. Yamada, K. D. Karlin, and S. Fukuzumi, *One-Step Selective Hydroxylation of Benzene to Phenol with Hydrogen Peroxide Catalysed by Copper Complexes Incorporated into Mesoporous Silica-Alumina*, Chem. Sci. **7**, 2856 (2016).

[14] G. Cerchiaro, G. A. Micke, M. F. M. Tavares, and A. M. da Costa Ferreira, *Kinetic Studies of Carbohydrate Oxidation Catalyzed by Novel Isatin–Schiff Base Copper(II) Complexes*, J. Mol. Catal. A Chem. **221**, 29 (2004).

[15] L. Khachatryan, C. A. McFerrin, R. W. Hall, and B. Dellinger, *Environmentally Persistent Free Radicals (EPFRs). 3. Free versus Bound Hydroxyl Radicals in EPFR Aqueous Solutions*, Environ. Sci. Technol. **48**, 9220 (2014).

[16] S. Hamulakova, P. Poprac, K. Jomova, V. Brezova, P. Lauro, L. Drostinova, D. Jun, V. Sepsova, M. Hrabinova, O. Soukup, P. Kristian, Z. Gazova, Z. Bednarikova, K. Kuca, and M. Valko, *Targeting Copper(II)-Induced Oxidative Stress and the Acetylcholinesterase System in Alzheimer's Disease Using Multifunctional Tacrine-Coumarin Hybrid Molecules*, J. Inorg. Biochem. **161**, 52 (2016).

[17] P. M. Hanna, W. Chamulitrat, and R. P. Mason, *When Are Metal Ion-Dependent Hydroxyl and Alkoxyl Radical Adducts of 5,5-Dimethyl-1-Pyrroline N-Oxide Artifacts?*, Arch. Biochem. Biophys. **296**, 640 (1992).

[18] E. H. Fowles, B. C. Gilbert, M. R. Giles, and A. C. Whitwood, *The Effects of Chelating Agents on Radical Generation in Alkaline Peroxide Systems, and the Relevance to Substrate Damage*, Free Radic. Res. **41**, 515 (2007).

[19] X. Qiao, S. Chen, L. Tan, H. Zheng, Y. Ding, and Z. Ping, *Investigation of Formation of Superoxide Anion Radical in DMSO by ESR: Part 1. Influence of Fe^{2+} and Cu^{2+}*, Magn. Reson. Chem. **39**, 207 (2001).

[20] D. A. Iovan, A. T. Wrobel, A. A. McClelland, A. B. Scharf, G. A. Edouard, and T. A. Betley, *Reactivity of a Stable Copper–Dioxygen Complex*, Chem. Commun. **53**, 10306 (2017).

[21] S. Van Doorslaer, *Hyperfine Spectroscopy: ESEEM*, EMagRes **6**, 51 (2017).

[22] J. R. Harmer, *Hyperfine Spectroscopy - ENDOR*, EMagRes **5**, 1493 (2016).

[23] H. Sterckx, C. Sambiagio, V. Médran-Navarrete, and B. U. W. Maes, *Copper-Catalyzed Aerobic Oxygenation of Benzylpyridine N -Oxides and Subsequent Post-Functionalization*, Adv. Synth. Catal. **359**, 3226 (2017).

[24] P. Höfer, A. Grupp, H. Nebenführ, and M. Mehring, *Hyperfine Sublevel Correlation (Hyscore) Spectroscopy: A 2D ESR Investigation of the Squaric Acid Radical*, Chem. Phys. Lett. **132**, 279 (1986).

[25] E. R. Davies, *A New Pulse Endor Technique*, Phys. Lett. A **47**, 1 (1974).

[26] S. Stoll and A. Schweiger, *EasySpin, a Comprehensive Software Package for Spectral Simulation and Analysis in EPR*, J. Magn. Reson. **178**, 42 (2006).

[27] F. Neese, *Prediction of Electron Paramagnetic Resonance g Values Using Coupled Perturbed Hartree–Fock and Kohn–Sham Theory*, J. Chem. Phys. **115**, 11080 (2001).

[28] F. Neese, *Theoretical Study of Ligand Superhyperfine Structure. Application to Cu(II) Complexes*, J. Phys. Chem. A **105**, 4290 (2001).

[29] F. Neese, *Metal and Ligand Hyperfine Couplings in Transition Metal Complexes: The Effect of Spin–Orbit Coupling as Studied by Coupled Perturbed Kohn–Sham Theory*, J. Chem. Phys. **118**, 3939 (2003).

[30] F. Neese, *Efficient and Accurate Approximations to the Molecular Spin-Orbit Coupling Operator and Their Use in Molecular g-Tensor Calculations*, J. Chem. Phys. **122**, 034107 (2005).

[31] S. Sinnecker, A. Rajendran, A. Klamt, M. Diedenhofen, and F. Neese, *Calculation of Solvent Shifts on Electronic g -Tensors with the Conductor-Like Screening Model (COSMO) and Its Self-Consistent Generalization to Real Solvents (Direct COSMO-RS)*, J. Phys. Chem. A **110**, 2235 (2006).

[32] J. P. Perdew, *Density-Functional Approximation for the Correlation Energy of the Inhomogeneous Electron Gas*, Phys. Rev. B **33**, 8822 (1986).

[33] J. P. Perdew, *Erratum: Density-Functional Approximation for the Correlation*

Energy of the Inhomogeneous Electron Gas, Phys. Rev. B **34**, 7406 (1986).

[34]   A. D. Becke, *Density-Functional Exchange-Energy Approximation with Correct Asymptotic Behavior*, Phys. Rev. A **38**, 3098 (1988).

[35]   A. Schäfer, H. Horn, and R. Ahlrichs, *Fully Optimized Contracted Gaussian Basis Sets for Atoms Li to Kr*, J. Chem. Phys. **97**, 2571 (1992).

[36]   P. J. Stephens, F. J. Devlin, C. F. Chabalowski, and M. J. Frisch, *Ab Initio Calculation of Vibrational Absorption and Circular Dichroism Spectra Using Density Functional Force Fields*, J. Phys. Chem. **98**, 11623 (1994).

[37]   A. D. Becke, *A New Mixing of Hartree–Fock and Local Density-functional Theories*, J. Chem. Phys. **98**, 1372 (1993).

[38]   C. Adamo and V. Barone, *Toward Reliable Density Functional Methods without Adjustable Parameters: The PBE0 Model*, J. Chem. Phys. **110**, 6158 (1999).

[39]   W. J. Hehre, R. Ditchfield, and J. A. Pople, *Self—Consistent Molecular Orbital Methods. XII. Further Extensions of Gaussian—Type Basis Sets for Use in Molecular Orbital Studies of Organic Molecules*, J. Chem. Phys. **56**, 2257 (1972).

[40]   R. Krishnan, J. S. Binkley, R. Seeger, and J. A. Pople, *Self-consistent Molecular Orbital Methods. XX. A Basis Set for Correlated Wave Functions*, J. Chem. Phys. **72**, 650 (1980).

[41]   D. P. Chong, *Recent Advances in Density Functional Methods, Part I* (World Scientific Publ Co, Singapore, 1995).

[42]   J. Ukpong, EJ and Akpanudo, NW and Prasad, *Redox and Spectral Behaviour of Copper (II)-Chloro and Bromo Complexes in Some Nonaqueous Solvents*, African J. Pure Appl. Chem. **4**, 038 (2010).

[43]   H. Sterckx, J. De Houwer, C. Mensch, I. Caretti, K. A. Tehrani, W. A. Herrebout, S. Van Doorslaer, and B. U. W. Maes, *Mechanism of the Cu II -Catalyzed Benzylic Oxygenation of (Aryl)(Heteroaryl)Methanes with Oxygen*, Chem. Sci. **7**, 346 (2016).

[44]   D. P. Freyberg, T. Isobe, and S. Misumi, *An ESR Study of Some Substituted Pyridine N -Oxide Copper(II) Complexes*, Bull. Chem. Soc. Jpn. **45**, 1654 (1972).

[45]   H. J. Scholl and J. Huettermann, *ESR and ENDOR of Copper(II) Complexes with Nitrogen Donors: Probing Parameters for Prosthetic Group Modeling of Superoxide Dismutase*, J. Phys. Chem. **96**, 9684 (1992).

[46]   A. Pöppl, M. Hartmann, W. Böhlmann, and R. Böttcher, *Coordination Geometry of the Copper−Pyridine Complex in Frozen Solution As Studied by Proton and Deuterium Two-Dimensional Hyperfine Sublevel Correlation Electron Spin Resonance Spectroscopy*, J. Phys. Chem. A **102**, 3599 (1998).

[47]   E. Carter, K. M. Sharples, J. A. Platts, and D. M. Murphy, *Structure Determination of Bound Nitrogen-Based Adducts with Copper(II) Acetylacetonato; an EPR, ENDOR and DFT Study*, Phys. Chem. Chem. Phys. **17**, 11445 (2015).

[48]   P. Nunes, N. V. Nagy, E. C. B. A. Alegria, A. J. L. Pombeiro, and I. Correia, *The Solvation and Electrochemical Behavior of Copper Acetylacetonate Complexes in Ionic Liquids*, J. Mol. Struct. **1060**, 142 (2014).

[49]   W. Libus, S. K. Hoffmann, M. Kluczkowski, and H. Twardowska, *Solution*

Equilibriums of Copper(II) Chloride in Pyridine and Pyridine-Diluent Mixtures, Inorg. Chem. **19**, 1625 (1980).

[50] G. M. Rosen, A. Beselman, P. Tsai, S. Pou, C. Mailer, K. Ichikawa, B. H. Robinson, R. Nielsen, H. J. Halpern, and A. D. MacKerell, *Influence of Conformation on the EPR Spectrum of 5,5-Dimethyl-1-Hydroperoxy-1-Pyrrolidinyloxyl: A Spin Trapped Adduct of Superoxide*, J. Org. Chem. **69**, 1321 (2004).

[51] K. Makino, A. Hagi, H. Ide, A. Murakami, and M. Nishi, *Mechanistic Studies on the Formation of Aminoxyl Radicals from 5,5-Dimethyl-1-Pyrroline- N - Oxide in Fenton Systems. Characterization of Key Precursors Giving Rise to Background ESR Signals*, Can. J. Chem. **70**, 2818 (1992).

[52] V. Balasubramanian, M. Ezhevskaya, H. Moons, M. Neuburger, C. Cristescu, S. Van Doorslaer, and C. Palivan, *Structural Characterization of a Highly Active Superoxide-Dismutase Mimic*, Phys. Chem. Chem. Phys. **11**, 6778 (2009).

[53] S. A. Dikanov, A. P. Spoyalov, and J. Hüttermann, *Exploiting the Properties of Line-Shape Singularities in Orientationally Selected Electron Spin Echo Envelope Modulation Spectra of $Cu^{2+}(^{15}N$-Imidazole$)_4$ for the Determination of Hyperfine Coupling with the Remote Imidazol*, J. Chem. Phys. **100**, 7973 (1994).

[54] S. Doorslaer, D. M. Murphy, and I. A. Fallis, *Evaluating π-π Stacking Effects in Macrocyclic Transition Metal Complexes Using EPR Techniques*, Res. Chem. Intermed. **33**, 807 (2007).

[55] N. Ritterskamp, K. Sharples, E. Richards, A. Folli, M. Chiesa, J. A. Platts, and D. M. Murphy, *Understanding the Coordination Modes of $[Cu(Acac)_2(Imidazole)_n=1,2]$ Adducts by EPR, ENDOR, HYSCORE, and DFT Analysis*, Inorg. Chem. **56**, 11862 (2017).

[56] N. M. Atherton and A. J. Horsewill, *An E.S.R. and Proton ENDOR Study of Copper-Doped Zinc Acetate Dihydrate*, Mol. Phys. **42**, 985 (1981).

[57] S. Stoll, C. Calle, G. Mitrikas, and A. Schweiger, *Peak Suppression in ESEEM Spectra of Multinuclear Spin Systems*, J. Magn. Reson. **177**, 93 (2005).

[58] M. Florent, I. Kaminker, V. Nagarajan, and D. Goldfarb, *Determination of the ^{14}N Quadrupole Coupling Constant of Nitroxide Spin Probes by W-Band ELDOR-Detected NMR*, J. Magn. Reson. **210**, 192 (2011).

[59] P. M. Woyciesjes, N. Janes, S. Ganapathy, Y. Hiyama, T. L. Brown, and E. Oldfield, *Nitrogen and Oxygen Nuclear Quadrupole and Nuclear Magnetic Resonance Spectroscopic Study of N O Bonding in Pyridine 1-Oxides*, Magn. Reson. Chem. **23**, 315 (1985).

Part III
EPR-spectroelectrochemistry and spin-trapping

CHAPTER 5

Reductive intramolecular cyclisation of allyl 2-bromobenzyl ether

This chapter focuses on the use of *in-situ* spin-trap EPR in electrocatalysis.The *in-situ* electrochemical activation of C-X bonds requires very negative electrode potentials. Lowering the overpotentials and increasing the catalytic activity requires intensive electrocatalytic research. A profound understanding of the reaction mechanism and the influence of the electrocatalyst allows optimal tuning of the electrocatalyst. This can be achieved by combining electrochemical techniques with EPR spectroscopy. Although this was introduced in the mid-twentieth century, the application of this combined approach in electrocatalytic research is underexploited. Several reasons can be listed, such as the limited availability of EPR instrumentation and electrochemical devices for such *in-situ* experiments. In this work, a simple and inexpensive construction adapted for *in-situ* EPR electrocatalytic research is proposed. The proof of concept is provided by studying a model reaction, namely the reductive cyclization of allyl 2-bromobenzyl ether which has interesting industrial applications.

This chapter redrafted from :

Own contribution: Deconvolution of the measured EPR spectra, DFT computations of the EPR parameters of the spin-trapped radicals.

5.1 Introduction

The electrosynthesis reduction of organic halides has attracted interest and accompanying research [1,2]. The numerous essential applications related to these reactions, such as pollution reduction, exploration of the DET (dissociative electron transfer) mechanism, carbon fixation, and organic upgrading via activation of the R-X bond, have kindled this interest [3–7]. The synthesis of heterocyclic compounds is of particular interest due to their essential uses in medicines [8–10], pesticides [11], dyes [12], and synthetic applications [13].

In this work, we investigated the electrochemical cyclisation of allyl 2-bromobenzyl ether to 4-methylisochromane (a benzopyran derivative) (Figure 5.1a). Benzopyran is of great importance in the pharmaceutical industry as an essential building block for numerous drugs. Conventional synthesis of heterocycles is complex and requires many reaction steps and auxiliaries, resulting in a lower selectivity [2]. As an alternative, electrosynthesis introduces many advantages with fewer steps, milder reaction conditions, higher selectivity, less pollutants, and waste streams, and avoid the need for expensive or hazardous reagents [14–16]. However, a major drawback of using organic halides in electrosynthesis is that the electrochemical activation of C-X bonds, especially in chlorides and bromides, requires very negative electrode potentials, which is impractical for industrial production processes due to exuberant energy costs. As discussed in chapter 1, electrocatalysis can decrease energy costs and increase selectivity. Previous strategies towards electrocatalysis include: investigating different bulk materials with potential for carbon halogen bond rupture such as Ag, Pd, Ni and Cu [17–20], tuning the morphology and geometrical characteristics of the electrode [21,22], and using a homogeneous electrocatalysis route with mainly transition-metal complexes [23–27]. The selection and optimal tuning of suitable catalytic material requires a thorough understanding of the complex reaction mechanism and effect of the catalyst. The present work aims to understand and introduce an efficient method to study these kinds of multi-step syntheses in which radical intermediates are generated. Figure 5.1b shows the possible electrocatalytic reduction process of the cyclisation of allyl 2-bromobenzyl ether [28]. The reduction of aryl halides occurs through a dissociative electron transfer leading to the scission of the carbon-halogen bond [6,17]. There are two possible pathways for this: a stepwise mechanism or a concerted mechanism. The former is shown by reaction (1) and (2) with the formation of an intermediate radical anion, the latter is presented by reaction (3) leading directly to the allyl benzyl ether radical. This radical can then undergo an intramolecular cyclisation reaction (4) after which it is reduced (5). Alternatively, the allyl benzyl ether radical can also be reduced directly (6). Since the product of interest is the benzopyran derivate obtained in reaction (5), the optimization of the electrocatalyst will also include preventing reaction (6) from taking place.

As discussed in chapters 1-3, EPR spectroelectrochemistry can offer a way to tackle this problem. In this work, a set-up for combined *in-situ* EPR and electrochemical experiments constructed by D. Pauwels (ELCAT group, University of Antwerp) (Figure 5.2) [29,30] was used to investigate the intermediates in the reductive cyclisation of allyl 2-bromobenzyl ether. In the following, I will mainly focus on my own contribution (DFT and EPR analysis), mentioning only those parts of electrochemistry that are

necessary for the understanding of EPR work. For all other details of the electrochemical set-up, I refer to [29]. The scope of the presented work is not to completely understand the electrocatalytic mechanism of cyclisation reaction on silver but to demonstrate the usefulness of these combination of electrochemistry, EPR and DFT in electrocatalytic research and to confirm the general scheme of the cyclisation reaction investigated.
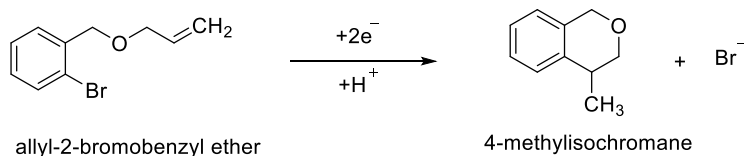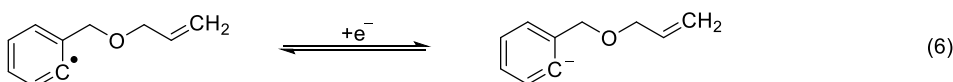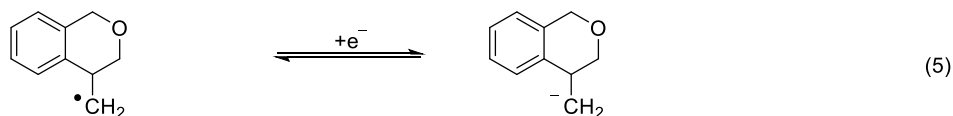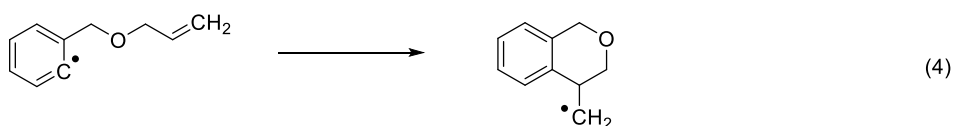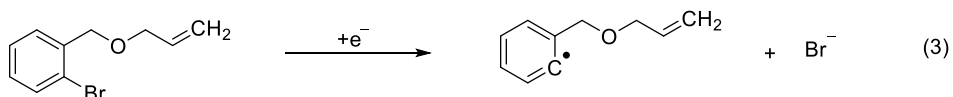

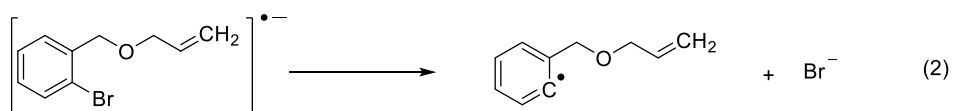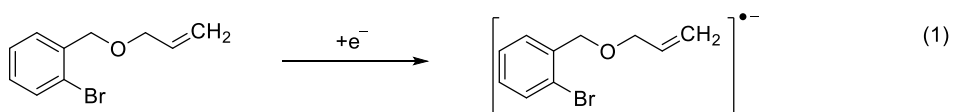Figure 5.1. a) The desired reaction. b) Possible reaction pathway of cyclisation of allyl-2-bromobenzyl ether [28].

5.2 Material and methods

5.2.1 Chemicals

Acetonitrile (ACN, HPLC gradient grade, ≥99.9 %) was purchased from Chem-Lab (Belgium). Allyl 2-bromobenzyl ether (ABBE, 95 %), (2,2,6,6-tetramethylpiperidin-1-yl)oxyl (TEMPO), the spin trapping agent N-tert-Butyl-α-phenylnitrone (PBN, for ESR-spectroscopy, ≥99.5 %) and the supporting electrolyte tetrabutylammonium perchlorate (n-Bu$_4$NClO$_4$, 99.0 %) were purchased from Sigma-Aldrich (Belgium).

5.2.2 Set-up and procedure

The combined EPR and electrochemical experiments were performed in a Wilmad WG-810 Suprasil® (quartz) electrolytic flat cell. The cell was positioned in a TE102 cavity in a Bruker E580 Elexsys spectrometer, and a custom-constructed electrode was used (Figure 5.2).
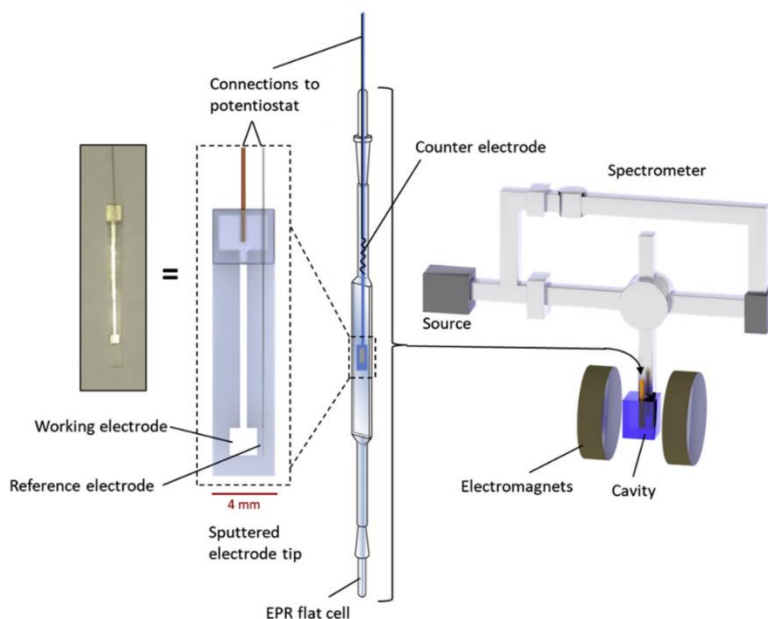

Figure 5.2 Picture of the electrode tip (left) and schematic illustration of the set-up. The electrode tip is positioned in the flat cell which is inserted in the cavity (depicted as a blue box) between the poles of the electromagnet of the spectrometer. The orange tube in the cavity represents the flat cell and shows its position.

This electrode is based upon the original Adams cell [31], from which many different designs have emerged, usually employing a metal mesh or foil as the working electrode. In this work, a 200 nm film of the target working electrode material was coated onto a 30 µm polypropylene substrate by means of sputter deposition. The geometrical surface area of the electrode was 4 mm². This provides a reproducible flat working electrode surface that is tunable in size and geometry. In addition, only a very small amount of

metal is brought into the active part of the cavity, so the EPR signal is not significantly disturbed. As a reference electrode, a Teflon-coated 75 µm diameter Ag wire was fixed to the substrate and stripped near the working electrode leading to a very small distance between both (<1 mm). This short distance results in an acceptable uncompensated resistance. A Pt wire wound around the electrode's base acts as a counter electrode and was positioned directly above the flat part of the cell. This set-up with a sputter-coated working electrode provides a simple, inexpensive and flexible platform for combined EPR and electrochemistry measurements (Figure 5.2). It was validated in both aqueous and non-aqueous environments using the reduction of methyl viologen and the reduction of benzoquinone as standard reactions (results shown in Figure S5.1 in the supporting information). In both cases, the set-up gave a good voltammetric response, and the expected EPR spectra could be obtained.

Experimental solutions were prepared with 0.1 M n-Bu$_4$NClO$_4$, 5 mM of the analyte and 15 mM of PBN. Prior to measurements, the solutions were extensively flushed with argon. To fill the cell, approximately 1.5-2 ml is pipetted under inert atmosphere. The filled cell is further flushed with argon, creating an argon blanket on top of the solution. The cell is closed by inserting the electrode construction from the top and is then transferred to the spectrometer and connected to the potentiostat. A PAR VersaSTAT 3 is used to apply and measure the electrochemical signal. Firstly, CVs are measured to determine the exact potential of the reduction peak versus the pseudo-reference electrode in this cell. Then the experiment is performed by applying a constant potential set at the cathodic peak potential. The EPR spectra are recorded simultaneously at X-band in continuous-wave (CW) mode (~9.7 GHz) at room temperature with 5 mW microwave power 0.1 mT modulation amplitude and 100 kHz modulation frequency.

5.2.3 EPR simulations and (DFT) calculations

The EPR spectra were simulated using the EasySpin-5.1.11 module [32] running in Matlab 2017a. Spin-unrestricted (UKS) DFT computations were performed with the ORCA package [33–36] for PBN-Ox, PBN-allyl benzyl ether and PBN-4-methylisochromane in ACN, and TEMPO, and (5,5-dimethyl-2-hydroxyl-pyrrolin-1-yl)oxyl (DMPO-OH) in water. To simulate the solvent effect, a dielectric surrounding with the dielectric constant of the respective solvents according to the COSMO model was used [37]. For the geometry optimizations, the Becke-Perdew density functional (BP86) [38,39] and the split-valence plus polarization (SVP) basis sets [40] were used for all atoms. The energy was converged to 1×10^{-8} Hartree (E_h), and the convergence tolerances in the geometry optimization were 3×10^{-4} E_h/Bohr for the gradient and 5×10^{-6} E_h for the total energy. The coordinates of the optimized geometries are given in Table S5.1 (supporting information). For benchmarking, single-point calculations with the B3LYP/EPR-II, B3LYP/6-31+G**, and PWPB95/EPR-II functional/basis sets [41–44] were used to predict the EPR spectral parameters from the optimized geometries.

5.3 Electrochemical validation

In previous work [28], several cathode materials were investigated as potential electrocatalysts for the electrochemical cyclisation of allyl 2-bromobenzyl ether to 4-methyl-3,4-dihydro-1*H*-2-benzopyran (4-methylisochromane). It was shown that silver exhibits the best activity with a very high selectivity towards the product of interest, explaining the choice of the electrode material. It was also shown that on silver, two distinct reduction waves were observable, corresponding with one or two electrons being transferred. Setting the potential to the first reduction peak (least negative potential) exclusively yields 4-methylisochromane, while at the second reduction peak, the major product is the undesired allyl benzyl ether (((allyloxy)methyl)benzene). Since 4-methylisochromane is the desired product, the reaction at the first reduction peak will be investigated. An electrode was constructed as described in section 5.2.2, with Ag as the working electrode material. Prior to the EPR electrochemical study, a complete validation of the set-up was done (see for the details [29,30]).

Importantly, *in-situ* voltammograms in the flat cell were compared with standard batch set-ups (Figure 5.3), a necessary but often forgotten step in EPR-spectroelectrochemistry. For the experiment in the flat cell, the presence of PBN in the electrolyte gave a comparable voltammogram as without PBN with only a slight change in shape as a result of the kinetic influences due to the interference of the spin trap with the mechanism. This is not an issue in the bulk electrolysis experiments as PBN itself is not electroactive in the potential window of the measurements [45].
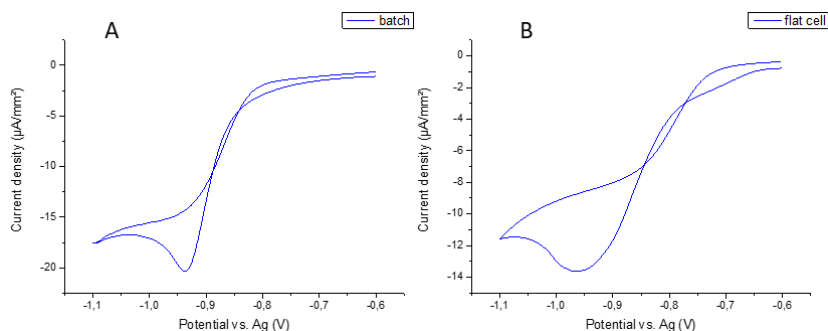

Figure 5.3. Cyclic voltammetry at 100 mV s^{-1} of 5 mM allyl 2-bromobenzyl ether in ACN + 0.1 M n-Bu$_4$NClO$_4$ on an Ag working electrode in a standard batch set-up (A) and in an EPR flat cell (B).

5.4 *In-situ* EPR electrochemical study of cyclisation reaction

The *in-situ* set-up shown in Figure 5.2 was used to perform potential-controlled electrochemistry experiments with simultaneous EPR measurements on samples containing allyl 2-bromobenzyl ether in ACN and TBAP as the supporting electrolyte. Due to the reactivity and thus extremely short lifetime of the intermediate radicals proposed in Figure 5.1, no signal of a radical was detected. Consequently, PBN was added in excess to the solutions to trap the radicals. Figure 5.4. shows the spin-trapping reaction of the two hypothesized intermediate radicals with PBN.
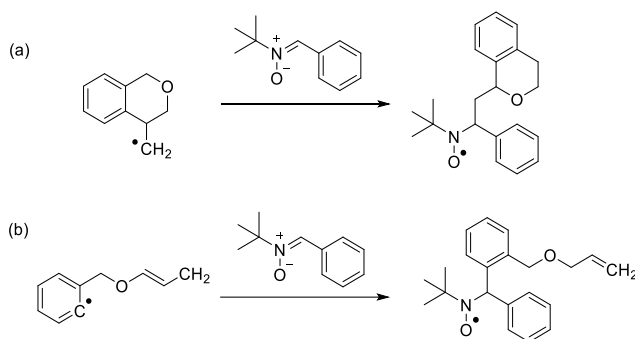

Figure 5.4 The PBN-trapping reaction of a) 4-methylisocromane radical and b)allyl benzyl ether radical, the two intermediates likely to be formed in the cyclisation reaction under study.

The current response of the experiment is shown in Figure 5.5. In the first quarter of the total experiment time up until 1800 s, the current is relatively unstable, gradually growing over time with several peaks approaching more negative currents. The repeated experiment proved that those peaks are reproducible and can be linked to the processes taking place. It is suggested that the peaks in the first 1800 s are due to the set-up transitioning into a steady state. After about 2700 s the current more or less stabilizes, after which the current slightly decreases. It is known that Br⁻ resulting from the C-X bond cleavage can adsorb onto Ag, blocking the surface [46]. However, this is only effective at potentials more negative than -1.2 V vs SCE. Since the exact potential during the electrolysis cannot be determined due to the changes in the environment of the pseudo-reference, it is not possible to definitely designate the fluctuation to this event. A decreasing current as seen from 2700 s onwards can be expected, even at steady state electrolysis.
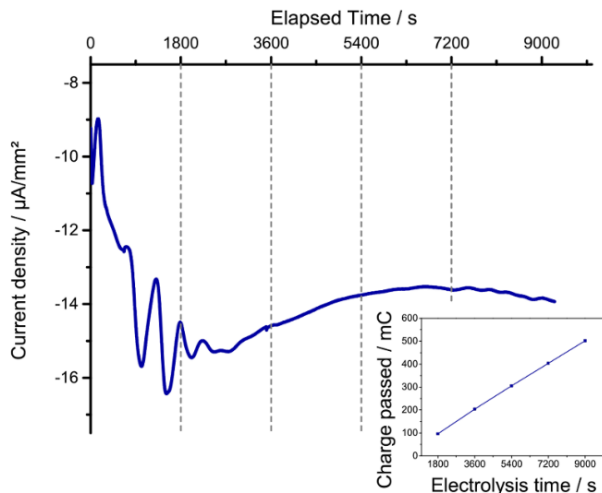
Figure 5.5. Current response of the potential controlled electrolysis in the EPR flat cell. 4mm^2 Ag WE, electrolyte = ACN + 0.1 M TBAP with 5 mM ABBE and 15 mM PBN. The dashed lines mark the 30 min (20 scans) periods over which the EPR scans are accumulated. Inset: cumulative charge passed during the electrolysis.

In correlation with the current response, a change in the CW-EPR spectrum over time is also observed. The scans were accumulated over a time period of 30 min or 20 scans at four points during the experiment (marked by the dashed lines in Figure 5.5) 20 scan accumulations were chosen to improve signal-to-noise (S/N) of the initial spectra. Clear changes in the spectral features over time can be observed in the CW-EPR spectra (normalized) (Figure 5.6). In the corresponding unnormalized spectra (Figure 5.7), an increase in the signal intensities over time is also observed. Also depicted in Figure 5.7 is the unnormalized spectrum of a potential controlled electrolysis experiment on a solution containing only PBN in ACN with *n*-Bu$_4$NClO$_4$ after 75 min. In this control experiment, a small EPR signal of an unknown PBN-trapped radical was also observed, but it was not present in the allyl 2-bromobenzyl ether experiments.

 As the changes in features and amount of splitting in the spectra suggest, all spectra are convoluted spectra of more than one species. All spectra agree with features expected for nitroxide radicals formed by trapping of a reactive organic radical with PBN [47]. The formed nitroxide radicals have a longer lifetime than the original radicals, which decayed too fast to be detected with CW EPR. The spectra can be interpreted in terms of an isotropic *g* value and the hyperfine interactions (*A*) between the unpaired electron and the magnetic nuclei in its vicinity. These parameters can be used as a unique fingerprint of the trapped radical. Due to the hyperfine interaction of the unpaired electron with the nitroxide ^{14}N nucleus (*I*=1), the room-temperature CW-EPR spectra of all nitroxide radicals consist of at least a triplet signal. Subsequent splitting of the three signals can occur through resolved hyperfine interaction with protons in the vicinity of the unpaired electron. The spectrum depicted in Figure 5.6A is a sum of a triplet (radical 1) and a triplet of doublets (radical 2). In the following spectrum, Figure 5.6B, the contribution of a third species emerges (radical 3). The EPR features of radical 3 are more pronounced in the third (Figure 5.6C) and fourth (Figure 5.6D) spectrum. All EPR spectra can be simulated in terms of these three contributions

(Figure 5.6), for which the parameters are listed in Table 5.1. From the simulations, the EPR spectrum of radical 3 was found to be a triplet of doublets of doublets of doublets. The individual EPR contributions of the three radicals are shown in Figure 5.6 E-G.
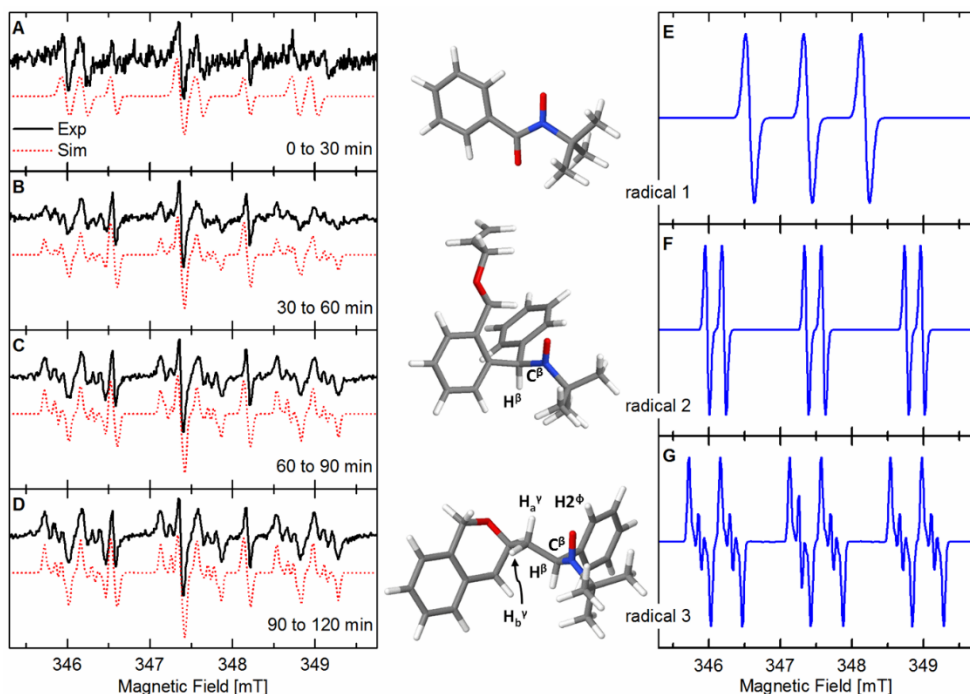

Figure 5.6: Accumulated experimental EPR spectra (black) and corresponding simulations (red) of the controlled-potential electrolysis of 5 mM ABBE + 15 mM PBN in ACN + 0.1 M TBAP (potential set at the peak potential of the reduction wave in the EPR flat cell, checked by in-situ CV) at different time intervals: 0-30 min, (A), 30-60 min (B), 60-90 min (C) and 90-120 min (D), and the simulated spectra and the molecular models derived from DFT calculations of radical 1/PBN-Ox (E), radical 2/PBN-allyl benzyl ether (F) and radical 3/PBN-4-methylisochromane (G). The spectra are shown normalized to allow easy comparison.

Based on the isotropic ^{14}N hyperfine coupling constant (22.66 MHz) of radical 1, it is assigned to benzoyl-*tert*-butyl nitroxide (PBN-Ox) (Figure 5.6) [47]. This species is often observed in PBN spin-trapping experiments, especially in the presence of oxygen [48]. Although the electrolyte was extensively deoxygenated during sample preparation and was under an argon atmosphere during the experiment, there still can be residual dioxygen in the electrolyte due to its high solubility in ACN (8.1 mM [49]). Alternatively, residual water in the ACN solvent (<150 ppm) can be oxidized at the counter electrode, and the generated dioxygen can diffuse to the working electrode part of the cell. Radicals 2 and 3 displayed ^{14}N and ^{1}H hyperfine couplings that are suggestive of carbon-centred radicals that have been spin-trapped such as the expected radical intermediates from reactions (3) and (4) in Figure 5.1. In order to assign radicals 2 and 3, DFT was used to compute the EPR parameters of the PBN spin-trapped allyl benzyl ether and 4-methylisochromane radicals.

Table 5.1 Experimental and calculated isotropic g and hyperfine coupling constants of the three spin-trapped radicals during the electrolysis of 5 mM ABBE + 15 mM PBN inACN + 0.1 M TBAP (potential set at the peak potential of the reduction wave in the EPR flat cell, checked by in-situ CV).

	radical 1		radical 2		radical 3	
	exp	*DFT*	*exp*	*DFT*	*exp*	*DFT*
g_{iso}	2.0069	2.0067	2.0063	2.0053	2.0062	2.0054
$A_{N\text{-}iso}$ [MHz]	22.66	22.53	39.09	40.35	39.53	43.17
$A_{H\beta}$ [MHz]	-	-	6.46	5.61	12.43	12.18
A_{H} [MHz] A_{H} [MHz]	- -	- -	- -	- -	4.03 2.19	1.43 $(A_{H2\varphi})$/ -0.82 $(A_{H a\gamma})$/ -0.94 $(A_{Hb\gamma})^{a}$

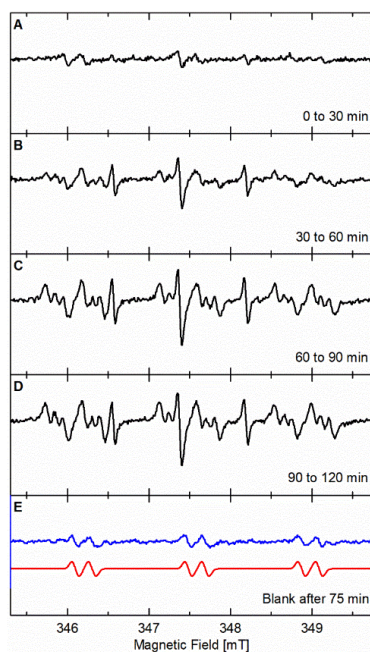*^{a} Possible assignments (see main text for details)*

Figure 5.7 Accumulated experimental EPR spectra (black, 20 scans) of the controlled potential electrolysis of allyl 2-bromobenzyl ether in ACN + 0.1 M TBAP at the peak potential of the reduction wave in the flat cell (-1 V vs pseudoref.) at different time intervals: 0-30 min, (A), 30-60 min (B), 60-90 min (C) and 90-120 min (D), and the spectrum (blue, 50 scans) and simulation (red) of a sample containing only PBN in ACN with n-Bu₄NClO₄ collected after 75 min of controlled potential electrolysis at -1 V vs the pseudoref. (E). The parameters for the simulation were g_{iso} =2.0057, $A_{N\text{-}iso}$ = 39.00 MHz, $A_{H\text{-}iso}$ = 5.8 MHz. (For interpretation of the references to colour in this figure legend, the reader is referred to the Web version of this article.)

5.5 DFT calculations

DFT calculations were used in order to identify the radical intermediates measured with spin-trap EPR. For this, several models of PBN-trapped radicals were considered. Their geometry was optimized, and the responding coordinates (see section 5.8, supplementary information) were then used for single-point computations and to estimate the EPR parameters.

5.5.1 Selection of the functionals and basis sets

As discussed in chapter 2, a good choice of functionals and basis sets plays an essential role in DFT. For the geometry optimizations, the Becke-Perdew density functionals (BP86) [50–52] and the split valence plus polarization (SVP) basis sets [40] were used for all atoms. In order to find the most accurate combination for the EPR calculations, different couples of functional and basis sets were benchmarked using standard nitroxide radicals (2,2,6,6-Tetramethylpiperidin-1-yl)oxyl (TEMPO) and 5,5-dimethyl-1-pyrroline N-oxide ($^{•}$DMPO)-OH, as well as the benzoyl-*tert*-butyl nitroxide (PBN-Ox) radical (Table 5.2). All three functional/basis sets that were tested reasonably predicted the g_{iso} values. The B3LYP/(6-31+G**) was found to be most accurate for calculating the hyperfine interactions (Figure 5.8), and thus was chosen for calculating the EPR parameters of the spin-trap radicals. Variations between different functional/basis sets and deviations from the exact experimental values are normal for DFT computations, but the observed trends are generally followed [53].
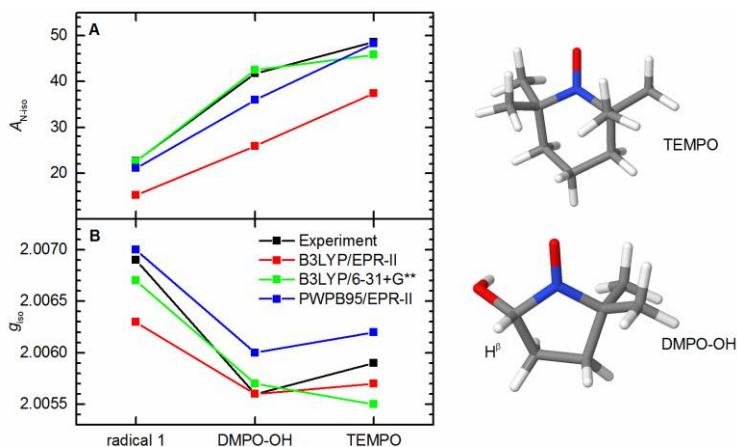

Figure 5.8 Comparisons of the trends in the $A_{N\text{-}iso}$ (A) and g_{iso} (B) between the experimental and calculated values using different functional/basis sets combinations and molecular models of TEMPO and DMPO-OH.

Table 5.2 Comparison between experimental and numerical EPR parameters from DFT calculations using different functional/basis sets combinations.

		PBN-Ox[a]	TEMPO[a]	DMPO-OH[b]
experimental	g_{iso}	2.0069	2.0059	2.0056
	$A_{N\text{-}iso}$ [MHz]	22.66	48.63	41.76
	$A_H{}^\beta$ [MHz]			41.76
B3LYP/EPR-II	g_{iso}	2.0063	2.0057	2.0056
	$A_{N\text{-}iso}$ [MHz]	15.14	37.047	25.90
	$A_H{}^\beta$ [MHz]			37.03
	$A_{CH_3}{}^{AVG}$ [MHz][c]	0.46	-0.54,-0.66	
B3LYP/6-31+G**	g_{iso}	2.0067	2.0055	2.0057
	$A_{N\text{-}iso}$ [MHz]	22.53	45.85	42.52
	$A_H{}^\beta$ [MHz]			35.30
	$A_{CH_3}{}^{AVG}$ [MHz][c]	0.46	-0.53,-0.53	
PWPB95/EPRII	g_{iso}	2.0070	2.0062	2.0060
	$A_{N\text{-}iso}$ [MHz]	21.07	48.32	35.96
	$A_H{}^\beta$ [MHz]			35.44
	$A_{CH_3}{}^{AVG}$ [MHz][c]	-0.03	-1.32,-0.79	

[a] *this work*

[b] *experimental values from* [54] *and DFT own work*

[c] *In solution, the hyperfine coupling of protons on methyl and tert-butyl groups are generally small and unresolved, owning to the free rotation around sp^3 C-C bonds that averages their contributions.*

5.5.2 DFT calculation of EPR parameters for PBN-4-methylisochromane and PBN-allylbenzyl ether.

The geometry-optimized models of PBN-Ox, PBN-allyl benzyl ether, and PBN-4-methylisochromane are depicted in Figure 5.6. Compared to PBN-Ox, the latter two PBN-adducts have greater degrees of freedom. To account for this, selected bonds close to the nitroxide moiety were manually rotated without subsequent relaxation of the system. Rotation around the N-C^β bond had the most significant impact on the EPR parameters calculated from the molecular models. Figure 5.9 shows the computed single-point energy values as a function of the rotational dihedral angles around the N-C^β bond and the corresponding EPR parameters. Since the EPR experiments have been performed in the liquid phase at room temperature, the thermal energy ($k_B T = 25.7\ meV\ at\ 298\ K$) will allow some rotations around the flexible bonds. Due to molecular motions in the fast motion regime, the EPR experiment will reflect the average of the EPR parameters of all rotamers that can be thermally accessed. The EPR parameters were therefore averaged in the range marked in pink (Figure 5.9), denoting the allowed rotational angle range. The computed EPR parameters for PBN-4-methylisochromane and PBN-allyl benzyl ether are comparable to radicals 2 and 3, respectively (Table 5.1), and thus are assigned accordingly. The g_{iso}-values are reasonably predicted for both radicals. For radical 2, the experimental and calculated hyperfine coupling values are in good agreement (Table 5.1). These are assigned to the

expected isotropic ^{14}N hyperfine interaction and the interactions between the unpaired electron and the H^β proton (see Figure 5.6 for proton assignment). For radical 3, the experimental and calculated values for the isotropic ^{14}N and H^β proton hyperfine interactions are also in good agreement. Two further ^{1}H interactions (4.03 and 2.19 MHz) are also used in the simulation of the spectrum of radical 3. After the isotropic ^{14}N and H^β proton, the next largest calculated hyperfine interactions are $A_{H2\phi}$ (1.43 MHz), $A_{Hb\gamma}$ protons (-0.94 MHz) and $A_{Ha\gamma}$ (-0.82 MHz). Two of these are likely candidates for the unattributed couplings in the spectrum of radical 3. However, the calculated values are close in magnitude and somewhat smaller than the experiment preventing definitive assignments.
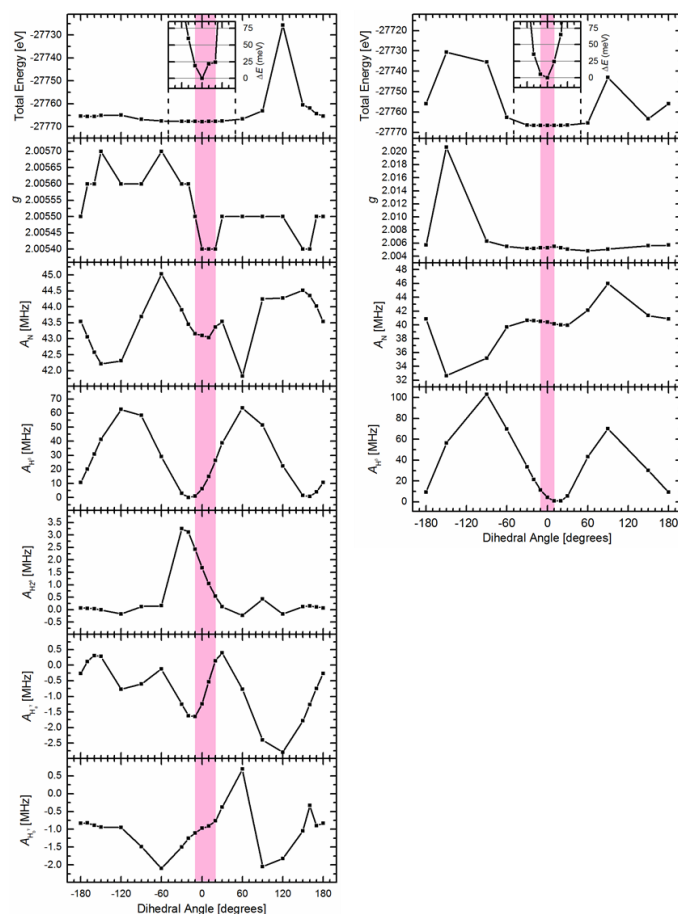

Figure 5.9: Evolution of the total energy (A), and EPR parameters g_{iso} (B), A_{N-iso} (C), A_H^β (D), A_{H2}^ϕ (E), A_{Ha}^γ (F) and A_{Hb}^γ (G) as a function of the dihedral angle manually rotated around the N-C^β bond for PBN-4-methylisochromane from calculations using B3LYP/EPR-II functional/basis set; the corresponding values for PBN-allylbenzyl ether (A' to D'); magnification of the region near the lowest energy (insets). The bands shade in pink indicates the dihedral angles which are thermally allowed at 298 K.

5.6 The reaction evolution

As shown in Figure 5.6, the three PBN-trapped radicals are not all present at each time interval. The relative weight of each radical in the spectrum correlates linearly with their relative concentration and can be plotted versus the elapsed time to visualize their evolution (Figure 5.10). The presence of the PBN-Ox increases with time, then plateaus, suggesting that the electrolytic generation of this species is exhaustive or that it reaches steady-state between PBN-Ox decay and spin-trapping reactions. Considering the very low concentration of residual dioxygen/water, exhaustive electrolysis is plausible. The concentration of PBN-allyl benzyl ether appears to decrease between the first and second time intervals. This change is small and may be due to the poor S/N of the first spectrum. Considering the few data points, it is assumed that this decrease is insignificant within the experimental error. From the second time interval to the remainder of the experiment, the concentration of PBN-allyl benzyl ether remains constant. PBN-4-methylisochromane, which arises from the spin-trapping of the radical intermediate from the intramolecular cyclisation of the allyl benzyl ether radical, is the most abundant product over time. This is expected as the experimental conditions favoured its formation. There is a strong increase in the concentration of PBN-4-methylisochromane in the beginning, which starts to plateaus in the last time interval.
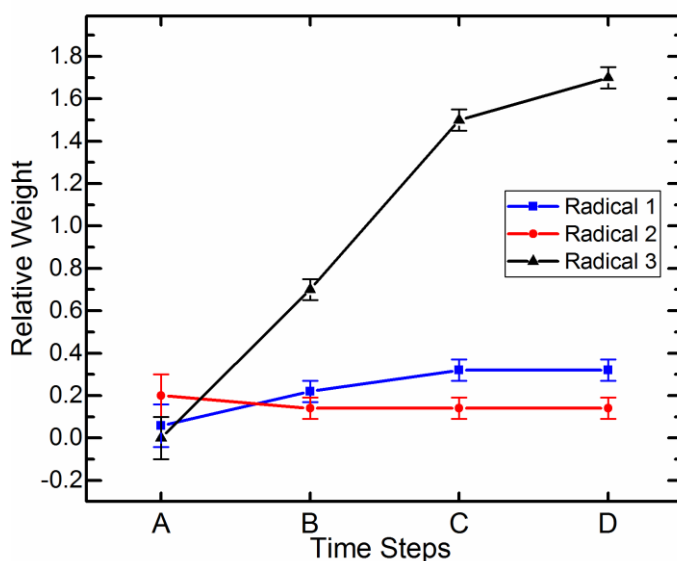

Figure 5.10: Relative weight of each radical in the different EPR spectra depicted in Figure 5.6, Figure 5.7

The data suggests that the cyclisation intermediate (4-methylisochromane radical) is not present during the first time interval, which is unexpected considering the precursor intermediate (allyl benzyl ether radical) is formed. However, it should be noted that the intermediates are not detected directly and that an extra spin-trapping reaction step is needed for detection. The reactivity of PBN with different radicals can vary [55], and thus the formation of certain radicals can be masked. It is possible that PBN-Ox is

formed much more easily than PBN-4-methylisochromane. Alternately, the 4-methylisochromane radical generated is reacting with the fast diffusing residue oxygen in the initial stages, which yields PBN-Ox after subsequent decay/reaction steps. Due to the geometry of the thin cell, natural convection quickly sets in. Over time the oxygen species becomes exhausted and more of the target radical will be spin-trapped and becomes detectable in the spectra. This appears to follow the course of the current in Figure 5.5 where after the first time interval, the current starts to stabilize (no longer strongly influenced by the dioxygen/water species), after which PBN-4-methylisochromane emerges in the subsequent spectra. In addition, the S/N is lower in the beginning, possibly masking the spectral features of a low amount of the PBN-4-methylisochromane. This correlates with the previous results of an electrochemical investigation [28] which shows that product distribution is not time-dependent and that the cyclisation product is formed at any point during the electrolysis. The concentration of the allyl benzyl ether radical remains almost constant throughout the electrolysis while the concentration of the 4-methylisochromane radical increases. This implies that the intramolecular cyclisation to 4-methylisochromane is faster or easier than the spin-trapping reaction. A possible cause is the difference in the adsorption strength of the radicals. The allyl benzyl ether radical could be strongly adsorbed on the surface, while the 4-methylisochromane radical is more easily desorbed due to the cyclisation, which breaks the Ag-radical bond. Since the trapping reaction with PBN happens in solution, the 4-methylisochromane will undergo this more easily, resulting in a larger concentration of trapped radicals. Furthermore, the decomposition of the trapped radicals plays a role. The stability of the trapped radicals may be different for the different adducts, which can lead to differences in the accumulated concentrations. A less stable radical reaches a steady-state concentration much faster.

5.7 Conclusion

Employing a platform for combined EPR and electrochemical measurements to elucidate mechanisms remains underexploited in electrocatalytic research. In this work, this approach is validated on a model reaction, and for the first time, the proposed mechanism for the reductive cyclisation of allyl 2-bromobenzyl ether to 4-methylisochromane was confirmed. Both the allyl benzyl ether radical and the 4-methylisochromane radical intermediates could be detected by spin-trapping and identified with the help of DFT calculations. As expected, the target cyclic radical was the most abundant product. The experiments show the strength of combining *in-situ* spin trap EPR with electrochemistry to unravel reaction pathways in electrocatalysis.
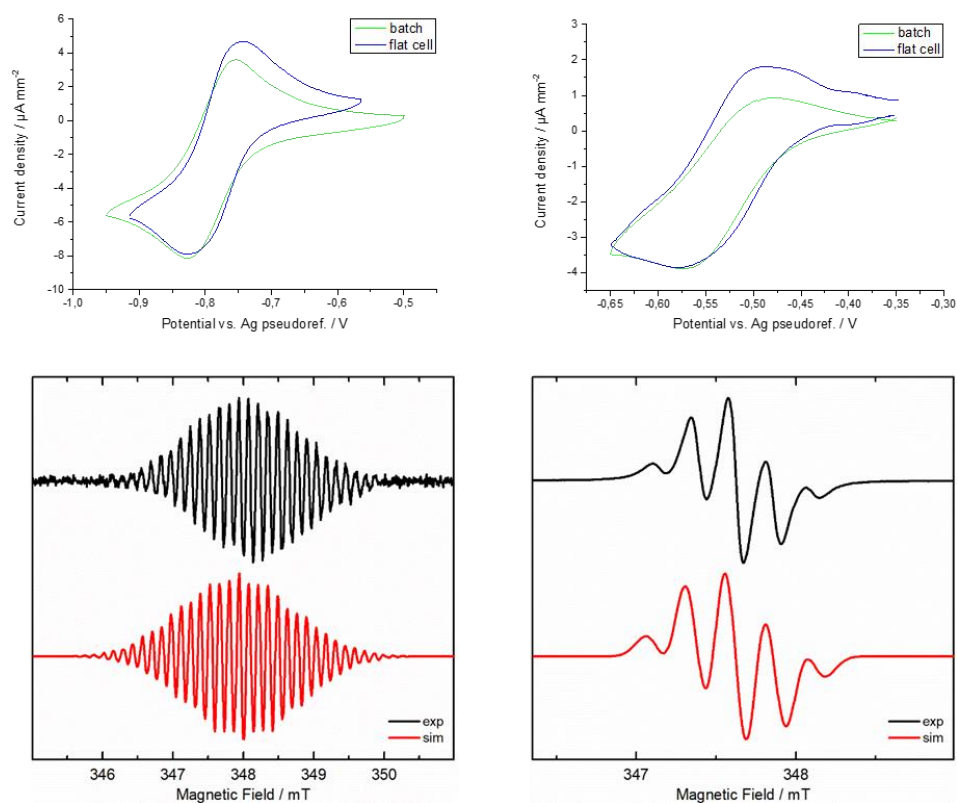
5.8 Supporting information

Figure S5.1.Cyclic voltammogram for the reduction of methyl viologen in H_2O + 0.2 M Na_2SO_4 (A) and in ACN + 0.1 M n-Bu_4NClO_4 (B) in both a standard batch cell and an EPR flat cell. EPR spectrum (black) recorded during electrolysis of methyl viologen (MV^{2+}) in H_2O + 0.2 M Na_2SO_4 and simulation in red (C) and EPR spectrum (black) recorded during electrolysis of benzoquinone in ACN + 0.1 M n-Bu_4NClO_4 and simulation in red (D). The spectra of the one-electron reduced species $MV^{+}$was simulated using the parameters: $A_{N\,iso}$ = 11.80 MHz (2N), A_H = 11.15 MHz (6H), A_H = 4.49 MHz (4H), A_H = 3.74 MHz (4H), which were comparable to those found in the literature [56]. The spectra of para-benzoquinone radical anion were simulated using the parameters: A_H = 6.78 MHz (4H), A_C = 6.00 MHz (1C), which were comparable to those found in literature [57]

Table S5.1. The optimized Geometries of the models for the radicals (in Å)

PBN-Ox (radical 1)

C	0.83334	-2.426262	-0.000411
C	0.895578	-1.006943	-0.000527
C	2.174021	-0.391232	-0.000153
C	1.997887	-3.203026	0.000096
C	3.259871	-2.579733	0.000441
C	3.338673	-1.176829	0.000271
C	-0.451269	-0.333573	-0.001141
O	-1.496104	-0.993588	-0.001771
N	-0.559165	1.101218	-0.00001
C	-1.940367	1.791462	0.00011
C	-1.676918	3.303862	-0.000052
C	-2.704507	1.395495	-1.280183
C	-2.704139	1.395717	1.280703
O	0.472418	1.837996	0.000573
H	-0.156123	-2.905361	-0.000743
H	2.25197	0.699955	-0.00026
H	1.921916	-4.301354	0.00021
H	4.178483	-3.186983	0.000789
H	4.321506	-0.680507	0.000506
H	-2.656334	3.821441	0.00002
H	-1.112402	3.623102	0.896748
H	-1.1126	3.622948	-0.897032
H	-3.653936	1.966699	-1.319184
H	-2.115311	1.652011	-2.183901
H	-2.940829	0.316997	-1.29867
H	-3.653841	1.966473	1.319615
H	-2.939906	0.317119	1.299747
H	-2.114911	1.652897	2.184207

PBN-allylbenzyl ether (radical 2)

C	-1.999244	-2.590714	-0.623569
C	-1.322674	-3.819311	-0.551555
C	0.575746	-2.837148	-1.705074
C	-0.102943	-1.606905	-1.777797
C	-1.396132	-1.469735	-1.23584
C	-0.029883	-3.947076	-1.092506
C	-2.204354	-0.168406	-1.333117

N	-1.507217	0.872787	-2.131364
O	-0.572078	1.543117	-1.565699
C	-1.967652	1.346505	-3.496559
C	-0.701397	1.537489	-4.356
C	-2.896556	0.321029	-4.165216
C	-2.690403	2.696601	-3.296703
C	-2.720381	0.395246	0.001701
C	-4.073652	0.800754	0.028638
C	-4.659674	1.365138	1.172769
C	-3.879482	1.531001	2.327447
C	-2.53527	1.124859	2.321832
C	-1.934144	0.554602	1.178473
C	-0.486531	0.108942	1.263722
O	0.146417	0.71219	2.388048
C	1.479255	0.246629	2.604443
C	1.540408	-1.16308	3.140231
C	2.29907	-2.148155	2.625763
H	-3.012265	-2.500717	-0.199136
H	-1.80967	-4.683119	-0.072223
H	1.587621	-2.924628	-2.130949
H	0.384777	-0.741622	-2.249483
H	0.502247	-4.909479	-1.036303
H	-3.1111	-0.422548	-1.911981
H	-0.976739	1.977366	-5.33468
H	0.011204	2.212838	-3.847177
H	-0.198372	0.566285	-4.53978
H	-3.092964	0.648486	-5.205524
H	-2.432332	-0.684722	-4.213019
H	-3.880662	0.239882	-3.661939
H	-2.977374	3.128117	-4.276737
H	-3.610141	2.571377	-2.69004
H	-2.021006	3.410168	-2.777067
H	-4.686147	0.666893	-0.877968
H	-5.717662	1.669372	1.158394
H	-4.315735	1.972601	3.237295
H	-1.916169	1.247546	3.221519
H	-0.442263	-1.004911	1.340613
H	0.040277	0.391157	0.325433
H	2.088526	0.333601	1.672538

H	1.908433	0.947289	3.353383
H	0.917401	-1.354475	4.034246
H	2.331162	-3.151807	3.080199
H	2.924723	-1.983313	1.731315

PBN-4-methylisochromane
(Radical 3)

C	1.029692	-2.261271	0.3991
C	2.268594	-2.901064	0.212957
C	3.45504	-2.147474	0.199326
C	3.394384	-0.75154	0.372131
C	2.156528	-0.112893	0.55197
C	0.958219	-0.861919	0.567668
C	-0.394969	-0.17193	0.752759
N	-0.427219	0.627878	2.011185
O	0.13645	1.780305	1.991813
C	-0.739444	0.044523	3.373153
C	-1.582753	1.099006	4.118574
C	-1.528269	-1.267224	3.25178
C	0.598942	-0.190914	4.107334
C	-0.781084	0.752297	-0.423631
C	-0.894741	0.03061	-1.77923
O	-0.850553	0.958022	-2.879584
C	-1.923663	1.893188	-2.907748
C	-3.290633	1.288273	-2.641088
C	-3.398169	-0.030511	-2.140025
C	-2.142538	-0.855888	-1.933229
C	-4.457181	2.052966	-2.854473
C	-5.726021	1.517944	-2.584164
C	-5.837667	0.205917	-2.084677
C	-4.679813	-0.555803	-1.863606
H	0.104368	-2.860466	0.409223
H	2.30487	-3.993674	0.079537
H	4.426392	-2.646057	0.055706
H	4.320303	-0.154994	0.366532
H	2.111856	0.976447	0.703593
H	-1.16653	-0.957325	0.859053
H	-1.766782	0.767998	5.159822
H	-1.050432	2.068492	4.13983

H	-2.562187	1.245524	3.619278
H	-1.791869	-1.615486	4.270334
H	-2.476236	-1.130048	2.692877
H	-0.938803	-2.073825	2.772907
H	0.410988	-0.524163	5.147816
H	1.203376	-0.966435	3.595797
H	1.183072	0.749678	4.135476
H	-1.738916	1.251236	-0.164393
H	-0.01493	1.547707	-0.516457
H	0.01169	-0.592944	-1.921862
H	-1.899091	2.352613	-3.9183
H	-1.746265	2.725994	-2.182091
H	-1.988091	-1.520737	-2.811397
H	-2.264625	-1.531852	-1.060743
H	-4.367131	3.081633	-3.241671
H	-6.628707	2.123216	-2.762056
H	-6.828544	-0.221592	-1.865074
H	-4.764909	-1.581438	-1.468032

TEMPO

O	-1.800226	-1.132621	-0.472929
N	-0.661718	-0.60076	-0.20991
C	1.666463	0.780404	0.803625
C	0.963651	1.29515	-0.454318
C	-0.516899	0.863658	-0.556201
C	-1.009538	1.037832	-2.005168
C	-1.416636	1.68662	0.396025
C	1.626497	-0.749195	0.809137
C	0.194541	-1.330567	0.799828
C	-0.475953	-1.214895	2.189241
C	0.237989	-2.809874	0.372815
H	1.190085	1.192066	1.719654
H	1.50674	0.912547	-1.346284
H	1.000674	2.403196	-0.514011
H	-0.411231	0.414324	-2.700363
H	-2.072079	0.745116	-2.096981
H	-0.901593	2.098603	-2.307779
H	-1.469191	2.739192	0.05155
H	-2.440495	1.263117	0.396767

H	-1.037051	1.686763	1.436632
H	2.15739	-1.164908	1.691202
H	2.166456	-1.121856	-0.08891
H	-0.4303	-0.184333	2.592734
H	-1.53996	-1.514502	2.113256
H	0.030433	-1.887046	2.911126
H	0.874197	-3.380327	1.078693
H	-0.777283	-3.248412	0.370553
H	0.667862	-2.911851	-0.644458
H	2.719175	1.131556	0.819474

DMPO-OH

C	-0.633335	-0.460217	-0.246221
C	1.595974	0.104601	-0.676498
C	0.996299	1.155199	0.284662
C	-0.538597	0.979566	0.17485
O	-1.734518	-1.102487	-0.294704
C	-1.165221	1.851591	-0.932568
C	-1.282213	1.169225	1.504292
C	0.667086	-1.100501	-0.543121
O	1.096065	-1.927972	0.52455
H	2.638645	-0.169745	-0.4257
H	1.581804	0.464877	-1.724934
H	1.313278	2.187701	0.039681
H	1.320053	0.939172	1.323004
H	-0.600809	1.767745	-1.88328
H	-2.208875	1.527098	-1.118988
H	-1.176157	2.916552	-0.625247
H	-1.224142	2.226905	1.830504
H	-2.349515	0.894595	1.386594
H	-0.842199	0.530911	2.296843
H	0.540963	-1.690375	-1.47894
H	0.457416	-2.66744	0.589222

5.9 References

[1] H. J. Schäfer, *Contributions of Organic Electrosynthesis to Green Chemistry*, Comptes Rendus Chim. **14**, 745 (2011).

[2] E. Duñach, M. José Medeiros, and S. Olivero, *Intramolecular Reductive Cyclisations Using Electrochemistry: Development of Environmentally Friendly Synthetic Methodologies*, New J. Chem. **30**, 1534 (2006).

[3] C. Durante, B. Huang, A. A. Isse, and A. Gennaro, *Electrocatalytic Dechlorination of Volatile Organic Compounds at Copper Cathode. Part II: Polychloroethanes*, Appl. Catal. B Environ. **126**, 355 (2012).

[4] C. Durante, V. Perazzolo, A. A. Isse, M. Favaro, G. Granozzi, and A. Gennaro, *Electrochemical Activation of Carbon-Halogen Bonds: Electrocatalysis at Palladium-Copper Nanoparticles*, ChemElectroChem **1**, 1370 (2014).

[5] C. Durante, A. A. Isse, G. Sandonà, and A. Gennaro, *Electrochemical Hydrodehalogenation of Polychloromethanes at Silver and Carbon Electrodes*, Appl. Catal. B Environ. **88**, 479 (2009).

[6] A. A. Isse, S. Gottardello, C. Durante, and A. Gennaro, *Dissociative Electron Transfer to Organic Chlorides: Electrocatalysis at Metal Cathodes*, Phys. Chem. Chem. Phys. **10**, 2409 (2008).

[7] D. F. Niu, L. P. Xiao, A. J. Zhang, G. R. Zhang, Q. Y. Tan, and J. X. Lu, *Electrocatalytic Carboxylation of Aliphatic Halides at Silver Cathode in Acetonitrile*, Tetrahedron **64**, 10517 (2008).

[8] M. M. Burbuliene, V. Jakubkiene, G. Mekuskiene, E. Udrenaite, R. Smicius, and P. Vainilavicius, *Synthesis and Anti-Inflammatory Activity of Derivatives of 5-[(2-Disubstitutedamino-6-Methyl-Pyrimidin-4-Yl)-Sulfanylmethyl]-3H-1,3,4-Oxadiazole-2-Thiones*, Farm. **59**, 767 (2004).

[9] L. Pieters, S. Van Dyck, M. Gao, R. Bai, E. Hamel, A. Vlietinck, and G. Lemière, *Synthesis and Biological Evaluation of Dihydrobenzofuran Lignans and Related Compounds as Potential Antitumor Agents That Inhibit Tubulin Polymerization*, J. Med. Chem. **42**, 5475 (1999).

[10] H. F. Roaiah, S. S. El-nakkady, W. S. El-serwy, M. A. A. Ali, and A. H. A. El-rahman, *Studies on Some Benzopyran Derivatives with Expected Antimicrobial and Antiviral Activity*, Nat. Sci. **8**, 20 (2010).

[11] E. Ayranci and N. Hoda, *Adsorption Kinetics and Isotherms of Pesticides onto Activated Carbon-Cloth*, Chemosphere **60**, 1600 (2005).

[12] A. S. Shawali, *Synthesis and Tautomerism of Aryl- and Hetaryl-Azo Derivatives of Bi- and Tri-Heterocycles*, J. Adv. Res. **1**, 255 (2010).

[13] K. Majumdar, G. Karunakar, and B. Sinha, *Formation of Five- and Six-Membered Heterocyclic Rings under Radical Cyclization Conditions*, Synthesis (Stuttg). **44**, 2475 (2012).

[14] R. Francke and R. D. Little, *Redox Catalysis in Organic Electrosynthesis: Basic Principles and Recent Developments*, Chem. Soc. Rev. **43**, 2492 (2014).

[15] H. Lund and O. Hammerich, *Organic Electrochemistry*, 4th ed. (Marcel Dekker, Inc., 1991).

[16] D. Pletcher and F. C. Walsh, *Industrial Electrochemistry*, 2nd ed. (Chapman

and Hall, London, 1990).

[17] A. A. Isse, G. Berzi, L. Falciola, M. Rossi, P. R. Mussini, and A. Gennaro, *Electrocatalysis and Electron Transfer Mechanisms in the Reduction of Organic Halides at Ag*, J. Appl. Electrochem. **39**, 2217 (2009).

[18] C. Bellomunno, D. Bonanomi, L. Falciola, M. Longhi, P. R. Mussini, L. M. Doubova, and G. Di Silvestro, *Building up an Electrocatalytic Activity Scale of Cathode Materials for Organic Halide Reductions*, **50**, 2331 (2005).

[19] P. Poizot and J. Simonet, *Silver-Palladium Cathode: Selective One-Electron Scission of Alkyl Halides: Homo-Coupling and Cross-Coupling Subsequent Reactions*, Electrochim. Acta **56**, 15 (2010).

[20] J. Simonet, *The One-Electron Reduction of Primary Alkyl Iodides at Palladium and Palladiated Surfaces: A Facile Source of Alkyl Radicals?*, Electrochem. Commun. **7**, 74 (2005).

[21] B. Geboes, B. Vanrenterghem, J. Ustarroz, D. Pauwels, S. Sotiropoulos, A. Hubin, and T. Breugelmans, *Influence of the Morphology of Electrodeposited Nanoparticles on the Activity of Organic Halide Reduction*, Chem. Eng. Trans. **41**, 73 (2014).

[22] B. Vanrenterghem, B. Geboes, S. Bals, J. Ustarroz, A. Hubin, and T. Breugelmans, *Influence of the Support Material and the Resulting Particle Distribution on the Deposition of Ag Nanoparticles for the Electrocatalytic Activity of Benzyl Bromide Reduction*, Appl. Catal. B Environ. **181**, 542 (2016).

[23] A. . Esteves, A. . Freitas, M. . Medeiros, and D. Pletcher, *Reductive Intramolecular Cyclisation of Unsaturated Halides by Ni(II) Complexes*, J. Electroanal. Chem. **499**, 95 (2001).

[24] X. Chaminade, E. Duñach, A. P. Esteves, M. J. Medeiros, C. S. Neves, and S. Olivero, *Electrosynthesis of Nitrogen Heterocycles Using Environmentally Friendly Methodologies*, Electrochim. Acta **54**, 5120 (2009).

[25] S. Olivero, J. C. Clinet, and E. Duñach, *Electrochemical Intramolecular Reductive Cyclisation Catalysed by Electrogenerated Ni(Cyclam)2+*, Tetrahedron Lett. **36**, 4429 (1995).

[26] E. Duñach, a. P. Esteves, M. J. Medeiros, D. Pletcher, and S. Olivero, *The Study of Nickel(II) and Cobalt(II) Complexes with a Chiral Salen Derivative as Catalysts for the Electrochemical Cyclisation of Unsaturated 2-Bromophenyl Ethers*, J. Electroanal. Chem. **566**, 39 (2004).

[27] E. Duñach, A. P. Esteves, M. J. Medeiros, C. S. dos Santos Neves, and S. Olivero, *Radical-Type Reactions in Protic and Aprotic Media: Comparisons in Nickel-Catalysed Electrochemical Reductive Cyclisations*, Comptes Rendus Chim. **12**, 889 (2009).

[28] B. Vanrenterghem and T. Breugelmans, *An Activity Scale of Cathode Materials for the Electrochemical Cyclisation of Allyl 2-Bromobenzyl Ether*, Electrochim. Acta **234**, 28 (2017).

[29] D. Pauwels, H. Y. Vincent Ching, M. Samanipour, S. Neukermans, J. Hereijgers, S. Van Doorslaer, K. De Wael, and T. Breugelmans, *Identifying Intermediates in the Reductive Intramolecular Cyclisation of Allyl 2-Bromobenzyl Ether by an Improved Electron Paramagnetic Resonance Spectroelectrochemical Electrode Design Combined with Density Functional*

Theory Calculations, Electrochim. Acta **271**, 10 (2018).

[30] D. Pauwels, Electrosynthesis as an Environmentally Friendly Production Method: Screening Methodology towards Upscaling, University of Antwerp, 2018.

[31] L. H. Piette, P. Ludwig, and R. N. Adams, *Electron Paramagnetic Resonance and Electrochemistry. Studies of Electrochemically Generated Radical Ions in Aqueous Solution.*, Anal. Chem. **34**, 916 (1962).

[32] S. Stoll and A. Schweiger, *EasySpin, a Comprehensive Software Package for Spectral Simulation and Analysis in EPR*, J. Magn. Reson. **178**, 42 (2006).

[33] F. Neese, *Prediction of Electron Paramagnetic Resonance g Values Using Coupled Perturbed Hartree-Fock and Kohn-Sham Theory*, J. Chem. Phys. **115**, 11080 (2001).

[34] F. Neese, *Theoretical Study of Ligand Superhyperfine Structure. Application to Cu(II) Complexes*, J. Phys. Chem. A **105**, 4290 (2001).

[35] F. Neese, *Metal and Ligand Hyperfine Couplings in Transition Metal Complexes: The Effect of Spin-Orbit Coupling as Studied by Coupled Perturbed Kohn-Sham Theory*, J. Chem. Phys. **118**, 3939 (2003).

[36] F. Neese, *Efficient and Accurate Approximations to the Molecular Spin-Orbit Coupling Operator and Their Use in Molecular g-Tensor Calculations*, J. Chem. Phys. **122**, 034107 (2005).

[37] S. Sinnecker, A. Rajendran, A. Klamt, M. Diedenhofen, and F. Neese, *Calculation of Solvent Shifts on Electronic g -Tensors with the Conductor-Like Screening Model (COSMO) and Its Self-Consistent Generalization to Real Solvents (Direct COSMO-RS)*, J. Phys. Chem. A **110**, 2235 (2006).

[38] A. D. Becke, *Density-Functional Exchange-Energy Approximation with Correct Asymptotic Behavior*, Phys. Rev. A **38**, 3098 (1988).

[39] J. P. Perdew, *Erratum: Density-Functional Approximation for the Correlation Energy of the Inhomogeneous Electron Gas*, Phys. Rev. B **34**, 7406 (1986).

[40] A. Schäfer, H. Horn, and R. Ahlrichs, *Fully Optimized Contracted Gaussian Basis Sets for Atoms Li to Kr*, J. Chem. Phys. **97**, 2571 (1992).

[41] P. J. Stephens, F. J. Devlin, C. F. Chabalowski, and M. J. Frisch, *Ab Initio Calculation of Vibrational Absorption and Circular Dichroism Spectra Using Density Functional Force Fields*, J. Phys. Chem. **98**, 11623 (1994).

[42] D. Moran, A. C. Simmonett, F. E. Leach, W. D. Allen, P. V. R. Schleyer, and H. F. Schaefer, *Popular Theoretical Methods Predict Benzene and Arenes to Be Nonplanar*, J. Am. Chem. Soc. **128**, 9342 (2006).

[43] L. Goerigk and S. Grimme, *Efficient and Accurate Double-Hybrid-Meta-GGA Density Functionals- Evaluation with the Extended GMTKN30 Database for General Main Group Thermochemistry, Kinetics, and Noncovalent Interactions*, J. Chem. Theory Comput. **7**, 291 (2011).

[44] V. BARONE, *Structure, Magnetic Properties and Reactivities of Open-Shell Species From Density Functional and Self-Consistent Hybrid Methods*, in *Recent Advances in Density Functional Methods* (1995), 287–334.

[45] G. L. McIntire, H. N. Blount, H. J. Stronks, R. V. Shetty, and E. G. Janzen, *Spin Trapping in Electrochemistry. 2. Aqueous and Nonaqueous Electrochemical Characterizations of Spin Traps*, J. Phys. Chem. **84**, 916 (1980).

[46] T. Wandlowski, J. X. Wang, and B. M. Ocko, *Adsorption of Bromide at the Ag(100) Electrode Surface*, J. Electroanal. Chem. **500**, 418 (2001).

[47] G. R. Buettner, *Spin Trapping - Electron-Spin-Resonance Parameters of Spin Adducts*, Free Radic. Bio. Med. **3**, 259 (1987).

[48] M. C. R. Symons, E. Albano, T. F. Slater, and A. Tomasi, *Radiolysis of Tetrachloromethane*, J. Chem. Soc. Faraday Trans. 1 Phys. Chem. Condens. Phases **78**, 2205 (1982).

[49] J. M. Achord and C. L. Hussey, *Determination of Dissolved Oxygen in Nonaqueous Electrochemical Solvents Determination of Dissolved Oxygen in Nonaqueous Electrochemical Solvents*, Anal. Chem. **52**, 601 (2002).

[50] J. P. Perdew, *Density-Functional Approximation for the Correlation Energy of the Inhomogeneous Electron Gas*, Phys. Rev. B **33**, 8822 (1986).

[51] J. P. Perdew, *Density-Functional Approximation for the Correlation Energy of the Inhomogeneous Electron Gas*, Phys. Rev. B **33**, 8822 (1986).

[52] A. D. Becke, *Density-Functional Exchange-Energy Approximation with Correct Asymptotic Behavior*, Phys. Rev. A **38**, 3098 (1988).

[53] F. Neese, *Prediction of Molecular Properties and Molecular Spectroscopy with Density Functional Theory: From Fundamental Theory to Exchange-Coupling*, Coord. Chem. Rev. **253**, 526 (2009).

[54] G. M. Rosen, A. Beselman, P. Tsai, S. Pou, C. Mailer, K. Ichikawa, B. H. Robinson, R. Nielsen, H. J. Halpern, and A. D. MacKerell, *Influence of Conformation on the EPR Spectrum of 5,5-Dimethyl-1-Hydroperoxy-1-Pyrrolidinyloxyl: A Spin Trapped Adduct of Superoxide*, J. Org. Chem. **69**, 1321 (2004).

[55] P. B. McCay, E. K. Lai, J. L. Poyer, C. M. DuBose, and E. G. Janzen, *Oxygen- and Carbon-Centered Free Radical Formation during Carbon Tetrachloride Metabolism. Observation of Lipid Radicals in Vivo and in Vitro.*, J. Biol. Chem. **259**, 2135 (1984).

[56] W. . Dunham, J. . Fee, L. . Harding, and H. . Grande, *Application of Fast Fourier Transforms to EPR Spectra of Free Radicals in Solution*, J. Magn. Reson. **40**, 351 (1980).

[57] E. W. Stone and A. H. Maki, *Electron Spin Resonance of Semiquinones in Aprotic Solvents*, J. Chem. Phys. **36**, 1944 (1962).

Re-evaluating the electrochemical self-condensation of acetone by EPR and DFT

This chapter investigates the self-condensation of acetone towards diacetone alcohol. Several reaction conditions can lead to the diacetone alcohol, both chemically and electrochemically. The mechanism for the electroreduction of acetone was investigated here, using a combination of electrochemistry and *in-situ* spin trap EPR. The hypothesised mechanisms from the literature are compared with the experimental data, and the presence of O_2 is shown to activate acetone at lower overpotentials through the oxygen reduction reaction. DFT calculations support the proposed mechanisms based on the experimental data. This chapter contains a collaboration with the ELCAT group at the University of Antwerp.

Own contribution: Performing and analysing *in-situ* EPR experiments; DFT calculations and analysis.

6.1 Introduction

Acetone is a broadly used chemical solvent and reagent which can serve as a feedstock for higher C-products through C-C bond formation, for instance, via self-condensation [1–4]. The initial product formed during the self-condensation of acetone is 4-hydroxy-4-methyl-pentane-2-one, also known as diacetone alcohol (DAA) [5]. The chemical structures of acetone and DAA are shown in Figure 6.1. Dehydration of DAA results in the formation of mesityl oxide [6], a precursor to methyl isobutyl ketone, which has a great number of industrial applications [7]. Conventionally, ketones can be chemically condensated with aldehydes by using homogeneous catalysts like H_2SO_4 and alkali metal bases [8,9]. Both of these options have downsides on the industrial scale because of the homogeneous nature and the harsh reaction conditions, requiring catalyst separation and corrosion-protective measures for the reactor. Therefore, several studies have focused on the performance of heterogeneous catalysts for these transformations by using fixed-bed reactors employing bases like $Ba(OH)_2$ and $Ca(OH)_2$ and various metal oxides with strong basic sites like MgO, BaO, SrO, La_2O_3, ZrO_2, *etc*. [10–18].
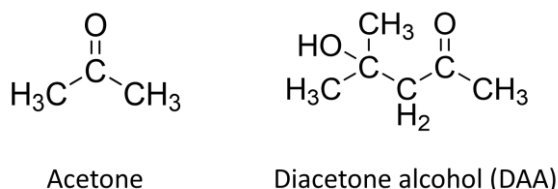
Figure 6.1 Chemical structures of acetone (left) and diacetone alcohol (DAA) (right)

Electrosynthesis combines the benefits of heterogeneous catalysis with mild reaction conditions and usually high selectivity due to the precise control over the electrode potential. Reports on the electrochemically induced condensation of aldehydes and ketones are abundant in aqueous solutions [19–24], organic solvents [25], such as DMF [26–28], DMSO, ACN [26], as well as ionic liquids [29]. Inherently, the selection of the solvent influences the reaction pathway and the formed products. Aqueous studies are mostly performed in the presence of H_2SO_4 on a Pt electrode, where electroreduction promotes the formation of 2-propanol at milder overpotentials and propane at higher overpotentials (close to the hydrogen evolution reaction). In other solvents, the electroreduction leads to combinatory products of the reagents like pinacols, diones or β-hydroxy ketones.

The electrosynthetic reduction of pure acetone with only a supporting electrolyte present has received much less attention. Inherently, it removes the need for the separation of an extra solvent component during the subsequent purification processes.

In previous studies from the ELCAT group (UAntwerp), this system has been investigated in batch and flow configurations [30,31]. Selectivity up to 90% was achieved for DAA at Pt cathodes in an undivided batch cell and up to 97% in a divided batch cell. Lower yields were observed with increasing water concentration or when Au and GC cathodes were used instead of Pt. Flow experiments showed that while Pt and GC cathodes gave similar yields per time unit, GC showed a fourfold increase in faradaic efficiency.

Mechanistically, the conventional acid-catalysed pathway is initiated by the enolisation of the reagent (Scheme S6.1) [32], while during the base-catalysed mechanism, an enolate anion is formed, followed by an nucleophilic addition to the reagent (Scheme S6.2) [32]. In contrast, the mechanism for the electrosynthesis of DAA from pure acetone with only a supporting electrolyte present in the solution is still unclear. To the best of our knowledge, three mechanisms for the electro synthetic aldol condensation of aldehydes or ketones have been postulated in literature for organic solvents.

In the mechanism proposed by Shono *et al.* [33], an electrochemically generated base (EGB) is formed at the electrode, which then deprotonates an aldehyde molecule to yield an anion. The anion reacts with a second aldehyde molecule to give the aldol addition product. The study of Shono *et al.* comprised of a small number of aliphatic aldehydes, which were self- or cross-condensed, yielding dimethylformamide. If this mechanism applies to acetone reduction, the most obvious EGB would be the acetone radical anion ($[CH_3C(O)CH_3]^{\bullet-}$, Scheme S6.3), but the EGB could also be an *in-situ* formed derivative. A mechanism towards DAA based on the initial steps in aldol condensations of aldehydes by Shono *et al.* can be found in Scheme 1.
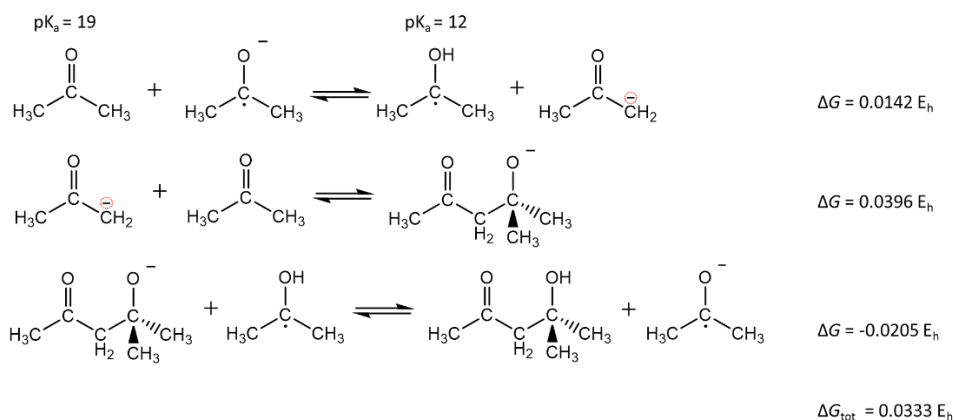
Scheme 1 Electrochemically-induced aldol condensation mechanism based on the aldol condensation mechanism for aldehydes of Shono et al. [33]. *The corresponding DFT computed ΔG-values are mentioned in front of each reaction as well as the ΔG$_{tot}$. The pK$_a$ values are taken from* [34] *for acetone and* [35] *for* $^{\bullet}C(CH_3)_2OH$. *The red circles are for clarification of the presence of a negative charge on the carbon atom.*

In contrast, Kumar *et al.* [36] proposed that an electrogenerated aldehyde radical anion undergoes homolytic C-H bond splitting to give an enolate anion and a hydrogen atom. The enolate anion couples with another electrogenerated aldehyde radical anion and loses an electron to give the alkoxide of an aldol product. This specie loses another electron and then couples with the previously generated hydrogen atom to give the aldol product. The authors do not mention the electron acceptor. The study of Kumar *et al.* comprised of a small number of benzaldehydes which were also self- or cross-condensed in a DMF/H$_2$O mixture. Scheme 2 shows the acetone to DAA pathway if the mechanism of Kumar *et al.* is followed. Once again, $[CH_3C(O)CH_3]^{\bullet-}$ is an important intermediate.
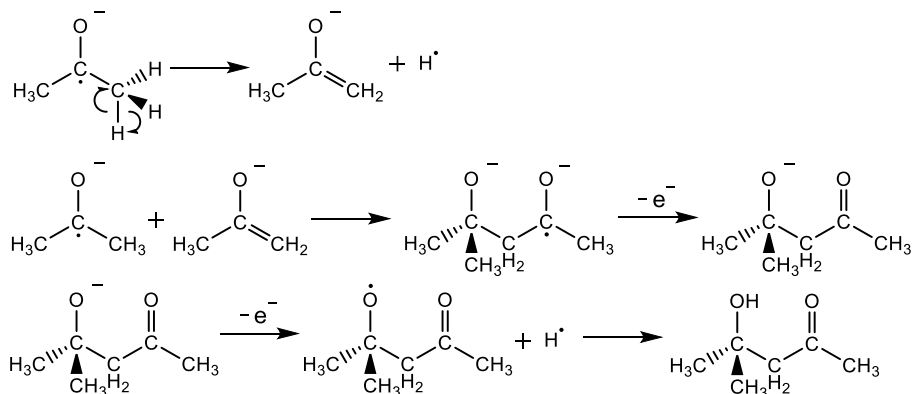
Scheme 2 Electrochemically-induced aldol condensation mechanism proposed by Kumar et al. [36] *applied to the acetone*

Tsai [37] proposed a mechanism for the self-condensation of acetone in water where a paired electrolysis occurs in an undivided cell with *in-situ* generated OH^- and H^+ catalysing the reaction in a classical way [38]. However, he proposed that without water, the reaction at the cathode would be similar to that shown in Scheme S6.3. At the anode, he states the formation of a carbocation. However, this mechanism appears to conflict with the higher selectivity observed when a divided batch cell is used [30,31]. In this chapter, the solvent-free electrochemical self-condensation of acetone to DAA was studied. Due to the radical nature of some reaction intermediates proposed in the literature, the reaction was studied by using *in-situ* spin-trap EPR spectroelectrochemistry. The trapped radicals were identified, and the effect of dissolved O_2 has been investigated. DFT computations of bond dissociation energies were used to evaluate the reaction mechanisms.
Finally, a detailed reaction mechanism is proposed considering the experimental findings and the DFT calculations.

6.2 Materials and methods

Combined EPR-spectroelectrochemical measurements were performed in a Wilmad Supracil WG-810-A-Q quartz flat cell. A PFA insulated Pt wire was used as a working electrode (WE). The PFA was stripped off for the section that was placed in the flat part. A leak-free reference electrode (RE)(W3 69-00) was used (Harvard Apparatus), which is equivalent to a Ag/AgCl 3 M KCl reference. The RE was positioned at the entrance of the flat part to ensure optimal potential control. The Pt rod counter electrode (CE) was put in the reservoir on top of the flat part. The tip was also put as close to the entrance of the flat part to reduce the cell potential. For experiments in the absence of O_2, solutions were prepared, and the cell was assembled in an N_2 atmosphere (Air Liquid 99.999%) glovebox. For experiments in the presence of O_2, the samples were prepared under air and bubbled with O_2 ballons. The setup was then placed in a TE_{102} rectangular cavity in a Bruker E580 Elexsys spectrometer. The EPR spectra were recorded at X-band (9.664 ± 0.001 GHz) in continuous wave mode at ambient temperature with 3.317 mW power, 0.1 mT modulation amplitude and 100 kHz modulation frequency. All electrochemical experiments were conducted with a PAR VersaSTAT 3 potentiostat.

The experiments performed in bulk were recorded versus a saturated Ag/AgCl reference electrode in a conventional undivided cell. The EPR spectra were simulated using the EasySpin-5.1.11 module running in Matlab [39].

Electrochemical measurements were performed in dry acetone stored in a glovebox (Acros Organics, 99.8%, Extra dry, Acroseal) with 0.1 M tetrabutylammonium perchlorate (TBAP, Sigma-Aldrich, 99.0 %). 10 mM 5,5-dimethyl-1-pyrroline-N-oxide (DMPO, TCI, >97.0 %) was added to the solutions as a radical trapping agent.

Spin-unrestricted (UKS) DFT calculations were carried out with the ORCA package [40–43]. The B3LYP functional [44], in combination with Gaussian basis sets 6-311+G** [45,46], were used to calculate the geometry optimisation and the Gibbs free energies (G) of each molecular structure. To mimic the solvent effect, the SMD (universal solvation model based on density) model [47] was used. The energy was converged to 1×10^{-8} Hartree (E_h), and the convergence tolerances in the geometry optimisation were 3×10^{-4} Eh/Bohr for the gradient and 5×10^{-6} E_h for the total energy.

In order to calculate the total Gibbs difference, ΔG, of the reaction mechanisms, first, the ΔG-values of every single intermediate reaction were calculated. Summation of all ΔG-values gives the total Gibbs energy change of the overall reaction. The Gibbs energy change ΔG_{tot} of a known reaction is given by Equations (6.1) and (6.2)

$$A + B \longrightarrow C + D \tag{6.1}$$

$$\Delta G_{tot} = G(C) + G(D) - [G(A)+G(B)] \tag{6.2}$$

The same DFT model as chapter 5 is used to determine the structures and EPR parameters of DMPO-trapped radicals.

6.3 Results and discussion

6.3.1 Electrochemical validation

Bulk CVs of acetone were performed on a Pt wire electrode with and without O_2 present (Figure 6.2). The presence of O_2 gave rise to a first irreversible reduction peak around -1.35 V vs Ag/AgCl. This is known to be the reduction of O_2 with the exact species formed depending on the solvent and impurities (see discussion). At more negative potentials, the solvent, here acetone, starts to reduce at the electrode.

The current increase with onset around -1.8 V cannot be caused by impurities due to its magnitude. Experiments in the flat cell show similar behaviour except for a shape distortion, probably due to the space limitations of the flat cell, as also observed in the previous chapter. Nevertheless, with a stable RE and the right choice of electrolysis potential, the two phenomena could be isolated for radical determination by EPR. The chosen potentials were -1.6 V and -2.1 V as the first isolates the O_2 reduction reaction when O_2 is present, and at -2.1 V, the direct acetone electroreduction occurs.

In previous work from the ELCAT group (UAntwerp), the reduction at -1.6 V in the presence of O_2 resulted in substantial yields of the product DAA comparable to those at -2.1 V for both circumstances [48]. This is an indication of an altered reaction mechanism for acetone reduction towards DAA when O_2 is present.
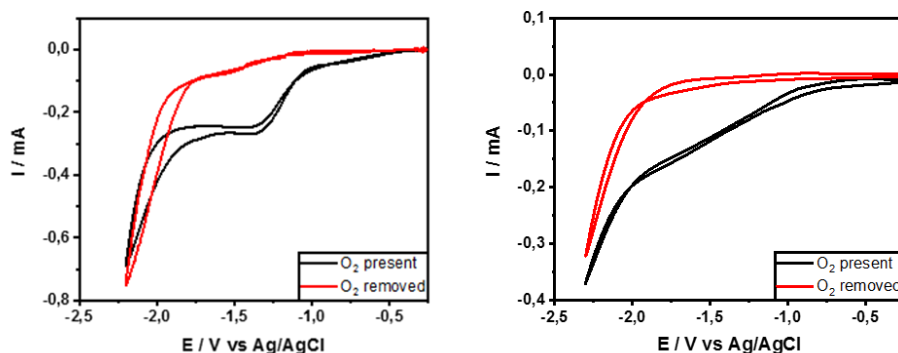
Figure 6.2. CV acetone + 0.1 M TBAP on Pt wire electrode in bulk (left) and flat cell (right) with and without the presence of O₂ at 50 mV s⁻¹

6.3.2 *In-situ* spin trap EPR spectroelectrochemistry

In order to determine potential radical intermediates that are generated in the electrochemical reactions, *in-situ* spin trap EPR spectroelectrochemistry was performed under four different conditions (i.e. -1.6 V, -2.1 V, O_2-rich environment and O_2-free environment). As explained in chapters 4 and 5, spin traps react with short-living radicals and convert them to more stable, EPR-detectable radical species. Experiments were performed with 10 mM DMPO spin trap (Figure 4.1), and the resulting EPR spectra are shown in Figure 6.3. No signal was observed when the electrolysis was performed at -1.6 V in the absence of O_2. When the electrolysis was performed at -2.1 V in the absence of O_2, a typical signal for a DMPO-trapped radical adduct (DMPO-R1) was observed. When the electrolysis was performed in the presence of O_2 at -1.6 V or -2.1 V, the R1 signal was observed combined with a second DMPO-trapped radical adduct signal (DMPO-R2). Simulations of the separated and combined DMPO-R1 and DMPO-R2 signals are also shown in Figure 6.3. The isotropic g-values (g_{iso}) and corresponding nitrogen ($A_{iso,N}$) and proton ($A_{iso,H}$) hyperfine couplings used for the simulations are given in Table 6.1.

Table 6.1 Simulated EPR parameters for the two trapped radicals and for similar/possible structures from literature.

DMPO-trapped radical	g_{iso}	$A_{iso, N}$ / mT	$A_{iso, H\beta}$ / mT	$A_{iso, H\gamma}$ / mT	Solvent	ref.
R1	2.0056	1.46	2.14	-	Acetone	this work
R2	2.0057	1.30	0.78	0.16	Acetone	this work
$^\bullet OCH(CH_3)_2$	-	1.343	0.782	0.179	7:1 ACN/IPA	[49]
	2.0061	1.28-1.30	0.6-0.7	0.2	Benzene	[50]
$^\bullet OC(CH_3)_3$	2.0061	1.31	0.8	0.2	Benzene	[50]
	-	1.311	0.79	0.197	Benzene	[51]
$^\bullet C(CH_3)_2OH$	2.0053	1.60	2.41	-	H_2O pH 7.8	[52]
	-	1.58	2.39	-	H_2O pH 11	[53]
	2.00537	1.579	2.436	-	IPA	[54]
	-	1.458	2.391	-	Benzene	[51]
$^\bullet CH_2C(O)CH_2C(O)OH$	2.0060	1.424	2.384	-	H_2O	[55]
$O_2^{\bullet -}$	-	1.31	0.91	-	Acetone	[56]
	-	1.275	1.019	0.13	Acetone	[57]
$^\bullet OOH$	2.0060	1.31	1.08	-	Acetone	[58]

The EPR parameters of DMPO-R1 fall within the range for trapping of carbon-centred radicals, while the values of DMPO-R2 are typical for trapping of oxygen-centred radicals. As seen in Table 6.1, the EPR values of DMPO-R1 are similar to those found in the literature for DMPO-trapped $^\bullet C(CH_3)_2OH$ (the protonated product of $[CH_3C(O)CH_3]^{\bullet -}$) and $^\bullet CH_2C(O)CH_2C(O)OH$ (structurally similar to the acetonyl radical ($^\bullet CH_2C(O)CH_3$), in which a H-atom has been abstracted from acetone). The EPR parameters of DMPO-R2 are consistent with those found for DMPO-trapped alkoxyl radicals such as $^\bullet OCH(CH_3)_2$ and $^\bullet OC(CH_3)_3$.
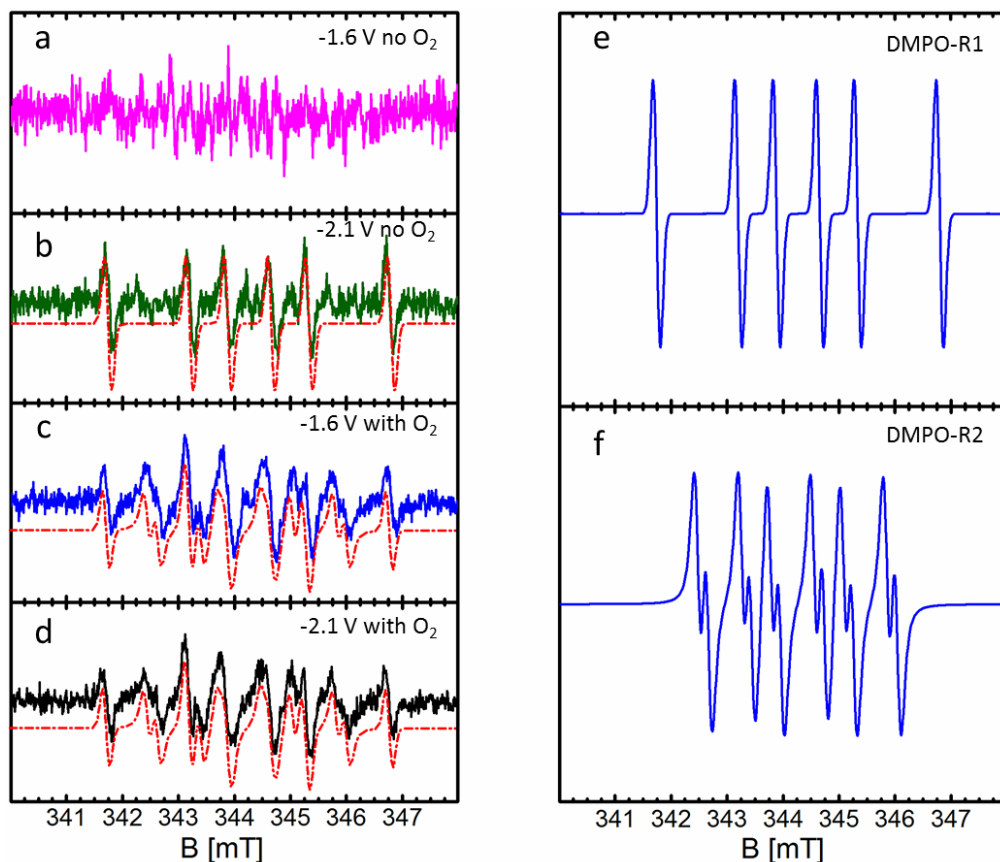
Figure 6.3. EPR spectra of in-situ generated DMPO-trapped radicals through cathodic reduction of acetone with 0.1 M TBAP and 10 mM of DMPO at -1.6 V and -2.1 V vs Ag/AgCl (3 M) under N_2 and O_2 atmosphere as well as related simulation spectra (dotted red lines). The experimental settings are stated in the experimental section (a-d). The simulated spectra of each DMPO-trapped radical are shown separately (e and f).

6.3.3 Gibbs free energy values

The above *in-situ* EPR measurements predict the presence of a carbon-centred radical in the absence of O_2 and carbon-centred and oxygen-centred radicals intermediates in the presence of O_2. DFT computations were subsequently performed in order to identify those intermediates.

Using DFT, the Gibbs energy (G) values for each reagent, product, and potential intermediate were determined (Table S6.1). The use of the functional/basis sets combination B3LYP/6-311+G** was benchmarked by others for similar molecular structures containing light atoms such as H, C, and O [59]. A similar level of theory was used in chapter 5 for the single-point calculations of radical species. Moreover, more extensive basis sets with higher computation costs (*e.g.* 6-311++G**) were utilised here as a test for some of the small molecules, such as acetone. The results did not show a significant change in energy values (Table S6.2) and were, therefore, abandoned. The

computed Gibbs energy values will be used to evaluate potential reaction mechanisms in the next section.

The DFT calculated ΔG_{tot} corresponding to several possible classical base-catalysed mechanisms initiated by OH⁻ were performed to validate the DFT approach. The ΔG_{tot} values of six different possible mechanisms to make DAA in the presence of acetone and enolated acetone were calculated (Table S6.3 and Figure S6.1). In mechanism 1, in the first step, OH⁻ deprotonates the first acetone to give water and $(CH_2C(O)CH_3)^-$ which then reacts with a second acetone to create $(OC(CH_3)_2CH_2C(O)CH_3)^-$. Then it deprotonates a third acetone and makes DAA and $(CH_2C(O)CH_3)^-$. This mechanism is not favoured due to a positive ΔG_{tot} (ΔG_{tot} = 0.0215 E$_h$). ΔG_{tot} becomes negative by replacing one acetone molecule with its enolate form in at least one of the steps 1 or 3 (mechanisms 2-4), which gives $\Delta G^{2,3}_{tot}$= -0.0029 E$_h$ for both mechanisms. The presence of a small amount of the enol form of acetone in the solvent is possible due to the keto-enol tautomerisation [60]. The most favoured mechanism with ΔG^4_{tot} = -0.0273 E$_h$ is mechanism 4, in which two enols replace acetone molecules in mechanism 1. These results show that the DFT approach is consistent with the classical base-catalysed mechanism [5].

6.3.4 Evaluation of putative reaction mechanisms

The detection of DMPO-R1 at -2.1 V vs Ag/AgCl during the *in-situ* EPR-spectroelectrochemical experiments of acetone in the absence of O$_2$ (Figure 6.3.b) suggests that radical R1 is a desorbed specie, unlike the species found on platinum in acidic aqueous media were acetone adsorbs on platinum [20,22,24]. In the light of the previously discussed reaction mechanisms, $^\bullet C(CH_3)_2OH$ is a candidate for R1 (Table 6.1). Trapping of $^\bullet C(CH_3)_2OH$ rather than $^\bullet OCH(CH_3)_2$ is corroborated by computation of the Loewdin charge and spin density distribution in $[CH_3C(O)CH_3]^{\bullet-}$. The spin density is mostly localised on the central carbon, with the negative charge localised more on the oxygen, favouring more the formation/trapping of $^\bullet C(CH_3)_2OH$. A similar charge distribution has also previously been discussed [61].
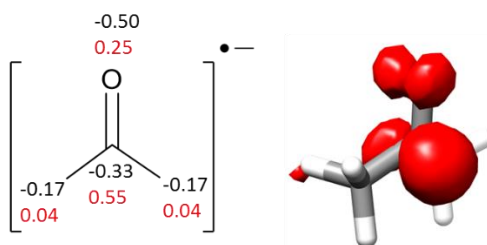

Figure 6.4 Acetone radical anion showing the Loewdin charge (black) and spin densities (red) on selected atoms (left) and the spin density distribution (right)

The negatively charged O-atom is protonated in the final DMPO-trapped adduct, but it is not possible to determine whether this occurs before or after the spin-trapping reaction. If the protonation step is assumed to be occurring before the spin-trapping reaction, then the presence of DMPO-R1 can be considered as evidence for $[CH_3C(O)CH_3]^{\bullet-}$, acting as an EGB within the mechanism proposed by Shono *et*

al. [33]. As shown in Scheme 1, after the EGB is formed, the mechanism essentially follows the classical base-catalysed pathway. For homogenous acetone self-condensation, a strong base such as an alkali metal hydroxide (pK$_a$ in H$_2$O is 14.00) is required [38]. However, the pK$_a$ of $^\bullet$C(CH$_3$)$_2$OH is only around 12 [35], meaning [CH$_3$C(O)CH$_3$]$^{\bullet-}$ is ~100 times less basic than an alkali metal hydroxide, and the increasing the total Gibbs energy of the overall reaction based on their proposed reaction (ΔG_{tot} = 0.0333 E$_h$) (see Scheme 1) makes it seem unlikely that [CH$_3$C(O)CH$_3$]$^{\bullet-}$ can catalyse the self-condensation to the degree of efficacy that has been observed.
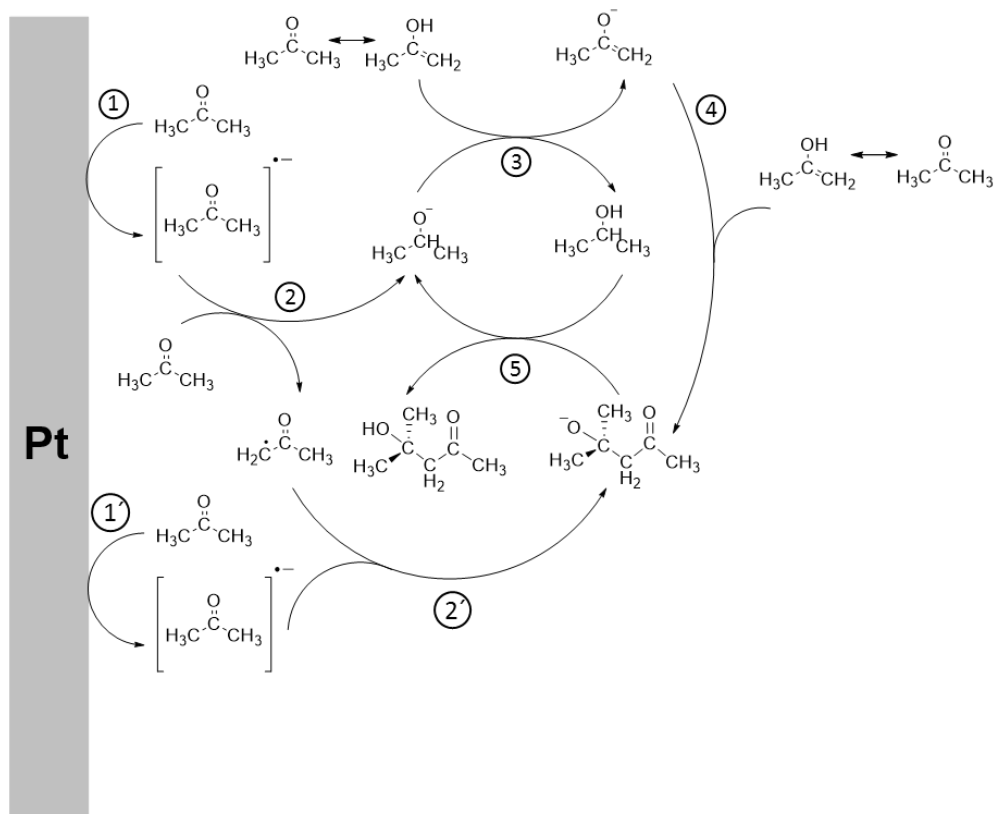
Figure 6.5. The proposed route for the direct reduction of acetone at Pt electrode towards DAA

An alternative route (Figure 6.5) could be that [CH$_3$C(O)CH$_3$]$^{\bullet-}$ in step 1, located on the electrode surface, first abstracts an H-atom to form isopropoxide ($^-$OCH(CH$_3$)$_2$) (step 2), which then acts as a strong base (pK$_a$ of isopropanol is 17.10 [62]) to initiate the base-catalysed pathway with the enolated acetone to make isopropanol and (CH$_2$C(O)CH$_3$)$^-$ (step 3), which then reacts with another enol to create (OC(CH$_3$)$_2$CH$_2$C(O)CH$_3$)$^-$ (step 4). Then by abstracting a proton from isopropanol, (OC(CH$_3$)$_2$CH$_2$C(O)CH$_3$)$^-$ makes DAA (step 5) (Figure 6.5).

Since the reaction mixture contains mostly acetone (13.5 M vs. 0.1 M of supporting electrolyte), the H-atom abstracted by [CH$_3$C(O)CH$_3$]$^{\bullet-}$ in step 2 most likely originates from another acetone molecule, which becomes $^\bullet$CH$_2$C(O)CH$_3$. Furthermore, it has been shown that [CH$_3$C(O)CH$_3$]$^{\bullet-}$ can be adsorbed on a Pt electrode in aqueous media [24,63]. Therefore, it is most likely that [CH$_3$C(O)CH$_3$]$^{\bullet-}$ first becomes

isopropoxide before leaving the surface along with the formation of $^{\bullet}CH_2C(O)CH_3$ from acetone in bulk. The assignment of R1 as $^{\bullet}CH_2C(O)CH_3$ would support this mechanism, and the results of the spin-trapping experiments in the presence of O_2 makes this assignment appear more likely (see further). Besides, the DFT computations show that the spin density is mainly localised on the carbon atom for $^{\bullet}CH_2C(O)CH_3$ (Figure 6.6 a), supporting the assignment of R1 as $^{\bullet}CH_2C(O)CH_3$.

Assuming that the reaction of $[CH_3C(O)CH_3]^{\bullet-}$ and acetone occurs on the surface of the Pt electrode (step 2 in Figure 6.5), the ΔG_{tot} of the mechanism initiated by isopropoxide calculated by DFT was negative (ΔG_{tot} = -0.0155E$_h$), meaning the proposed mechanism is favoured (see Scheme S6.4). Replacement of the enol by acetone in the step in which deprotonated DAA is made (step 4) gives ΔG_{tot} = 0.0089E$_h$ (the ΔG values and chemical structures given in red in Scheme S6.4), which suggests that the presence of the enol form of acetone is crucial to complete the reaction mechanism. Alternatively, radical termination between $^{\bullet}CH_2C(O)CH_3$ and $[CH_3C(O)CH_3]^{\bullet-}$ (step 2´) yields a deprotonated DAA (($OC(CH_3)_2CH_2C(O)CH_3$)$^-$) which also feeds into the base-catalysed pathway. According to DFT, this pathway is even valid, assuming that the formation of $^{\bullet}CH_2C(O)CH_3$ occurs in the solution taking into account its high ΔG = 0.0285 E$_h$. Since the radical termination step (step 2´) has a very negative (ΔG = -0.0560 E$_h$) thus results in ΔG_{tot} = -0.0273 E$_h$ for the overall reaction (Scheme S6.5). The more negative ΔG_{tot} value suggests that the mechanism in Scheme S6.5 drives the reaction.

The concentration difference between DMPO and acetone (10 mM vs ~13.5 M) influences the relative rate of the reaction between $[CH_3C(O)CH_3]^{\bullet-}$ and either acetone or DMPO. The reaction with acetone will be favoured due to this excess. Assuming that $[CH_3C(O)CH_3]^{\bullet-}$ is consumed almost quantitatively after its formation, the probability of R1 being $^{\bullet}CH_2C(O)CH_3$ increases significantly.

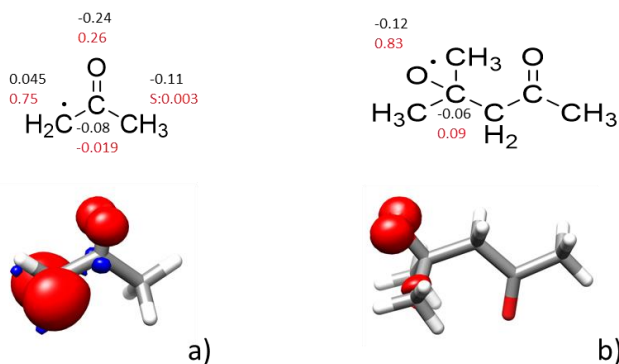*Figure 6.6 structure of the a) $^{\bullet}CH_2C(O)CH_3$ and b) DAA alkoxyl radical $^{\bullet}OC(CH_3)_2CH_2C(O)CH_3$. The numbers on the C and O atoms show the Loewdin charge (black) and spin (red) densities on selected atoms.*

When the *in-situ* EPR spectroelectrochemistry experiment was performed at -1.6 V vs Ag/AgCl, no spin-trapped species were detected, consistent with the lack of product formation during electrosynthesis at this potential. In contrast, when O_2 was introduced to the experiment, signals for DMPO-R1 and DMPO-R2 were observed. The presence of R1 at a potential where the reduction of acetone to $[CH_3C(O)CH_3]^{\bullet-}$ is not expected supports the assignment of R1 as $^{\bullet}CH_2C(O)CH_3$.

An obvious candidate to abstract an H-atom from acetone to give $^\bullet CH_2C(O)CH_3$ is $O_2^{\bullet-}$ formed from the one-electron reduction of O_2 ($E_{1/2}$ = -0.88 V vs SCE at Hg electrode in anhydrous acetone [64]). However, $O_2^{\bullet-}$ has been shown to be relatively stable in anhydrous acetone [64,65]. Indeed chemically or photochemically generated $O_2^{\bullet-}$ is stable enough in acetone to be readily spin-trapped by DMPO [56–58]. Since no $^\bullet$DMPO-OO or $^\bullet$DMPO-OOH adducts were observed in the *in-situ* EPR-spectroelectrochemical experiments (see the comparison of EPR parameters of $^\bullet$DMPO-R1 and $^\bullet$DMPO-R2 and the reported EPR values for $^\bullet$DMPO-OO and $^\bullet$DMPO-OOH, Table 6.1), it is unlikely that a significant amount of desorbed $O_2^{\bullet-}$ was generated. Furthermore, the DFT calculations do not support the occurrence of the reaction mechanisms initiated by $O_2^{\bullet-}$ shown in Table S6.4, since the computed ΔG_{tot} values are positive (Table S6.5, Figure S6.1). In these reaction mechanisms, $O_2^{\bullet-}$ deprotonates acetone (or its enol) to make $(CH_2C(O)CH_3)^-$ and an $^\bullet$OOH radical. Then, the deprotonated DAA anion is made by a reaction between acetone and $(CH_2C(O)CH_3)^-$, which afterwards reacts with $^\bullet$OOH to give DAA and superoxide $O_2^{\bullet-}$ (mechanisms 7 and 8 in Table S6.4). The other possibilities involve replacing $^\bullet$OOH with acetone (enol) in the last step of mechanisms 7(8) to make DAA and $(CH_2C(O)CH_3)^-$ (mechanisms 9-12, Table S6.4). All mechanisms mentioned in Table S6.4 do not yield DAA since the ΔG_{tot} values are positive. These results suggest that other intermediates of the O_2 reduction reaction are responsible for the formation of $^\bullet CH_2C(O)CH_3$ in solution. Noel *et al.* [66] reported that electroreduction of O_2 in aprotic polar solvents at a Pt surface can produce desorbed $^\bullet$OH with the following overall reaction:

$$O_2 + 2H^+ + 3e^- \rightarrow \, ^\bullet OH + OH^-$$
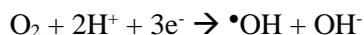
The irreversibility of the CV suggests that this may also be occurring in acetone. Previous studies [67,68] have shown that $^\bullet$OH can abstract an H-atom from acetone to give H_2O and $^\bullet CH_2C(O)CH_3$, and it is most likely also to be the case here since acetone is both the substrate and solvent (Figure 6.7). $[CH_3C(O)CH_3]^{\bullet-}$ is not present to terminate with $^\bullet CH_2C(O)CH_3$ to give deprotonated DAA, unlike in the O_2-free experiments at -2.1 V vs Ag/AgCl. $^\bullet CH_2C(O)CH_3$ instead propagates with acetone to give DAA and the DAA alkoxyl radical ($^\bullet OC(CH_3)_2CH_2C(O)CH_3$) as an intermediate. The detection of DMPO-R2, a secondary or tertiary alkoxyl radical adduct, is consistent with this pathway. The DFT calculations corroborate that ($^\bullet OC(CH_3)_2CH_2C(O)CH_3$) is an oxygen-centred radical (Figure 6.6 b). The detailed calculation of ΔG_{tot} of the mechanism is shown in Scheme S6.6 (ΔG_{tot} = -0.0051 E_h). By replacing acetone with enol, the ΔG_{tot} becomes more negative (Scheme S6.6 blue numbers).

Furthermore, OH^- is also generated in this mechanism, which can also initiate the classical base catalysed pathway in bulk. The DFT calculations of the ΔG values of the latter base-catalysed mechanisms are already explained in section 6.3.3. The fact that the parameters of R1 were the same for the experiments with and without O_2 confirms the hypothesis that $^\bullet CH_2C(O)CH_3$ is also the trapped intermediate in the O_2-free experiments.
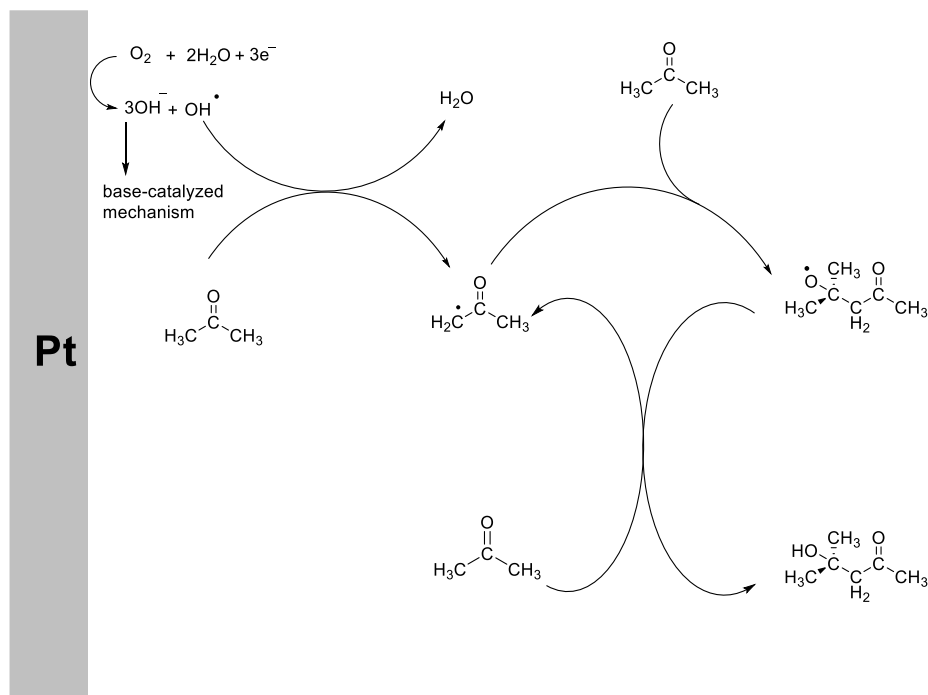
Figure 6.7. The proposed route for the oxygen-mediated reduction of acetone at Pt electrode towards DAA.

6.4 Validation of the DFT model for the trapped radicals

The reaction mechanisms in Figure 6.5 and Figure 6.7 suggest that $^\bullet CH_2C(O)CH_3$ and $^\bullet OC(CH_3)_2CH_2C(O)CH_3$ are the radicals trapped by DMPO. As validation of the presence of those radicals and, consequently, the proposed reaction mechanisms, first, the geometry of $^\bullet DMPO\text{-}CH_2C(O)CH_3$ and $^\bullet DMPO\text{-}OC(CH_3)_2CH_2C(O)CH_3$ were optimised, and then EPR parameters of optimised geometries were calculated using DFT.

The geometry-optimised molecular structures of these DMPO-trapped radicals are shown in Figure 6.8. as well as the related EPR spectra simulated using the DFT calculated EPR parameters of these radicals from Table 6.2. Although there are slight differences between the computed and experimental data, the calculated g and hyperfine values radicals follow a similar trend to the experimental values. These results support the assignment of $^\bullet DMPO\text{-}R1$ and $^\bullet DMPO\text{-}R2$ radicals to $^\bullet DMPO\text{-}CH_2C(O)CH_3$ and $^\bullet DMPO\text{-}OC(CH_3)_2CH_2C(O)CH_3$, respectively.
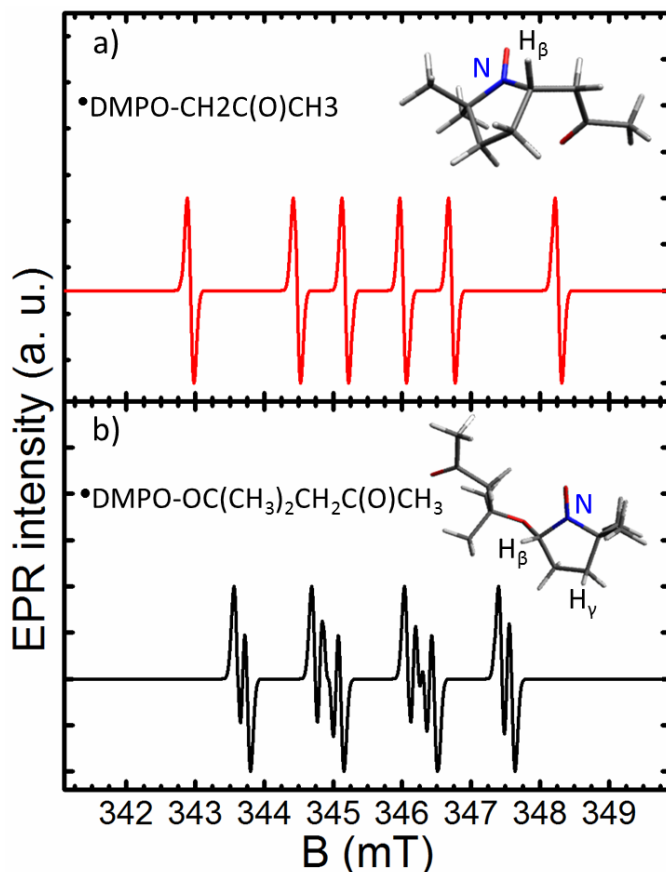
Figure 6.8 The simulated CW-EPR spectra based on the DFT-computed EPR values of a) •DMPO-CH₂C(O)CH₃ and b) •DMPO-OC(CH₃)₂CH₂C(O)CH₃ (Table 6.2).

Table 6.2 The DFT-computed EPR parameters of •DMPO-CH₂C(O)CH₃ and b) •DMPO-OC(CH₃)₂CH₂C(O)CH₃.

| DMPO-trapped radical	g_{iso}	$A_{iso, N}$/mT	$A_{iso, H\alpha}$/mT	$A_{iso, H\gamma}$/mT
•CH₂C(O)CH₃	2.0053	1.55	2.25	-
•OC(CH₃)₂CH₂C(O)CH₃	2.0053	1.36	1.12	0.14

6.5 Conclusion

The reaction mechanisms for the electroreduction of acetone reported in the literature have been assessed by performing *in-situ* EPR in the presence of a spin-trapping agent with corroborating DFT computations. Electrochemical measurements have indicated that DAA was the main product for solutions with and without the presence of O₂. The EPR results indicate that the direct acetone reduction at the electrode proceeds through the acetone radical anion which has been proposed as an adsorbed species in the literature. At the electrode, it can react with the excess solvent molecules in its vicinity to form the isopropoxide and acetonyl radical. Both intermediates have a pathway

towards DAA; the isopropoxide through the base-catalysed pathway (isopropoxide as EGB) and the acetonyl radical through a termination with the acetone radical anion formed at the electrode or in the solution.

The presence of O_2 resulted in a significant reduction of the overpotential at which the radical intermediates in the acetone reduction are formed. O_2 can be considered as an electrochemical mediator for the reaction towards DAA. The mechanism of oxygen reduction on Pt in aprotic polar solvents was suggested to produce hydroxide anions and hydroxyl radicals, considering that the superoxide radical anion nor the hydroperoxyl radical were spin-trapped. Also, here, both formed species have a route towards DAA; the hydroxide anion through the base-catalysed mechanism and the hydroxyl radical through reaction with acetone to form the acetonyl radical. The subsequent reaction with acetone will then yield a DAA alkoxyl radical, which disproportionates with acetone to DAA and the acetonyl radical.
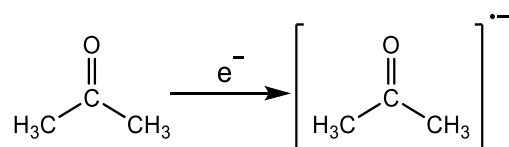
6.6 Supporting information
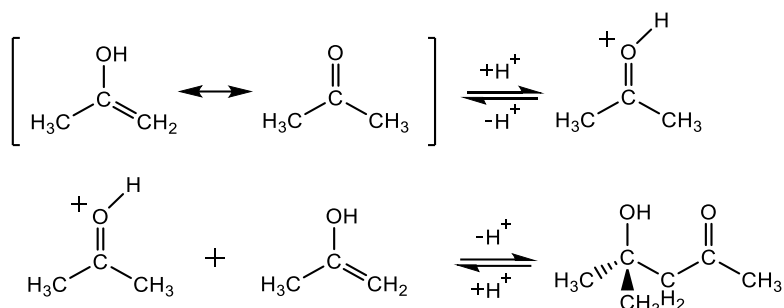
Scheme S6.1 Homogeneous acid-catalysed self-condensation of acetone.
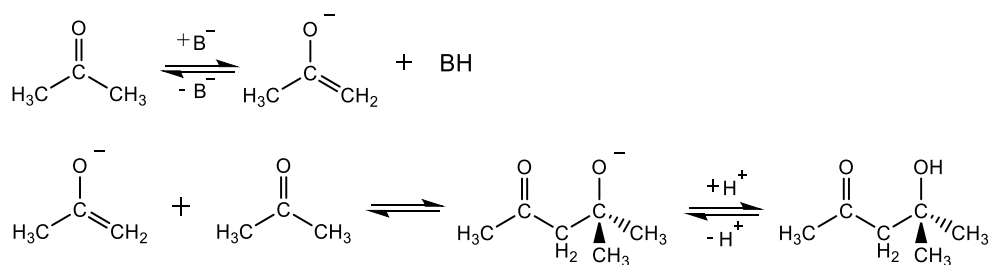
Scheme S6.2 Homogeneous base-catalysed self-condensation of acetone.

Scheme S6.3. Electrode reduction of acetone towards the radical anion [CH₃C(O)CH₃]•⁻.

*Table S6.1.Gibbs free energy values of the possible reagent, products, and intermediates participating in the proposed mechanisms. The values were calculated by DFT using B3LYP/6-311+G** as functional/basis sets combination. The SMD model was applied to mimic the solvent effect.*

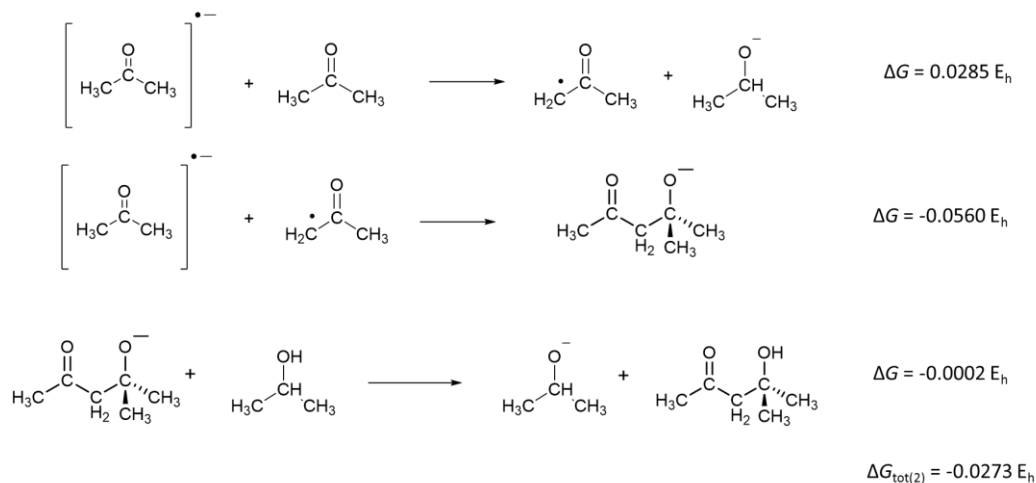| Reactants and intermediates	Gibbs energy (G) / Hartree
(acetone, $H_3C-C(=O)-CH_3$)	-193.05540430
($H_3C-\overset{\cdot}{C}(O^-)-CH_3$)	-193.10160897
($H_3C-\overset{\cdot}{C}(OH)-CH_3$)	-193.59056542
($H_3C-C(O^-)=CH_2$)	-192.55222319
($H_2\overset{\cdot}{C}-C(=O)-CH_3$)	-192.41047485
($H_3C-C(OH)=CH_2$)	-193.03098982
($H_3C-CH(O^-)-CH_3$)	-193.71808591
($H_3C-CH(OH)-CH_3$)	-194.22775492
($H_3C-CH(O^{\cdot})-CH_3$)	-193.57373369
($H_3C-C(O^{\cdot})(CH_3)-CH_2-C(=O)-CH_3$)	-385.42073397
($H_3C-C(O^-)(CH_3)-CH_2-C(=O)-CH_3$)	-385.56804125
($H_3C-C(OH)(CH_3)-CH_2-C(=O)-CH_3$)	-386.07747903
H_2O	-76.42764448
$^{\bullet}OH$	-75.74438542
OH^-	-75.91273908
$O_2^{\bullet-}$	-150.45109079
$^{\bullet}OOH$	-150.91529936

Table S6.2 The DFT-computed Gibbs free energy values using different functionals and basis sets for a set of acetone-derived structures.

Functional/ Basis sets	BP86/SVP	B3LYP/6-311+G**	B3LYP/6-311++G**
Molecular structure	Gibbs energy values (Hartree)		
	-192.96654105	-193.05540430	-193.05547222
	-192.99989189	-193.10160897	-193.10283507
	-192.31972721	-192.41047485	-192.41049777
	-193.61276014	-193.71808591	-193.71819626

$\Delta G = -0.0309\ E_h$

$\Delta G = 0.0396\ E_h$

$\Delta G = 0.0152\ E_h$

$\Delta G = 0.0002\ E_h$
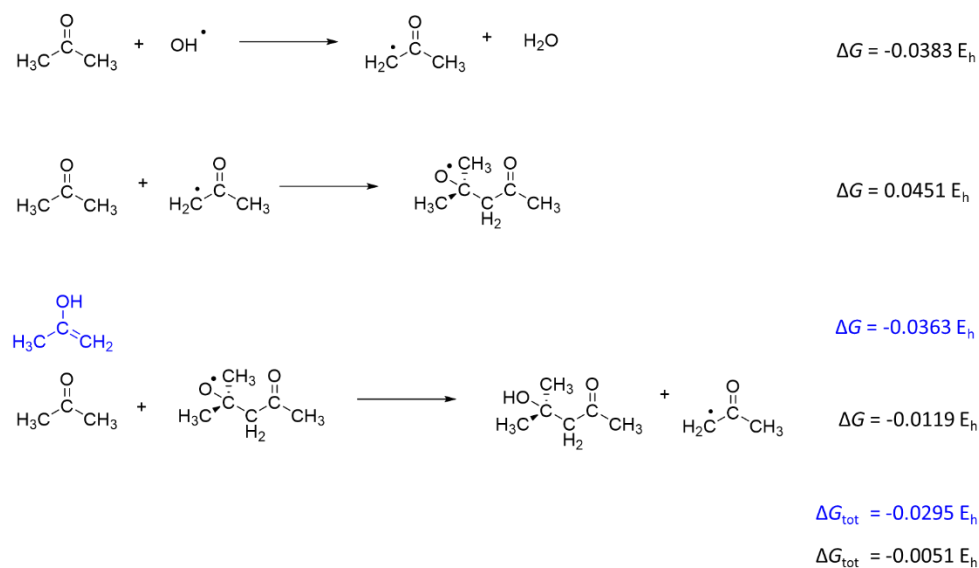
$\Delta G_{tot(1)} = 0.0089\ E_h$
$\Delta G_{tot(1)} = -0.0155\ E_h$
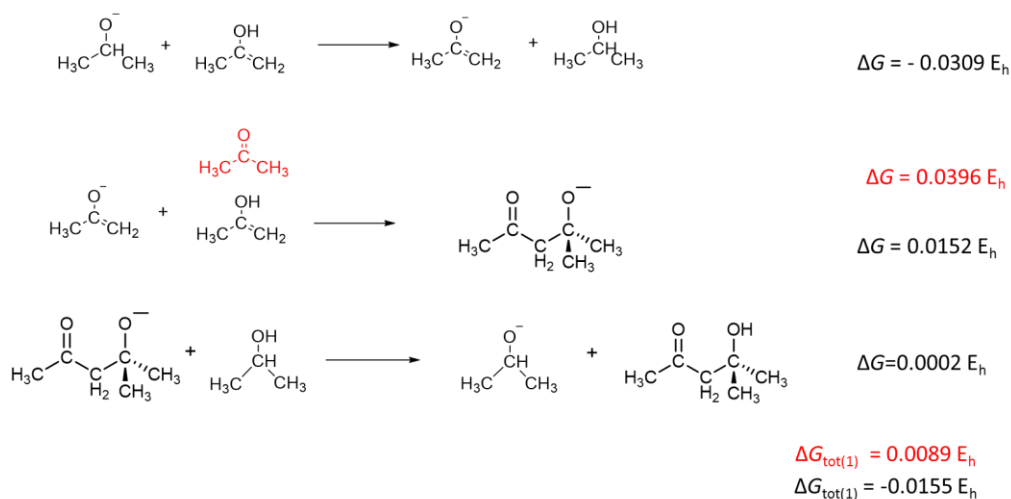
Scheme S6.4 The proposed route in Figure 6.5 by the creation of isopropoxide (⁻OCH(CH₃)₂). The corresponding DFT computed ΔG-values are mentioned in front of each reaction as well as the ΔG_{tot}.

$\Delta G = 0.0285\ E_h$

$\Delta G = -0.0560\ E_h$

$\Delta G = -0.0002\ E_h$

$\Delta G_{tot(2)} = -0.0273\ E_h$

Scheme S6.5 The proposed route in Figure 6.5 by the radical termination between •CH₂C(O)CH₃ and [CH₃C(O)CH₃]•⁻. The corresponding DFT computed ΔG-values are mentioned in front of each reaction as well as the ΔGtot.

$\Delta G = -0.0383\ E_h$

$\Delta G = 0.0451\ E_h$

$\Delta G = -0.0363\ E_h$

$\Delta G = -0.0119\ E_h$

$\Delta G_{tot} = -0.0295\ E_h$

$\Delta G_{tot} = -0.0051\ E_h$

Scheme S6.6 The proposed route in Figure 6.7. The corresponding DFT computed ΔG-values are mentioned in front of each reaction as well as the ΔGtot.

Table S6.3. Proposed base-catalysed mechanisms involving a hydroxide anion

Mechanism	
	1
	2
	3
	4
	5

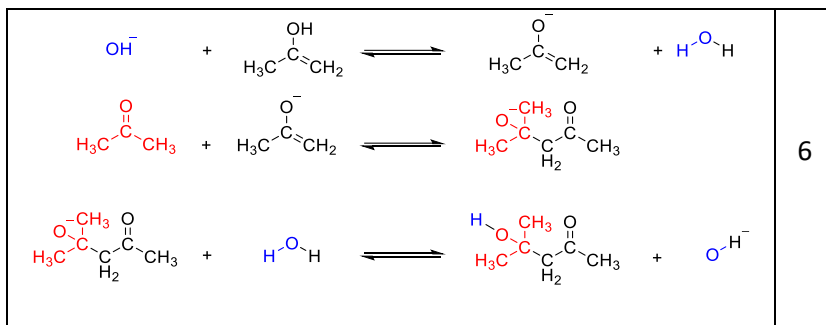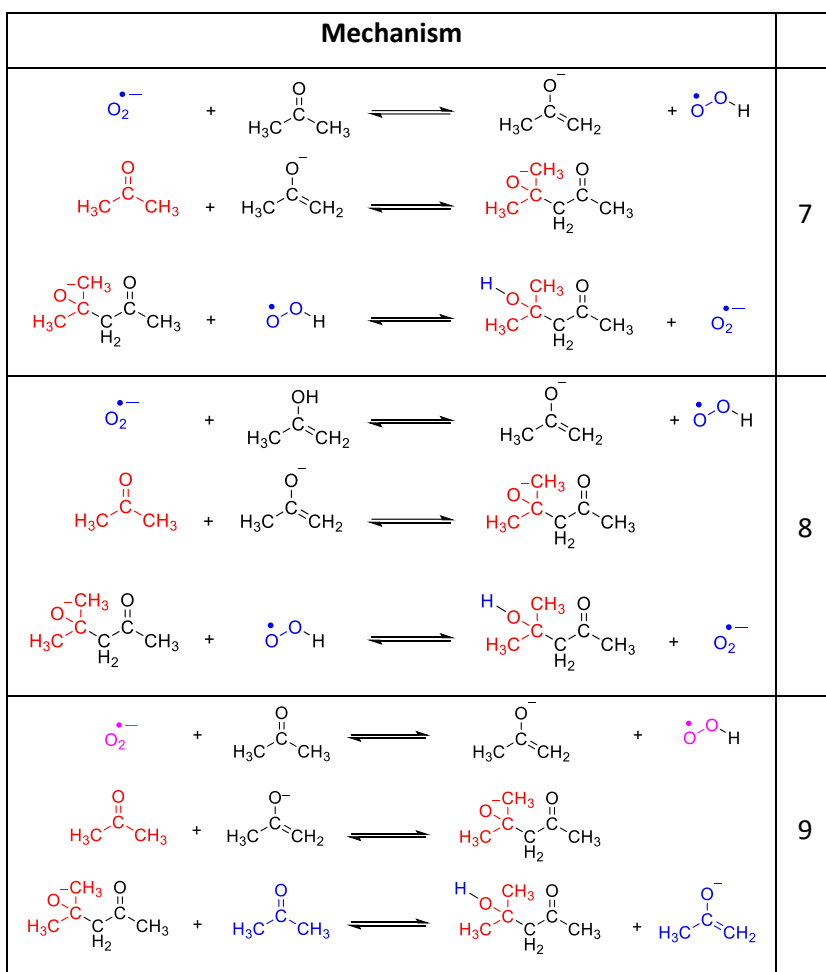Table S6.4 . Proposed base-catalysed mechanisms involving superoxide
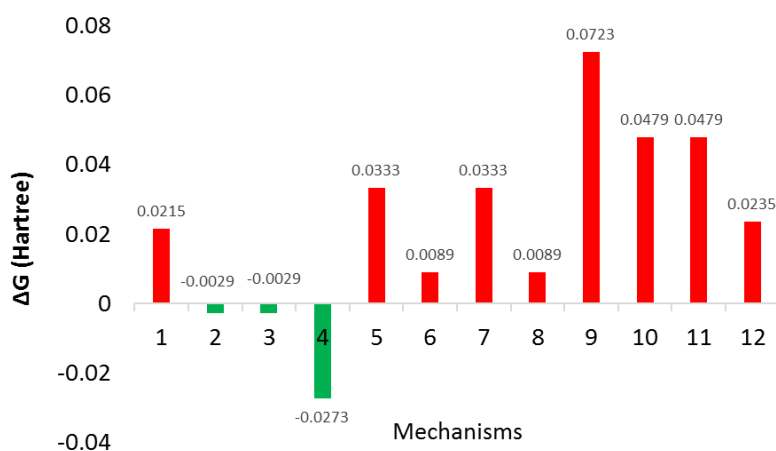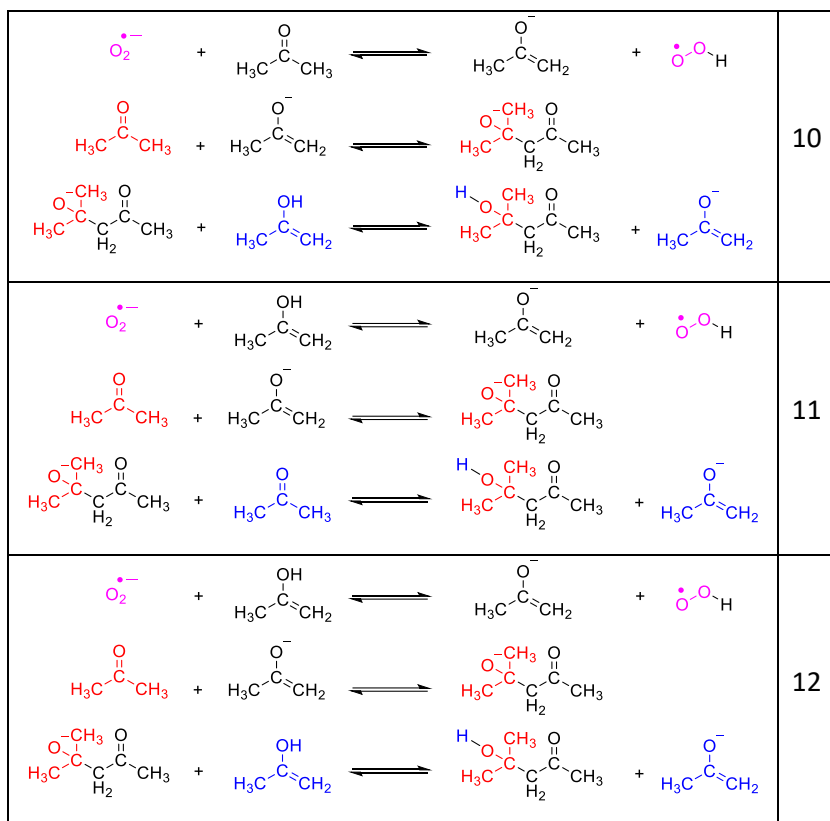
Figure S6.1 Change in free Gibbs energy values of the different proposed base-catalysed mechanisms (mechanisms 1-6) and radical mechanisms (mechanism 7-12). The negative values (green) represent the favoured mechanisms, and the positive values (red) represent the reaction paths that are not favoured.

Table S6.5. Change in free Gibbs energy values of the proposed base-catalyzed mechanisms (conditions1-6) and superoxide catalysed radical mechanisms (conditions 7-12).

Mechanism	ΔG (Hartree)
1	0.0215
2	-0.0029
3	-0.0029
4	-0.0273
5	0.0333
6	0.0089
7	0.0333
8	0.0089
9	0.0723
10	0.0479
11	0.0479
12	0.0235

6.7 References

[1]   G. S. Salvapati, K. V. Ramanamurty, and M. Janardanarao, *Selective Catalytic Self-Condensation of Acetone*, J. Mol. Catal. **54**, 9 (1989).

[2]   K. V. Ramanamurty and G. S. Salvapati, *New Dimensions on Value Added Aldol Chemicals of Acetone*, J. Sci. Ind. Res. (India). **59**, 339 (2000).

[3]   M. J. Darabi Mahboub, J. L. Dubois, F. Cavani, M. Rostamizadeh, and G. S. Patience, *Catalysis for the Synthesis of Methacrylic Acid and Methyl Methacrylate*, Chem. Soc. Rev. **47**, 7703 (2018).

[4]   H. Li, A. Riisager, S. Saravanamurugan, A. Pandey, R. S. Sangwan, S. Yang, and R. Luque, *Carbon-Increasing Catalytic Strategies for Upgrading Biomass into Energy-Intensive Fuels and Chemicals*, ACS Catal. **8**, 148 (2018).

[5]   G. G. Podrebarac, F. T. T. Ng, and G. L. Rempel, *A Kinetic Study of the Aldol Condensation of Acetone Using an Anion Exchange Resin Catalyst*, Chem. Eng. Sci. **52**, 2991 (1997).

[6]   H. . Siegel and M. Eggersdorfer, *Ketones*, in *Ullmann's Encyclopedia of Industrial Chemistry* (Wiley-VHC, Weinheim, 2000).

[7]   K. . Weissermel and H.-J. . Arpe, *Industrial Organic Chemistry*, Fourth edi (Wiley-VHC, Weinheim, 2003).

[8]   M. Hiersemann, *Modern Aldol Reactions*, Synthesis (Stuttg). **2007**, 483 (2007).

[9]   L. Baigrie, R. Cox, H. Slebockatilk, M. Tencer, and T. Tidwell, *Acid-Catalyzed Enolization and Aldol Condensation of Acetaldehyde*, J. Am. Chem. Soc. **107**, 3640 (1985).

[10]   G. Zhang, H. Hattori, and K. Tanabe, *Aldol Addition of Acetone, Catalyzed by Solid Base Catalysts: Magnesium Oxide, Calcium Oxide, Strontium Oxide, Barium Oxide, Lanthanum (III) Oxide and Zirconium Oxide*, Appl. Catal. **36**, 189 (1988).

[11]   S. Lippert, W. Baumann, and K. Thomke, *Secondary Reactions of the Base-Catalyzed Aldol Condensation of Acetone*, J. Mol. Catal. **69**, 199 (1991).

[12]   P. Kuśtrowski, D. Sułkowska, R. Pytlowany, and R. Dziembaj, *Kinetics of Self-Condensation of Acetone over Heterogeneous Ba(OH) 2 and Sr(OH)2 Catalysts*, React. Kinet. Catal. Lett. **81**, 3 (2004).

[13]   F. A. Carey and R. J. Sundberg, *Advanced Organic Chemistry Part A: Structure and Mechanisms* (Springer Science & Business Media, Virginia, 2007).

[14]   S. Ordóñez, E. Díaz, M. León, and L. Faba, *Hydrotalcite-Derived Mixed Oxides as Catalysts for Different C-C Bond Formation Reactions from Bioorganic Materials*, Catal. Today **167**, 71 (2011).

[15]   G. Zhang, H. Hattori, and K. Tanabe, *Aldol Condensation of Acetone/Acetone D6 over Magnesium Oxide and Lanthanum Oxide*, Appl. Catal. **40**, 183 (1988).

[16]   C. Du, Y. Shen, L. Sun, and X. Meng, *Condensation of Acetone to Diacetone Alcohol over Structured MgO/Al 2O3-Al Catalyst Packing*, Adv. Mater. Res. **347**–**353**, 3050 (2012).

[17]   K. Tanabe, G. Zhang, and H. Hattori, *Addition of Metal Cations to Magnesium Oxide Catalyst for the Aldol Condensation of Acetone*, Appl. Catal. **48**, 63 (1989).

[18] M. Paulis, M. Martin, D. . Sirua, A. Diaz, J. . Odriozola, and M. Montes, *Preparation and Characterization of Niobium Oxide for the Catalytic Aldol Condensation of Acetone*, Appl. Catal. A Gen. **180**, 411 (1999).

[19] P. J. . Elving and J. T. Leone, *Mechanism of the Electrochemical Reduction of Phenyl Ketones*, J. Am. Chem. Soc. **80**, 5284 (1958).

[20] X. de Hemptinne and K. Schunck, *Electrochemical Reduction of Acetone*, Trans. Faraday Soc. **65**, 591 (1969).

[21] G. A. . Noubi, M. F. . El-Shahed, F. . El-Cheikh, and H. . Mansour, *Electrochemical Reduction of Acetaldehyde, Benzaldehyde in Ethanol-Water Mixture*, Indian J. Chem. **17A**, 564 (1979).

[22] B. Bänsch, T. Härtung, H. Baltruschat, and J. Heitbaum, *Reduction and Oxidation of Adsorbed Acetone at Platinum Electrodes Studied by DEMS*, J. Electroanal. Chem. **259**, 207 (1989).

[23] M. L. Tsai and T. C. Chou, *Aldol Condensation of Acetone in an Undivided Cell via Electrochemical Catalyzed Reaction*, J. Chinese Inst. Chem. Eng. **28**, 381 (1997).

[24] C. J. Bondue, F. Calle-Vallejo, M. C. Figueiredo, and M. T. M. Koper, *Structural Principles to Steer the Selectivity of the Electrocatalytic Reduction of Aliphatic Ketones on Platinum*, Nat. Catal. **2**, 243 (2019).

[25] N. R. Armstrong, N. E. Vanderborgh, and R. K. Quinn, *Rotating Ring-Disk Electrode Studies of the Electrochemistry of Aromatic Carbonyl Compounds in the Solvent Sulfolane*, J. Electrochem. Soc. **122**, 615 (1975).

[26] W. R. Fawcett and A. Lasia, *The Electroreduction of Aromatic Aldehydes in Aprotic Solvents*, Can. J. Chem. **59**, 3256 (1981).

[27] T. Shono, S. Kashimura, M. Sawamura, and T. Soejima, *Selective C-Alkylation of β-Diketones*, J. Org. Chem. **53**, 907 (1988).

[28] T. Shono, M. Ishifune, T. Okada, and S. Kashimura, *A Novel Trifluoromethylation of Aldehydes and Ketones Promoted by an Electrogenerated Base*, J. Org. Chem. **56**, 2 (1991).

[29] S. F. Zhao, M. Horne, A. M. Bond, and J. Zhang, *Electrochemical Reduction of Aromatic Ketones in 1-Butyl-3-Methylimidazolium-Based Ionic Liquids in the Presence of Carbon Dioxide: The Influence of the Ketone Substituent and the Ionic Liquid Anion on Bulk Electrolysis Product Distribution*, Phys. Chem. Chem. Phys. **17**, 19247 (2015).

[30] D. Pauwels, J. Hereijgers, K. Verhulst, K. De Wael, and T. Breugelmans, *Investigation of the Electrosynthetic Pathway of the Aldol Condensation of Acetone*, Chem. Eng. J. **289**, 554 (2016).

[31] D. Pauwels, B. Geboes, J. Hereijgers, D. Choukroun, K. De Wael, and T. Breugelmans, *The Application of an Electrochemical Microflow Reactor for the Electrosynthetic Aldol Reaction of Acetone to Diacetone Alcohol*, Chem. Eng. Res. Des. **128**, 205 (2017).

[32] M. Braun, *Fundamentals and Transition-State Models. Aldol Additions of Group 1 and 2 Enolates*, ChemInform **37**, (2006).

[33] T. Shono, S. Kashimura, and K. Ishizaki, *Electroinduced Aldol Condensation*, Electrochim. Acta **29**, 603 (1984).

[34] Y. Chiang, A. J. Kresge, Y. S. Tang, and J. Wirz, *The PKa and Keto-Enol Equilibrium Constant of Acetone in Aqueous Solution*, J. Am. Chem. Soc. **106**,

460 (1984).

[35] P. Toffel and A. Henglein, *Temperature Dependence of the Electrolytic Dissociation of Some 1-Hydroxy-Alkyl Radicals in Aqueous Solution (a Pulse Radiolysis Study).*, Berichte Der Bunsengesellschaft/Physical Chem. Chem. Phys. **80**, 525 (1976).

[36] S. . Kumar, L. X. . Sharma, and R. K. P. Singh, *Electroinduced Aldol Condenstation at Platinum Electrode*, J. Indian Chem. Soc. **83**, 1160 (2006).

[37] M. L. Tsai, *The Production of Diacetone Alcohol via Paired Electrolysis in an Undivided Cell*, J. Chinese Inst. Chem. Eng. **36**, 263 (2005).

[38] A. T. Nielsen and W. J. Houlihan, *Organic Reactions* (JOHN WILEY & SONS, INC., New Yorkr, 1968).

[39] S. Stoll and A. Schweiger, *EasySpin, a Comprehensive Software Package for Spectral Simulation and Analysis in EPR*, J. Magn. Reson. **178**, 42 (2006).

[40] F. Neese, *Prediction of Electron Paramagnetic Resonance g Values Using Coupled Perturbed Hartree–Fock and Kohn–Sham Theory*, J. Chem. Phys. **115**, 11080 (2001).

[41] F. Neese, *Theoretical Study of Ligand Superhyperfine Structure. Application to Cu(II) Complexes*, J. Phys. Chem. A **105**, 4290 (2001).

[42] F. Neese, *Metal and Ligand Hyperfine Couplings in Transition Metal Complexes: The Effect of Spin–Orbit Coupling as Studied by Coupled Perturbed Kohn–Sham Theory*, J. Chem. Phys. **118**, 3939 (2003).

[43] F. Neese, *Efficient and Accurate Approximations to the Molecular Spin-Orbit Coupling Operator and Their Use in Molecular g-Tensor Calculations*, J. Chem. Phys. **122**, 034107 (2005).

[44] P. J. Stephens, F. J. Devlin, C. F. Chabalowski, and M. J. Frisch, *Ab Initio Calculation of Vibrational Absorption and Circular Dichroism Spectra Using Density Functional Force Fields*, J. Phys. Chem. **98**, 11623 (1994).

[45] W. J. Hehre, R. Ditchfield, and J. A. Pople, *Self—Consistent Molecular Orbital Methods. XII. Further Extensions of Gaussian—Type Basis Sets for Use in Molecular Orbital Studies of Organic Molecules*, J. Chem. Phys. **56**, 2257 (1972).

[46] R. Krishnan, J. S. Binkley, R. Seeger, and J. A. Pople, *Self-consistent Molecular Orbital Methods. XX. A Basis Set for Correlated Wave Functions*, J. Chem. Phys. **72**, 650 (1980).

[47] A. V. Marenich, C. J. Cramer, and D. G. Truhlar, *Universal Solvation Model Based on Solute Electron Density and on a Continuum Model of the Solvent Defined by the Bulk Dielectric Constant and Atomic Surface Tensions*, J. Phys. Chem. B **113**, 6378 (2009).

[48] D. Pauwels, Electrosynthesis as an Environmentally Friendly Production Method: Screening Methodology towards Upscaling, University of Antwerp, 2018.

[49] L. Ebersen, *Formation of Hydroxyl Spin Adducts via Nucleophilic Adittion-Oxidation to 5,5-Dimethyl-1-Pyrroline N-Oxide*, Achta Chem. Scand. **53**, 584 (1999).

[50] R. Borghi, L. Lunazzi, G. Placucci, G. Cerioni, and A. Plumitallo, *Photolysis of Dialkoxy Disulfides: A Convenient Source of Alkoxy Radicals for Addition to the Sphere of Fullerene C60*, J. Org. Chem. **61**, 3327 (1996).

M.Samanipour

[51]   E. G. Janzen and J. I. P. Liu, *Radical Addition Reactions of 5,5-Dimethyl-1-Pyrroline-1-Oxide. ESR Spin Trapping with a Cyclic Nitrone*, J. Magn. Reson. **9**, 510 (1973).

[52]   S. Tero-Kubota, Y. Ikegami, T. Kurokawa, R. Sasaki, K. Sugioka, and M. Nakano, *Generation of Free Radicals and Initiation of Radical Reactions in Nitrones - Fe^{2+} - Phosphate Buffer Systems*, Biochem. Biophys. Res. Commun. **108**, 1025 (1982).

[53]   M. Faraggi, A. Carmichael, and P. Riesz, *OH Radical Formation by Photolysis of Aqueous Porphyrin Solutions. A Spin Trapping and E.S.R. Study*, Int. J. Radiat. Biol. **46**, 703 (1984).

[54]   H. Taniguchi and K. P. Madden, *DMPO-Alkyl Radical Spin Trapping: An in Situ Radiolysis Steady-State ESR Study*, Radiat. Res. **153**, 447 (2000).

[55]   B. C. Gilbert, G. R. Hodges, J. R. L. Smith, P. MacFaul, and P. Taylor, *Photo-Decarboxylation of Substituted Alkylcarboxylic Acids Brought about by Visible Light and Iron(III) Tetra(2-N-Methylpyridyl)Porphyrin in Aqueous Solution*, J. Chem. Soc. Perkin Trans. 2 **4**, 519 (1996).

[56]   J. R. Harbour and M. L. Hair, *Detection of Superoxide Ions in Nonaqueous Media. Generation by Photolysis of Pigment Dispersions*, J. Phys. Chem. **82**, 1397 (1978).

[57]   K. Reszka, P. Bilski, R. H. Sik, and F. Chignell, *Photosensitized Generation of Superoxide Radical in Aprotic Solvents: An EPR and Spin Trapping Study*, Free Rad. Res. Comms. **19(s1)**, S33 (1993).

[58]   M. Yamada, K. D. Karlin, and S. Fukuzumi, *One-Step Selective Hydroxylation of Benzene to Phenol with Hydrogen Peroxide Catalysed by Copper Complexes Incorporated into Mesoporous Silica-Alumina*, Chem. Sci. **7**, 2856 (2016).

[59]   M. P. Andersson and P. Uvdal, *New Scale Factors for Harmonic Vibrational Frequencies Using the B3LYP Density Functional Method with the Triple-Zeta Basis Set 6-311+G(d,P).*, J. Phys. Chem. A **109**, 2937 (2005).

[60]   S. K. Pollack and W. J. Hehre, *The Enol of Acetone*, J. Am. Chem. Soc. **99**, 4845 (1977).

[61]   R. Koppe and P. H. Kasai, *Aliphatic Ketone Anion-Radicals: A Matrix Isolation ESR Study*, J. Phys. Chem. **98**, 12904 (1994).

[62]   G. P. Laroff and R. W. Fessenden, *Equilibrium and Kinetics of the Acid Dissociation of Several Hydroxyalkyl Radicals*, J. Phys. Chem. **77**, 1283 (1973).

[63]   B. Demir, T. Kropp, K. R. Rivera-Dones, E. B. Gilcher, G. W. Huber, M. Mavrikakis, and J. A. Dumesic, *A Self-Adjusting Platinum Surface for Acetone Hydrogenation*, Proc. Natl. Acad. Sci. U. S. A. **117**, 3446 (2020).

[64]   M. E. Peover and B. S. White, *The Formation of the Superoxide Ion by Electrolysis of Oxygen in Aprotic Solvents*, Chem. Commun. **11**, 183 (1965).

[65]   M. Mohammad, A. Y. Khan, M. S. Subhani, N. Bibi, S. Ahmad, and S. Saleemi, *Kinetics and Electrochemical Studies on Superoxide*, Res. Chem. Intermed. **27**, 259 (2001).

[66]   J. M. Noël, A. Latus, C. Lagrost, E. Volanschi, and P. Hapiot, *Evidence for OH Radical Production during Electrocatalysis of Oxygen Reduction on Pt Surfaces: Consequences and Application*, J. Am. Chem. Soc. **134**, 2835 (2012).

[67]   R. K. Talukdar, T. Gierczak, D. C. McCabe, and A. R. Ravishankara, *Reaction*

of Hydroxyl Radical with Acetone. 1. Kinetics of the Reactions of OH, OD, and 18OH with Acetone and Acetone-D6, J. Phys. Chem. A **107**, 5014 (2003).

[68] G. S. Tyndall, J. J. Orlando, T. J. Wallington, M. D. Hurley, M. Goto, and M. Kawasaki, *Mechanism of the Reaction of OH Radicals with Acetone and Acetaldehyde at 251 and 296 K*, Phys. Chem. Chem. Phys. **4**, 2189 (2002).

CHAPTER 7

How EPR can help in developing a screening strategy for ecstasy

This chapter describes the development of an electrochemical screening strategy for 3,4-methylenedioxymethamphetamine (MDMA), the regular psychoactive compound in ecstasy (XTC) pills. The work results from a collaboration with A-Sense Lab at UAntwerp (PI K. De Wael), where the electrochemistry was performed. We have investigated the specific electrochemical profile of MDMA and its electro-oxidation mechanisms at disposable graphite screen-printed electrodes. I here focus mainly on how the formation of a radical cation and subsequent reactions are responsible for the electrode surface passivation, evidenced by using spin-trap EPR, DFT and electrochemistry. Furthermore, I summarise how the proposed electrochemical screening strategy has demonstrated to be a rapid, sensitive and selective detection method of MDMA, resolving most of the false positives and negatives given by the traditional Marquis colour tests, thus exhibiting remarkable promises for the on-site screening of MDMA.

7.1 Introduction

Amphetamine-type stimulants (ATS) are globally prevalent in the field of synthetic drugs with an international pattern of supply and demand [1]. Amphetamine (AMP), methamphetamine and "ecstasy" (XTC) belong to the class of ATS, with the XTC market becoming increasingly multifaceted [2,3]. The main psychoactive compound in XTC tablets is 3,4-methylenedioxymethamphetamine (MDMA). According to the 2021 world drug report, three main types of XTC are available: ecstasy tablets with a high content of MDMA, tablets containing little or no MDMA, and XTC sold in crystals/powder form under different street names [4]. Until 2010, the XTC drugs were frequently adulterated by various cutting agents and/or cheaper chemicals such as caffeine, amphetamine, procaine, paracetamol, ketamine, dextromethorphan (DXM) and bath salts [5–8], essentially to mimic the stimulant effects. Besides the psychoactive adulterants, XTC tablets might also contain excipients such as diluents, binders, lubricants disintegrators, dyes or flavourings and sometimes prescription drugs [9]. According to the latest world drug report 2021, the content of MDMA in XTC tablets increases yearly, particularly in the European market, with an estimate of 50-70 million tablets produced in the European Union and EU-member states yearly [4]. Adding to the trend of increasing the purity of MDMA pills, there has also been an increase in the size of some of the tablets available [2]. With this ever-changing vogue of drug product compositions, it is of crucial importance to develop a detection strategy for increasingly diversified ecstasy products.

The prevention of drug trafficking benefits from a highly selective detection of drugs of abuse in the field. A two-fold approach is traditionally followed to identify the drug in seized samples: (i) screening with presumptive tests and (ii) confirmatory lab analysis. Presumptive tests enable an on-site screening of suspicious samples. Law enforcement agencies (LEAs) use portable rapid testing kits, typically colour tests, with the Marquis colour test kit being the test of choice for ecstasy identification [10]. A Marquis colour test is based on the formation of a purple to a black coloured complex containing two carbenium ions when MDMA reacts with sulfuric acid in the presence of formaldehyde [11]. However, selectivity issues are reported showing false positives or false negatives with the use of presumptive colour tests [12–14]. Moreover, uncertainty in the qualitative analysis is given by subjective judgements due to individual perceptions of colours. Therefore, the forensic analyst must confirm a positive colour test with additional laboratory tests for any legally controlled compound [13]. Alternative analytical methods such as Fourier Transform Infra-Red (FTIR) spectroscopy and Raman spectroscopy have been employed as an initial screening approach for ATS, followed by GC/LC-MS (Gas Chromatography/Liquid Chromatography-Mass Spectrometry) (qualitative), GC-FID (Gas Chromatography-Flame Ionization Detection) (quantitative) as confirmatory analysis [15]. Indeed, portable Raman, FTIR and mass spectrometers have been proposed for use in airports/customs and at crime scenes for the rapid analysis of illicit drugs [16,17]. However, this instrumentation is rather expensive, bulky and mostly requires specialised personnel to interpret the results. Thus, there is a great interest in developing fast, easy-to-use, portable and reliable screening methods to on-site detect ecstasy drugs by law enforcement personnel.

Due to its sheer simplicity, affordability, portability and fast analysis, electrochemical detection is an inviting approach for the selective detection of target compounds in many fields. Electrochemical sensors have broadly been used for forensic analysis [18] and particularly in the detection of drugs of abuse [19,20]. For example, screen printed electrodes (SPEs) have been used to determine amphetamine [21] and heroin [22] in confiscated samples. Moreover, few studies report on the electrochemical detection of MDMA and related substances [23–32]. For example, Garrido *et al*. explored the electrochemical oxidation of amphetamine-like drugs and its application to the electroanalysis of ecstasy in human serum [28]. In 2014, Tadini *et al*. developed chemically modified electrodes to detect MDMA by voltammetry [29]. A year later, Cumba *et al*. used SPEs for the simultaneous detection of MDMA and para-methoxyamphetamine (PMA) [31]. Recently, the oxidation mechanism was demonstrated on boron-doped diamond electrode with differential pulse voltammetry by Teófilo *et al.* [32]. However, an extensive study on the influence of a wide range of cutting agents and excipients on the electrochemical detection of XTC products has not yet been conducted. Moreover, the electrode mechanism behind MDMA oxidation at graphite screen printed electrodes (G-SPEs) has not been explored in detail.

In this chapter, I report about the collaborative work on the development of an electrochemical sensor using G-SPEs to detect MDMA in ecstasy pills, adulterated powder or crystal forms, based on the electrochemical profile of MDMA at pH 7. An additional test, based on the electrochemical profile of MDMA at pH 12, is also developed to boost the accuracy of the methodology if necessary. First, the electrode processes observed at G-SPEs are investigated in aqueous buffer solutions. During the electrochemical oxidation, the formation of a highly unstable radical cation was hypothesised and supported by electron paramagnetic resonance (EPR) experiments using *N-tert*-butyl-α-phenylnitrone (PBN) as the spin-trap and DFT computations, as will be detailed in this chapter. I will also summarise some of the essential outcomes of the electrochemistry experiments. For more details, I refer to the published work [33]. In particular, the passivation of the electrode surface during the electrochemical screening of MDMA, caused by these oxidised products, is studied with electrochemistry. Second, the effect of cutting agents on the electrochemical signal of MDMA is investigated. The cutting agents of interest are psychoactive adulterants, excipients and other related compounds. Both the sensitivity and specificity of this approach are compared with the results obtained from the Marquis colour tests and commercially available XTC colour test kits to demonstrate the strength of the approach. Finally, the results from the electrochemical analysis of confiscated MDMA street samples are validated with laboratory standard methods (i.e., GC-MS and GC-FID). Herein, the electrochemical screening method allows the rapid and low-cost profiling of MDMA in seized samples, which ultimately will allow easy on-site discrimination of ecstasy samples by LEAs.

7.2 Materials and methods

7.2.1 Reagents and sampling

Psychoactive standards such as d,l-MDMA·HCl, 3,4-methylenedioxy-N-ethylamphetamine (d,l-MDEA·HCl), d,l-MBDB·HCl, d-amphetamine·HCl, methamphetamine·HCl, para-methoxymethapmphetamine (d,l-PMMA·HCl), d,l-PMA·HCl, ketamine·HCl, mephedrone·HCl, 1-(3-chlorophenyl)-piperazine·HCl (mCPP·HCl), 1-(4-chlorophenyl)-piperazine·HCl (pCPP·HCl), butylone·HCl, methylone·HCl, cocaine·HCl, heroin and 3,4-methylendioxypyrovalerone·HCl (MDPV·HCl) with purity >98.5% were purchased from Lipomed (Arlesheim, Switzerland). DXM was purchased from Sigma-Aldrich (Diegem, Belgium). PMK (piperonyl methyl ketone) was provided by the National Institute for Criminalistics and Criminology (NICC) in Belgium. Caffeine and excipients such as lactose, glucose, myo-inositol, starch, cellulose, and magnesium stearate were purchased from VWR Chemicals (Leuven, Belgium). Ecstasy street samples were provided by the NICC in Belgium. The street samples were analysed by GC-MS (qualitatively) and GC-FID (quantitatively) to define their chemical composition. 1,3-Benzodioxole (BZX) was purchased from Sigma-Aldrich (Belgium); 1,3-Benzodioxole (BZX) was purchased from Sigma-Aldrich (Belgium); sulfuric acid and formaldehyde (37%) used in the colour tests were purchased from Merck and Sigma-Aldrich (Belgium), respectively. Phosphate buffer saline (PBS) solutions were prepared for the electrochemical measurements, containing 20 mM KH_2PO_4 and 100 mM KCl, purchased from Sigma-Aldrich (Belgium). The pH of these buffer solutions was adjusted with KOH and H_3PO_4 solutions to reach the desired pH (pH 2 – pH 13). All aqueous solutions were prepared using Milli-Q water (R > 18 MΩcm). The spin-trap PBN (> 98%) was purchased from TCI Europe N.V.

The XTC related compounds were subjected to both colour tests and electrochemical analysis as individual compounds and binary mixtures with MDMA (1:1). For real samples analysis, such as ecstasy pills, tablets were crushed or scrapped with a spatula for collecting the sample (approximately 1 mg) and dissolved in 1 mL PBS pH 7 in a 1.5 mL tube.

7.2.2 Electrochemistry

Electrochemical measurements were performed using an Autolab PGSTAT101 potentiostat with NOVA software. Disposable graphite screen-printed electrodes (G-SPEs) were purchased from ItalSens or PalmSens (Utrecht, The Netherlands). The G-SPEs consist of a graphite working electrode (geometric area of 7.07 mm²), a carbon counter electrode and a silver reference electrode on a flexible polyester support. Measurements were performed in a 50 µL drop placed on the G-SPE. Voltammetric techniques such as linear sweep voltammetry (LSV) and cyclic voltammetry (CV) were carried out for a better understanding of the electrochemical behaviour of MDMA on G-SPEs. Both CV and LSV of MDMA were performed in the potential window of -0.1 V to 1.5 V vs Ag/AgCl at a scan rate of 50 mV/s, and the CV of the redox probe,

potassium ferrocyanide ($K_4[Fe(CN)_6] \cdot 3H_2O$) was carried out in the potential window of -0.4 V – 0.6 V at 50 mV/s. Square wave voltammetry (SWV) was used for unravelling the electrochemical profile of all substances owing to its high sensitivity. SWVs were corrected for the background current by a moving average principle, integrated into the NOVA 1.11 software. All electrochemical measurements were performed at room temperature. The SWV parameters were optimised by studying the variation of the peak currents with the square wave frequency, pulse amplitude and step potential. The optimised parameters are: frequency 10 Hz, amplitude 25 mV and step potential 5 mV. The potential was swept from -0.1 V to 1.5 V vs Ag/AgCl.

A detailed protocol to prepare samples and analyse street samples is given in the supplementary information of ref [33].

7.2.3 Electron paramagnetic resonance spectroscopy

EPR measurements were carried out with a 0.9 mm inner diameter capillary tube containing the electrolysed solution positioned in a TE102 cavity in a Bruker E580 Elexys spectrometer. The EPR spectra are measured at X-band in continuous-wave (CW) mode (~9.7 GHz) with a microwave power of 5 mW, 0.1 mT modulation amplitude and 100 kHz modulation frequency. The measurements were carried out at room temperature. The EPR spectra were simulated with Matlab2017a using the EasySpin-5.1.11 module [34].

7.2.4 Density functional theory

DFT calculations were performed using the ORCA package [35]; adapting the method described earlier in chapter 5 and in D. Pauwels *et al.* [36]. To mimic the solvent effect, a dielectric surrounding with the dielectric constant of water according to the COSMO model was used [37]. For the geometry optimisations, the Becke-Perdew density functional (BP86) [38–40] and the split-valence plus polarisation (SVP) basis sets [41] were used for all atoms. The energy was converged to 1×10^{-8} Hartree (E_h), and the convergence tolerances in the geometry optimisation were 3×10^{-4} E_h/Bohr for the gradient and 5×10^{-6} E_h for the total energy. For benchmarking, single-point calculations with the B3LYP/EPR-II, B3LYP/6-31+G**, and PWPB95/EPRII functional/basis sets [42–45] were used to predict the EPR spectral parameters from the optimised geometries. Since static structures are assumed in the DFT computations, the computations should be done for the different conformers that are caused by rotations of the molecule in solution. Table S2 shows calculated EPR parameters of the different conformers as a result of rotation around the N-C_α bond. The green blocks indicate the dihedral angles, which are thermally allowed at 298 K (± 0.0009 E_h).

7.2.5 Colour tests

In-lab Marquis colour test kits with concentrated sulphuric acid and 37% formaldehyde were prepared in the laboratory and the tests were conducted according to the United Nations recommended guidelines [13]. Commercial Marquis colour tests for ecstasy

were purchased from EZ Test (Amsterdam, The Netherlands). Colour tests were performed according to the producer's instructions, by adding little sample material (i.e., in powder form), about the size of a pinhead to the test vial, mixing and observing the colour change visually.

7.3 Results and discussion

7.3.1 Electro-oxidation of MDMA at G-SPE

To define the electrochemical profile of MDMA in ecstasy (XTC) samples, the voltammetric behaviour of MDMA at G-SPEs was first explored in phosphate-buffered saline (PBS) using three electrochemical techniques, i.e. cyclic voltammetry (CV), linear sweep voltammetry (LSV) and square wave voltammetry (SWV). Initially, CV was performed at pH 7 as a first screening method to understand the redox behaviour of MDMA in the measuring conditions. The resulting cyclic voltammogram presented an irreversible oxidation peak at +1.06 V and an anodic feature at +1.26 V (Figure 7.1a). Subsequently, SWV was employed as the electroanalytical technique to enhance the peak resolution and sensitivity of MDMA analysis. Moreover, a baseline-corrected SWV indicated the characteristic but more pronounced oxidation peak at +1.04 V (peak P1) (Figure 7.1b). Because of the linear current response and excellent reproducibility, SWV was chosen as the main electrochemical method for this study. More information about the electrochemical experiments is given in ref [33].
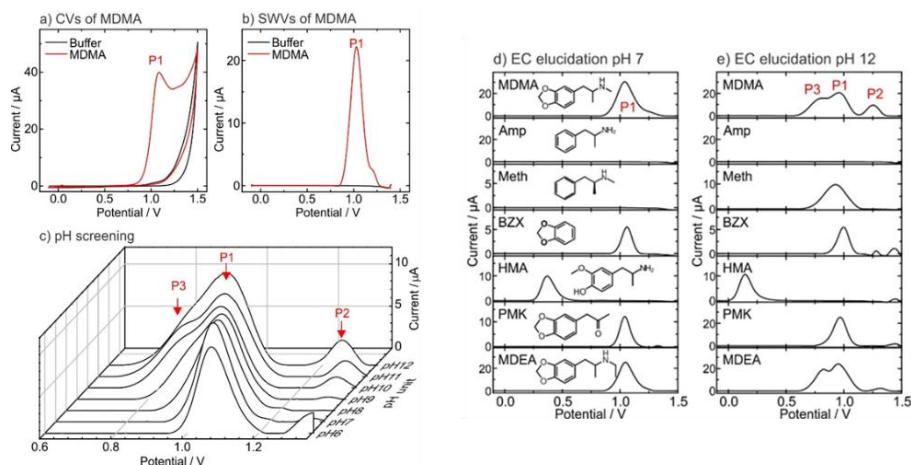

Figure 7.1.(a) Cyclic voltammogram and (b) baseline-corrected square wave voltammogram of 1 mM MDMA in PBS solution (pH 7) at a G-SPE, scan rate 50 mV/s (black), (c) baseline-corrected SWVs of 1 mM MDMA in PBS solutions at different pHs (6-12), and (d) baseline-corrected SWVs of 1mM MDMA and structurally related compounds at pH 7 and (e) pH 12 (right) PBS solution. The chemical structures of the respective compounds are indicated at the side of the voltammograms. The dotted lines show the typical oxidation peak of MDMA appearing at both pH 7 and pH 12.

Following the choice of the voltammetric technique, it is important to comprehend the influence of the pH on the oxidation process and to define the electrochemical profile of MDMA at different pH conditions. For this purpose, SWV was performed for 1 mM MDMA in PBS over a broad pH range (pH 1-13) (Figure S7.1). The characteristic peak (P1) was observed throughout the entire pH range, slightly shifting to more negative potentials as the pH increases (Figure 7.1c). Besides, an anodic shoulder appears at +1.26 V starting from pH 7 (P2), leading to a well-defined peak at alkaline conditions, as well as another oxidation shoulder appeared at lower potentials at basic pH (P3). These peaks define the profile of MDMA at different measuring pH conditions. To better understand the process of MDMA oxidation behind these peaks, as a first step, structurally similar compounds (i.e. MDEA, PMK and BZX) were subjected to SWV at pH 7 (Figure 7.1d) and pH 12 (Figure 7.1e).

Through comparison with the literature [28,32], the peak P1 can be linked to the oxidation of the methylenedioxy-functionality present on the aromatic ring (similar to MDEA, PMK and BZX). Moreover, this peak has been ascribed to the oxidation of the aromatic nuclei of the molecule to form radical cations. Thus, the anodic shoulder peak P2 (+1.26 V) starting from pH 7, clearly visible at pH 12 (Figure 7.1e) for MDMA, MDEA, PMK and BZX can be attributed to the further oxidation of the polymeric species from the radical cation generated earlier. The additional peak (P3) appears at +0.77 V as a shoulder of P1 when the pH is greater than the pK_a value of MDMA (pK_a = 9.9, strongly basic) [46] in MDMA and MDEA, whereas they are absent for PMK, BZX and AMP. This suggests that P3 is related to the oxidation of the secondary amine linked to the aromatic ring with methylenedioxy-functionality. From the above experiments, it is also clear that the electrochemical profile of MDMA can be enriched by changing from pH 4 (one redox process), to pH 9 (two redox processes) and further to pH 12 (three redox processes).

To evidence the formation of a radical cation in the oxidation of MDMA, EPR was employed. We have utilised this technique by analysing the samples after performing a short *ex-situ* electrolysis at G-SPEs using PBS. Due to the fact that the methylenedioxy-functionality is both oxidised in pH 7 and 12, an EPR study was only performed in the pH 7 solution. 1 mM MDMA was subjected to amperometry at +0.98 V for 30 minutes using G-SPE at ambient conditions. The solution (25 µL) was then transferred to a small capillary tube for EPR measurements. No detectable signals were seen (Figure 7.2), possibly due to the high instability of radical cations formed in the aqueous solution. To characterise the radical cations, an excess amount of PBN (structure given in Figure 7.3) was added to the solution during the electrochemistry, acting as a spin-trap, which reacts with the reactive radical and forms a more stable radical detectable by EPR. Figure 7.2 shows the X-band CW EPR spectra (in black, accumulated over 40 scans) of MDMA with excess PBN. The spectra appear as a triplet of doublets, which agrees with nitroxide radicals formed by the reaction of PBN with radicals [47]. Besides, the spectra of control experiments measured using similar settings showed insignificant EPR signals.
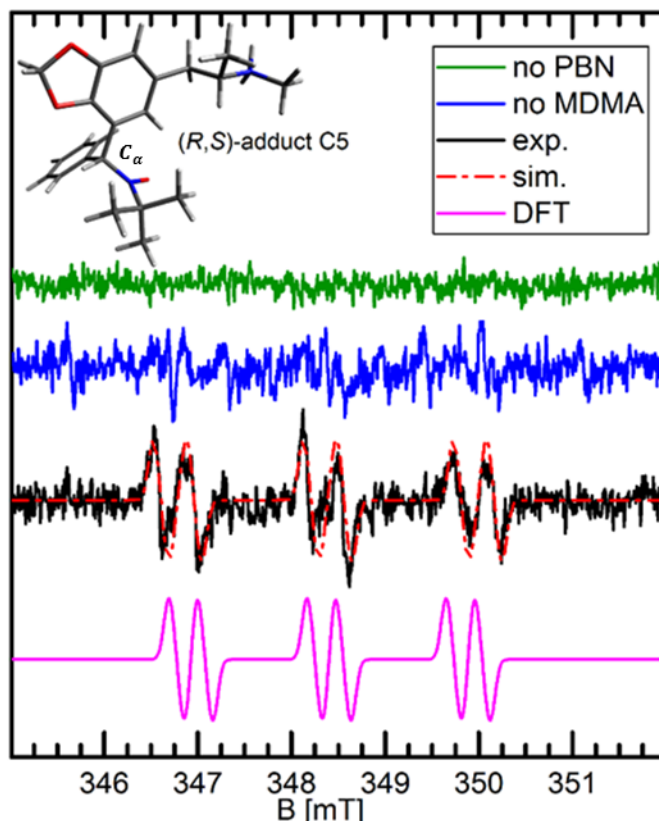
Figure 7.2 X-band CW EPR spectra of 1 mM MDMA.HCl with 50 mM PBN after controlled potential electrolysis in PB solution at pH 7 (black), the corresponding control experiments in the absence of MDMA (green) or PBN (blue), simulation of the experimental spectra (red), and the spectra of (R,S)-adduct C5 derived from density functional theory (DFT) calculations (magenta). The parameters for the simulations were g_{iso} =2.0055, A_N =45.0 MHz, $A_{H\alpha}$ =9.8 MHz, and the calculations were g_{iso} =2.0054, A_N =41.5 MHz, $A_{H\alpha}$ =8.5 MHz. A geometry optimised molecular model of (R,S)-adduct C5 is also depicted..

Parameters such as isotropic g-value (g_{iso}) and the isotropic hyperfine interactions (A_N, $A_{H\alpha}$) between the unpaired electron and the adjacent magnetic nuclei were obtained from the simulation of the spectra. The values of isotropic ^{14}N and ^1H hyperfine coupling constants ($A_{N=}$45.0 MHz, $A_{H\alpha}$= 9.8 MHz), are suggestive of carbon-centred radicals that have been trapped by PBN.
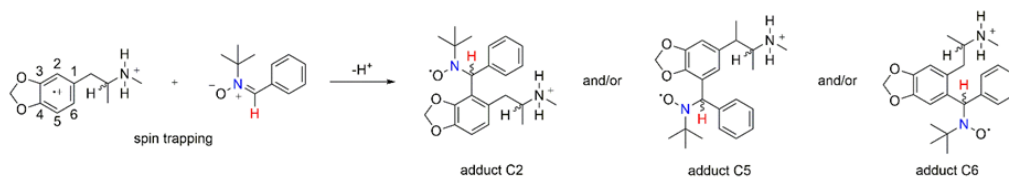

Figure 7.3. Possible reaction pathways of the spin-trapping of MDMA by PBN in PBS at pH 7

A series of molecular models of the possible PBN-MDMA radical adducts (Figure 7.3) were constructed, and their geometries were optimised by density functional theory

(DFT) (Figure S7.2). The choice of basis sets and functionals were based on the previously published method [48]. The series included adducts formed by spin-trapping at the three different unsubstituted carbons (C2, C5 or C6) on the proposed aromatic radical cation, as well as diastereomers formed by the spin-trapping reaction on racemic MDMA. The models were also protonated ($pK_{a(MDMA)} \sim 9.9$ [49]). The corresponding EPR parameters were calculated for each optimised structure as well as thermally allowed conformers which were then averaged (Table S7.1 and Table S7.2). See the method outlined in chapter 5 for more details. From these calculations, the EPR parameters of the PBN-MDMA radical adducts where the spin-trapping occurred at the C5 ((R,R)-adduct C5 and (R,S)-adduct C5) were in close agreement with the experimental data (Figure 7.2, Table S7.2,), suggesting these to be the most likely products, providing strong evidence of radical cation formation in the MDMA oxidation process.

Radical adducts with PBN at C5 suggest that the unstable radical cation, in the absence of any spin trap, would undergo rapid dimerisation or polymerisation and/or passivate the working electrode surface in an electrochemical setup. Further electrochemical experiments provide evidence of the formation of a passivation layer by the radical formation after the SWV, which correlates with our EPR as detailed in [33].

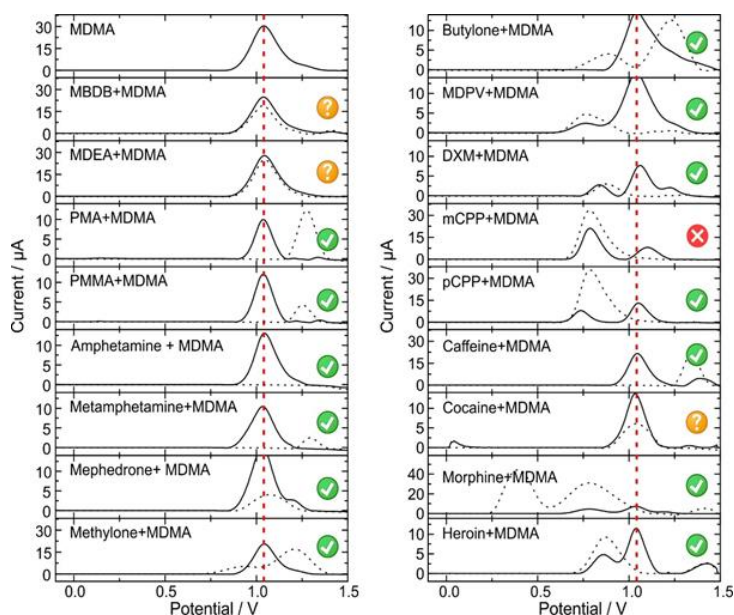## 7.3.2 Electrochemical analysis of XTC related compounds

Figure 7.4. SWVs for MDMA related psychoactive compounds in 1mM standard solutions (dotted curves) and as binary mixtures with 1 mM MDMA (full curves) in PBS pH 7 at G-SPEs. The question mark indicates overlapping signals of the compounds with the MDMA signal, resulting in a false positive. Cross indicates peak shift and/or suppression of the MDMA signal in binary mixtures, resulting in a false negative.

Following the mechanistic elucidation, it is also essential to assess the analytical capability of the proposed screening method by evaluating the efficiency of the

technique to detect MDMA in the presence of common adulterants and cutting agents found in street samples [2,6–8]. Therefore, the voltammetric behaviour was firstly investigated in binary mixtures to detect possible overlaying peaks in the electrochemical profile (EP) region of MDMA in PBS at pH 7 by SWV. A positive result for MDMA was considered if the peak potential of the signal fits into the profile region of MDMA (E_p value between 1.053 V - 1.034 V).

A series of psychoactive compounds (encountered in XTC tablets) was analysed and compared with the profile of MDMA for interference assessment (Figure 7.4). For this reason, pure compounds and binary mixtures of MDMA with potential interferent (equimolar concentration at 1 mM) were interrogated in PBS pH 7 by SWV. Most of the investigated compounds did not pose problems for MDMA detection displaying peaks outside the profile region of MDMA. Nonetheless, methylenedioxy-related (MDx) compounds, such as MDEA and MBDB, share a methylenedioxy functionality with MDMA, and thus oxidise at the same potential, resulting in false positives. However, mephedrone can become a false positive as the oxidation peak is allocated at the same potentials as MDMA. A challenge is raised by cocaine, which oxidises at 1.038 V, overlapping with the signal of MDMA and thus resulting in a false positive in the absence of MDMA. Interestingly, mCPP shifted the MDMA oxidation peak towards a more positive potential, leading to false negatives. Adulterants (i.e., caffeine and DXM) did not hinder the determination of MDMA. To overcome the issues of false positives and negatives, the effect of pH 12 on the electrochemical response of these compounds and mixtures was further investigated (Figure S7.3). The electrochemical response of each sample is discussed in detail in the original article [33].

7.3.3 Presumptive colour tests versus electrochemical strategy for MDMA analysis

To define the potential of electrochemistry for the on-site sensing of ecstasy, the SWV results of the XTC related compounds and mixtures were compared with regular on-site tests (i.e., presumptive colour test) obtained with both laboratory-made Marquis reagent and commercially available Marquis test kits (Table S7.3). A more detailed comparison between the different methods is shown in ref [33].

In short, the sensitivity of the colour test, electrochemical approach at pH 7 and electrochemical approach at pH 12 for the binary mixtures and pure compounds was determined to be 62.5%, 87.5% and 93.75%, respectively, whereas the specificity was determined to be 63.16%, 78.95% and 89.47%, respectively. This indicates that the electrochemical approach is highly sensitive in detecting the presence of MDMA in mixtures, especially at pH 12, in comparison to presumptive colour tests. However, in future work, the ideal approach would be to have an electrochemical methodology that differentiates MDMA from other drugs as well with only one test.

7.3.4 Electrochemical analysis of street samples

The electrochemical detection of MDMA in 21 random ecstasy street samples was carried out at pH 7 (see details in [33]). The additional test in pH 12 was not executed here because the additional accuracy it could provide does not outmatch the added time and effort for this set of ecstasy street samples. The results were compared with confirmatory tests from regular laboratory methods (i.e., GC-MS and GC-FID). All the MDMA containing samples gave the desired "Positive" result. The sample with MDEA also displayed a "Positive" result (false positive, FP) due to MDEA having the same oxidation potential as that of MDMA. However, this does not represent a major problem as MDEA is also an illicit substance. Remarkably, samples containing illicit drugs such as ketamine, amphetamine and even mCPP were correctly identified as "Negative". Additionally, the methamphetamine precursor APAAN was also subjected to analysis and correctly identified as "Negative". For the 21 random street samples tested, the accuracy of the electrochemical method was 95%, showing high promises for the use of the proposed method in the field.

7.4 Conclusion

This chapter highlights the use of spin-trap EPR to unravel reaction mechanisms when developing new electrochemical sensors.
We have demonstrated a rapid and selective electrochemical screening to detect MDMA in XTC pills and powder in confiscated samples by using unmodified G-SPE. The MDMA oxidation at G-SPEs has been explored by a combined EPR-DFT approach and SWV, unravelling the oxidation processes occurring during the electrochemical interrogation. The proposed strategy of electrochemical screening by performing SWV at pH 7 has demonstrated to give a more sensitive and selective detection of MDMA either in pure or binary mixtures when compared to other on-site methods such as the Marquis colour tests, and the electrochemical strategy showed an outstanding accuracy for detecting MDMA in 21 street samples of different compositions. Overall, the developed electrochemical strategy represents progress for the portable detection of illicit drugs in the field which will set the next army of tools to hinder drug trafficking and drug consumption among society.
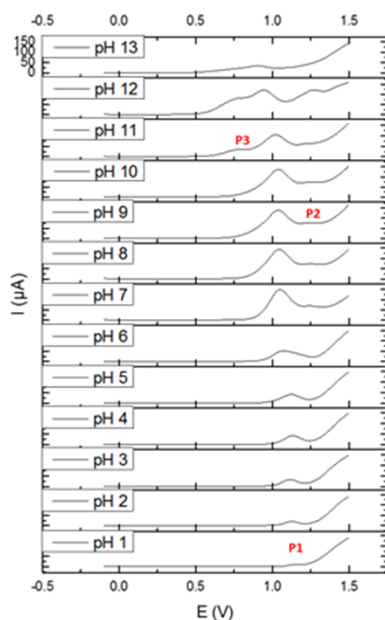
7.5 Supporting information

Figure S7.1 Square wave voltammograms for 1 mM MDMA solutions in PBS of different pH values depicting peaks P1, P2 and P3

MDMA is a racemic mixture. Spin-trapping of MDMA derived radicals introduces a second chiral centre, resulting in two diastereomeric pairs of enantiomers, (*R,R* and *S,S* or *R,S* and *S,R*). Enantiomers are not distinguishable by EPR, therefore, DFT calculations have been performed for *R,R* and *R,S* isomers only.

Table S7.1. Calculated EPR parameters for thermally allowed conformers derived from varying the N-C$_\alpha$ bond dihedral angles

	g_{iso}	A_N (MHz)	$A_{H\alpha}$ (MHz)
Simulation of experiment	2.0055	45.0	9.8
Calculated (*R,R*)-adduct C2	2.0045	46.1	1.03
Calculated (*R,S*)-adduct C2	2.0038	44.4	3.8
Calculated (*R,R*)-adduct C5	2.0057	42.2	10.5
Calculated (*R,S*)-adduct C5	2.0054	41.5	8.5
Calculated (*R,R*)-adduct C6	2.0065	41.9	11.1
Calculated (*R,S*)-adduct C6	2.0066	41.0	10.0

Table S7.2. Calculated EPR parameters for thermally allowed (green blocks) conformers derived from varying the N-C$_\alpha$ bond dihedral angles.

(R,R)-adduct C2	Angle	Energy (Eh)	g_{iso}	$A_{H\alpha}$ (MHz)	$A_{N(nitroxide)}$ (MHz)	$A_{N(amine)}$ (MHz)
	-30	-1190.6753	2.0049	61.95	49.38	0.46
	-20	-1190.6771	2.0059	54.27	46.62	-0.73
	-10	-1190.6780	2.0055	40.03	45.61	-0.69
Min.	0	-1190.6782	2.0042	28.61	45.87	0.55
	10	-1190.6781	2.0039	16.65	46.88	3.24
	20	-1190.6770	2.0047	8.71	46.45	4.87
	30	-1190.6756	2.0038	3.94	45.33	4.78
Avg. green			2.0045	28.43	46.12	1.03

(R,S)-adduct C2	Angle	Energy (Eh)	g_{iso}	$A_{H\alpha}$ (MHz)	$A_{N(nitroxide)}$ (MHz)	$A_{N(amine)}$ (MHz)
	-30	-1190.6889	2.0044	22.23	47.29	-0.74
	-20	-1190.6892	2.0039	13.53	45.53	0.12
	-10	-1190.6897	2.0037	6.44	44.84	2.20
Min.	0	-1190.6902	2.0036	2.17	44.34	3.89
	10	-1190.6894	2.0042	0.91	44.06	5.17
	20	-1190.6880	2.0059	2.85	43.90	5.9
	30	-1190.6859	2.0063	7.91	43.44	5.58
Avg. green			2.0038	3.17	44.41	3.75

(R,R)-adduct C5	Angle	Energy (Eh)	g_{iso}	$A_{H\alpha}$ (MHz)	$A_{N(nitroxide)}$ (MHz)	$A_{N(amine)}$ (MHz)
	-30					
	-20	-1190.6955	2.0064	27.12	45.83	-0.00
	-10	-1190.6962	2.0061	17.22	44.31	-0.00
Min.	0	-1190.6968	2.0059	9.15	42.61	-0.00
	10	-1190.6963	2.0050	5.21	39.71	-0.00
	20	-1190.6953	2.0047	1.18	39.62	-0.00
	30	-1190.6943	2.0052	1.07	38.98	0.05
Avg. green			2.0057	10.52	42.21	-0.00

(R,S)-adduct C5	Angle	Energy (Eh)	g_{iso}	$A_{H\alpha}$ (MHz)	$A_{N(nitroxide)}$ (MHz)	$A_{N(amine)}$ (MHz)
	-30	-1190.6949	2.0067	28.11	46.04	-0.00
	-20	-1190.6955	2.0061	18.26	44.36	-0.00
	-10	-1190.6957	2.0056	12.87	39.68	-0.00
Min.	0	-1190.6959	2.0053	5.99	40.14	-0.00
	10	-1190.6952	2.0050	1.61	40.43	-0.00
	20	-1190.6950	2.0050	0.99	39.59	0.00
	30	-1190.6955	2.0052	4.64	39.59	0.00
	40	-1190.6958	2.0053	7.84	43.63	0.00
	50	-1190.6952	2.0054	15.77	44.39	0.00
	60	-1190.6944	2.0052	25.31	45.71	0.00
Avg. green			2.0054	8.5	41.48	0.00

(R,R)-adduct C6	Angle	Energy (Eh)	g_{iso}	$A_{H\alpha}$ (MHz)	$A_{N(nitroxide)}$ (MHz)	$A_{N(amine)}$ (MHz)
	-40	-1190.6862	2.0067	7.41	41.52	-0.00
	-30	-1190.6880	2.0062	7.41	41.52	-0.00
	-20	-1190.6884	2.0065	23.06	44.23	-0.00
	-10	-1190.6883	2.0066	14.06	42.79	-0.00
Min	0	-1190.6886	2.0065	7.48	41.04	-0.00
	10	-1190.6879	2.0068	3.31	40.05	-0.01

|	20	-1190.4856	2.0058	0.64	39.96	-0.00
	30	-1190.6835	2.0063	1.44	3924	-0.00
Avg green			2.0065	11.06	41.93	-0.00
(*R,S*)-adduct C6						
	Angle	**Energy (Eh)**	g_{iso}	$A_{H\alpha}$ **(MHz)**	$A_{N(nitroxide)}$ **(MHz)**	$A_{N(amine)}$ **(MHz)**
	-30					
	-20	-1190.6850	2.0070	28.67	45.70	0.03
	-10	-1190.6860	2.0071	19.67	43.65	0.04
Min.	0	-1190.6864	2.0066	12.06	41.58	0.04
	10	-1190.6859	2.0062	6.05	39.90	0.05
	20	-1190.5856	2.0064	2.20	39.04	0.04
	30	-1190.6837	2.0069	0.55	39.29	0.04
Avg. green			2.0066	9.99	41.04	0.04
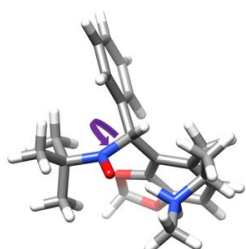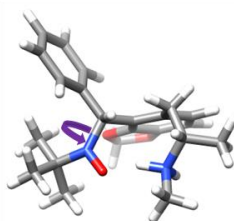
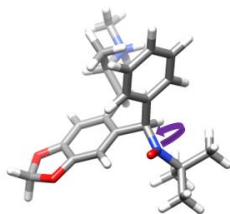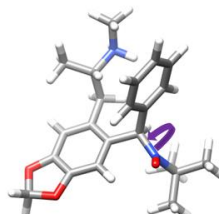(R,R)-adduct C2   (R,S)-adduct C2
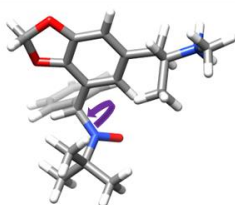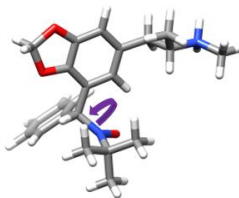
(R,R)-adduct C5   (R,S)-adduct C5

(R,R)-adduct C6   (R,S)-adduct C6

Figure S7.2. Optimised structure of the different possible PBN-MDMA adducts. The purple arrow indicates the N-C$_\alpha$ bond where the thermally allowed rotations take place around it.

Table S7.3. Presumptive colour tests versus SWV results

Sample content	Colour tests result		SWV result	
	Marquis test	EZ test	pH 7	pH 12
MDMA (M)	TP	TP	TP	TP
MBDB	**FP**	**FP**	**FP**	**FP**
MBDB + M	TP	TP	TP	TP
MDEA	**FP**	**FP**	**FP**	**FP**
MDEA + M	TP	TP	TP	TP
PMMA	TN	TN	TN	TN
PMMA + M	TP	TP	TP	TP
PMA	TN	TN	TN	TN
PMA + M	TP	TP	TP	TP
Amphetamine	TN	TN	TN	TN
Amphetamine + M	**FN**	**FN**	TP	TP
Methamphetamine	TN	TN	TN	TN
Methamphetamine + M	**FN**	**FN**	TP	TP
Mephedrone	TN	TN	TN	TN
Mephedrone + M	**FN**	**FN**	TP	TP
Butylone	TN	TN	TN	TN
Butylone + M	**FN**	**FN**	TP	TP
Methylone	TN	TN	TN	TN
Methylone + M	**FN**	**FN**	TP	TP
MDPV	TN	TN	TN	TN
MDPV + M	**FN**	**FN**	TP	TP
DXM	**FP**	**FP**	TN	TN
DXM + M	TP	TP	TP	TP
mCPP	TN	TN	TN	TN
mCPP + M	TP	TP	**FN**	TP
pCPP	TN	TN	TN	TN
pCPP + M	TP	TP	TP	TP
Caffeine	TN	TN	TN	TN
Caffeine + M	TP	TP	TP	TP
Morphine	**FP**	**FP**	TN	TN
Morphine + M	TP	TP	TP	**FN**
Cocaine	**FP**	**FP**	**FP**	TN
Codeine	**FP**	**FP**	**FP**	TN
Heroin	**FP**	**FP**	TN	TN
Ketamine	TN	TN	TN	TN

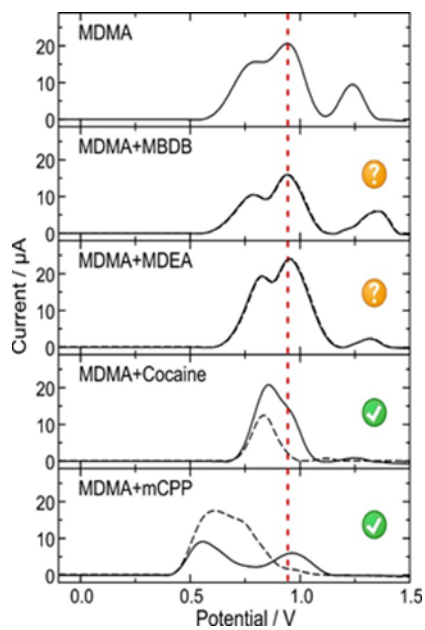*TN, true negative; TP, true positive; FN, false negative; FP, false positive*

Figure S7.3. SWVs for MDMA related psychoactive compounds as 1 mM standard solutions and as binary mixtures with

7.6 References

[1] European Monitoring Centre for Drugs and Drug Addiction and Europol, *EU Drug Markets Report 2019* (Lisbon, 2019).

[2] EMCDDA, *Recent Changes in Europe's MDMA/Ecstasy Market*, EMCDDA Rapid Commun. 5 (2016).

[3] H. Chung and S. Choe, *Amphetamine-Type Stimulants in Drug Testing*, Mass Spectrom. Lett. **10**, 1 (2019).

[4] United Nations Office on Drugs and Crime, *World Drug Report 2021*, https://www.unodc.org/unodc/en/data-and-analysis/wdr2021.html.

[5] C. Cole, L. Jones, J. Mcveigh, A. Kicman, Q. Syed, and M. Bellis, *CUT: A Guide to Adulterants, Bulking Agents and Other Contaminants Found in Illicit Drugs* (John Moores Universit, Liverpool, 2010).

[6] J. J. Palamar, A. Salomone, M. Vincenti, and C. M. Cleland, *Detection of "Bath Salts" and Other Novel Psychoactive Substances in Hair Samples of Ecstasy/MDMA/"Molly" Users*, Drug Alcohol Depend. **161**, 200 (2016).

[7] J. Mazina, V. Aleksejev, T. Ivkina, M. Kaljurand, and L. Poryvkina, *Qualitative Detection of Illegal Drugs (Cocaine, Heroin and MDMA) in Seized Street Samples Based on SFS Data and ANN: Validation of Method*, J. Chemom. **26**, 442 (2012).

[8] R. V. Moreira, J. L. da Costa, M. R. Menezes, and D. L. A. de Faria, *Accessing the Chemical Profile of Ecstasy Tablets Seized in São Paulo (Brazil) by FT-Raman Spectroscopy*, Vib. Spectrosc. **87**, 104 (2016).

[9] I. Baer, The Analysis of Excipients in Ecstasy Tablets and Their Contribution in a Drug Profiling, Université de Lausanne, 2007.

[10] N. T. Lappas and C. M. Lappas, *Forensic Toxicology: Principles and Concepts*, 1st ed. (Academic press, Cambridge, Massachusetts, 2016).

[11] J. I. Khan, T. J. Kennedy, and D. R. Christian, *Basic Principles of Forensic Chemistry* (Humana Press, Totowa, NJ, 2012).

[12] Rebecca A. Murray et. al., *Putting an Ecstasy Test Kit to the Test: Harm Reduction or Harm Induction?*, Pharmacotherapy **23**, 1238 (2003).

[13] United Nations Office on Drugs and Crime Vienna, *Recommended Methods for the Identification and Analysis If Amphentamine, Methamphetamine and Their Ring-Substituted Analogues in Seized Materials* (United Nations Publications, New York, 2006).

[14] A. M. Camilleri and D. Caldicott, *Underground Pill Testing, down Under*, Forensic Sci. Int. **151**, 53 (2005).

[15] J. Eliaerts, P. Dardenne, N. Meert, F. Van Durme, N. Samyn, K. Janssens, and K. De Wael, *Rapid Classification and Quantification of Cocaine in Seized Powders with ATR-FTIR and Chemometrics*, Drug Test. Anal. **9**, 1480 (2017).

[16] C. Weyermann, Y. Mimoune, F. Anglada, G. Massonnet, P. Esseiva, and P. Buzzini, *Applications of a Transportable Raman Spectrometer for the in Situ Detection of Controlled Substances at Border Controls*, Forensic Sci. Int. **209**, 21 (2011).

[17] H. Brown, B. Oktem, A. Windom, V. Doroshenko, and K. Evans-Nguyen, *Direct Analysis in Real Time (DART) and a Portable Mass Spectrometer for*

Rapid Identification of Common and Designer Drugs on-Site, Forensic Chem. **1**, 66 (2016).

[18] W. R. de Araujo, T. M. G. Cardoso, R. G. da Rocha, M. H. P. Santana, R. A. A. Muñoz, E. M. Richter, T. R. L. C. Paixão, and W. K. T. Coltro, *Portable Analytical Platforms for Forensic Chemistry: A Review*, Anal. Chim. Acta **1034**, 1 (2018).

[19] A. Florea, M. de Jong, and K. De Wael, *Electrochemical Strategies for the Detection of Forensic Drugs*, Curr. Opin. Electrochem. **11**, 34 (2018).

[20] J. Schram, M. Parrilla, N. Sleegers, N. Samyn, S. M. Bijvoets, M. W. J. Heerschop, A. L. N. van Nuijs, and K. De Wael, *Identifying Electrochemical Fingerprints of Ketamine with Voltammetry and Liquid Chromatography– Mass Spectrometry for Its Detection in Seized Samples*, Anal. Chem. **92**, 13485 (2020).

[21] M. Parrilla, N. F. Montiel, F. Van Durme, and K. De Wael, *Derivatization of Amphetamine to Allow Its Electrochemical Detection in Illicit Drug Seizures*, Sensors Actuators B. Chem. **337**, 129819 (2021).

[22] N. Felipe Montiel, M. Parrilla, V. Beltrán, G. Nuyts, F. Van Durme, and K. De Wael, *The Opportunity of 6-Monoacetylmorphine to Selectively Detect Heroin at Preanodized Screen Printed Electrodes*, Talanta **226**, 122005 (2021).

[23] G. Murilo Alves, A. Soares Castro, B. R. McCord, and M. F. de Oliveira, *MDMA Electrochemical Determination and Behavior at Carbon Screen-Printed Electrodes: Cheap Tools for Forensic Applications*, Electroanalysis **33**, 635 (2021).

[24] R. Zhang, K. Fu, F. Zou, H. Bai, G. Zhang, F. Liang, and Q. Liu, *Highly Sensitive Electrochemical Sensor Based on Pt Nanoparticles/Carbon Nanohorns for Simultaneous Determination of Morphine and MDMA in Biological Samples*, Electrochim. Acta **370**, 137803 (2021).

[25] R. A. S. Couto, S. S. Costa, B. Mounssef, J. G. Pacheco, E. Fernandes, F. Carvalho, C. M. P. Rodrigues, C. Delerue-Matos, A. A. C. Braga, L. Moreira Gonçalves, and M. B. Quinaz, *Electrochemical Sensing of Ecstasy with Electropolymerized Molecularly Imprinted Poly(o-Phenylenediamine) Polymer on the Surface of Disposable Screen-Printed Carbon Electrodes*, Sensors Actuators, B Chem. **290**, 378 (2019).

[26] É. Naomi Oiye, J. Midori Toia Katayama, M. Fernanda Muzetti Ribeiro, L. Oka Duarte, R. de Castro Baker Botelho, A. José Ipólito, B. Royston McCord, and M. Firmino de Oliveira, *Voltammetric Detection of 3,4-Methylenedioxymethamphetamine (Mdma) in Saliva in Low Cost Systems*, Forensic Chem. **20**, 100268 (2020).

[27] A. Doménech, R. Aucejo, J. Alarcón, and P. Navarro, *Electrocatalysis of the Oxidation of Methylenedioxyamphetamines at Electrodes Modified with Cerium-Doped Zirconias*, Electrochem. Commun. **6**, 719 (2004).

[28] E. M. P. J. Garrido, J. M. P. J. Garrido, N. Milhazes, F. Borges, and A. M. Oliveira-Brett, *Electrochemical Oxidation of Amphetamine-like Drugs and Application to Electroanalysis of Ecstasy in Human Serum*, Bioelectrochemistry **79**, 77 (2010).

[29] M. C. Tadini, M. A. Balbino, I. C. Eleoterio, L. S. De Oliveira, L. G. Dias, G. Jean-François Demets, and M. F. De Oliveira, *Developing Electrodes*

Chemically Modified with Cucurbit[6]Uril to Detect 3,4-Methylenedioxymethamphetamine (MDMA) by Voltammetry, Electrochim. Acta **121**, 188 (2014).

[30]   N. Milhazes, P. Martins, E. Uriarte, J. Garrido, R. Calheiros, M. P. M. Marques, and F. Borges, *Electrochemical and Spectroscopic Characterisation of Amphetamine-like Drugs: Application to the Screening of 3,4-Methylenedioxymethamphetamine (MDMA) and Its Synthetic Precursors*, Anal. Chim. Acta **596**, 231 (2007).

[31]   L. R. Cumba, J. P. Smith, K. Y. Zuway, O. B. Sutcliffe, D. R. do Carmo, and C. E. Banks, *Forensic Electrochemistry: Simultaneous Voltammetric Detection of MDMA and Its Fatal Counterpart "Dr Death" (PMA)*, Anal. Methods **8**, 142 (2016).

[32]   K. R. Teófilo, L. C. Arantes, P. A. Marinho, A. A. Macedo, D. M. Pimentel, D. P. Rocha, A. C. de Oliveira, E. M. Richter, R. A. A. Munoz, and W. T. P. dos Santos, *Electrochemical Detection of 3,4-Methylenedioxymethamphetamine (Ecstasy) Using a Boron-Doped Diamond Electrode with Differential Pulse Voltammetry: Simple and Fast Screening Method for Application in Forensic Analysis*, Microchem. J. **157**, 105088 (2020).

[33]   S. Thiruvottriyur Shanmugam, R. Van Echelpoel, G. Boeye, J. Eliaerts, M. Samanipour, H. Y. V. Ching, A. Florea, S. Van Doorslaer, F. Van Durme, N. Samyn, M. Parrilla, and K. De Wael, *Towards Developing a Screening Strategy for Ecstasy: Revealing the Electrochemical Profile*, ChemElectroChem **8**, 4826 (2021).

[34]   S. Stoll and A. Schweiger, *EasySpin, a Comprehensive Software Package for Spectral Simulation and Analysis in EPR*, J. Magn. Reson. **178**, 42 (2006).

[35]   F. Neese, *The ORCA Program System*, Wiley Interdiscip. Rev. Comput. Mol. Sci. **2**, 73 (2012).

[36]   D. Pauwels, H. Y. Vincent Ching, M. Samanipour, S. Neukermans, J. Hereijgers, S. Van Doorslaer, K. De Wael, and T. Breugelmans, *Identifying Intermediates in the Reductive Intramolecular Cyclisation of Allyl 2-Bromobenzyl Ether by an Improved Electron Paramagnetic Resonance Spectroelectrochemical Electrode Design Combined with Density Functional Theory Calculations*, Electrochim. Acta **271**, 10 (2018).

[37]   S. Sinnecker, A. Rajendran, A. Klamt, M. Diedenhofen, and F. Neese, *Calculation of Solvent Shifts on Electronic g -Tensors with the Conductor-Like Screening Model (COSMO) and Its Self-Consistent Generalization to Real Solvents (Direct COSMO-RS)*, J. Phys. Chem. A **110**, 2235 (2006).

[38]   J. P. Perdew, *Density-Functional Approximation for the Correlation Energy of the Inhomogeneous Electron Gas*, Phys. Rev. B **33**, 8822 (1986).

[39]   J. P. Perdew, *Erratum: Density-Functional Approximation for the Correlation Energy of the Inhomogeneous Electron Gas*, Phys. Rev. B **34**, 7406 (1986).

[40]   A. D. Becke, *Density-Functional Exchange-Energy Approximation with Correct Asymptotic Behavior*, Phys. Rev. A **38**, 3098 (1988).

[41]   A. Schäfer, H. Horn, and R. Ahlrichs, *Fully Optimized Contracted Gaussian Basis Sets for Atoms Li to Kr*, J. Chem. Phys. **97**, 2571 (1992).

[42]   P. J. Stephens, F. J. Devlin, C. F. Chabalowski, and M. J. Frisch, *Ab Initio Calculation of Vibrational Absorption and Circular Dichroism Spectra Using*

Density Functional Force Fields, J. Phys. Chem. **98**, 11623 (1994).

[43] D. Moran, A. C. Simmonett, F. E. Leach, W. D. Allen, P. V. R. Schleyer, and H. F. Schaefer, *Popular Theoretical Methods Predict Benzene and Arenes to Be Nonplanar*, J. Am. Chem. Soc. **128**, 9342 (2006).

[44] L. Goerigk and S. Grimme, *Efficient and Accurate Double-Hybrid-Meta-GGA Density Functionals—Evaluation with the Extended GMTKN30 Database for General Main Group Thermochemistry, Kinetics, and Noncovalent Interactions*, J. Chem. Theory Comput. **7**, 291 (2011).

[45] V. Barone, *Structure, Magnetic Properties and Reactivities of Open-Shell Species From Density Functional and Self-Consistent Hybrid Methods*, in *Recent Advances in Density Functional Methods* (1995), pp. 287–334.

[46] M. Navarro, S. Pichini, M. Farré, J. Ortuño, P. N. Roset, J. Segura, and R. De La Torre, *Usefulness of Saliva for Measurement of 3,4-Methylenedioxymethamphetamine and Its Metabolites: Correlation with Plasma Drug Concentrations and Effect of Salivary PH*, Clin. Chem. **47**, 1788 (2001).

[47] G. R. Buettner, *Spin Trapping - Electron-Spin-Resonance Parameters of Spin Adducts*, Free Radic. Bio. Med. **3**, 259 (1987).

[48] D. Pauwels, H. Y. Vincent Ching, M. Samanipour, S. Neukermans, J. Hereijgers, S. Van Doorslaer, K. De Wael, and T. Breugelmans, *Identifying Intermediates in the Reductive Intramolecular Cyclisation of Allyl 2-Bromobenzyl Ether by an Improved Electron Paramagnetic Resonance Spectroelectrochemical Electrode Design Combined with Density Functional Theory Calculations*, Electrochim. Acta **271**, 10 (2018).

[49] N. A. Desrosiers, A. J. Barnes, R. L. Hartman, K. B. Scheidweiler, E. A. Kolbrich-Spargo, D. A. Gorelick, R. S. Goodwin, and M. A. Huestis, *Oral Fluid and Plasma 3,4-Methylenedioxymethamphetamine (MDMA) and Metabolite Correlation after Controlled Oral MDMA Administration*, Anal. Bioanal. Chem. **405**, 4067 (2013).

Reactive oxygen species formation at Pt nanoparticles

This chapter focuses on a combined electrochemical and electron paramagnetic resonance (EPR) procedure for the study of oxygen reduction reaction (ORR) intermediates generated at Pt nanoparticles (NPs). It concerns a collaborative study with the Electrochemical and Surface Engineering research group at VUB (PI A. Hubin). Using *ex-situ* spin-trap EPR complemented by electrochemical analysis, we show that we can detect and identify the free radicals that are produced during the ORR through trapping with 5,5-dimethyl-1-pyrroline-N-oxide (DMPO). These radicals are otherwise difficult to detect. Experiments with 5-(diethoxyphosphoryl)-5-methyl-1-pyrroline-N-oxide (DEPMPO) as a spin trap show no clear evidence of ˙DEPMPO-OOH and indicate that only ˙OH radicals are trapped during the ORR. The results of this study serve as a functional proof of concept for further research on the identification of radical ORR intermediates in solution. The chapter focuses on the EPR investigation while summarising the essential points of the electrochemical experiments.

This chapter was redrafted from:

Own contribution: Performing and analysing the EPR experiments.

8.1 Introduction

The loss of electrochemical active surface area (EASA) and degradation of the proton exchange membrane are two major problems plaguing the cost-effectiveness of Pt nanoparticles (NPs) for use as electrocatalysts in proton-exchange membrane fuel cells [1,2]. It has been proposed that both problems may be caused by the presence of free reactive oxygen species (ROS) in solution, which cause Pt dissolution and attack the carbon support [3–6]. These free ROS are the desorbed intermediates from the ORR that takes place at the surface of the NPs. Numerous studies have attempted to shed light on the ORR mechanism in acidic conditions, often with conflicting conclusions [7–9]. Electrochemical studies typically employ surface analysis techniques to investigate the absorbed intermediates or make use of the rotating ring disk electrode (RRDE) technique to study the desorbed intermediates in solution [10,11]. Literature on fuel cell technology generally focuses on membrane degradation using commercial catalysts and cites hydroxyl radicals ($^{\bullet}$OH) as the responsible intermediates [12,13]. This is due to evidence of $^{\bullet}$OH formation at both anode and cathode [14,15], as well as its strong oxidative properties compared to superoxide ($O_2^{\bullet -}$) and hydroperoxyl ($^{\bullet}$OOH) [16].

As shown in previous chapters, EPR spectroscopy in the presence of DMPO as a spin trap can help to elucidate the nature of the free radicals.

In this chapter, we propose and validate a procedure using *ex-situ* EPR complemented by electrochemical analysis to detect, identify and semi-quantify the produced radicals. Relating the charge consumed during the electrochemical reaction with the intensity of the observed EPR signal is a starting point to better quantify the free radicals produced in the reaction. This approach will be further developed to allow us to investigate the ORR mechanism through the identification of the soluble intermediates.

8.2 Materials and methods

8.2.1 Electrochemical methods

The electrochemical experiments were carried out in a standard three electrode setup in 0.1 M $HClO_4$ electrolyte prepared from concentrated $HClO_4$ (Sigma) and Millipore water. DMPO (TCI Chemicals) was added to the electrolyte as a spin trapping agent at the start of each chronoamperometry (CA) experiment. For ORR measurements, the electrolyte was saturated with O_2 before and during the CA experiments by bubbling pure O_2 through the solution. For the deoxygenated CA experiments, the electrolyte was purged with N_2 instead of O_2 before and during electrolysis. All CA experiments were performed at 0.5 V vs Ag/AgCl near the onset potential of the ORR. This work was a proof-of-concept for the (semi)quantitative correlation between EPR and electrochemical data.

Custom working electrodes with a large surface area were constructed by embedding a vitreous carbon disk in an epoxy resin and milling it in a cylindrical shape. This was necessary to generate enough radicals to capture and detect *via* spin trapping EPR spectroscopy. Nanoporous Pt NPs were deposited on the carbon surface *via* a double pulse electrodeposition process [17]. This procedure was chosen for several reasons. Pt

NPs exhibiting nanoporosity have been reported to have high catalytic activity towards the ORR [18–20]. These particles are sensitive to degradation, possibly due to Pt dissolution *via* soluble radicals [21], making them ideal for our study. Secondly, the procedure ensures that all the electrocatalytic material is located in areas accessible during the ORR. Nine electrodepositions were prepared according to the same procedure and used as working electrodes. A saturated Ag/AgCl electrode was used as a reference, and a Pt mesh was used as the counter electrode. More information about the electrochemical cell is given in the published paper [22].
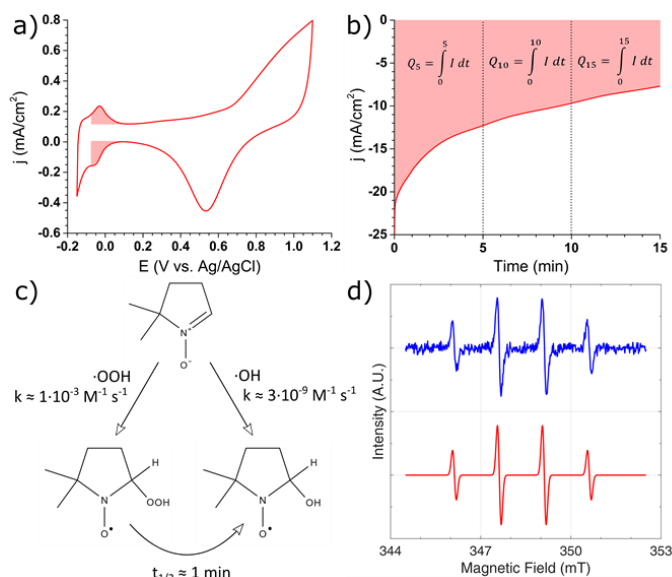

Figure 8.1 (a) Cyclic voltammogram obtained during pre-treatment of the electrode in deoxygenated 0.1 M HClO$_4$ (scan rate 50 mV/s). EASA was determined by integration of the filled areas, which correspond to the hydrogen underpotential deposition. (b) A typical chronoamperogram, obtained during the CA experiments using the custom electrodes in oxygenated 0.1 M HClO$_4$ at 0.5 V vs. Ag/AgCl. The filled area indicates the charge Q passed during the ORR. (c) Reaction pathways of DMPO with •OH and •OOH to the respective radical adducts. •DMPO-OOH spontaneously degrades to •DMPO-OH with a half-life of approximately one minute. (d) Typical experimental (blue) and simulated (red) EPR spectra of •DMPO-OH. •DMPO-OH shows a characteristic equivalent hyperfine coupling of four peaks with 1:2:2:1 amplitude ratios. The simulated spectra were double integrated and normalised to the EASA to obtain the EPR intensity DI. See Table 8.1 for details of the EPR simulations.

Before every CA experiment, a cyclic voltammetry (CV) experiment was performed as a surface cleaning pre-treatment in 0.1 M HClO$_4$ that was cleaned with nitrogen and kept under nitrogen atmosphere during CV. The electrochemical active surface area (EASA) for each experiment was determined by integrating the hydrogen underpotential deposition peaks from the cyclic voltammogram (Figure 8.1a). We found that the EASA of our NPs changed with each experiment due to the degradation of the NPs [18,23]. Three experiments were performed in oxygenated electrolyte and one in deoxygenated electrolyte for each electrodeposited electrode. The cumulative consumed charge was determined from the chronoamperograms by integrating the current (Figure

8.1b) and is from here on referred to as charge Q. For EPR analysis, samples were taken from the stirred electrolyte at five-minute intervals and analysed in the EPR spectrometer in continuous-wave mode. Each measurement consists of 25 consecutive single scans taken during these five minutes that were averaged to improve the signal-to-noise ratio. No radical adduct was detected after 15 minutes in samples that did not undergo electrolysis. CV experiments in deoxygenated electrolyte with DMPO confirmed that DMPO is not reduced or oxidised within the electrochemical window of our experiments (see Figure S8.1) [24,25]. The consumed charge in CA experiments in oxygenated electrolyte is lower in the presence of DMPO (see Figure S8.2). This indicates that DMPO adsorbs on the electrode surface and decreases catalytic activity, but it may also be partially due to DMPO reacting with free intermediates that may otherwise have reacted further. However, since there is no change in ORR onset potential upon the addition of DMPO, we do not believe DMPO is influencing the reaction mechanism (see Figure S8.3).

8.2.2 Electron paramagnetic resonance

For all experiments in presence of DMPO, the EPR measurements were performed in an X-band Bruker E580 Elexsys spectrometer in continuous-wave (CW) mode with a microwave power of 10 mW, sweep width of 8 mT, modulation amplitude 0.3 mT and sweep time of 11 s. Each measurement was taken by averaging 25 consecutive single sweeps to improve the signal-to-noise ratio. The total measurement time per sample was a little under five minutes.

For the DEPMPO experiments, the sweep width was 11 mT and the sweep time was 13 s. Each measurement was taken by averaging 75 consecutive single sweeps to improve the signal-to-noise ratio. The total measurement time per sample was fifteen minutes.

Figure 8.1c shows the reaction pathways of $^{\bullet}$OH and $^{\bullet}$OOH with DMPO to form their respective radical adducts. Unfortunately, $^{\bullet}$DMPO-OOH quickly decays to $^{\bullet}$DMPO-OH in ambient conditions [26]. Although trapping of $^{\bullet}$OOH has a much lower rate constant compared to that of $^{\bullet}$OH, we expect no trapping competition between $^{\bullet}$OH and $^{\bullet}$OOH because an excess of DMPO is present in the solution [27–29].

The EPR spectra were simulated using EasySpin 5.2.28 [30], a toolbox in MATLAB R2020a only showed a $^{\bullet}$DMPO-OH signal. A typical experimental spectrum and simulation are shown in Figure 8.1d.

Despite our high electrode surface area and averaging over multiple single EPR sweeps, some spectra still show a low signal-to-noise ratio. In order to avoid offsets due to the noise, each spectrum was first simulated. This spectrum was then double integrated and normalised to the EASA, the result of which is referred to as the EPR intensity DI (double integral) in Figure 8.2 and 8.3 and related discussions.

8.3   Result and discussion

Figure 8.2b shows a plot of the EPR intensity DI versus time for three electrodes performed in oxygenated electrolyte. As the experiments progress over time, the average EPR intensity DI of the ˙DMPO-OH signal becomes stronger. The biggest increase is observed after the first five minutes, after which the intensity slowly increases for some electrodes or stays constant for others. The increase in EPR intensity DI is consistent with the increase in consumed charge Q, as is evident from Figure 8.2a, which shows a plot of the charge Q passed during the ORR over time as calculated according to Figure 8.1b. In experiments where the increase in consumed charge is more significant, the EPR intensity DI is also greater, with the exception of PtNP9.

We performed control CA experiments in the deoxygenated electrolyte to check that the ˙DMPO-OH signal indeed originates from the trapping of free ORR radicals and not from an electrochemical reaction of DMPO on the electrode surface. No EPR signal was observed in the absence of dissolved oxygen. Initial experiments were performed at lower potentials more favourable for H_2O_2 production and yielded false-positive results due to Fenton side reactions with iron ions that were present in the initial system. We would like to stress the importance of avoiding any iron-based substances, such as Hamilton needles, to prevent such mishaps.
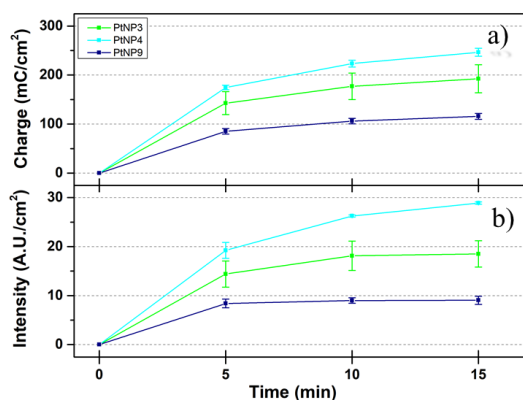

Figure 8.2 Plots of (a) the average charge Q and (b) the average EPR intensity DI versus time and PtNP3 (green), PtNP4 (cyan) and PtNP9 (dark blue) correspond to the experimental results of three of the electrodeposited electrodes. Error bars are normal standard error, with N =3.

Figure 8.3 shows the EPR intensity Q versus the charge DI of the oxygenated CA experiments shown in Figure 8.2a and b for all nine electrodes that were used in this study. The results were fitted with a linear fit. A linear relation between consumed charge and EPR intensity DI is observed that is consistent over time. We can thus conclude that the number of radicals produced during the ORR is directly proportional to the charge that is measured. The relation does not appear to be influenced by the morphology of the electrodeposited electrode within the studied NP distributions, nor by the electrochemically active surface area shown in Figure S8.2. The study is currently being extended with different electrodeposited electrode morphologies, commercially available electrodes and the effect of potential [31].
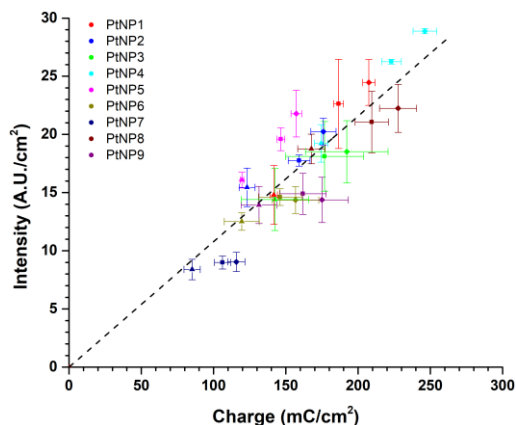
Figure 8.3 Plot of the EPR intensity DI versus the charge Q for all nine electrodeposited electrodes. Circles, triangles, squares and diamonds represent the results after 0, 5, 10 and 15 minutes of electrolysis, respectively. The dotted line is a linear fit of the results. Error bars are normal standard error, with N = 3.

So far, our combined electrochemical and EPR procedure allows for the detection of ORR radicals, but does not directly distinguish between different intermediates due to the fast decay of ˙DMPO-OOH and the poor ˙OOH trapping kinetics (Figure 8.1a). ˙DMPO-OOH would only be detected if the rate of ˙OOH production was high enough, which does not appear to be the case for our system. However, this problem can in principle, be circumvented through the use of a different spin trap: 5-(diethoxyphosphoryl)-5-methyl-1-pyrroline-*N*-oxide (DEPMPO). DEPMPO is a suitable spin trap for ROS but is slightly more reactive towards ˙OOH than DMPO (Figure 8.4a) [32]. In addition, the decay of ˙DEPMPO-OOH to ˙DEPMPO-OH is much slower: ±20 min in acid medium [33]. This is sufficiently large for the time frame of our measurements. Like DMPO, DEPMPO appears to be electrochemically inert within the electrochemical window of our experiments (see Figure S8.2) [24]. Prior to the CA experiment, 10 mM DEPMPO was added to the electrolyte instead of DMPO. Samples were taken before and after electrolysis and analysed immediately in the EPR spectrometer.
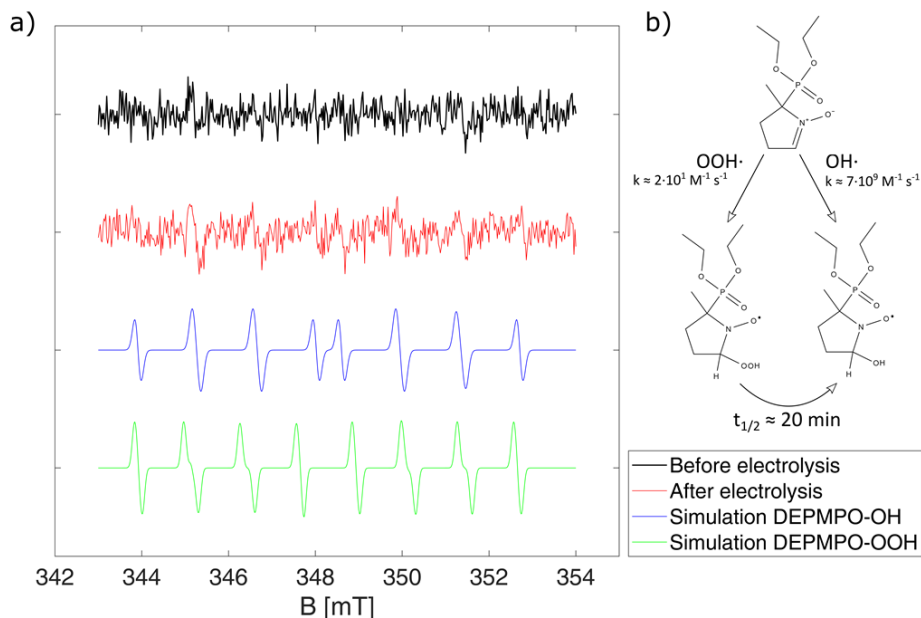
Figure 8.4 (a) EPR spectra taken immediately before (black) and after (red) 15 min of electrolysis in oxygenated 0.1 M HClO₄ at 0.5 V vs Ag/AgCl in presence of 10 mM DEPMPO. Simulations of ˙DEPMPO-OH (blue) and ˙DEPMPO-OOH (green) show that the signals in the experimental spectra belong to ˙DEPMPO-OH. (See Table 8.1 for details of the EPR simulations) (b) Reaction pathways of DEPMPO with ˙OH and ˙OOH to the respective radical adducts. ˙DEPMPO-OOH spontaneously degrades to ˙DMPO-OH with a half-life of approximately 20 minutes.

Figure 8.4 shows the typical spectra that were obtained during the DEPMPO experiments. In the sample taken before electrolysis, a small background signal is present that is likely due to degradation in the bottle. In the sample taken after electrolysis, a similar signal with a higher intensity is observed. The peaks match those of the simulated spectrum of ˙DEPMPO-OH and agree with spectra of ˙DEPMPO-OH reported in the literature [33,34]. Although the signal is rather weak, the known signature spectrum for ˙DEPMPO-OOH is not noticeable. A DFT study by Keith & Jacobs calculated that while the binding strength of ˙OOH is about twice as strong that of ˙OH on Pt surfaces, desorption of ˙OOH still takes place [35]. Other studies have postulated the ˙OOH intermediate as a possible soluble intermediate [8,9]. Therefore, the absence of the ˙OOH adduct suggests that mainly ˙OH intermediates desorb during the ORR. This would mean that either no ˙OOH intermediate is formed, that it reacts before it can desorb, or that the desorbed quantity of ˙OOH is below the detection limit. We hope to investigate this matter further in future by increasing the charge consumed during the ORR, thus increasing the intensity of the EPR signal of any DEPMPO adducts. Hopefully, this will provide us with definite proof of the absence or presence of ˙DEPMPO-OOH.

Table 8.1 Simulation parameters for •DMPO-OH, •DEPMPO-OH and •DEPMPO-H.

product	g_{iso}	$A_P(mT)$	$A_N(mT)$	$A_{H\beta}(mT)$	$A_{H\gamma}(mT)$	$A_{H\gamma}(mT)$	ref
•DMPO-OH	2.0055	-	1.51	1.52	-	-	tw[a]
•DMPO-OH	2.0055	-	1.50	1.50	-	-	ref[b]
•DEPMPO-OH	2.0057	4.70	1.40	1.31	0.03 (3H)	-	tw[a]
•DEPMPO-OH	2.0059	4.74	1.40	1.30	0.03 (3H)	-	ref[c]
•DEPMPO-OOH	2.0058	5.02	1.30	1.13	0.08 (3H)	0.04 (6H)	tw[a]
•DEPMPO-OOH	2.0059	5.25	1.34	1.19	0.08 (1H)	0.04 (6H)	ref[c]

a: this work, b: ref [36],.c: ref [37]

8.4   Conclusion

Using a combined electrochemical and *ex-situ* EPR approach, we have shown that we can detect, identify and (semi)quantify free oxygen radicals produced by the ORR at porous electrodeposited Pt NPs. Experiments with DEPMPO as a spin trap show that only •DEPMPO-OH is detectably formed. We show that our approach is a valid additional technique for investigating the reaction mechanism of the ORR from solution. Our procedure allows for a more rigorous quantification of free radicals involved in electrochemical reactions and may provide future insights on the identification of soluble intermediates responsible for the degradation of electrocatalysts.

8.5 Supporting information

8.5.1 Electrochemical activity spin traps on Pt nanoparticles

Figure S8.1 shows CVs obtained in deoxygenated 0.1 M $HClO_4$ in the presence or absence of 2.5 mM DMPO. In the absence of DMPO, the characteristic hydrogen underpotential deposition absorption and desorption peaks are visible, whereas these disappear in the presence of DMPO. This is a strong indication that DMPO adsorbs to the electrode surface and thus decreases catalyst activity. The Pt oxide reductive peak is clearly visible around 0.5 V for both cases. No peaks corresponding to the reduction or oxidation of DMPO are visible within this electrochemical window.
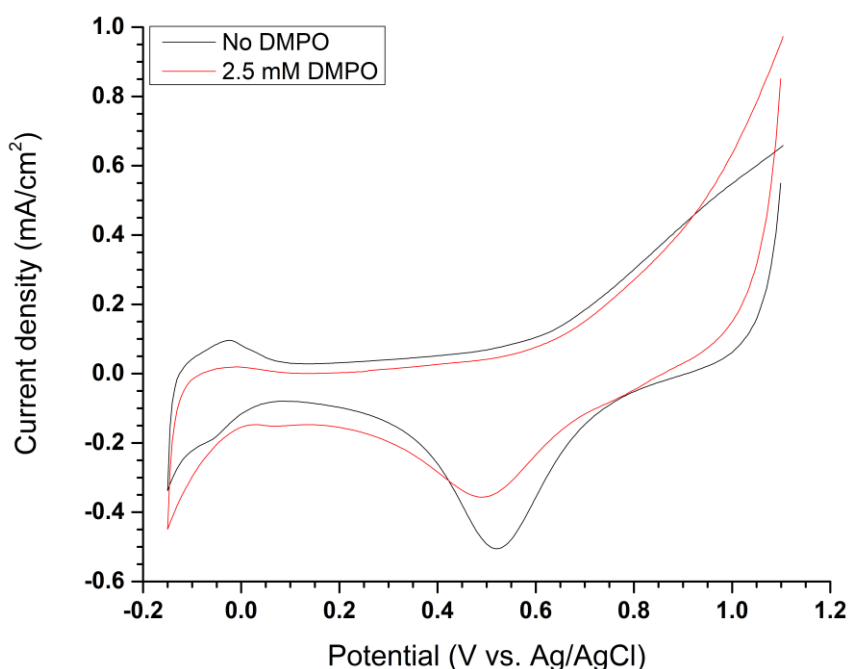

Figure S8.1: Cyclic voltammograms in deoxygenated 0.1 M $HClO_4$ with DMPO (red) and without DMPO (black). Scan speed is 50 mV/s.

Figure S8.2 shows CVs obtained in oxygenated 0.1 M $HClO_4$ in the presence or absence of 5 mM DMPO or 5 mM DEPMPO. In presence of DMPO (red), the overall current density decreases, which is likely due to the surface adsorption of DMPO as well as DMPO reacting with soluble intermediates that may otherwise have further reacted on the surface. The ORR onset potential is not or barely changed in presence of DMPO, indicating that DMPO does not affect the reaction mechanism. In presence of 5 mM DEPMPO (green), a similar effect is observed: the current density is drastically decreased, but the ORR onset potential is not.
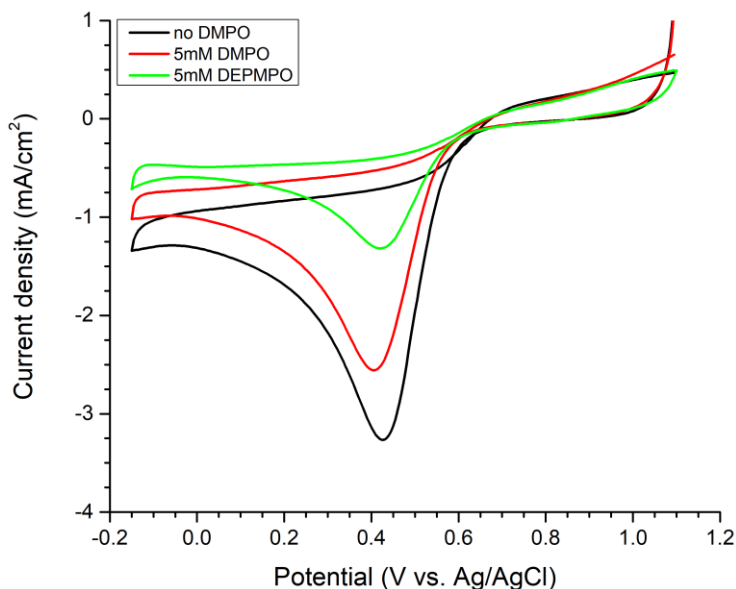
Figure S8.2: Cyclic voltammograms in oxygenated 0.1 M HClO₄ without DMPO (black), with 5 mM DMPO (red) and with 5 mM DEPMPO (green). Scan speed is 50 mV/s.

Figure S8.3 shows the first two minutes of chronoamperograms obtained in oxygenated 0.1 M HClO₄ in the presence or absence of 5 mM DMPO or 5 mM DEPMPO. In presence of DMPO (red/orange) or DEPMPO (green/dark green), the overall current density is decreased, but apart from the higher initial current density in the DMPO experiments, no major difference can be discerned between either spin trap.
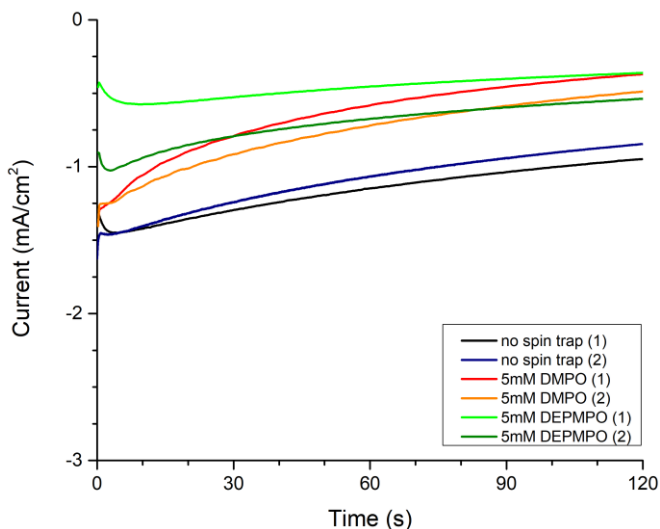

Figure S8.3: Chronoamperograms in oxygenated 0.1 M HClO₄ without spin trap (black/blue), with 5 mM DMPO (red/orange) and with 5 mM DEPMPO (green/dark green). Scan speed is 50 mV/s.

8.6   References

[1]   Y. Nosaka, K. Ohtaka, N. Ohguri, and A. Y. Nosaka, *Detection of OH Radicals Generated in Polymer Electrolyte Membranes of Fuel Cells*, J. Electrochem. Soc. **158**, B430 (2011).

[2]   J. Ustarroz, I. M. Ornelas, G. Zhang, D. Perry, M. Kang, C. L. Bentley, M. Walker, and P. R. Unwin, *Mobility and Poisoning of Mass-Selected Platinum Nanoclusters during the Oxygen Reduction Reaction*, ACS Catal. **8**, 6775 (2018).

[3]   J. Ustarroz, I. M. Ornelas, G. Zhang, D. Perry, M. Kang, C. L. Bentley, M. Walker, and P. R. Unwin, *Mobility and Poisoning of Mass-Selected Platinum Nanoclusters during the Oxygen Reduction Reaction*, ACS Catal. **8**, 6775 (2018).

[4]   S. Cherevko, N. Kulyk, and K. J. J. Mayrhofer, *Durability of Platinum-Based Fuel Cell Electrocatalysts: Dissolution of Bulk and Nanoscale Platinum*, Nano Energy **29**, 275 (2016).

[5]   J. M. Noël, Y. Yu, and M. V. Mirkin, *Dissolution of Pt at Moderately Negative Potentials during Oxygen Reduction in Water and Organic Media*, Langmuir **29**, 1346 (2013).

[6]   A. Pavlišič, P. Jovanovič, V. S. Šelih, M. Šala, N. Hodnik, and M. Gaberšček, *Platinum Dissolution and Redeposition from Pt/C Fuel Cell Electrocatalyst at Potential Cycling*, J. Electrochem. Soc. **165**, F3161 (2018).

[7]   S. Nayak, I. J. McPherson, and K. A. Vincent, *Adsorbed Intermediates in Oxygen Reduction on Platinum Nanoparticles Observed by In Situ IR Spectroscopy*, Angew. Chemie Int. Ed. **57**, 12855 (2018).

[8]   J. C. Dong, M. Su, V. Briega-Martos, L. Li, J. B. Le, P. Radjenovic, X. S. Zhou, J. M. Feliu, Z. Q. Tian, and J. F. Li, *Direct in Situ Raman Spectroscopic Evidence of Oxygen Reduction Reaction Intermediates at High-Index Pt(Hkl) Surfaces*, J. Am. Chem. Soc. **142**, 715 (2020).

[9]   A. M. Gómez-Marín, J. M. Feliu, and E. Ticianelli, *Oxygen Reduction on Platinum Surfaces in Acid Media: Experimental Evidence of a CECE/DISP Initial Reaction Path*, ACS Catal. **9**, 2238 (2019).

[10]   O. Antoine and R. Durand, *RRDE Study of Oxygen Reduction on Pt Nanoparticles inside Nafion: H2O2 Production in PEMFC Cathode Conditions*, J. Appl. Electrochem. **30**, 839 (2000).

[11]   F. Yin, Y. Liu, S. Wang, C. Wang, and H. Liu, *Validation of H2O2-Mediated Pathway Model for Elucidating Oxygen Reduction Mechanism: Experimental Evidences and Theoretical Simulations*, Electrochim. Acta **313**, 378 (2019).

[12]   A. Panchenko, H. Dilger, J. Kerres, M. Hein, A. Ullrich, T. Kaz, and E. Roduner, *In-Situ Spin Trap Electron Paramagnetic Resonance Study of Fuel Cell Processes*, Phys. Chem. Chem. Phys. **6**, 2891 (2004).

[13]   B. Vogel, E. Aleksandrova, S. Mitov, M. Krafft, A. Dreizler, J. Kerres, M. Hein, and E. Roduner, *Observation of Fuel Cell Membrane Degradation by Ex Situ and In Situ Electron Paramagnetic Resonance*, J. Electrochem. Soc. **155**, B570 (2008).

[14]   H. Wang and G. A. Capuano, *Behavior of Raipore Radiation-Grafted Polymer*

Membranes in H 2 / O 2 Fuel Cells, J. Electrochem. Soc. **145**, 780 (1998).

[15] Y. Nosaka, K. Ohtaka, M. Kitazawa, S. Kishioka, and A. Y. Nosaka, *Spin-Trapping ESR Detection of OH Radicals Generated in the Electrode Reactions for PEFCs*, Electrochem. Solid-State Lett. **12**, B14 (2009).

[16] L. Gubler, S. M. Dockheer, and W. H. Koppenol, *Radical (HO •, H • and HOO •) Formation and Ionomer Degradation in Polymer Electrolyte Fuel Cells*, J. Electrochem. Soc. **158**, B755 (2011).

[17] L. León and J. D. Mozo, *Designing Spectroelectrochemical Cells: A Review*, TrAC Trends Anal. Chem. **102**, 147 (2018).

[18] B. Geboes, J. Ustarroz, K. Sentosun, H. Vanrompay, A. Hubin, S. Bals, and T. Breugelmans, *Electrochemical Behavior of Electrodeposited Nanoporous Pt Catalysts for the Oxygen Reduction Reaction*, ACS Catal. **6**, 5856 (2016).

[19] H. E. M. Hussein, H. Amari, and J. V. Macpherson, *Electrochemical Synthesis of Nanoporous Platinum Nanoparticles Using Laser Pulse Heating: Application to Methanol Oxidation*, ACS Catal. **7**, 7388 (2017).

[20] L. Gan, M. Heggen, R. O'Malley, B. Theobald, and P. Strasser, *Understanding and Controlling Nanoporosity Formation for Improving the Stability of Bimetallic Fuel Cell Catalysts*, Nano Lett. **13**, 1131 (2013).

[21] W. Yu, C. Batchelor-McAuley, X. Chang, N. P. Young, and R. G. Compton, *Porosity Controls the Catalytic Activity of Platinum Nanoparticles*, Phys. Chem. Chem. Phys. **21**, 20415 (2019).

[22] S. den Hartog, M. Samanipour, H. Y. V. Ching, S. Van Doorslaer, T. Breugelmans, A. Hubin, and J. Ustarroz, *Reactive Oxygen Species Formation at Pt Nanoparticles Revisited by Electron Paramagnetic Resonance and Electrochemical Analysis*, Electrochem. Commun. **122**, 106878 (2021).

[23] C. Baldizzone, L. Gan, N. Hodnik, G. P. Keeley, A. Kostka, M. Heggen, P. Strasser, and K. J. J. Mayrhofer, *Stability of Dealloyed Porous Pt/Ni Nanoparticles*, ACS Catal. **5**, 5000 (2015).

[24] G. L. McIntire, H. N. Blount, H. J. Stronks, R. V. Shetty, and E. G. Janzen, *Spin Trapping in Electrochemistry. 2. Aqueous and Nonaqueous Electrochemical Characterizations of Spin Traps*, J. Phys. Chem. **84**, 916 (1980).

[25] J. G. Roberts, M. A. Voinov, A. C. Schmidt, T. I. Smirnova, and L. A. Sombers, *The Hydroxyl Radical Is a Critical Intermediate in the Voltammetric Detection of Hydrogen Peroxide*, J. Am. Chem. Soc. **138**, 2516 (2016).

[26] E. Finkelstein, G. M. Rosen, and E. J. Rauckman, *Spin Trapping of Superoxide and Hydroxyl Radical: Practical Aspects*, Arch. Biochem. Biophys. **200**, 1 (1980).

[27] F. A. Villamena, S. Xia, J. K. Merle, R. Lauricella, B. Tuccio, C. M. Hadad, and J. L. Zweier, *Reactivity of Superoxide Radical Anion with Cyclic Nitrones: Role of Intramolecular H-Bond and Electrostatic Effects*, J. Am. Chem. Soc. **129**, 8177 (2007).

[28] F. A. Villamena, C. M. Hadad, and J. L. Zweier, *Kinetic Study and Theoretical Analysis of Hydroxyl Radical Trapping and Spin Adduct Decay of Alkoxycarbonyl and Dialkoxyphosphoryl Nitrones in Aqueous Media*, J. Phys. Chem. A **107**, 4407 (2003).

[29] F. A. Villamena, J. K. Merle, C. M. Hadad, and J. L. Zweier, *Superoxide*

Radical Anion Adduct of 5,5-Dimethyl-1-Pyrroline N -Oxide (DMPO). 1. The Thermodynamics of Formation and Its Acidity, J. Phys. Chem. A **109**, 6083 (2005).

[30] S. Stoll and A. Schweiger, *EasySpin, a Comprehensive Software Package for Spectral Simulation and Analysis in EPR*, J. Magn. Reson. **178**, 42 (2006).

[31] S. den Hartog, Characterisation of Nanoparticle Electrocatalysts by Combining Electrochemistry with Electron Paramagnetic Resonance, PhD Thesis, Vrije Universiteit Brussel, 2021.

[32] F. A. Villamena and J. L. Zweier, *Detection of Reactive Oxygen and Nitrogen Species by EPR Spin Trapping*, Antioxid. Redox Signal. **6**, 619 (2004).

[33] B. Tuccio, R. Lauricella, C. Fréjaville, J.-C. Bouteiller, and P. Tordo, *Decay of the Hydroperoxyl Spin Adduct of 5-Diethoxyphosphoryl-5-Methyl-1-Pyrroline N-Oxide: An EPR Kinetic Study*, J. Chem. Soc., Perkin Trans. 2 **2**, 295 (1995).

[34] M. Mojovic, M. Vuletic, and G. G. Bacic, *Detection of Oxygen-Centered Radicals Using EPR Spin-Trap DEPMPO: The Effect of Oxygen*, Ann. N. Y. Acad. Sci. **1048**, 471 (2005).

[35] J. A. Keith and T. Jacob, *Theoretical Studies of Potential-Dependent and Competing Mechanisms of the Electrocatalytic Oxygen Reduction Reaction on Pt(111)*, Angew. Chemie Int. Ed. **49**, 9521 (2010).

[36] C. Frejaville, H. Karoui, B. Tuccio, F. Le Moigne, M. Culcasi, S. Pietri, R. Lauricella, and P. Tordo, *5-(Diethoxyphosphoryl)-5-Methyl-1-Pyrroline N-Oxide: A New Efficient Phosphorylated Nitrone for the in Vitro and in Vivo Spin Trapping of Oxygen-Centered Radicals*, J. Med. Chem. **38**, 258 (1995).

[37] G. R. Buettner, *Spin Trapping: ESR Parameters of Spin Adducts 1474 1528V*, Free Radic. Biol. Med. **3**, 259 (1987).

Part IV
Direct EPR spectroelectrochemistry

In-situ SEC-EPR cells, design and validation

In the previous chapters, *ex-situ* EPR measurements as more standard SEC-EPR cells were used. This chapter summarises the design and validation of two different *in-situ* SEC-EPR cells. In the first cell, a versatile electrode is constructed with commercially available indium tin oxide (ITO) on polyethylene terephthalate (PET), which can fit in commonly used EPR flat cells. It allows reproducible electrodeposition of catalytic material combined with sensitive radical detection, owing to its large surface area and minimal disruption to the resonator's Q-factor. The conductivity of the thin semiconductor electrode is high enough to provide desired surface potential within the resonator allowing targeted radical production. The second cell is a hydrodynamic electrochemical flow cell. The created platform enables the fast and accurate screening of new electrocatalytic materials, providing insights into their effects on radical products of a reaction. Furthermore, it is essential that the reaction kinetics are not influenced by the setup, and that mass transfer can be controlled. Our modular design allows for fast and easy replacement of parts and adjustments to electrodes in order to unravel the catalysts' influence on radical formation. The proximity of the pseudo-reference electrode to the working electrode, in combination with the flow and electrode positioning, allows for good potential control. The POM housing allows easy manipulation of the channel and excludes the use of sealing agents. The cell design was prepared by Dr S. Neukermans (ELCAT, Faculty of Applied Engineering, University of Antwerp). I tested and validated both SEC-EPR cells using the electroreduction of benzoquinone (BQ) and methyl viologen (MV). No radical trap was used.

This chapter combines and redrafts parts of:
Sander Neukermans, **Mohammad Samanipour**, H. Y. Vincent Ching, Jonas Hereijgers, Sabine Van Doorslaer, Annick Hubin, and Tom Breugelmans, A Versatile *In-Situ* Electron Paramagnetic Resonance Spectro-electrochemical Approach for Electrocatalyst Research, ChemElectroChem, **7,** 4578, (2020)

Sander Neukermans, Jonas Hereijgers, H.Y. Vincent Ching, **Mohammad Samanipour,** Sabine Van Doorslaer, Annick Hubin, Tom Breugelmans, A continuous *in-situ* EPR electrochemical reactor as a rapid in-depth mechanistic screening tool for electrocatalysis, Electrochemistry Communications, **97,** 42, (2018)

Own contribution: EPR experiments and analysis

9.1 Introduction

The applications and challenges of EPR spectroscopy in combination with electrochemistry were discussed in chapters 1 and 3. It was mentioned already that many *in-situ* SEC-EPR setups use commercial flat cells to avoid Q-factor losses for polar solvents. The working electrodes vary from wires to mesh/gauze structures to metal rods [1,2]. In analytical electrochemistry, flat and uniformly accessible working electrodes are preferable to derive kinetic parameters or the diffusion coefficient. When doing combined experiments for the qualitative detection of radical intermediates, it is desirable that the working electrode has the highest possible electroactive surface to produce the desired radical instantly.

One of the promising substrate materials possessing properties suitable for spectroscopic analysis techniques is Indium Tin Oxide (ITO) or other Transparent Conductive Oxides (TCO) like Aluminum Zinc Oxide (AZO). Multiple papers describe glass-supported ITO as a suitable substrate because of its optical transparency, and others deposited metallic particles on the surface [3–6]. ITO is being used in photovoltaic devices and thus has already been incorporated into EPR setups for electrically detected magnetic resonance [7]. However, the dimensions of commercial glass-supported electrodes do not allow their utilisation in EPR flat cell applications. The combination of *in-situ* UV-VIS/EPR spectroelectrochemistry was exploited by Neudeck and Dunsch in several publications using wire working electrodes [8], laminated Au and Pt meshes [9–11], LIGA electrodes [12] and laminated ITO-glass electrodes [13,14]. The latter focuses on the behaviour of a polypyrrole layer on the surface and other hole-transporting organic substrates. Recently the use of mesoporous layers of ITO particles was reported for water oxidation and alcohol oxidation [15–17] and applied for the investigation of redox reactions in biomolecules. This electrode consisted of a Ti wire decorated with 50 nm ITO particles with the subsequent immobilisation of proteins on the surface and was used in combination with an EPR tube [18].

In the first part of this work, the construction of a promising ITO-on-PET-based EPR-electrochemical setup fitting the commercial Wilmad flat cell for aqueous samples in a rectangular cavity in an X-band EPR spectrometer is demonstrated. The ITO working electrode has a flat surface allowing reproducible integration of (electro)deposited nano-scale catalysts. The construction is inexpensive and straightforward so experiments can easily be repeated multiple times. The setup is applicable in a broad range of reactions in both aqueous and non-aqueous environments and demonstrates reasonable electrochemical behaviour in the EPR flat cell. Consequently, targeted *in-situ* radical generation is possible. It is optically transparent and very thin, which is an improvement compared to the bulk metal electrodes because the material does not significantly interfere with the Q-factor of the resonator. The electrode surface area approaches the maximally available space in the flat cell producing the maximum radical concentration possible. As a proof of concept, the electrodeposition of Ag nanoparticles and NiO layer was performed with consecutive *in-situ* use for the reduction of MV in aqueous solutions and BQ in ACN with detection of their radical intermediates, demonstrating the sensitivity of the constructed electrode.

From an electrochemical perspective, the use of the flat cells has some drawbacks: i) the cell surfaces are mostly irreproducible, ii) the shape of the surface and the small cell size compared to the electrode surface prevent semi-infinite linear diffusion, and iii) the potential control is done by a pseudo reference electrode [2,19], which needs to be well-positioned for data collection to be reliable, *i.e.* adjacent to the working electrode and in a stable environment. Often in static setups, the pseudo reference and the working electrode are positioned in the flat section of the cell where radicals are generated using chronoamperometric techniques. However, the potential of the pseudo reference electrode can fluctuate during the experiment, as reactants are consumed and products are generated that subsequently diffuse from the electrode surface. These shifts in potential cannot be detected before or after the experiment using a known redox couple. Therefore an *in-situ* flow cell was constructed utilising channel electrodes made out of polyoxymethylene (POM) with the advantages of being modular, facilitating flow electrochemistry, allowing good potential control and the use of POM as a sealing agent. We have evaluated this platform using CV and LSV on BQ in water and chronoamperometry coupled to CW EPR at X-band on BQ in ACN and MV in water.

9.2 Materials and methods

9.2.1 Chemicals

Electrochemical measurements were performed in acetonitrile (ACN) (Chem-Lab, HPLC Grade, $\geq$99.9%) and MilliQ water (18.2 MΩ cm^{-1}) with respectively 0.1 M TBAP (Sigma-Aldrich, 99.0 %) and sodium sulphate (Acros Organics, 99.0%) as supporting electrolyte. BQ (Sigma-Aldrich, $\geq$99.5%) solutions were prepared in ACN and MV (Sigma-Aldrich, 98%) in water. Depositions of Ag were performed using 1 mM AgNO$_3$ (Sigma-Aldrich, $\geq$ 99.0%) in ACN with 0.1 M LiClO$_4$ (Acros Organics, >99%). Ni depositions were performed in an aqueous solution with 0.01 M Ni (SO$_3$NH$_2$)$_2$ (Fluka, $\geq$ 99.0%), 0.227 mM NiCl$_2$ (Merck, $\geq$ 97.0%) and 0.025 M H3BO3 (Sigma-Aldrich 99.7%). Toluene was purchased from Merck (Uvasol for spectroscopy). All chemicals were used without any further purification. All solutions for the flow cell were purged with nitrogen before being introduced to the setups.

9.2.2 EPR spectrometry

The EPR spectra were recorded on a Bruker 580 Elexsys spectrometer at X-band (frequencies specified in captions) in continuous wave mode at ambient temperature with a 0.1 mT field modulation amplitude and 100 kHz field modulation frequency,5.12 ms time constant, sweep time of 10.49 s scan^{-1}.
For the flat cell experiments, a 0.2 mW and 0.8 mW microwave power were used for BQ and MV, respectively.
For the flow cell experiments, 0.15 and 1.00 mW microwave power was used for BQ and MV, respectively.
All Q-factors reported were determined by the built-in Q indicator of the Xepr programme. TEMPO (2,2,6,6-Tetramethyl-1-piperidinyloxy, Sigma-Aldrich, 98%)

spin-count calibration was performed in the flat cell for concentrations ranging from 0.5 mM to 0.025 mM. at a power of 0.2 mW, sweep time of 10.49 s scan⁻¹ and with a time constant of 5.12 ms. The integral of the absorption curve was calculated considering that every molecule of TEMPO was EPR active. The same method and settings were used to determine the spin concentration of BQ and MV radicals generated on the custom ITO electrode.

9.2.3 Electrochemistry

All electrochemical experiments for the flat cell were conducted with a PAR VersaSTAT 3 potentiostat. The experiments were performed in bulk, and the depositions were recorded versus a saturated Ag/AgCl reference electrode with a Pt auxiliary electrode in a conventional undivided cell.

Electrochemical measurements for the flow cell were performed using an Autolab PGSTAT302N potentiostat without any need for a current booster. Potentials applied in the experiments were derived from CV cathodic peaks. Electrodes were subsequently polished with 1 µm and 0.3 µm Al_2O_3 powder from Streurs. See ref [20,21] for further details.

9.2.4 Combined setups

In the first set of experiments, combined EPR-spectroelectrochemical measurements were performed in a Wilmad Supracil WG-810-A-Q quartz flat cell assembled, as shown in Figure 9.1. The setup was placed in a TE_{102} rectangular cavity in a Bruker E580 Elexsys spectrometer. Custom-made ITO working electrodes were made using ITO-on-PETmicroscope slides (8-10 Ω sq⁻¹, 200 µm thickness with a 700 nm ITO layer) obtained from SPI supplies and (60 Ω sq⁻¹, 178 µm thickness with a 100 nm ITO layer) from Sigma-Aldrich. This allowed it to fit inside the 500 µm thin gap of the quartz flat cell. The ITO layer of the SPI product had a homogeneous surface promoting reproducible electrodeposition of particles. The increase in conductivity as a function of the ITO layer thickness reaches a plateau as does transmittance at higher wavelengths [22,23]. The work of Do-Hyoung Kim *et al*. even suggests that electromagnetic wave shielding occurs with increasing film thickness [24]. The slides were cut to rectangles of 37.5 x 3.5 mm. The tip of the ITO working electrode was placed at the centre of the flat part, which coincided with the most sensitive section of the resonator. The junction with the connecting Cu wire was kept in the bulk section on top and was shielded by a PP encapsulation using a heat gun whilst being pressed against the semiconductor surface by carbon tape for maximum conductivity.
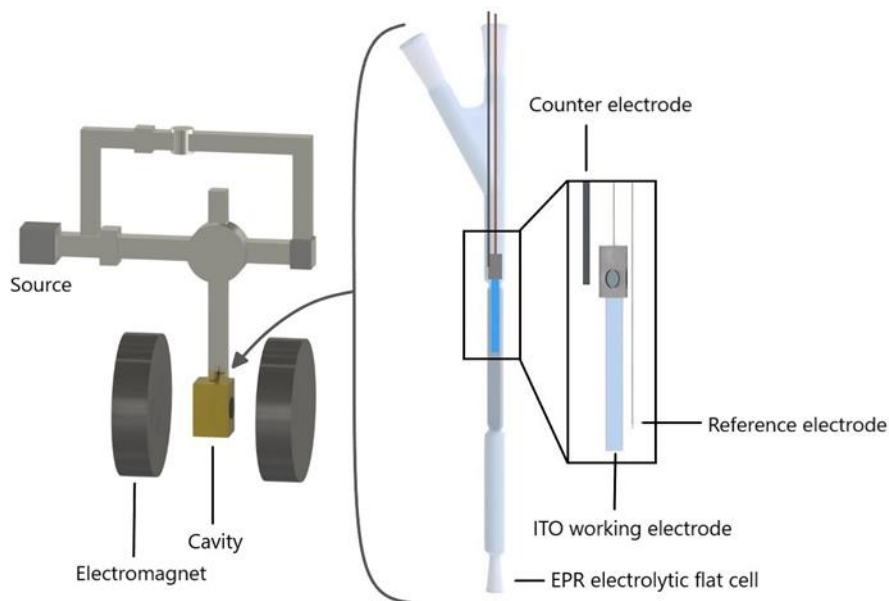
Figure 9.1. Schematic drawing of the EPR-spectroelectrochemical setup

The PP covered 10 mm of the ITO surface resulting in 0.96 cm² exposed working electrode surface area. A PFA coating covering a Ag wire with a diameter of 75 µm was used as pseudo reference electrode (stripped of the PFA at both ends) and positioned as close to the tip of the ITO electrode without causing a short circuit (<1 mm). The Pt auxiliary electrode was placed in the bulk section on top as close to the entry of the flat part as possible. The cell was filled with 1 ml solution, submerging all electrodes while leaving the exposed Cu connection wire dry. This setup provided a cheap, straightforward and versatile method for combined *in-situ* EPR and electrochemical measurements of electrodeposited catalytic materials.

The second constructed cell, a flow cell, was made out of two pieces of POM (Eriks Baudoin), of which one contained a small channel with a width of 6 mm and a height of 0.4 mm. This is an adaptation of the previously reported modular design [25]. The electrodes were embedded in the second part by heat treatment. The working electrode was a silver foil (99.9985%) from Alfa Aesar, the counter electrode was a platinum sheet (99.95%) from Goodfellow, and the pseudo reference electrode was a platinum wire (99.99%) from Science Products. The reference was located <1 mm upstream of the 4 by 5 mm working electrode, and the counter electrode was positioned 3.3 cm downstream of the working electrode and measured 4 by 25 mm (Figure 9.2). It could be further observed that between the working and counter electrode, the use of POM is minimised. From here on, this part will be called 'the window'. This part was positioned in the sensitive part of the resonator. The window provided a visual detection of the formation of coloured radicals and products when not positioned in the resonator. By sealing the setup with the same material, the use of potentially reactive sealing agents was avoided. The POM elements were easy to reproduce, and precious metal components could be recovered for reuse. More details are explained in the related paper [21].
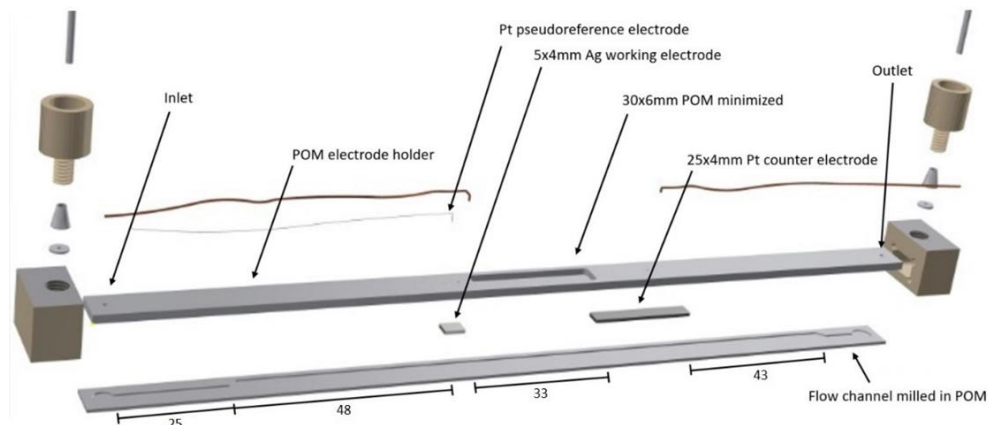

Figure 9.2. Expanded drawing of the in-situ EPR channel electrode

9.3 Results and discussion

9.3.1 Testing ITO-based cell for electrocatalytic research

We first focus on the performance of the ITO-based cell (Figure 9.1). In order to do *in-situ* electrocatalytic research, a catalytic material should first be deposited on the ITO surface. Ag and Ni are active electrode materials for a number of reactions [26–31] and were therefore selected as catalyst materials. They were electrodeposited on the ITO as described in reference [20].

CVs of the bare ITO on PET, and the Ag- or Ni-deposited electrodes were done in an undivided bulk setup and in the EPR flat cell. The reduction of benzoquinone (BQ) in acetonitrile and that of methyl viologen (MV) in water were selected as test cases because they allow the assessment of the setup in both organic and aqueous solutions as well as starting from neutral or positively charged reagents. Reducing BQ with one electron yields the semiquinone radical anion in aprotic environment (Eq. (9.1)). In the flat part of the EPR flat cell, this could be observed visually because of the change in colour of the solution from pale yellow to darker yellow and even orange in higher concentrations. MV^{2+} also undergoes a one electron reduction with the formation of the methyl viologen radical cation (Eq. (9.2)). This radical has a very distinct blue colour, and the 2-electron reduced species is again colourless (Eq. (9.3)).

$$BQ + e^- \rightarrow BQ^{\bullet-} \tag{9.1}$$

$$MV^{2+} + e^- \rightarrow MV^{\bullet+} \tag{9.2}$$

$$MV^{\bullet+} + e^- \rightarrow MV^0 \tag{9.3}$$

$$MV^0 \rightarrow MV^{\bullet+} + e^- \tag{9.4}$$

$$MV^0_{ads} \rightarrow MV^{\bullet+}_{aq} + e^- \tag{9.5}$$

Figure 9.3 shows the response of the bare ITO electrode in both cases (BQ and MV). The splitting between oxidation and reduction peak of BQ was similar for both the bulk cell as the flat cell (0.6 V). The potential shift of 0.9 V between the cells was caused by the use of a pseudo reference electrode in the flat cell. The reduction reaction of BQ in the flat cell did not show a notable reagent depletion fallback after the reduction potential was reached. Methyl viologen was scanned to the second electron transfer in bulk and past the first in the flat cell. The peak splitting of the first wave was equivalent for both measurements (120 mV), and the currents were comparable.
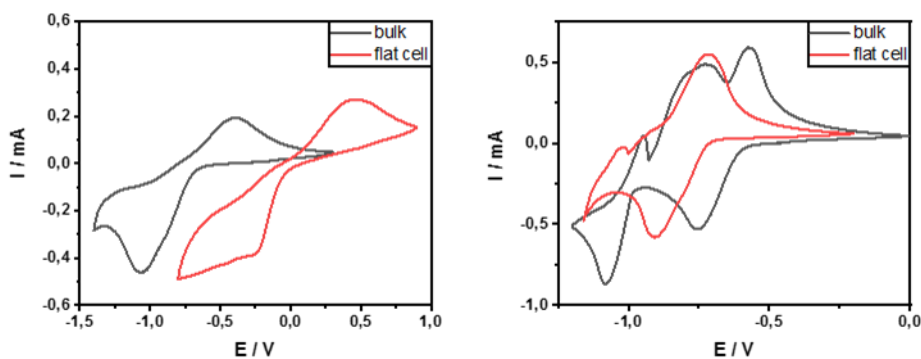

Figure 9.3. CV of 5 mM BQ (left) and 5 mM MV (right) on bare ITO-on-PET electrode in bulk vs (sat.) Ag/AgCl and in EPR flat cell vs Ag wire at 25 mV s^{-1} (not deoxygenated).

Figure 9.4 presents the voltammetric data for the electrode with Ag particles deposited on ITO (Ag/ITO). The bulk experiment showed a bigger reduction current than that in the flat cell. This could be explained by the non-parallel positioning of the ITO surface to the flat cell wall, causing a smaller volume and thus less analyte to reach the surface of the electrode resulting in a lower current. Peak separation for both experiments was similar to that of the bare ITO electrode (0.6 V). A difference exists between these CVs and the ones in Figure 9.3.

A more gradual current response for BQ can be seen between the peaks, which could imply slower kinetics on this electrode or a contribution of the substrate material to the reaction. The back scan for MV^{2+} reduction had, besides the oxidation peak of $MV^{\bullet+}$ radical cation, a clear oxidation peak at a lower potential. It was positioned at similar potentials as the oxidation of the neutral MV^0 in the bulk experiments but was much more pronounced even though the forward scan did not reach the second reduction peak. Some electrode materials promote the formation of an adsorbed MV^0 layer on the surface of which the oxidation peak in the back scan convolutes with its oxidation to $MV^{\bullet+}$ in solution (Eqs. (9.4) and (9.5)), giving a likely explanation.
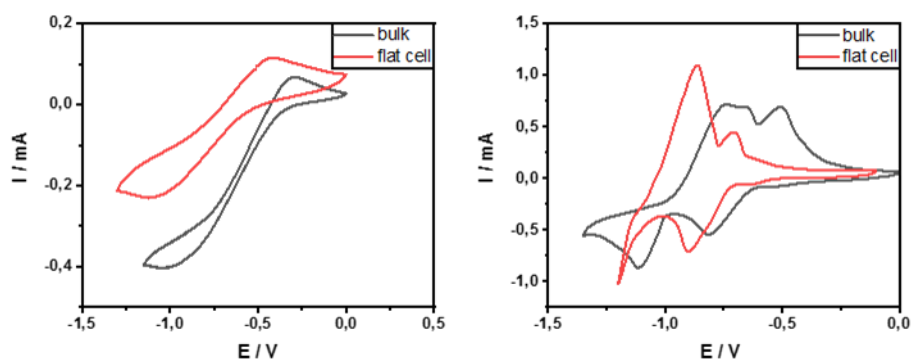
Figure 9.4 CV of 5 mM BQ (left) and 5 mM MV (right) on Ag/ITO-on-PET electrode in bulk vs (sat.) Ag/AgCl and in EPR flat cell vs Ag wire at 25 mV s^{-1} (not deoxygenated).

For BQ reduction, the electrode with a NiO layer deposited on ITO (NiO/ITO) behaved similarly to the analogue Ag/ITO electrode. See [20] for further details.

In the next step, the EPR cell is validated through SEC-EPR experiments. The Q-factor for the empty flat cell in the cavity was 2600 ± 100, which was in accordance with the specifications of the spectrometer for an empty cavity. Introduction of ACN + 0.1 M TBAP led to a Q-factor of 700 ± 100, while H_2O + 0.2 M Na_2SO_4 reduced it even more to 300 ± 100. Introduction of a non-lossy solvent (toluene) lead to a Q-factor of 2000 ± 100. These Q-factors did not change when the ITO electrode was introduced into the electrolyte filled flat cell, which was beneficial for the sensitivity.

in-situ electrolysis experiments were performed as described above. The employed electrodes were bare ITO, Ag/ITO and the NiO/ITO. Potentials in the kinetic region of the corresponding CVs were applied. Figure 9.5 displays the EPR spectra that were obtained for BQ and MV reductions. The EPR spectra were simulated using the following isotropic g and hyperfine values of the BQ radical anion: $g_{BQ} = 2.0050$ with $A_H = 6.75$ MHz (4), while for the MV radical cation $g_{MV} = 2.0024$, $A_N = 11.85$ MHz (2), $A_H = 11.18$ MHz (6), $A_H = 4.4$ MHz (4), $A_H = 3.7$ MHz (4). The numbers between brackets give the number of the equivalent nuclei with the same A_{iso}-value in the vicinity of the paramagnetic centre. These are in accordance with the literature values [32,33].

The spectra showed that for the three electrodes that were utilised, the formed radicals for each reduction reaction were the same, indicating the formed radical was independent of the deposited electrocatalyst. This was as expected, considering the mechanism of the reduction reaction being analogous on each of the catalytic materials and the substrate. The peak intensities differ depending on the electrode due to the different active surface area resulting from the electrodeposition. Comparison of the double integral of the acquired spectra with that of a TEMPO spin-counting calibration gave radical concentrations of approximately 83 µM BQ and 66 µM for MV reduction reactions (Table S9.1 and Table S9.2). When the concentration of BQ was increased, its reduction at the Ag/ITO electrode gave a broadened spectrum (Figure 9.6). Using the same EPR parameters as above, the broadened spectrum can be simulated by simply increasing the Voigt linewidth from $\sigma = 0.02$ mT and $\gamma = 0.034$ mT to $\sigma = 0.144$ mT and $\gamma = 0.095$ mT, where σ and γ are the Gaussian and Lorentzian components, respectively.
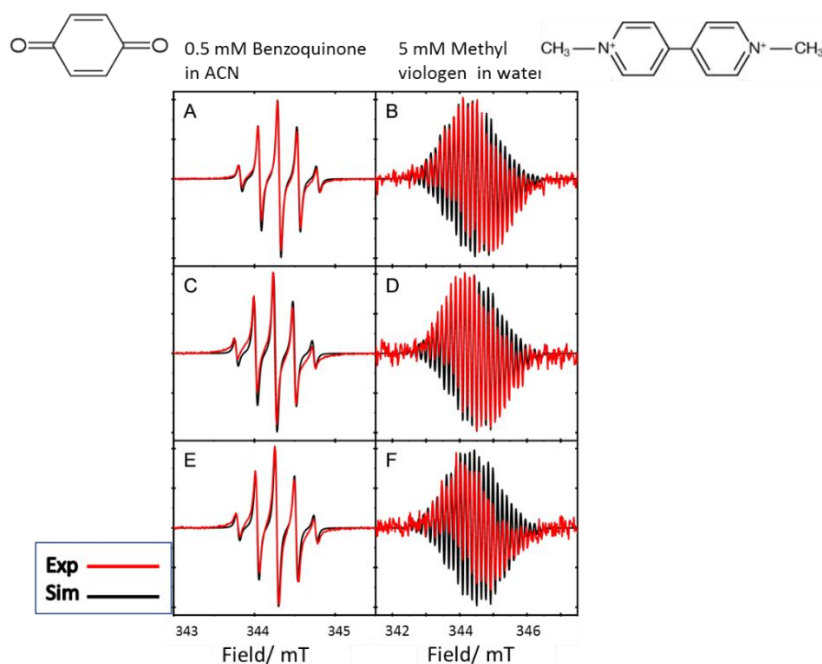
Figure 9.5. EPR spectra obtained from in-situ electrolyzing 0.5 mM BQ at 9.655 ± 0.001 GHz and 0.2 mW microwave power (left) and 5 mM MV at 9.661 ± 0.001 GHz and 0.8 mW microwave power (right) on bare ITO-on-PET (A,B) electrode, Ag/ITO-on-PET (B,C) and NiO/ITO-on-PET (E,F). The spectra are a mean of 10 scans over ~ 105 s. Red: experimental, black: simulation (not deoxygenated).

Broadening could be due to adsorption on the electrode surface and/or higher viscosity of the solution resulting in restricted mobility of the radicals. However, these phenomena were unlikely as broadening was not observed in the lower concentration experiments. A more probable reason for the spectral broadening is that a high concentration of the BQ radical anion is being generated, leading to dipolar interaction between the radicals. The high radical concentration may also result in the formation of aggregates which reduces the mobility of the radicals, further broadening the spectra. The combination of favourable conditions for electrodeposition of catalytic material on the commercial ITO-on-PET substrate with generation of paramagnetic species or radicals in the sensitive part of the resonator on a high surface area electrode is critical for the detection of short-living radicals (lifetime shorter than the timescale of 1 scan) in electrocatalytic research.
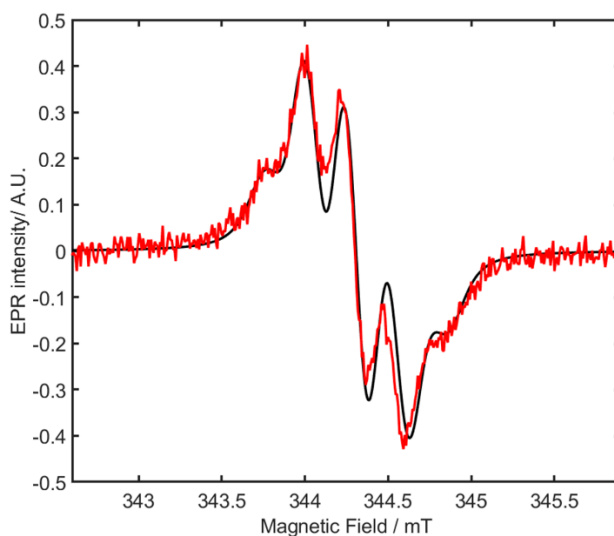
Figure 9.6 EPR spectrum obtained from in-situ electrolysing 5 mM BQ at 9.661 ± 0.001 GHz and 0.2 mW on Ag/ITO-on-PET electrode with the simulation of the broadened spectrum. The spectrum is the mean of 10 scans over ~ 105 s (not deoxygenated).

9.3.2 Testing the SEC-EPR performance of the POM-based flow cell

The earlier-mentioned two-electron reduction of BQ (Eq. (9.1)) in unbuffered water was further used to characterise the electrochemical properties of the flow cell. During the electrochemical characterisation, multiple Ag working electrodes were used in order to evaluate the influence of the replacement of electrodes. This did not result in any changes on the measurements.

Other than the increase in current, the CVs recorded with and without flow display some differences (Figure 9.7). The static CV was distorted in the sense that the oxidation peak had a more negative potential than the reduction peak. This effect could be caused by a local change in pH or a changing environment of the pseudo reference electrode. In flow, the reduction peak was broader and bigger than the oxidation peak. This was most likely caused by the convection of recently reduced species away from the electrode in the microchannel reactor, hindering reversible oxidation afterwards. It needs to be stressed that the usage of CV had the purpose of determining the potential that should be applied for radical generation.
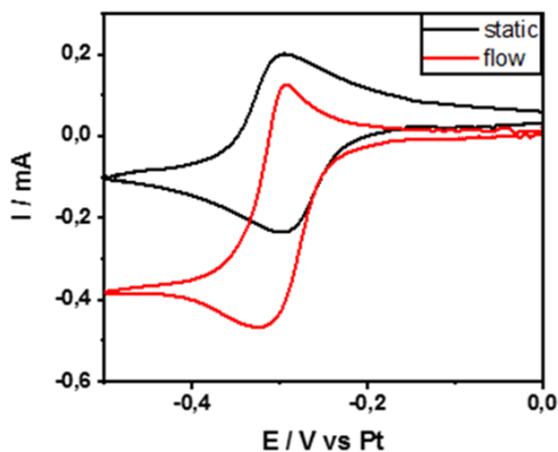
Figure 9.7. CV at 0.007847 ml s^{-1} and 50 mV s^{-1}. The solution consisted of 5 mM BQ in water with 0.2 M Na$_2$SO$_4$ at pH 4.5.

As in section 9.3.1, the one electron reductions of BQ (Eq. (9.1)) in ACN [34] and of MV (Eq. (9.2)) in water [35] are used to assess the performance of the channel flow cell inside the resonator for *in-situ* generation and EPR detection of radicals. The applied potentials for radical generation are derived from the *in-situ* CVs (Figure 9.8). Similar EPR spectra as Figure 9.5 were found. BQ$^{•-}$ showed a very clear spectrum after one scan, which indicated that the lifetime of this radical is sufficient to reach the sensitive part of the cell in the resonator before decaying. On the other hand, MV$^{•+}$ showed a noisier spectrum even after 35 scans which is consistent with the relatively shorter lifetime of the radical. In *ex-situ* CV experiments at a flow rate of 0.00416 ml min$^{-1,}$ the blue colour of MV$^{•+}$ did not "migrate" to the most sensitive part of the window. This suggests that a substantial amount of the generated MV$^{•+}$ had already decayed before arriving at the centre of the window, which coincides with the centre of the resonator where its sensitivity is maximised.

It should be noted that water is not an ideal solvent because its polarity makes it susceptible for electromagnetic radiation. The use of higher flow rates and higher microwave power only resulted in small improvements to the signal. In previous static measurements using wire electrodes in a flat-cell [2], a period of time was needed for MV$^{•+}$ to accumulate before it could be detected. Accumulation was not possible in a flow cell, at a certain time, the concentration gradient of MV$^{•+}$ along the channel will reach steady-state. The decay of the MV$^{•+}$ was almost not visible in the CV in Figure 9.8.A because of the experimental timescale of such experiments. Chronoamperometry at more negative potentials (−1.1 V vs the Pt pseudo-reference), did not give an EPR signal in *in-situ*, nor blue colouration in *ex-situ* measurements. This was consistent with the CV of MV, where at a second reduction wave MV$^{•+}$ undergoes a second electron transfer to give neutral and diamagnetic MV^0 [36]**.** During CVs of 50–100 mV s^{-1} with a flowing solution of 0.00083 ml s^{-1} to 0.00417 ml s^{-1}, colouration at the first reduction wave, followed by decolourisation at the second reduction wave, confirmed the two-step reduction process. This precise control over the potential

highlights the stability of the pseudo reference electrode potential arising from this channel flow cell design. Furthermore, the EPR spectra in Figure 9.8 B and C clearly show that this design is suitable for the electrochemical generation and detection of radicals.

Redox couples of BQ in both water and ACN showed the same peak shape indicating that the solvent does not cause this shape change compared to bulk experiments. The redox couple of MV did not show any distortions due to the dimensions or the electrode configuration of the cell. This may be due to the positive charges of the MV species, which allows migration or better kinetics of the reaction.
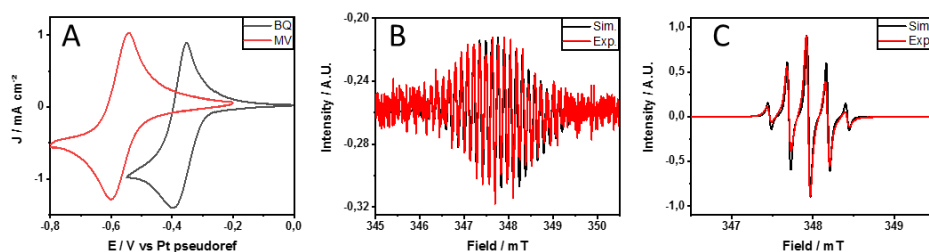

Figure 9.8. A) CV of 5 mM BQ in acetonitrile with 0.1 M TBAP with a flow speed of 0.00333 ml s⁻¹ and 50 mV s⁻¹ and of 5 mM MV in H₂O + 0.2 M Na₂SO₄ with a flow speed of 0.00167 ml s⁻¹ and 100 mV s⁻¹. B) EPR spectrum of electroreduction of the methyl viologen at −0.8 V and flow speed of 0.00667 ml s⁻¹ at 1.00 mW microwave power and 9.746 ± 0.001 GHz microwave frequency C) EPR spectrum of electroreduction of the BQ solution at −0.5 V and flow speed of 0.00167 ml s⁻¹ at 0.15 mW microwave power and 9.763 ± 0.001 GHz microwave frequency.

9.4 Conclusion

Combining electrochemical catalyst research with *in-situ* EPR detection provides some challenges but also opportunities for the electrochemist. A working electrode material that is thin, inert, conductive and spectroscopically transparent can be found in an ITO layer deposited on PET as presented in the first part of this chapter. This commercially available substrate provided a reproducible surface area for electrocatalyst deposition and fitted in the flat part of the measuring cell, reaching the most sensitive part of the cavity. The electrode was thin and optically transparent and did not disturb the cavity tuning resulting in a good Q-factor. Both electrodeposited Ag nanoparticles and NiO layer were electrochemically and spectroscopically evaluated as electrodes for the BQ and MV reduction. Particles were evenly distributed across the total surface and could be tuned in size. The resistivity of the ITO layer was low enough to avoid a potential gradient from an order that would be detrimental for radical generation at the tip of the electrode. In general, the number of radicals formed can be increased by raising the concentration of analyte or enlarging the active surface area. Especially the latter is of primordial importance for detecting short living radicals, as an increase in the bulk concentration is not always feasible or desirable. This setup maximally used the available space in terms of active surface area for commercial flat cells.

In the second part of this chapter, a new modular electrochemical EPR flow cell was introduced and tested. It featured (i) the use of POM as a material suitable for the setups combining electrochemistry and EPR, (ii) an increased modularity and surface reproducibility in order to have rapid change of material, (iii) an enhanced potential control by reducing electrode distances and optimising the position of the pseudo reference electrode, and (iv) a well-defined hydrodynamic flow pattern by the chosen dimensions of the channel. The flow cell was validated in both aqueous and organic media using the test cases.

Both setups open the possibility to study in detail radical intermediates formed in electrocatalysis.

9.5 Supporting information

Table S9.1 Data TEMPO spin count calibration in flat cell. The spin count calibration was performed in the presence of the same ITO electrodes as MV and BQ experiments inside the flat cell.

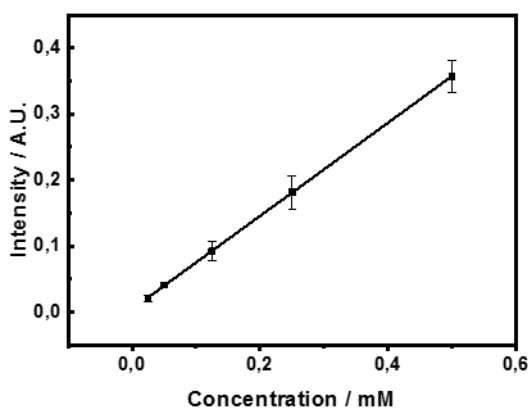| TEMPO concentration /mM	Double integral / A.U.
0.025	0.021 ± 0.005
0.050	0.041 ± 0.003
0.125	0.092 ± 0.015
0.250	0.181 ± 0.025
0.500	0.357 ± 0.024

Figure S9.1 TEMPO spin count calibration curve ($y = 0.7061x + 0.0043$)

Table S9.2 Spin count of experiments with spectra in Figure 9.5.

BQ double int. / A.U.	BQ spin concentration / mM	MV double int. / A.U.	MV spin concentration / mM	Electrode
(A) 0.076	0.101	(B) 0.062	0.082	ITO
(C) 0.060	0.078	(D) 0.048	0.062	Ag/ITO
(E) 0.054	0.071	(F) 0.042	0.053	Ni/ITO

9.6 References

[1]   R. D. Allendoerfer and J. B. Carroll, *A Coaxial Microwave Cavity for Improved Electron Paramagnetic Resonance Sensitivity with Lossy Solvents*, J. Magn. Reson. **37**, 497 (1980).

[2]   D. Pauwels, H. Y. Vincent Ching, M. Samanipour, S. Neukermans, J. Hereijgers, S. Van Doorslaer, K. De Wael, and T. Breugelmans, *Identifying Intermediates in the Reductive Intramolecular Cyclisation of Allyl 2-Bromobenzyl Ether by an Improved Electron Paramagnetic Resonance Spectroelectrochemical Electrode Design Combined with Density Functional Theory Calculations*, Electrochim. Acta **271**, 10 (2018).

[3]   A. A. Shah and R. Holze, *Spectroelectrochemistry of Aniline-o-Aminophenol Copolymers*, Electrochim. Acta **52**, 1374 (2006).

[4]   S. Bilal and R. Holze, *In Situ UV-Vis Spectroelectrochemistry of Poly(o-Phenylenediamine-Co-m-Toluidine)*, Electrochim. Acta **52**, 5346 (2007).

[5]   G. Sandmann, H. Dietz, and W. Plieth, *Preparation of Silver Nanoparticles on ITO Surfaces by a Double-Pulse Method*, J. Electroanal. Chem. **491**, 78 (2000).

[6]   K. Zhang, J. Wei, H. Zhu, F. Ma, and S. Wang, *Electrodeposition of Gold Nanoparticle Arrays on ITO Glass as Electrode with High Electrocatalytic Activity*, Mater. Res. Bull. **48**, 1338 (2013).

[7]   A. Schnegg, J. Behrends, M. Fehr, and K. Lips, *Pulsed Electrically Detected Magnetic Resonance for Thin Film Silicon and Organic Solar Cells*, Phys. Chem. Chem. Phys. **14**, 14492 (2012).

[8]   S. Klod and L. Dunsch, *A Combination of in Situ ESR and in Situ NMR Spectroelectrochemistry for Mechanistic Studies of Electrode Reactions: The Case of p-Benzoquinone*, Magn. Reson. Chem. **49**, 725 (2011).

[9]   A. Petr, L. Dunsch, and A. Neudeck, *In Situ UV-Vis ESR Spectroelectrochemistry*, J. Electroanal. Chem. **412**, 153 (1996).

[10]   A. Neudeck and L. Kress, *Laminated Micro-Meshes - A New Kind of Optically Transparent Electrode*, J. Electroanal. Chem. **437**, 141 (1997).

[11]   A. Goux, D. Pratt, and L. Dunsch, *The Reaction Mechanism of P-Toluenediamine Anodic Oxidation: An in Situ ESR-UV/Vis/NIR Spectroelectrochemical Study*, ChemPhysChem **8**, 2101 (2007).

[12]   L. Dunsch, A. Neudeck, and P. Rapta, *LIGA-Electrodes in Voltammetric and Spectroelectrochemical Studies*, Fresenius. J. Anal. Chem. **367**, 314 (2000).

[13]   P. Rapta, A. Neudeck, A. Petr, and L. Dunsch, *In Situ EPR/UV-VIS Spectroelectrochemistry of Polypyrrole Redox Cycling*, J. Chem. Soc. - Faraday Trans. **94**, 3625 (1998).

[14]   P. Rapta, R. Fáber, L. Dunsch, A. Neudeck, and O. Nuyken, *In Situ EPR and UV-Vis Spectroelectrochemistry of Hole-Transporting Organic Substrates*, Spectrochim. Acta - Part A Mol. Biomol. Spectrosc. **56**, 357 (2000).

[15]   P. G. Hoertz, Z. Chen, C. A. Kent, and T. J. Meyer, *Application of High Surface Area Tin-Doped Indium Oxide Nanoparticle Films as Transparent Conducting Electrodes*, Inorg. Chem. **49**, 8179 (2010).

[16]   M. Kato, T. Cardona, A. W. Rutherford, and E. Reisner, *J. Am. Chem. Soc. 2012, 134, 8332−8335.Pdf*, J. Am. Chem. Soc. **134**, 8332 (2012).

[17] M. A. Bajada, S. Roy, J. Warnan, K. Abdiaziz, A. Wagner, M. M. Roessler, and E. Reisner, *A Precious-Metal-Free Hybrid Electrolyzer for Alcohol Oxidation Coupled to CO 2 -to-Syngas Conversion*, Angew. Chemie **132**, 2 (2020).

[18] K. Abdiaziz, E. Salvadori, K. P. Sokol, E. Reisner, and M. M. Roessler, *Protein Film Electrochemical EPR Spectroscopy as a Technique to Investigate Redox Reactions in Biomolecules †*, Chem. Commun **55**, 8840 (2019).

[19] P. R. Murray, D. Collison, S. Daff, N. Austin, R. Edge, B. W. Flynn, L. Jack, F. Leroux, E. J. L. McInnes, A. F. Murray, D. Sells, T. Stevenson, J. Wolowska, and L. J. Yellowlees, *An in Situ Electrochemical Cell for Q- and W-Band EPR Spectroscopy*, J. Magn. Reson. **213**, 206 (2011).

[20] S. Neukermans, M. Samanipour, H. Y. Vincent Ching, J. Hereijgers, S. Van Doorslaer, A. Hubin, and T. Breugelmans, *A Versatile In-Situ Electron Paramagnetic Resonance Spectro-electrochemical Approach for Electrocatalyst Research*, ChemElectroChem **7**, 4578 (2020).

[21] S. Neukermans, J. Hereijgers, H. Y. Vincent Ching, M. Samanipour, S. Van Doorslaer, A. Hubin, and T. Breugelmans, *A Continuous In-Situ EPR Electrochemical Reactor as a Rapid in-Depth Mechanistic Screening Tool for Electrocatalysis*, Electrochem. Commun. **97**, (2018).

[22] T. Minami, *Transparent Conducting Oxide Semiconductors for Transparent Electrodes*, Semicond. Sci. Technol. **20**, S35 (2005).

[23] A. El Amrani, F. Hijazi, B. Lucas, J. Bouclé, and M. Aldissi, *Electronic Transport and Optical Properties of Thin Oxide Films*, Thin Solid Films **518**, 4582 (2010).

[24] D. H. Kim, H. K. Yoon, D. H. Shin, and R. I. Murakami, *Electromagnetic Wave Shielding Properties of ITO/PET Thin Film by Film Thickness*, Key Eng. Mater. **345**-**346 II**, 1585 (2007).

[25] B. A. Coles and R. G. Compton, *Photoelectrochemical ESR*, J. Electroanal. Chem. Interfacial Electrochem. **144**, 87 (1983).

[26] S. Neukermans, F. Vorobjov, T. Kenis, R. De Wolf, J. Hereijgers, and T. Breugelmans, *Electrochemical Reduction of Halogenated Aromatic Compounds at Metal Cathodes in Acetonitrile*, Electrochim. Acta **332**, 135484 (2020).

[27] B. Vanrenterghem and T. Breugelmans, *An Activity Scale of Cathode Materials for the Electrochemical Cyclisation of Allyl 2-Bromobenzyl Ether*, Electrochim. Acta **234**, 28 (2017).

[28] H. Quan, S. U. Park, and J. Park, *Electrochemical Oxidation of Glucose on Silver Nanoparticle-Modified Composite Electrodes*, Electrochim. Acta **55**, 2232 (2010).

[29] A. M. Ghonim, B. E. El-Anadouli, and M. M. Saleh, *Electrocatalytic Glucose Oxidation on Electrochemically Oxidized Glassy Carbon Modified with Nickel Oxide Nanoparticles*, Electrochim. Acta **114**, 713 (2013).

[30] M. Fleischmann, K. Korinek, and D. Pletcher, *The Oxidation of Organic Compounds at a Nickel Anode in Alkaline Solution*, J. Electroanal. Chem. **31**, 39 (1971).

[31] Z. Li, X. Lu, B. Li, L. Bai, and Q. Wang, *Research on Electrochemical Oxidation of Formaldehyde on the Nanoporous Silver Electrode in Alkaline*

Solution, ECS Electrochem. Lett. **4**, H24 (2015).

[32] E. W. Stone and A. H. Maki, *Electron Spin Resonance of Semiquinones in Aprotic Solvents*, J. Chem. Phys. **36**, 1944 (1962).

[33] W. . Dunham, J. . Fee, L. . Harding, and H. . Grande, *Application of Fast Fourier Transforms to EPR Spectra of Free Radicals in Solution*, J. Magn. Reson. **40**, 351 (1980).

[34] M. Quan, D. Sanchez, M. F. Wasylkiw, and D. K. Smith, *Voltammetry of Quinones in Unbuffered Aqueous Solution : Reassessing the Roles of Proton Transfer and Hydrogen Bonding in the Aqueous Electrochemistry of Quinones*, **9**, 12847 (2007).

[35] M. A. Tamski, J. V. MacPherson, P. R. Unwin, and M. E. Newton, *Electrochemical Electron Paramagnetic Resonance Utilizing Loop Gap Resonators and Micro-Electrochemical Cells*, Phys. Chem. Chem. Phys. **17**, 23438 (2015).

[36] M. A. Tamski, J. V. MacPherson, P. R. Unwin, and M. E. Newton, *Electrochemical Electron Paramagnetic Resonance Utilizing Loop Gap Resonators and Micro-Electrochemical Cells*, Phys. Chem. Chem. Phys. **17**, 23438 (2015).

Identifying reaction intermediates in carbon-halogen bond electroreduction

This chapter focuses on how SEC-EPR can be a useful tool for studying carbon-halogen (C-X) electroreduction. In particular, I focus on the electroreduction of 1-bromonaphthalene and 2-bromonaphthalene, for which a mechanism was proposed earlier. EPR spectra of intermediate radicals were measured *in-situ*.

Different combinations of solvents and supporting electrolytes were used to test their effect on the generation of the radicals intermediates. DFT of different model systems was used to corroborate the interpretation of the EPR data.

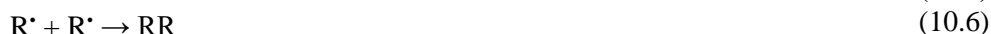**Own contribution**: EPR experiments, spectral analysis and DFT calculations

10.1 Introduction

The electrochemical reductive cleavage of carbon-halogen bonds (C-X) has attracted much interest in the last decades. It offers many possibilities in synthesis [1–3] and the reduction of organic pollutants [4–6]. However, as mentioned in chapter 5, a significant drawback of using organic halides is the high activation energy costs, especially for chlorides and bromides. The use of catalytic electrode materials can decrease the activation energy. Several studies have been carried out to map the reaction mechanism of the reduction of bromides at catalytic and non-catalytic electrodes [5,7–16]. I here summarise the key reaction steps proposed in these papers. The electron transfer from the electrode to the organic halide happens in the first step and forms a radical anion (Eq (10.1)), which subsequently undergoes cleavage of the C-X bond to form the halide anion and an organic radical (Eq (10.2)).

For bromides and chlorides, this organic radical has a lower reduction potential than the parent molecule and is therefore reduced almost instantaneously afterwards (Eq(10.4)), making this a stepwise two-electron transfer.

$$RX + e^- \leftrightarrow RX^{\bullet-} \tag{10.1}$$
$$RX^{\bullet-} \rightarrow R^{\bullet} + X^- \tag{10.2}$$
$$RX + e^- \rightarrow R^{\bullet} + X^- \tag{10.3}$$
$$R^{\bullet} + e^- \leftrightarrow R^- \tag{10.4}$$

Several reports show that the bond cleavage can occur in a concerted mechanism in the presence of Ag electrode (Eq (10.3)) with the subsequent reduction of the formed organic radical yielding an organic anion Eq (10.4) [5,11,17]. The organic radical can react with the radical anion intermediate to yield an anion and the initial reagent (Eq. (10.5) or with another radical to form a dimer (Eq. 10.6). The produced organic anions from Eq.(10.4) and Eq. (10.5) bind with a proton from the solvent/residual water to form the corresponding aromatic compound (Eq.(10.7)).

$$R^{\bullet} + RX^{\bullet-} \leftrightarrow R^- + RX \tag{10.5}$$
$$R^{\bullet} + R^{\bullet} \rightarrow RR \tag{10.6}$$
$$R^- + H^+ \rightarrow RH \tag{10.7}$$

At more negative potentials, depending on the molecular structure of the halide and the electrochemical window of the solvent, one can produce the radical anion of this hydrogenated dehalogenated compound (Eq.(10.8).

$$RH + e^- \leftrightarrow RH^{\bullet-} \tag{10.8}$$

The organic radical $R^{\bullet}$ can abstract a hydrogen atom from the solvent (SH) to form the solvent radical (Eq.(10.9)). The solvent radical can be reduced at the electrode (Eq. (10.10)) or by the radical anion. (Eq-(10.11).

$$R^{\bullet} + SH \rightarrow RH + S^{\bullet} \tag{10.9}$$

$$S^{\bullet} + e^{-} \leftrightarrow S^{-} \qquad (10.10)$$
$$S^{\bullet} + RX^{\bullet-} \leftrightarrow S^{-} + RX \qquad (10.11)$$

According to previous studies, there are several possibilities for the formation of intermediates and products in the proposed mechanisms. The SEC-EPR experiment may provide comprehensive information by detecting the radical intermediates, as mentioned in previous chapters. This information can remove the ambiguity in the mechanism, such as distinguishing between the concerted and stepwise mechanisms by detecting the $RX^{\bullet-}$ or $R^{\bullet}$ radicals. The electrochemical reduction of these different organic halides in bulk using different cathode materials was investigated by S. Neukermans *et al.* [18].

In this chapter, direct *in-situ* SEC-EPR methods are employed to study the electrochemical C-X reduction of 1-bromonaphthalene (1BN) and 2-bromonaphathalne (2BN) using some of the wire electrodes that were used in [18] for bulk electrolysis. Ag, Au, and Cu wire electrodes were used for *in-situ* SEC-EPR experiments. The structures of 1BN and 2BN are shown in Figure 10.1.
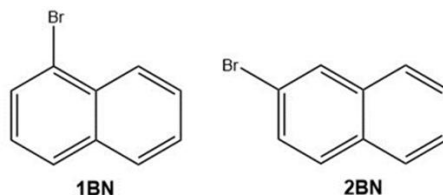

Figure 10.1 Molecular structure of the aromatic bromides used for the electroreduction experiments.

10.2 Materials and methods

10.2.1 Chemicals

Electrochemical reductions of 1-bromonaphthalene (1BN, 97%), 2-bromonaphthalene (2BN, 99.0%), were performed in ACN and 0.1 M TBAP (99.0%) by means of CV.These chemicals were used as received and were all purchased from Sigma-Aldrich. Spectroelectrochemical measurements were performed in ACN, DMF (Biosolve, HPLC grade) and DMSO (Acros Organics, >99.8%). TBAP, tetrabutylammonium bromide (TBAB, Acros Organics, >99%) and tetramethylammonium hexafluorophosphate (TMAFP, TCI, >98.0%) were used as supporting electrolyte. Toluene (Uvasol for spectroscopy) was purchased from Merck.

10.2.2 *In-situ* SEC-EPR spectrometry

Combined CW-EPR-spectroelectrochemical measurements were performed with a Wilmad Supracil WG-810-A-Q quartz flat cell in a TE_{102} rectangular cavity of the Bruker E580 Elexsys spectrometer. The EPR spectra were recorded at X-band (≈9.7

GHz) in CW mode at ambient temperature with 2 mW power, 0.1 mT modulation amplitude (unless mentioned differently in the caption) and 100 kHz modulation frequency. Reductions were carried out with an Autolab PGSTAT 302 N. Wire working electrodes were used for all *in-situ* experiments. A leak-free reference electrode (W3 69-00) was used (Harvard Apparatus), which is equivalent to a Ag/AgCl 3 M KCl reference. The RE was positioned at the entrance of the flat part to ensure optimal potential control. The Pt rod counter electrode CE was put in the reservoir on top of the flat part. The tip was also put as close to the entrance of the flat part to reduce the cell potential.

All solutions were purged with Ar for several minutes before measurement, and the atmosphere above the solution was purged continuously with Ar during the measurement to avoid the influence of O_2.

10.2.3 DFT computations and EPR simulations

The EPR spectra were simulated using the EasySpin-5.1.11 module [19] running in Matlab 2020a. Spin-unrestricted (UKS) DFT computations were performed with the ORCA package [20–23]. In order to mimic the solvent effect, a dielectric surrounding with the dielectric constant of the respective solvents according to the COSMO model was used [24]. For the geometry optimizations, the Becke-Perdew density functional (BP86) [25,26] and the split-valence plus polarization (SVP) basis sets [27] were used for all atoms. The energy was converged to 1×10^{-8} Hartree (E_h), and the convergence tolerances in the geometry optimization were 3×10^{-4} E_h/Bohr for the gradient and 5×10^{-6} E_h for the total energy. For benchmarking, single-point calculations with the B3LYP/EPR-II, functional/basis sets [28,29] were used to predict the EPR spectral parameters from the optimized geometries.

10.3 Results and discussion

According to the previous work of Neukermans *et al*. [18] the electroreduction of 1BN and 2BN follows a concerted mechanism on Ag and a stepwise mechanism on Au and Cu electrode materials. In principle, the only radical intermediate species that can be formed are the 1- and 2-bromonaphthalene radical anions (1BN$^{•-}$ and 2BN$^{•-}$) and deprotonated naphthalene radicals (1N$^{•}$ and 2N$^{•}$) for the stepwise pathway. The latter should be the only species formed under concerted conditions. A side reaction (hydrogen atom transfer (HAT)) with the solvent could occur, forming a deprotonated acetonitrile radical (S$^{•}$). A poor potential control could result in the formation of a naphthalene radical anion (N$^{•-}$). The observed EPR parameters of N$^{•-}$ have been reported. The reported isotropic *g*-value ($g_{iso} = 2.00270$) and hyperfine coupling of $|A^{H1}|$ = 16.53 MHz (4) and $|A^{H2}| = 5.016$ MHz (4) [30,31] lead to the simulated CW-spectrum shown in Figure 10.2a. The numbers in parentheses show the number of the equivalent nuclei. The DFT-computed EPR values ($g_{iso} = 2.00265$, A^{H1} = -17.02 MHz (4), A^{H2}= -5.47 MHz (4)) are in a good agreement with the literature (the corresponding simulated EPR spectrum is shown in Figure 10.2b). The DFT-optimised geometry and the

corresponding spin density distribution of $N^{\bullet-}$ are shown in Figure 10.2.d. The spin density is distributed over the aromatic rings.
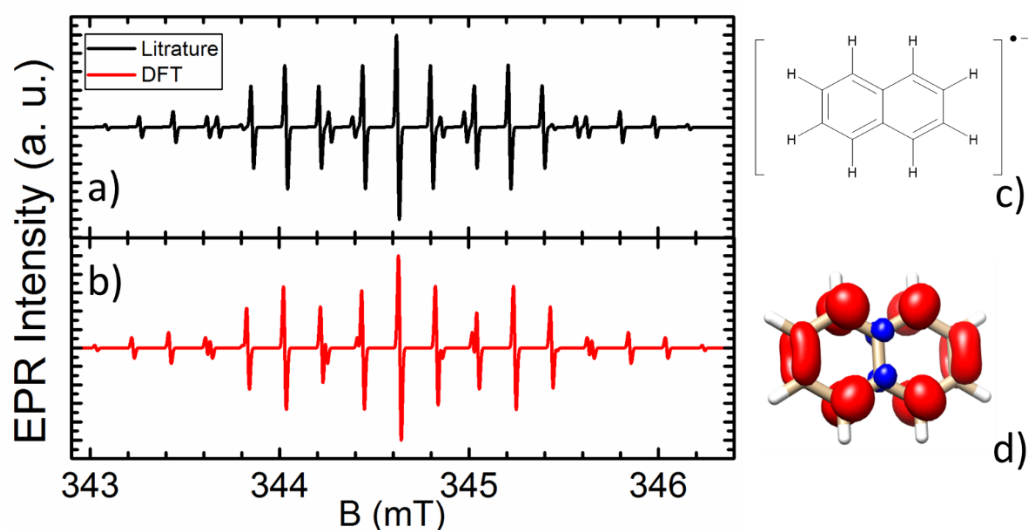

Figure 10.2 The simulated EPR spectrum of the naphthalene radical anion using EPR parameters from a) the literature [30,31] and b) the DFT calculations. A linewidth of 0.015 mT and a MW frequency of 9.66 GHz was chosen. c) Chemical structure of naphthalene radical anion. d) DFT-computed molecular structure of the naphthalene radical anion with the distribution of the spin density. Red and blue are positive and negative spin densities, respectively.

In a next step, the DFT calculations were performed on candidates for the radical intermediates that can potentially be trapped by SEC-EPR, focussing on their EPR parameters and spin density. The same level of theory of DFT as for $N^{\bullet-}$ is used for these radical intermediate candidates. Figure 10.3 shows the CW-EPR spectra of $1BN^{\bullet-}$ (blue), $1N^{\bullet}$ (red), $2BN^{\bullet-}$ (magenta), and $2N^{\bullet}$ (black) using the DFT-computed EPR parameters shown in Table 10.1 and their molecular structures with their spin density distribution. The isotropic g-values are close to what literature and DFT give for $N^{\bullet-}$. The somewhat higher g_{iso} of $1BN^{\bullet-}$ and $2BN^{\bullet-}$ may result from the presence of Br in the structure. The spectra are different in the splitting pattern due to the different hyperfine couplings. The spin density distribution is also different for these radical intermediates. In the case of deprotonated naphthalene radicals ($1N^{\bullet}$ and $2N^{\bullet}$), the spin density is mainly localised in the vicinity of the C atom from the dissociated C-X bond. Hence largest hyperfine couplings belong to the closest protons to that C atom (A^H ~57.67 MHz for $1N^{\bullet}$ and A^H ~ 57.78 MHz and 46.00 MHz for $2N^{\bullet}$). For $1BN^{\bullet-}$ and $2BN^{\bullet-}$ the spin density is mainly on the aromatic rings with a smaller hyperfine coupling.
For $1BN^{\bullet-}$, the hyperfine coupling of ^{79,81}Br ($I = 3/2$) nuclei is an order of magnitude smaller than for $2BN^{\bullet-}$, but both remain significant.

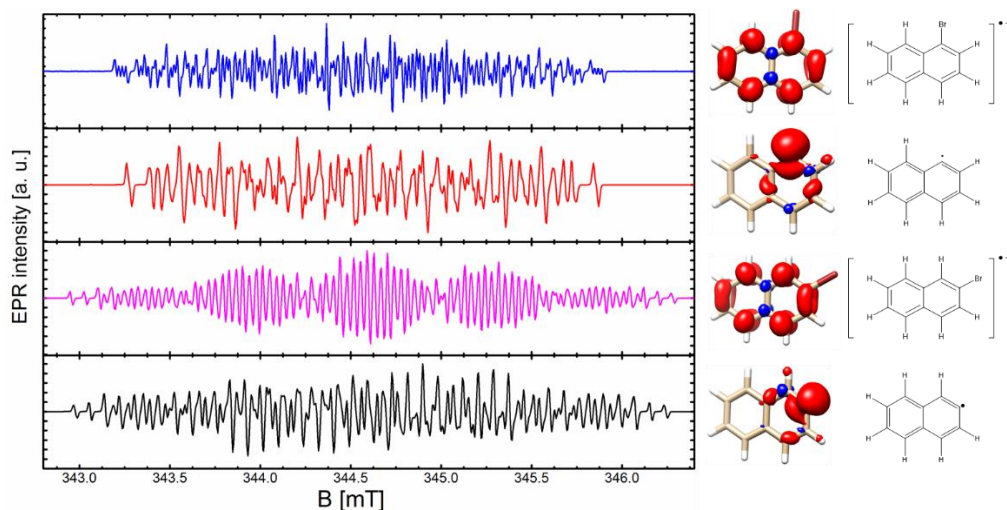*Figure 10.3 The simulated EPR spectra of 1BN•⁻ (blue), 1N• (red), 2BN•⁻ (magenta) and 2N• (black) in ACN using the DFT-computed EPR parameters. The corresponding chemical structures are shown on the right side of each spectrum, as well as the DFT-optimised geometries with the spin density distributions. A linewidth of 0.015 mT was chosen, and a ME frequency of 9.66 GHz.*

Table 10.1 The DFT-computed EPR parameters of possible naphthalene radical intermediates in electroreduction of 1BN and 2BN. Only the isotropic g and largest hyperfine values are given. For Br, only the hyperfine values for the ⁷⁹Br isotope are mentioned

Sample	g_{iso}	A^{79Br}/MHz	A^H/MHz
1BN•⁻	2.0030	-0.181	-18.32, -16.07,-15.46, -8.08, -6.25, -4.70, -3.46
1N•	2.0023	-	57.67, 17.19, 9.65, 6.9
2BN•⁻	2.0028	-2.22	-19.52,-19.01, -15.65, -14.78, -6.11, -4.87, -4.57
2N•	2.0023	-	57.98, 46.00, 17.16

In-situ SEC-EPR experiments were performed to identify the radical intermediates and compare them with the above DFT calculations to verify earlier models for C-X electroreduction [18].

The CVs taken when using Ag, Au and Cu wire WEs in the EPR cell for 1BN reductions are shown in Figure 10.4 (left) as an indication of the difficulty of the determination of the peak potentials. The peaks were shifted compared to the potentials of bulk experiments in ref [18] and were less pronounced. Overpotentials of the onset were in the same order in ref [18] Au > Cu > Ag. The electroreduction experiments were performed for 2BN at -2.4 V on Cu and Au electrodes and at -1.85 V on Ag electrode, and for 1BN at -2.4 V for Au electrode and -1.85 V for Cu electrode and -1.60 V for Ag electrode. 2BN reduction was performed in the glovebox and the outside glovebox but with Ar bubbling. No difference in the CW-EPR spectrum could be observed between the two samples. 1BN solutions were only prepared by Ar bubbling. For both 1BN and 2BN samples, the use of the three cathode materials resulted in similar CW-EPR spectra. The CW-EPR spectra of 1BN and 2BN reductions are shown in Figure 10.4 (right) and Figure 10.5, respectively. The EPR spectrum of the 1BN radical product had a clear

splitting in 2 peaks with a minor shoulder around 344.5 mT with a total width of 0.46 mT, while the spectrum of the 2BN electroreduction product is wider (width ~ 0.56 mT) with less resolved splittings plus an extra feature around 344.5 mT. Adjusting the magnetic field modulation amplitude and concentration of 2BN from 0.1 mT to 0.05 mT and from 1 mM to 26 mM revealed more substructures in the EPR spectrum (Figure 10.5 (right)). Nevertheless, according to the literature and the above DFT calculations, none of the observed spectra represents the naphthalene-based radical intermediates expected to be created in 1BN or 2BN elecrtroreductions. Despite similar g-values, both experimental EPR spectra show a clear difference from the DFT calculated spectra (Figure 10.3). The fewer number of lines and smaller splittings (indicating smaller hyperfine coupling values) in the experimental EPR spectra do not match the literature and DFT calculations. Interestingly, similar to the DFT calculations, the spectrum of electroreduced 1BN is narrower than 2BN. The difference between the EPR spectra of 1BN and 2BN electroreduction experiments indicates that the radical intermediates are related to the naphthalene and are not a solvent based radical.
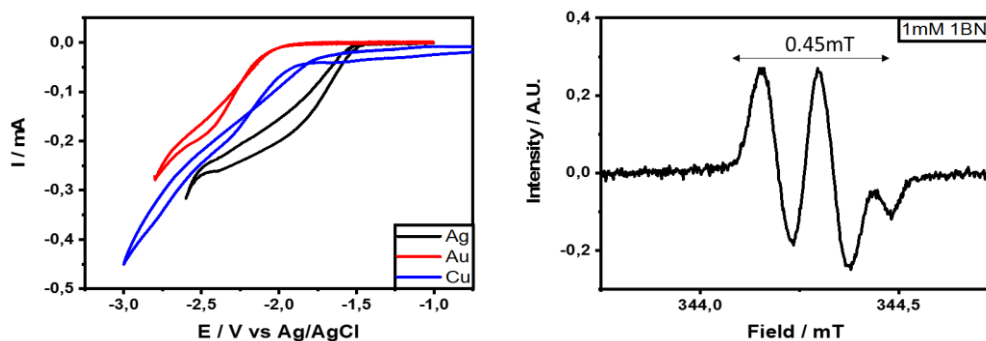

Figure 10.4. CV using Ag, Au and Cu wire WE in ACN (left) and in-situ EPR spectra on Ag wire WE with 1 mM 1BN in ACN + 0.1 M TBAP (right) at 9.659 ± 0.001 GHz.
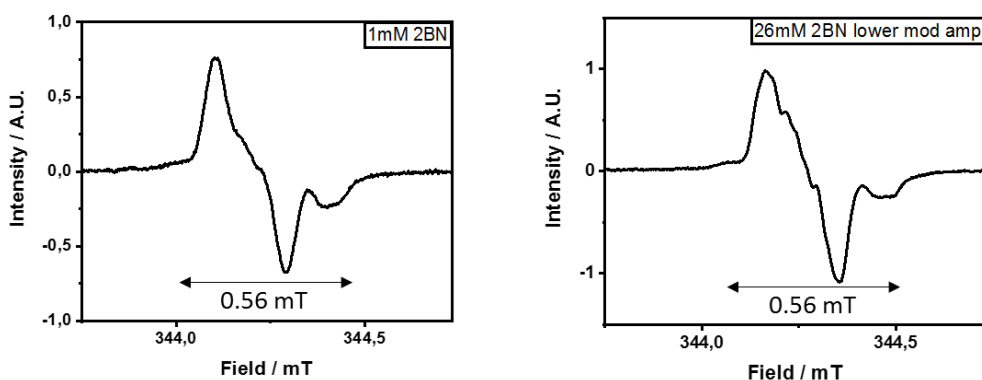

Figure 10.5. In-situ EPR spectra of electroreduction on Ag wire electrode with 1mM 2BN (mod. amp. 0.1 mT and 0.4 mW power at 9.656 ± 0.001 GHz) (left) and 26 mM 2BN (mod. amp. 0.05 mT) (right) in ACN + 0.1 M TBAP at 9.660 ± 0.001 GHz.
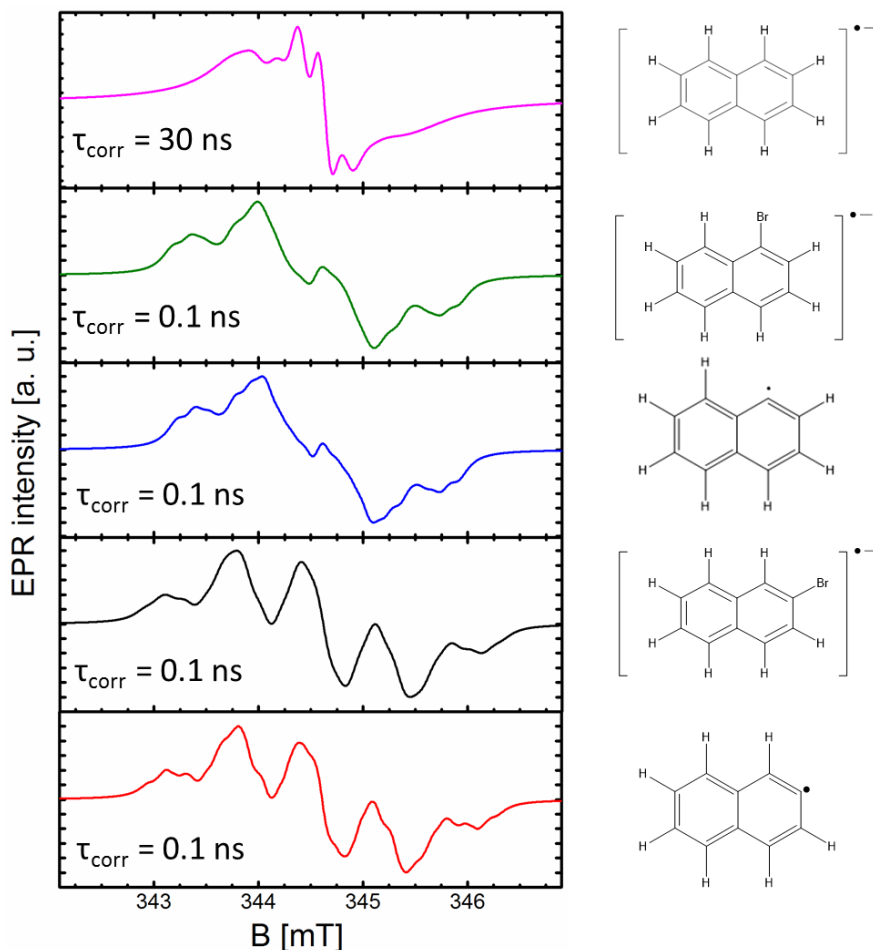
Figure 10.6. The simulated EPR spectra of the naphthalene radicals using DFT computed parameters considering the slow-motion effect. The corresponding rotational correlation times (τcorr) are given in the figure legend.

The CW spectra are not isotropic, and such anisotropy in the solutions can be a mobility effect due to the slow motion of the species. Since the ACN is not a viscose solvent at room temperature, the slow motion can be explained by considering that after the electron transfer, the radicals stick to the surface of the electrode and lose their free movement in the solution, causing anisotropy detection by EPR. By adjusting the rotational correlation time for isotropic Brownian rotational diffusion, we can simulate the slow-motion effect on the EPR spectra. Figure 10.6 shows the EPR spectra corresponding to the ones shown in Figure 10.2 and Figure 10.3 in the slow-motion regime (corresponding rotational correlation times (τ_{corr}) are given in the legend of Figure 10.6). Although the broadening of the lines changes, the overall width of EPR spectra remains much larger than what we see in the experiment.
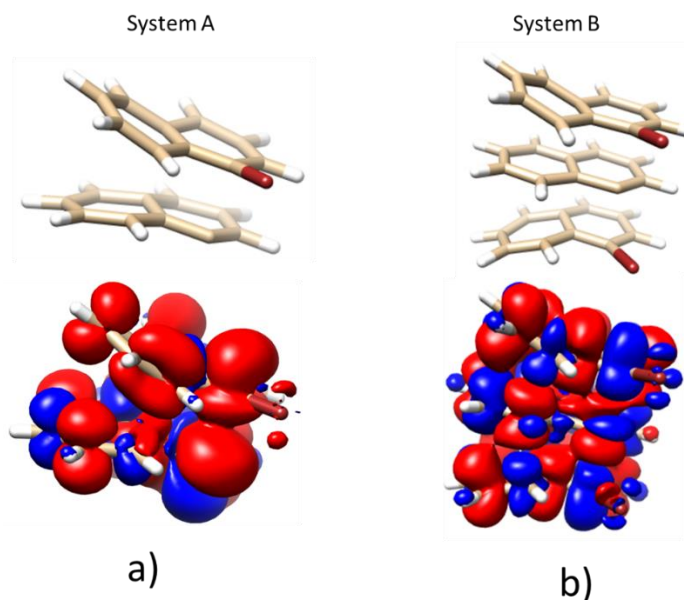
Figure 10.7 The DFT optimised geometry and DFT-computed spin density of a) 1BN in the distance of 2.29 Å from 1N• (system A) and b) 1N• molecule between two 1BN molecules with the distance of 2.29Å from each 1BN molecule (system B)

One of the explanations for the considerable decrease of the hyperfine couplings might be the stacking of 1BN or 2BN molecules on the surface or in the solution. In this case, the 1BN/2BN molecules get close enough to the radical so that the spin-density can also be delocalised over the several molecules in the stack. The redistribution of the spin density changes the hyperfine coupling values. In order to mimic the staking of BN molecules and study their effect on the spin density, DFT calculations for 1N• in close proximity (~ 2.29 Å) in the arbitrary z-axis direction (and 0 in the xy plane) to 1BN molecules were performed for two example structures: 1N• next to one 1BN molecule (System A in Figure 10.7.a), and a 1N• between two 1BN molecules (System B in Figure 10.7.b). In both cases, the spin density spreads out in the stack. The calculations with a larger intermolecular distance (3.28 Å) did not result in spin delocalisation. The DFT-computed EPR parameters for these structures shown in Table 10.2 do not seem small enough to give the EPR spectrum in Figure 10.4, although the magnitude of the largest proton hyperfine coupling is decreased from 57 MHz for 1N• to 20 MHz in system A, and 32 MHz in system B (see Table 10.1 and Table 10.2). In turn, a hyperfine coupling is found on the Br nuclei of the adjacent molecules.

Table 10.2 The DFT-computed g-values and the hyperfine couplings of the ^{79}Br nuclei and the largest hyperfine couplings of proton nuclei for systems A and B.

Complex	g_{iso}	A^{79Br}/MHz	A^H/MHz
System A	1.9992	18.69	-20.01, -14.60, 7.80
System B	2.0016	8.24 -3.99	-32.126, 12.20, -11.67, 10.63, -10.33, -9.89, 9.14, -9.08, -8.88, -8.85, 8.088

Systems A and B are not perfect stacking models since we only used two structures with only one intermolecular distance in only one direction, showing the more extensive DFT model requirement. Although this nonperfect model resulted in decreasing the largest proton hyperfine couplings and delocalisation of the spin density, the evidence is not enough to conclude that the narrowing is due to a stacking process. Moreover, 2.29 Å is extremely small compared to the reported intermolecular distances in stacks of aromatics.

In a final investigation, different combinations of solvents and supporting electrolytes were used. The reduction reactions were first performed in DMF and DMSO with TBAP as a supporting electrolyte in bulk (Figure S10.1) to assess if the solvent variation had an influence on the electrochemical behaviour. No EPR signal was detected in the *in-situ* experiments in DMF and DMSO. Varying the supporting electrolyte anion from perchlorate to hexafluorophosphate did also not result in any detectable EPR signal. The presence of perchlorate together with the ACN whilst performing these reductions seems to be crucial for forming and/or stabilising the radicals, of which the spectra are shown in Figure 10.4 and Figure 10.5.

10.4 Conclusion

In-situ SEC-EPR experiments were performed to study the electroreduction of 1BN and 2BN using Au, Ag, and Cu wires as WE. Different WE wire materials did not change the EPR spectra for both samples. However, the solvent electrolyte combination did have a large effect. The experimental EPR spectra were unique for the combination of ACN with TBAP and did not occur in DMF or DMSO as a solvent and with TBAP or TMAPF$_6$ as the supporting electrolyte.

DFT calculations were used to calculate the EPR parameters of radical species that may be generated in the process. The experimental EPR spectra obtained for electroreduction of 1BN and 2BN did not match what had been expected from literature and DFT calculations.

Including slow molecular motion in the EPR simulation mimicking the possible absorbance of radical species on the electrode surface broadens the experimental EPR features but does not match with the EPR data.

Stacking of radicals with 1BN or 2BN molecules leads to a spreading of the spin density over more molecules and may lead to an overall reduction of the width of the EPR spectrum, as follows from preliminary DFT data. The stacking may be influenced by solvent and electrolyte, potentially explaining the the the strong dependence of these parameters. However, the current data is inconclusive.

In future work, the use of spin traps may help to trap the possible reactive radical intermediates.
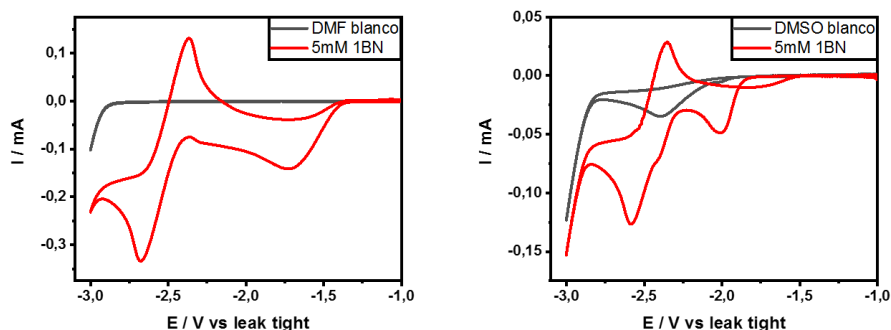
10.5 Supporting information

Figure S10.1 CV of 5 mM 1BN and blank control in DMF (left) and DMSO (right) in bulk on a Ag disc electrode at 50 mV s⁻¹

Table S10.1 The coordinates (in Å) of the geometry-optimized naphthalene radical anion (N•⁻)

C	-1.657023	-0.157496	-0.008839
C	-0.396850	-0.838772	-0.008725
C	0.832880	-0.127568	-0.008714
C	0.832904	1.275335	-0.009166
C	-0.396825	1.986581	-0.009311
C	-1.657036	1.305292	-0.009336
C	-2.917167	-0.838783	-0.008452
C	-4.146878	-0.127584	-0.008904
C	-4.146881	1.275345	-0.009399
C	-2.917180	1.986565	-0.009783
H	1.786396	-0.682867	-0.008560
H	1.786432	1.830611	-0.009199
H	-0.395162	3.090542	-0.009507
H	-2.918782	-1.942732	-0.007921
H	-5.100398	-0.682875	-0.008647
H	-5.100410	1.830622	-0.009687
H	-2.918817	3.090515	-0.010309
H	-0.395204	-1.942732	-0.008541

Table S10.2 The coordinates (in Å) of the geometry-optimized 1-bromonaphthalene radical anion (1BN•⁻)

C	-1.662321	-0.156357	-0.019227
C	-0.380437	-0.795930	-0.026307
C	0.854098	-0.093297	-0.022899
C	0.831377	1.307469	-0.011791
C	-0.401402	2.005246	-0.004317
C	-1.654312	1.310012	-0.008023

C	-2.922248	-0.830397	-0.022262
C	-4.147187	-0.113079	-0.015125
C	-4.143943	1.288257	-0.004517
C	-2.912179	1.990581	-0.001107
H	1.804554	-0.647754	-0.028951
H	1.782701	1.865166	-0.008953
H	-0.412876	3.107894	0.004407
H	-2.928723	-1.931203	-0.030535
H	-5.100379	-0.667827	-0.017846
H	-5.094301	1.847893	0.001076
H	-2.905727	3.093895	0.007301
Br	-0.287696	-2.736570	-0.040922

Table S10.3 The coordinates (in Å) of the geometry-optimized deprotonated naphthalene radical derived from 1-bromonaphthalene (1N•)

C	-1.660883	-0.185115	-0.008713
C	-0.393343	-0.800489	-0.008336
C	0.825291	-0.175230	-0.008514
C	0.813926	1.259950	-0.009167
C	-0.389625	1.954620	-0.009520
C	-1.647439	1.272368	-0.009332
C	-2.912734	-0.875767	-0.008556
C	-4.106605	-0.165550	-0.009008
C	-4.100335	1.259008	-0.009550
C	-2.900206	1.959515	-0.009726
H	1.780696	-0.725145	-0.008204
H	1.771813	1.804471	-0.009368
H	-0.389242	3.056107	-0.009974
H	-2.911334	-1.976432	-0.008079
H	-5.066297	-0.705159	-0.008910
H	-5.055689	1.806308	-0.009859
H	-2.897993	3.061541	-0.010183

Table S10.4 The coordinates (in Å) of the geometry-optimized 2-bromonaphthalene radical anion (2BN•-)

C	-1.716293	-0.134580	-0.020121
C	-0.458816	-0.828473	-0.032953
C	0.749808	-0.091324	-0.038185
C	0.782133	1.305323	-0.031137
C	-0.453827	2.009103	-0.018205
C	-1.713174	1.326860	-0.012718
C	-2.972060	-0.815828	-0.014268
C	-4.200653	-0.104653	-0.001892
C	-4.199306	1.298251	0.004964
C	-2.971445	2.007744	-0.000367

H	1.738575	1.849549	-0.035449
H	-0.445128	3.111963	-0.012398
H	-2.973478	-1.919220	-0.019786
H	-5.153591	-0.659990	0.002279
H	-5.151941	1.854290	0.014541
H	-2.972168	3.111237	0.005162
H	-0.445615	-1.928990	-0.038642
Br	2.422979	-1.072261	-0.055824

Table S10.5 The coordinates (in Å) of the geometry-optimized deprotonated naphthalene radical derived from 2-bromonaphthalene (2N•)

C	-1.713109	-0.140180	-0.018954
C	-0.456305	-0.843186	-0.030370
C	0.684320	-0.085815	-0.034482
C	0.760287	1.315799	-0.028699
C	-0.452918	2.007462	-0.017618
C	-1.701883	1.308914	-0.012542
C	-2.966510	-0.825387	-0.013781
C	-4.161447	-0.115629	-0.002770
C	-4.154644	1.308379	0.003586
C	-2.951775	2.003578	-0.001221
H	1.720748	1.855926	-0.032586
H	-0.457833	3.110023	-0.012631
H	-2.970456	-1.926931	-0.018658
H	-5.121088	-0.655814	0.001122
H	-5.108752	1.857765	0.012331
H	-2.944965	3.105262	0.003668
H	-0.449671	-1.946167	-0.035395

Table S10.6 The coordinates (in Å) of the geometry-optimized 1BN in the distance of 2.29 Å from 1N• (system A)

C	-0.534557	1.882059	2.354047
C	-1.779904	1.199205	2.364422
C	-1.706656	-0.280528	2.368237
C	-0.445447	-0.953860	2.510436
C	0.750825	-0.261098	2.352929
C	0.678838	1.146279	2.348997
C	-3.071126	1.793868	2.368451
C	-4.179043	1.036778	2.762610
C	-4.077045	-0.363214	2.987982
C	-2.865829	-1.012590	2.787589
H	-0.454892	-2.054440	2.566678
H	1.722596	-0.777053	2.397446
H	1.629262	1.710708	2.341556
H	-3.139096	2.891163	2.347239

H	-5.154414	1.533777	2.884001
H	-4.957728	-0.921146	3.342096
H	-2.773733	-2.094326	2.978026
C	-0.656721	2.031616	0.070541
C	-1.913832	1.342312	0.081012
C	-1.994561	-0.076863	0.085683
C	-0.756414	-0.778224	-0.091356
C	0.449279	-0.108742	0.070504
C	0.528779	1.312142	0.065594
C	-3.121390	2.098740	0.083746
C	-4.329673	1.512129	-0.314721
C	-4.391833	0.111679	-0.485747
C	-3.253519	-0.665589	-0.251590
H	-0.765152	-1.873546	-0.200391
H	1.388662	-0.676152	0.007586
H	1.505870	1.810133	0.058210
H	-3.054740	3.193384	0.147266
H	-5.231734	2.131016	-0.435006
H	-5.330179	-0.372823	-0.796157
H	-3.302717	-1.762014	-0.348991
Br	-0.483175	3.921223	-0.291925

Table S10.7 10.8 The coordinates (in Å) of the geometry-optimized 1N• molecule between two 1BN molecules with the distance of 2.29Å from each 1BN molecule (system B)

C	-0.520496	1.877558	2.364293
C	-1.836032	1.161262	2.365227
C	-1.751635	-0.388891	2.339769
C	-0.455670	-1.034167	2.261066
C	0.768229	-0.320047	2.318560
C	0.726468	1.116496	2.341502
C	-3.185876	1.628846	2.382606
C	-4.311447	0.749613	2.397670
C	-4.184927	-0.637251	2.392959
C	-2.895262	-1.204979	2.363056
H	-0.435386	-2.132946	2.246460
H	1.724316	-0.859850	2.265536
H	1.672243	1.679844	2.342198
H	-3.368341	2.709584	2.370749
H	-5.309434	1.212047	2.422490
H	-5.079760	-1.276740	2.413394
H	-2.766622	-2.299666	2.368004
C	-0.579202	2.075716	0.104825
C	-1.813521	1.402146	0.104739
C	-1.869828	-0.045648	0.082214
C	-0.627134	-0.766223	-0.004586
C	0.601842	-0.072660	0.059739

C	0.642370	1.329078	0.081424
C	-3.039257	2.153227	0.124981
C	-4.209431	1.569664	-0.357782
C	-4.228137	0.177052	-0.633021
C	-3.097753	-0.607076	-0.396522
H	-0.646452	-1.845118	-0.211853
H	1.540435	-0.632893	-0.052654
H	1.605700	1.853897	0.081366
H	-2.976750	3.242932	0.248843
H	-5.125598	2.169136	-0.472924
H	-5.141191	-0.293952	-1.028945
H	-3.129183	-1.690461	-0.593352
Br	-0.398567	3.975485	-0.223568
C	-0.362649	1.951185	4.631798
C	-1.589670	1.287983	4.604962
C	-1.672208	-0.161260	4.590164
C	-0.436605	-0.890878	4.691557
C	0.788986	-0.213300	4.631003
C	0.848962	1.204753	4.644599
C	-2.813871	2.061656	4.588936
C	-3.949038	1.510740	5.180064
C	-3.978164	0.116503	5.459540
C	-2.888121	-0.693395	5.144062
H	-0.463993	-1.981943	4.823467
H	1.725323	-0.782068	4.728765
H	1.821138	1.712838	4.665857
H	-2.730554	3.148453	4.456341
H	-4.849937	2.124501	5.336016
H	-4.872664	-0.334338	5.916972
H	-2.939875	-1.779325	5.323428
Br	-0.165769	3.852880	4.294003

10.6 References

[1]   G. J. Rowlands, *Radicals in Organic Synthesis: Part 2*, Tetrahedron **66**, 1593 (2010).

[2]   M. S. Mubarak and D. G. Peters, *Using Silver Cathodes for Organic Electrosynthesis and Mechanistic Studies*, Curr. Opin. Electrochem. **2**, 60 (2017).

[3]   E. Duñach, M. José Medeiros, and S. Olivero, *Intramolecular Reductive Cyclisations Using Electrochemistry: Development of Environmentally Friendly Synthetic Methodologies*, New J. Chem. **30**, 1534 (2006).

[4]   Y. Wang and X. Lu, *Study on the Effect of Electrochemical Dechlorination Reduction of Hexachlorobenzene Using Different Cathodes*, J. Anal. Methods Chem. **2014**, (2014).

[5]   A. A. Isse, S. Gottardello, C. Durante, and A. Gennaro, *Dissociative Electron Transfer to Organic Chlorides: Electrocatalysis at Metal Cathodes*, Phys. Chem. Chem. Phys. **10**, 2409 (2008).

[6]   E. Duñach, a. P. Esteves, M. J. Medeiros, D. Pletcher, and S. Olivero, *The Study of Nickel(II) and Cobalt(II) Complexes with a Chiral Salen Derivative as Catalysts for the Electrochemical Cyclisation of Unsaturated 2-Bromophenyl Ethers*, J. Electroanal. Chem. **566**, 39 (2004).

[7]   C. Durante, A. A. Isse, F. Todesco, and A. Gennaro, *Electrocatalytic Activation of Aromatic Carbon-Bromine Bonds toward Carboxylation at Silver and Copper Cathodes*, J. Electrochem. Soc. **160**, G3073 (2013).

[8]   D. Pauwels, H. Y. Vincent Ching, M. Samanipour, S. Neukermans, J. Hereijgers, S. Van Doorslaer, K. De Wael, and T. Breugelmans, *Identifying Intermediates in the Reductive Intramolecular Cyclisation of Allyl 2-Bromobenzyl Ether by an Improved Electron Paramagnetic Resonance Spectroelectrochemical Electrode Design Combined with Density Functional Theory Calculations*, Electrochim. Acta **271**, 10 (2018).

[9]   L. Perini, C. Durante, M. Favaro, S. Agnoli, G. Granozzi, and A. Gennaro, *Applied Catalysis B : Environmental Electrocatalysis at Palladium Nanoparticles : Effect of the Support Nitrogen Doping on the Catalytic Activation of Carbon Halogen Bond*, "Applied Catal. B, Environ. **144**, 300 (2014).

[10]   A. Ahmed, S. Arnaboldi, C. Durante, and A. Gennaro, *Electrochemical Reduction of Organic Bromides in 1-Butyl-3- Methylimidazolium Tetra Fl Uoroborate*, J. Electroanal. Chem. **804**, 240 (2017).

[11]   B. Vanrenterghem and T. Breugelmans, *An Activity Scale of Cathode Materials for the Electrochemical Cyclisation of Allyl 2-Bromobenzyl Ether*, Electrochim. Acta **234**, 28 (2017).

[12]   B. Geboes, B. Vanrenterghem, J. Ustarroz, D. Pauwels, S. Sotiropoulos, A. Hubin, and T. Breugelmans, *Influence of the Morphology of Electrodeposited Nanoparticles on the Activity of Organic Halide Reduction*, Chem. Eng. Trans. **41**, 73 (2014).

[13]   B. Vanrenterghem, P. Jovanovič, M. Šala, M. Bele, V. S. Šelih, N. Hodnik, and T. Breugelmans, *Stability Study of Silver Nanoparticles towards the Halide*

Electroreduction, Electrochim. Acta **286**, 123 (2018).

[14] B. Vanrenterghem, B. Geboes, S. Bals, J. Ustarroz, A. Hubin, and T. Breugelmans, *Influence of the Support Material and the Resulting Particle Distribution on the Deposition of Ag Nanoparticles for the Electrocatalytic Activity of Benzyl Bromide Reduction*, Appl. Catal. B Environ. **181**, 542 (2016).

[15] B. Vanrenterghem, N. Hodnik, M. Bele, M. Šala, G. Amelinckx, S. Neukermans, R. Zaplotnik, G. Primc, M. Mozetič, and T. Breugelmans, *Increase of Electrodeposited Catalyst Stability via Plasma Grown Vertically Oriented Graphene Nanoparticle Movement Restriction*, Chem. Commun. **53**, 9340 (2017).

[16] B. Vanrenterghem, A. Papaderakis, S. Sotiropoulos, D. Tsiplakides, S. Balomenou, S. Bals, and T. Breugelmans, *The Reduction of Benzylbromide at Ag-Ni Deposits Prepared by Galvanic Replacement*, Electrochim. Acta **196**, 756 (2016).

[17] A. A. Isse, P. R. Mussini, and A. Gennaro, *New Insights into Electrocatalysis and Dissociative Electron Transfer Mechanisms : The Case of Aromatic Bromides*, 14983 (2009).

[18] S. Neukermans, F. Vorobjov, T. Kenis, R. De Wolf, J. Hereijgers, and T. Breugelmans, *Electrochemical Reduction of Halogenated Aromatic Compounds at Metal Cathodes in Acetonitrile*, Electrochim. Acta **332**, 135484 (2020).

[19] S. Stoll and A. Schweiger, *EasySpin, a Comprehensive Software Package for Spectral Simulation and Analysis in EPR*, J. Magn. Reson. **178**, 42 (2006).

[20] F. Neese, *Prediction of Electron Paramagnetic Resonance g Values Using Coupled Perturbed Hartree-Fock and Kohn-Sham Theory*, J. Chem. Phys. **115**, 11080 (2001).

[21] F. Neese, *Theoretical Study of Ligand Superhyperfine Structure. Application to Cu(II) Complexes*, J. Phys. Chem. A **105**, 4290 (2001).

[22] F. Neese, *Metal and Ligand Hyperfine Couplings in Transition Metal Complexes: The Effect of Spin-Orbit Coupling as Studied by Coupled Perturbed Kohn-Sham Theory*, J. Chem. Phys. **118**, 3939 (2003).

[23] F. Neese, *Efficient and Accurate Approximations to the Molecular Spin-Orbit Coupling Operator and Their Use in Molecular g-Tensor Calculations*, J. Chem. Phys. **122**, 034107 (2005).

[24] S. Sinnecker, A. Rajendran, A. Klamt, M. Diedenhofen, and F. Neese, *Calculation of Solvent Shifts on Electronic g -Tensors with the Conductor-Like Screening Model (COSMO) and Its Self-Consistent Generalization to Real Solvents (Direct COSMO-RS)*, J. Phys. Chem. A **110**, 2235 (2006).

[25] A. D. Becke, *Density-Functional Exchange-Energy Approximation with Correct Asymptotic Behavior*, Phys. Rev. A **38**, 3098 (1988).

[26] J. P. Perdew, *Erratum: Density-Functional Approximation for the Correlation Energy of the Inhomogeneous Electron Gas*, Phys. Rev. B **34**, 7406 (1986).

[27] A. Schäfer, H. Horn, and R. Ahlrichs, *Fully Optimized Contracted Gaussian Basis Sets for Atoms Li to Kr*, J. Chem. Phys. **97**, 2571 (1992).

[28] P. J. Stephens, F. J. Devlin, C. F. Chabalowski, and M. J. Frisch, *Ab Initio Calculation of Vibrational Absorption and Circular Dichroism Spectra Using*

Density Functional Force Fields, J. Phys. Chem. **98**, 11623 (1994).

[29]   V. Barone, *Structure, Magnetic Properties and Reactivities of Open-Shell Species From Density Functional and Self-Consistent Hybrid Methods*, in *Recent Advances in Density Functional Methods* (1995), pp. 287–334.

[30]   T. R. Tuttle, R. L. Ward, and S. I. Weissman, *Spin Density in Naphthalene Negative Ion*, J. Chem. Phys. **25**, 189 (1956).

[31]   C. L. Dodson and A. H. Reddoch, *Effects of Ion Pairing on the EPR Spectrum of the Naphthalene Anion in Solution*, J. Chem. Phys. **48**, 3226 (1968).

SEC-EPR study of the catalytic activity of Mo-Cu complexes in CO_2 reduction

This final research chapter focuses on the EPR detection of the Mo-Cu complexes employed as catalysts for CO_2 reduction. The results of both *ex-situ* and quasi-*in-situ* methods will be reported. A sample-collecting method using a vacuum pump will be used for the *ex-situ* experiments. A setup for the quasi-*in-situ* experiment using freeze-quenching designed in collaboration with the ELCAT group of UAntwerp will be introduced and validated for the SEC-EPR experiments. Both CW and pulse EPR techniques, as well as the DFT calculations, will be used in order to evaluate the paramagnetic species generated in a reaction mechanism proposed earlier.

Own contribution: Involved in making the *ex-situ* transfer setup, performing all EPR experiments and data analysis and the DFT

11.1 Introduction

The importance of decreasing the emission of CO_2 gas in nature was discussed in chapter 1. To this end, one of the strategies is converting CO_2 generated in chemical processes into other alternative products, which can be achieved via electrocatalysis by CO_2 reduction. The development of proper catalysts for the electroreduction of CO_2 is a crucial step toward the sustainable production of carbon-based chemicals. Several efficient molecular catalysts based on non-noble metals for CO_2 reduction, such as $Mn(bpy)(CO)_3BrY$ [1], Fe-quaterpyridine [2], $Fe_4N(CO)_{12}$ [3] and Co^{II}diphosphine complexes [4], have been reported in recent years. As a member of non-noble metals, Mo complexes were reported to show catalytic activity for CO_2 reduction [5–9].

Mouchfiq *et al*. [10] reported a study on the catalytic activity of a Mo-Cu complex for CO_2 reduction. The complex under study is $[(bdt)Mo^{VI}(O)S_2Cu^ICN]^{2-}$, (bdt = benzenedithiolate), in which the Mo and Cu ions are connected by two sulfide ligands (complex **1** in Figure 11.1). Using IR-SEC combined with DFT, the authors showed that complex **1** is only a pre-catalyst, and the active catalyst state is formed after the reduction and deoxygenation of complex **1** in the presence of CO_2. According to their proposed reaction mechanism (Figure 11.1), in the first step in the mechanism, a two-electron reduction of complex **1** forms complex **3** by transferring the oxo group on Mo to a CO_2 molecule. By a further one-electron reduction, complex **3** forms complex **3$_{red}$**, which is the active catalyst. The presence of a proton source was proven to be necessary for the formation of Mo^VH intermediates to react with CO_2 and complete the catalytic cycle. They showed that adding 2,2,2-trifluoroethanol (TFE) or water can supply the proton source, whereby TFE provides higher efficiency.

In some steps in the proposed reaction mechanism (Figure 11.1), the intermediates contain an EPR-active Mo centre. EPR experiments can thus potentially provide further information to understand the CO_2 reduction by Mo-Cu complexes. As mentioned in chapter 3, in order to detect most transition-metal centres, such as Mo^V centres, by EPR, low temperatures are required, which calls for freeze-quenching in electrochemical experiments. The frozen sample should be placed in a commonly used EPR tube before the EPR experiment. Hence *ex-situ* or quasi-*in-situ* methods should be employed.

This chapter focuses on studying the proposed reaction mechanism for the catalytic activity of Mo-Cu complexes synthesised by Muchfiq *et al.* in Laboratoire de Chimie des Processus Biologiques (Collège de France) for CO_2 electroreduction using both *ex-situ* and quasi-*in-situ* SEC-EPR methods.

For the *ex-situ* study, the electrochemistry procedure can be performed in bulk solution, and then the sample is transferred to the EPR tube and immediately frozen, as described in section 11.3.1.1.

The quasi-*in-situ* study can take place with a proper setup in which the sample is quench-frozen while the electrochemistry process is running inside an EPR tube. A cell designed in collaboration with the ELCAT group of UAntwerp was used. The setup was first validated for the reduction of MV and BQ in batch and in the EPR tube (similar approach as in chapter 9).
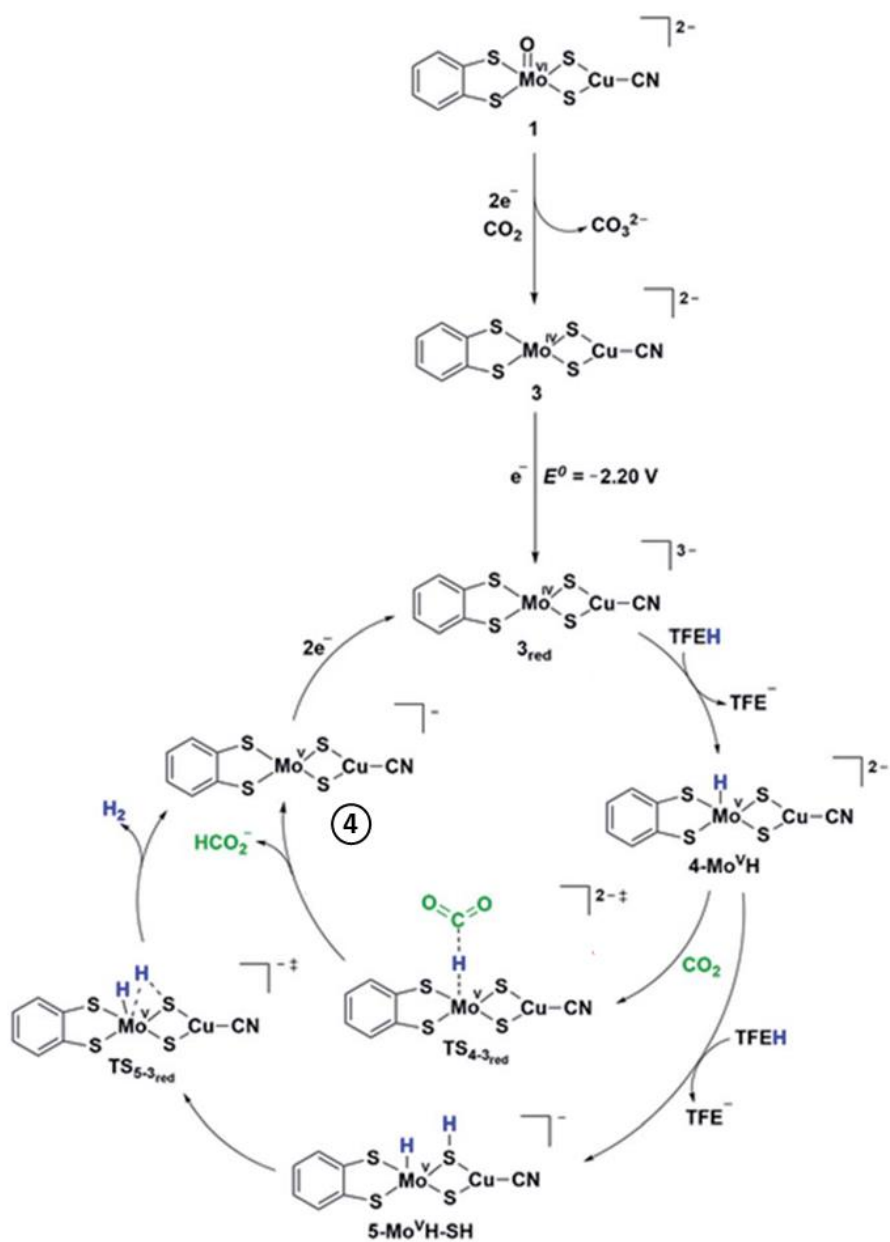
*Figure 11.1 Proposed reaction mechanisms of CO₂ reduction using pre-catalyst 1. Note that the added electron in complex **3**red resides on the sp³ orbitals of the ligands. The figure is adapted from [10].*

11.2 Materials and methods

11.2.1 Chemicals

Electrochemical measurements were performed in acetonitrile (ACN) (Chem-Lab, HPLC Grade, $\geq$ 99.9%) and MilliQ water (18.2 MΩ cm^{-1}) with, respectively, 0.1 M TBAP (Sigma-Aldrich, 99.0 %) and sodium sulphate (Acros Organics, 99.0%) as supporting electrolyte. BQ (Sigma-Aldrich, $\geq$99.5%) solutions were prepared in ACN and MV (Sigma-Aldrich, 98%) in water. All chemicals were used without any further purification. All solutions for the flow cell were purged with nitrogen before being introduced to the setups. The details of the preparation of the catalyst are given in [10].

11.2.2 EPR spectrometry

The EPR spectra were recorded on a Bruker 580 Elexsys spectrometer at X-band frequency equipped with a liquid-helium cryostat (Oxford Inc).
All CW experiments were performed at 50K and 100 kHz field modulation frequencies. For the BQ, a field modulation amplitude of 0.1 mT and a MW power of 1.5 mW were used. The field modulation amplitude for the EPR of the Mo-Cu sample was 0.2 mT for quasi *in-situ* experiments and 0.5 mT for the *ex-situ* experiments. Different MW power values were used for different experiments, which are mentioned in the figure captions. HYSCORE (hyperfine sublevel correlation spectroscopy) [11] experiments were performed with a $\frac{\pi}{2} - \tau - \frac{\pi}{2} - t_1 - \pi - t_2 - \frac{\pi}{2} - \tau - echo$ pulse sequence (see section 2.1.3.3). The pulse lengths were $t_{\pi/2}$=16 ns and t_π=32 ns. The times t_1 and t_2 were varied from 96 to 4896 ns with time steps of 16 ns. The HYSCORE spectra are the sum of spectra taken at different τ-values (see figure captions). The same pulse lengths were used for 2P and 3P ESEEM experiments. The 3P ESEEM experiments were performed at 50 different τ-values varying from 96 ns to 496 ns with the steps of 8 ns.
Mims ENDOR using the stimulated echo pulse sequence $\frac{\pi}{2} - \tau - \frac{\pi}{2} - T - \frac{\pi}{2} - \tau - echo$ were performed with a 15 μs radio-frequency (RF) π-pulse applied during time T (=17 μs). A shot repetition time of 1 ms was used. Lengths of the $\frac{\pi}{2}$-microwave pulses are16 ns. The rf frequency was swept from 1 to 31 MHz in steps of 100kHz. An ENI A-300 rf amplifier was used. The spectra were taken at 20 different τ-values varying from 96 ns to 256 ns with the steps of 8 ns
All the pulse experiments were performed at 25 K.
The EPR, ENDOR and HYSCORE spectra were analysed using EasySpin v6.0.0 [12], a MATLAB toolbox developed for EPR simulations. All data were processed and simulated using the MATLAB R2020a version (The MathWorks, Inc., Natrick, MA). HYSCORE and 3P-ESEEM time traces were baseline-corrected with a third order-polynomial, apodized with a Hamming window and zero-filled. After two (for HYSCORE) and one (for 3P ESEEM) -dimensional Fourier transformations, the absolute-value spectra were computed. The spectra recorded for different τ-values were added together to avoid blind-spot effects.

11.2.3 Electrochemistry

Electrochemical experiments were conducted with a PAR VersaSTAT 3 potentiostat. The experiments for BQ and MV performed in bulk were done in a conventional undivided cell, while those performed *ex-situ* on the Mo-Cu complexes were done in a cell containing two parts separated by a membrane.

In all experiments, glassy carbon (GC) is used as WE, as it was also used in the electrochemical characterisation by Mouchfiq *et al*. [10]. GC has the advantage of being relatively chemically inert. For the *ex-situ* experiment, an (Ag/AgCl) and for the quasi-*in-situ* experiments, a Pt wire is used as the RE, and a Pt wire is used as the CE for both experiments.

11.2.4 Computational methods

Spin-unrestricted density functional theory (DFT) calculations were performed using the ORCA package [13–16]. To mimic the solvent effect for all samples, the COSMO model was used [17]. For the geometry optimizations of the Mo-Cu complexes under study, the Becke-Perdew density functional (BP86) [18–20] was used. The Ahlrichs split-valence plus polarization (SVP) basis set was used for all atoms except copper, molybdenum, and sulfur [21]. The Ahlrich (2df,2pd) polarization functions were obtained from the TurboMole basis set library as implemented in ORCA. For the copper, molybdenum and sulfur atoms, the doubly polarized triple-zeta (TZVPP) (Ahlrichs, unpublished) basis set was used. The energy was converged to 1×10^{-8} Hartree (E_h), and the tolerances of convergence in the geometry optimization were 3×10^{-4} E_h/Bohr for the gradient and 5×10^{-6} E_h for the total energy. The coordinates of the optimized structures are given in the Supplementary Information. For the single-point calculations of the EPR parameters of the Mo-Cu complexes the combination B3LYP as functional and the 6-31+G** basis set [22,23] was used. For the copper, atom the triply polarized Core Properties basis set (CP(PPP)) and for the Molybdenum and sulfur atoms doubly polarized triple-zeta (TZVPP) (Ahlrichs, unpublished) basis set were used as implemented in ORCA.

11.3 Results and Setups

The CV experiments were performed to reproduce the results of Mouchfiq *et al*. [10]. Figure 11.2 shows the CV of 2 mM of complex **1** in ACN and 0.1 M TBAP under Ar in the presence (red) and absence (black) of CO_2. Similar to [10], there is a second reduction wave in the presence of CO_2 (Figure 11.2 (red)), indicating the appearance of the catalytic activity at E ~ -2 V. The active catalyst (complex 3_{red}) is generated at the first charge-transfer potential at E ~ -1.5 V. In the absence of CO_2 gas there is no catalytic wave in the CV.
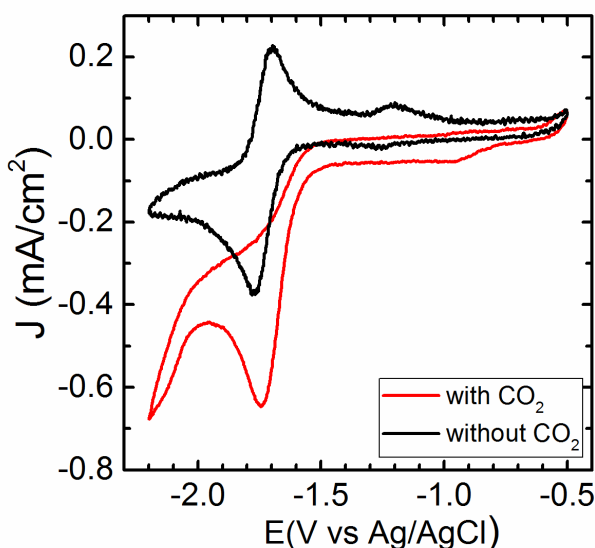
Figure 11.2. The CV experiment of 2 mM od complex 1 in ACN under Ar in the presence (red) and the absence (black) of CO_2.

11.3.1 *Ex-situ* SEC-EPR experiments

11.3.1.1 Setup and sample preparation

A classical electrochemical H-cell where the WE and CE compartments were separated by a membrane was used. The CA experiments were performed at -2.1 V. The solvent was purged by Ar gas and transferred to the glove box. All samples were prepared and transferred to the electrochemical cell in an MBraun glovebox with an internal Ar atmosphere with O_2 and H_2O content of less than 1 ppm. The cell was sealed before being taken from the glovebox for electrolysis. In the case of the CO_2 experiments, the solutions were flushed by CO_2 before the electrolysis.

A setup shown in Figure 11.3 was used in order to insert and freeze-quench the solution in the EPR tube. In this setup, a vacuum pump connected to the EPR tube via valve 1 evacuates the EPR tube (valve 1 is open and valve 2 is closed). After sufficient evacuation time, we close valve 1 and put the bottom part of the EPR tube in the liquid nitrogen, and then we open valve 2, which connects the EPR tube to the WE

compartment of the electrochemical cell. Due to the lower pressure, the solution rapidly moves from the cell to the bottom of the EPR tube and immediately becomes frozen.
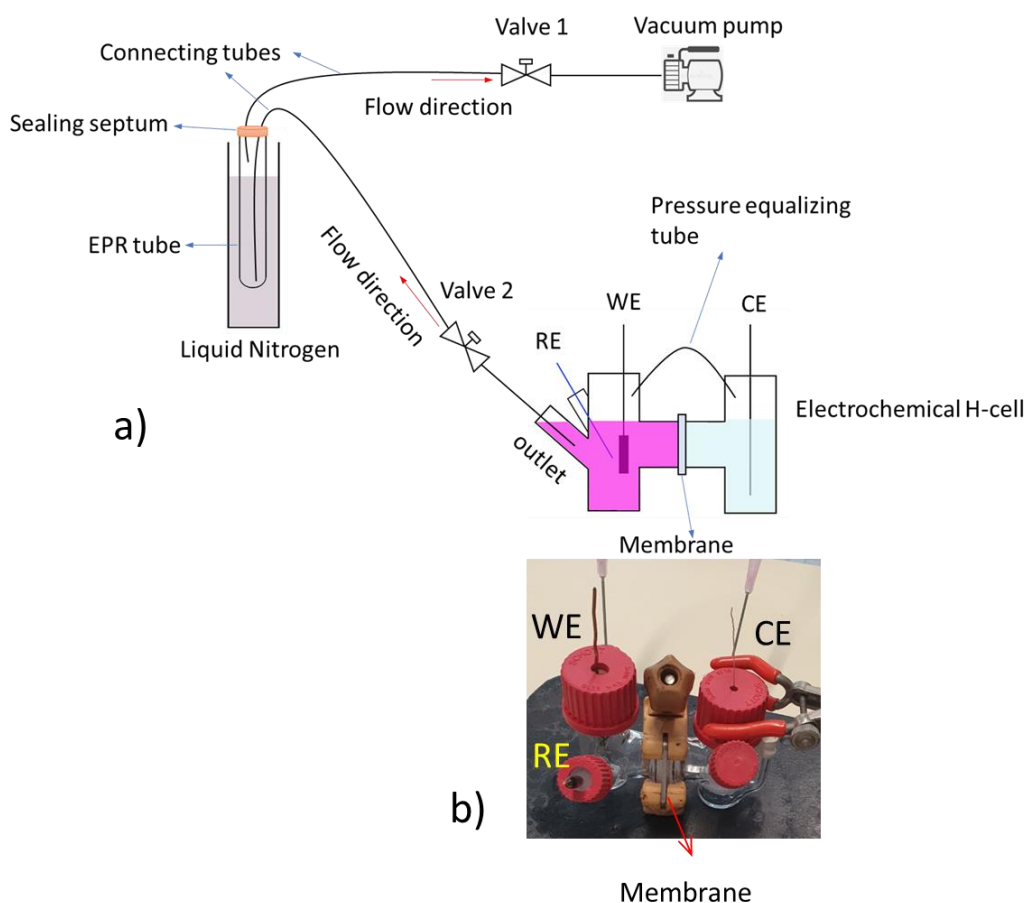
Figure 11.3. a) Schematic of the transferring setup, used for the ex-situ experiment. The red arrows show the direction of the flow. A view of the real system is shown in the supplementary information (Figure S11.1), and b) Different parts of the real two-compartment H-cell.

11.3.1.2 SEC-EPR experiments

Figure 11.4 shows the current response over time for CA experiments of 2 mM of complex **1** in ACN under CO_2 in the presence and absence of 2,2,2-trifluoroethanol (TFE) at -2.1 V. In both cases, the current increases over time, showing the occurrence of a charge transfer in the electrochemistry process. The sample was collected after 2 hours of electrolysis.
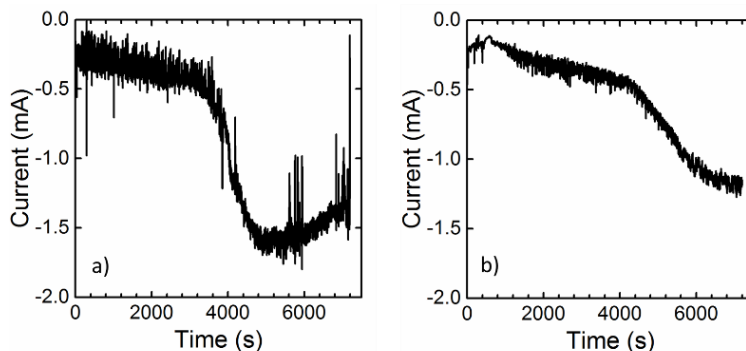
*Figure 11.4. The current response over time of the CA experiment for 2mM of complex **1** in ACN in the presence of CO_2 a) without and b) with 2,2,2-trifluoroethanol (TFE).*

Figure 11.5 shows the CW-EPR spectra of 2 mM complex **1** in ACN under Ar taken at 50K. There is a small signal in the samples before electrolysis under Ar (Figure 11.5a) and CO_2 (Figure 11.5b). These signals are typical for Mo^V paramagnetic centres [24,25], indicating that a small portion of complex **1** reduces to a paramagnetic state even before electrolysis.
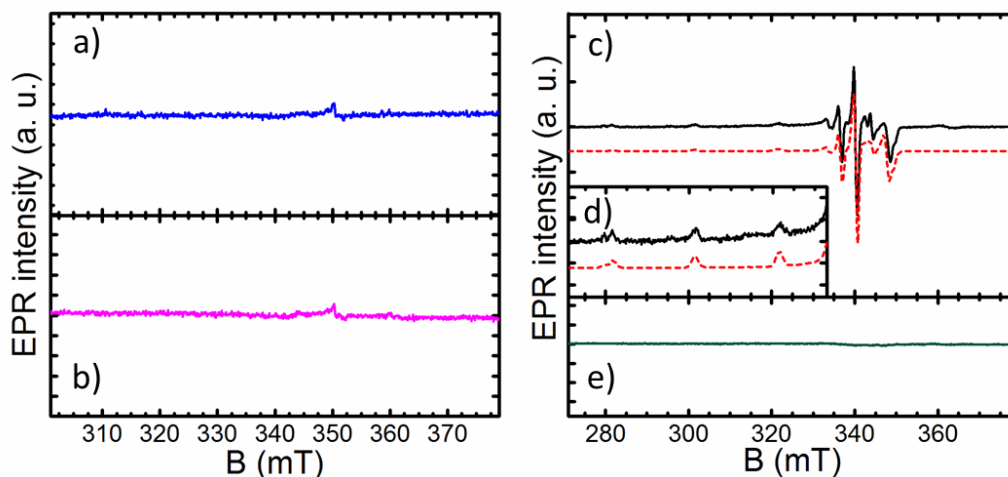
*Figure 11.5. The CW EPR spectra of the 2 mM of Complex **1** in ACN under different conditions. (Left) without electrolysis a) under Ar gas and b) under CO_2 (Right) after 2 h electrolysing at -2.1 V under CO_2 c) without TFE and e) with TFE. (d) shows an amplification of the low-field region of the spectrum (c). All the CW-EPR experiments were performed at 50 K with 0.015 mW (a,b) and 0.075 mW (c,e) MW power.*

Figure 11.5c shows the CW-EPR spectra for the Mo-Cu complex under CO_2 without TFE after electrolysis. The spectrum with g = [2.050 2.050 2.235] and A = [100 60 620] MHz are typical for Cu(II) centres [26,27] (see also chapter 4). The presence of Cu(II) species are not expected as intermediates in the proposed mechanism (Figure 11.1). EPR quantification (Figure S11.2 and Table S11.1) shows that the concentration of the Cu(II) complex is only 14% (0.28 mM) of the initial complex concentration. In the presence of TFE as an extra proton source, no Cu(II) centre

complexes are detected (Figure 11.5 e). The formation of Cu(II) complexes can be explained considering that the absence of enough proton sources makes the catalytic cycle stop, and a small portion of the Mo-Cu complex decomposes and creates Cu(II) complexes during the electrolysis. In both samples with CO_2 in the presence and absence of TFE, no Mo(V) signal was detected after more than 2 hours of electrolysing (Figure 11.5.c and e). It shows that either the proposed mechanism is incorrect or due to the high reactivity of the intermediates, they react too fast and reach the EPR-silent states before transferring and quench-freezing of the sample in the EPR tube.

These results show the importance of the quasi-*in-situ* experiments for fast sampling and quench-freezing. Hence in the next section, I will introduce a setup to do the electrolysis inside the EPR tube.

11.3.2 Quasi-*in-situ* experiment

The importance of a quasi-*in-situ* method for the SEC-EPR experiment was discussed in the previous section. Hence, an electrochemical cell was designed in collaboration with the ELCAT group (University of Antwerp) [28] to perform electrochemistry in an EPR tube and quench-freeze the solution simultaneously. This design is also based on a glassy carbon (GC) electrode, which should be removed before freezing. When frozen, the GC could break. Moreover, the GC electrode also gives an EPR signal. Apart from the advantages of using GC electrodes that were mentioned before, this setup requires a small amount of the sample (~100 µl).

11.3.2.1 Setup

The outer diameter of the used X-band tube was 4 mm, and the inner diameter was 3 mm. The GC electrode was purchased from ALS and had a diameter of 1.6 mm (GC surface) with a total diameter of 3 mm (embedded in Polyether Ether Ketone (PEEK)). A polyfluoroalkane (PFA) insulated Pt wire was led to the tip of the GC electrode with the PFA stripped from the tip as a pseudo reference electrode. The same type of wire was used as a counter electrode and wound around the PEEK body of the electrode. The insulated wire had a diameter of 200 µm and kept the lead of the reference electrode in place, 127 µm without insulation. The assembled electrode measured 2.6 mm on the widest point, leaving 0.4 mm solution between the counter electrode and the tube wall. The GC electrode was connected through a brass rod which was hollow at the end connection and fitted tightly around the electrode connection. The Pt wires were led out of the tube and fixated with tape at the top. Figure 11.6 a and c.shows the assembled electrode in an EPR tube. More information about the cell design is given in [28].

Visual inspection for electroreduction of BQ solutions performed in the EPR tube indicated that the BQ radical anion has a lifetime long enough to spread through the solution, turning it darker yellow. The reduction of MV^{2+} to the MV radical cation only resulted in a blue solution layer at the surface of the GC electrode (Figure 11.6c). It indicates the shorter lifetime of the radical.
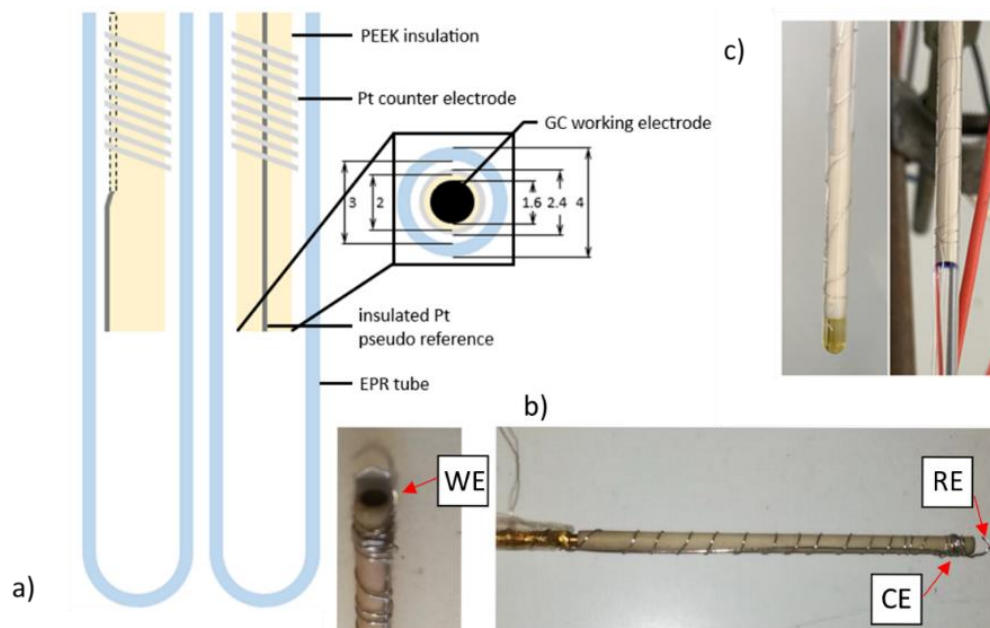
Figure 11.6. a) Two side views of the GC electrode in an EPR tube and zoom of the electrode surface (not to scale). The numbers indicated are dimensions in mm; b) real image of different parts of the used electrochemical cell, and c) Appearance of the electrode/EPR tube assembly with BQ radical anion (left) and MV radical cation generation (right). Figures adapted from [28]*.*

The sample preparation and the electrochemical process of Mo-Cu experiments were performed in a glovebox manually flushed with N_2 gas in order to avoid the presence of oxygen. The glovebox was connected to a nitrogen gas source, and N_2 was continuously flowing through the glovebox during the sample preparation. In order to control the pressure inside the glovebox, an outlet was embedded as an exit for the extra gas (Figure 11.7).

The sample was collected during the electrolysis inside the glovebox. To this end, the sample was inserted into a custom EPR tube holder (the yellow object in Figure 11.7), and a lego setup held the tube holder itself. For sample collection, the tube holder was lowered down slowly (± 0.5 mm s^{-1}) while the electrochemical setup was staying still. The movement was established remotely by using an electrical motor with an adjustable resistor for power control and gears to transfer the movement to the EPR tube holder (Figure 11.7). The counter electrode started to be increasingly exposed to the atmosphere, and the tube was then 'dropped' in liquid nitrogen (the white box in Figure 11.7) during electrolysis to flash freeze the formed paramagnetic species. This 'dropping' was done by increasing the speed of the downward movement, still gently sliding the tube in the liquid nitrogen to prevent it from breaking.
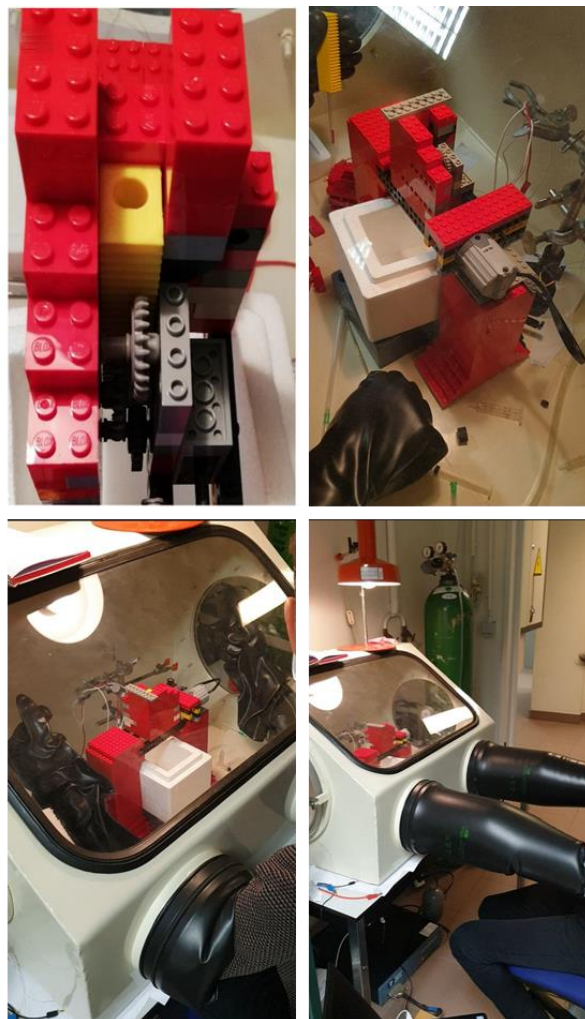
Figure 11.7. Four views of the lego setup in the glovebox, used for quasi-in-situ experiments. The EPR tube is inserted into the tube holder (the yellow object), and then the tube holder is moved downwards by the gears and electrical motor into the white box located below the lego setup, which is filled with liquid nitrogen in order to freeze quenching. The electrical motor was controlled remotely from outside of the glovebox.

11.3.2.2 SEC-EPR validation

Similar to the previous chapters, reduction of MV and BQ were used for the validation of the cell. Figure 11.8 shows the CVs for both test cases in the EPR tube and bulk solution. In both cases, the tube experiments behaved similarly to the bulk experiments. Most of the differences in the CVs can be caused by the cell geometry.

To prepare the EPR sample, the electrolysis was performed at peak potential with the electrode positioned at around 1 mm from the bottom of the tube. While the electrolysis was running, the tube was slowly moving downward, so the majority of the solution first located at the CE moved to the WE (since the electrochemical cell stays still). This

convection helped to refresh the solution and ensured that the reduced species from the working electrode were not able to diffuse to the counter electrode to be reoxidised.

The electrolysis of BQ at peak potential and subsequent freezing resulted in the EPR signal presented in Figure 11.9. The EPR spectrum shows a single line at X-band MW frequency. Earlier studies with high-field EPR revealed indeed a very small g-anisotropy for the BQ radical ($\mathbf{g}$ = [2.00654 2.00526 2.00223]) in a frozen isopropyl alcohol solution [29]). This anisotropy is not resolved at the X-band, where only a single line at $g \sim 2.0052$ with a linewidth of [0.5 (Gaussian), 0.8 (Lorentzian)] mT is found. The heterogeneous line broadening is caused by the hyperfine interaction with the 4 protons of the radical ($\mathbf{A}$ = [-9.9   -1.5   -8.7] MHz [30]).
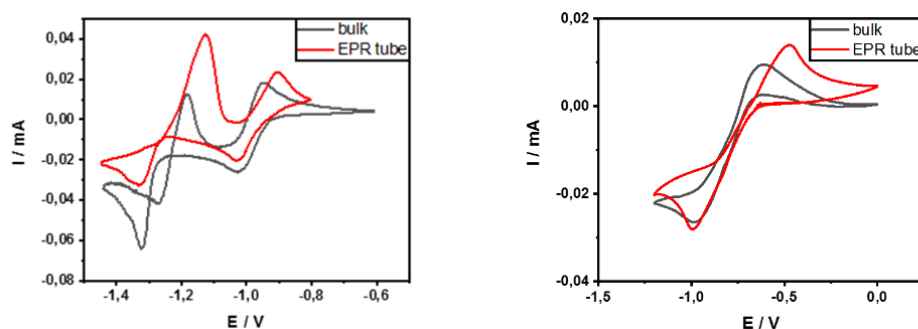
Figure 11.8. CV of 5 mM BQ (left) and 5 mM MV (right) on GC vs Ag wire at 50 mV s^{-1} in bulk and in the EPR tube.
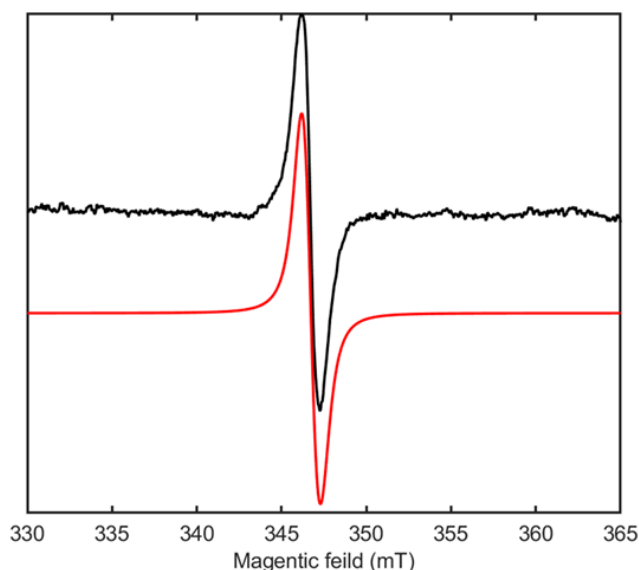
Figure 11.9. EPR Spectrum and simulation for BQ radical anion in ACN at 50 K. The radical was formed electrochemically in a quasi-in-situ experiment.

11.3.2.3 SEC-EPR on Mo-Cu complexes

After testing and validating the setup for the MV and BQ samples, it was employed to study the Mo-Cu complexes. The electrochemistry and quench-freezing were performed in the glovebox flushed with N_2 gas. The solutions and EPR tubes were flushed with CO_2 from balloons inside the glovebox. The CA experiments were performed at -1.6 V and -2.1V in the presence of CO_2 (Figure 11.10). In both cases, the current response proves that charge transfer happens. The current, however, is relatively unstable. This may be due to moving the electrode upwards during the electrolysis.
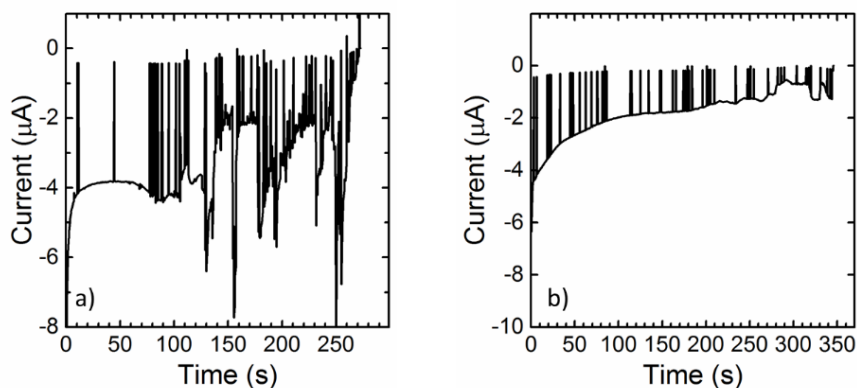
*Figure 11.10 The CA experiment of 2mM of complex **1** in ACN at a) -1.6 V and b) -2.1 V*

Complex **1** in ACN kept under N_2 was bubbled by CO_2, and CW-EPR spectra were recorded before and after the electrochemistry process (Figure 11.11). No EPR signal due to a Mo^V centre is resolved in the presence of CO_2 prior to electrolysis (Figure 11.11 magenta), although this was the case in the *ex-situ* experiments (Figure 11.5).

By electrolysing under CO_2 at -1.6 V, the CW-EPR spectrum (Figure 11.11 blue) shows the presence of two paramagnetic species. The simulated spectrum consists of two different spin systems with parameters known for Mo^V. The *g*-values of both species indicate that the unpaired electron is mainly localised on the Mo ion [24,25] (see Table 11.1, Figure 11.11, Figure S11.3 and Figure S11.4). The first EPR component (complex A) shows a resolved hyperfine interaction with ^{95,97}Mo ($I = 5/2$, with the natural abundances of 16% for ^{95}Mo and 10% for ^{97}Mo) at $B = 355$ mT, whereas complex B only shows weakly resolved features of a rhombic structure with a smaller *g*-anisotropy (*g* = [1.9771 1.9888 2.0050]) (see Table 11.1, Figures S2 and Figure S11.4). The *g*-values of complexes A and B resemble the ones reported before for other Mo^V centres (see Table 11.1). The Mo hyperfine values are not resolved for complex B due to its low contribution to the EPR spectra (Table S11.2).
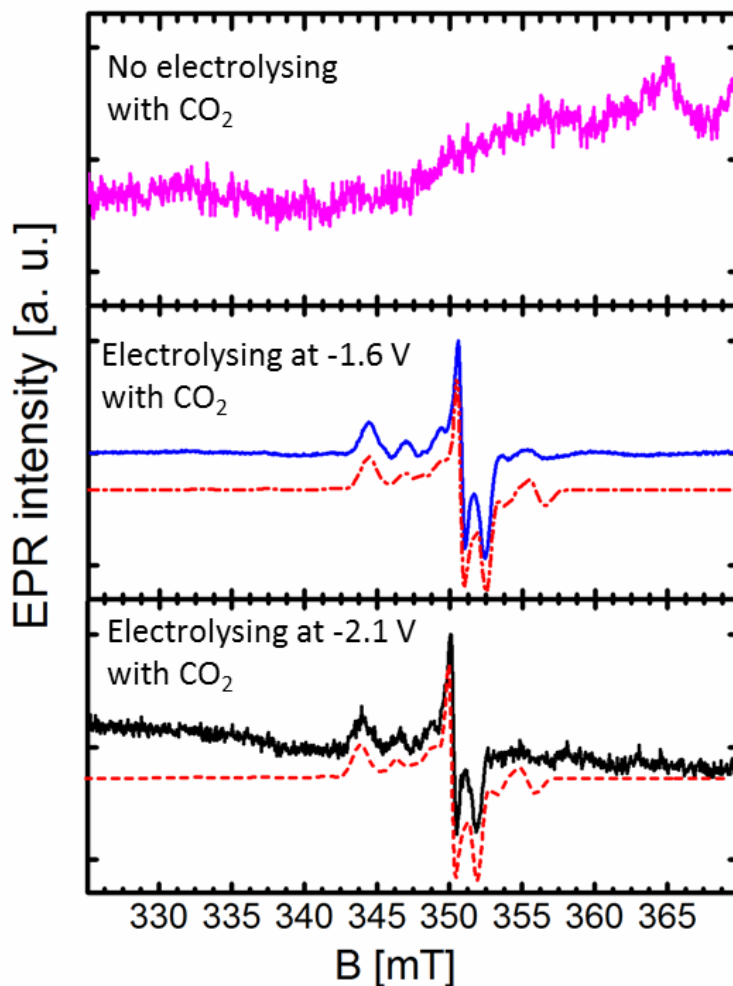
*Figure 11.11 Normalised CW-EPR spectra of 2mM complex **1** in ACN under CO₂ without electrolysis (magenta), with electrolysis at -1.6 V (blue) and -2.1 V (black), as well as the simulated spectra (red dash line). A MW power of 0.015 mW was used for all experiments.*

As mentioned before, the presence of a proton source is necessary to complete the catalytic cycle. Here we did not add TFE to the samples. However, since the sample preparation did not happen in a perfect water-free situation in this glovebox, water may be present as the proton source. The presence of water can also explain how complex **4** receives two electrons to complete the cycles in the earlier proposed mechanism (Figure 11.12).
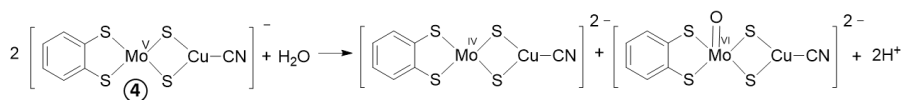
Figure 11.12 The reaction of complex 4 in the presence of water

Table 11.1. The EPR parameters obtained from simulation (Figure 11.11) in comparison with EPR data of Mo^V complexes. Note that the experiment does not allow to determine the absolute sign of the hyperfine values

Complex	g-values	A_{Mo}-values /MHz	A_H/A_{Cu}-values/ MHz	ref
Complex A	$g_x = 1.97350$ $g_y = 1.98290$ $g_z = 2.0196$	$A_x = 27$ $A_y = 26$ $A_z = 128$ $A_{iso} = 60.33$	-	tw
Complex B	$g_x = 1.9771$ $g_y = 1.9888$ $g_z = 2.0050$	Not resolved	-	tw
Complex C1	$g_x = 1.949$ $g_y = 1.9550$ $g_z = 2.0250$	$A_x = 57.3$ $A_y = 54.7$ $A_z = 133$ $A_{iso} = 82.66$	-	[24,32]
Complex C2	$g_x = 1.944$ $g_y = 1.9590$ $g_z = 2.0279$	Not reported-	-	[24,33]
Complex C3	$g_x = 1.965$ $g_y = 1.969$ $g_z = 1.989$	$A_x = 77.0$ $A_y = 74.0$ $A_z = 184.0$ $A_{iso} = 111.66$	$^H A_x = 38.5$ $^H A_y = 38.3$ $^H A_z = 36.2$	[24,32,34]
Complex C4	$g_x = 1.955$ $g_y = 1.967$ $g_z = 1.972$	$A_x = 81.24$ $A_y = 78.0$ $A_z = 196.0$ $A_{iso} = 118.33$	$^H A_x = 42.6$ $^H A_y = 44.4$ $^H A_z = 44.7$	[24,35]
Complex C5	$g_x = 1.9549$ $g_y = 1.9604$ $g_z = 2.0010$	$A_{iso} = 158.89$	$^{Cu} A_x = 117$ $^{Cu} A_y = 164$ $^{Cu} A_z = 132$	[24,36,37]
Complex C6	$g_x = 1.9850$ $g_y = 1.9910$ $g_z = 2.0080$	-	-	[31]
Complex C7	$g_x = 1.995$ $g_y = 2.001$ $g_z = 2.024$			[38]
$(Mo^V S_4)^{3-}$	$g_\parallel = 1.953$ $g_\perp = 1.973$	$A_\parallel = 139.95$ $A_\perp = 82.84$		[39]
Complex C8	$g_\parallel = 1.86$ $g_\perp = 1.98$	$A_\parallel = NR$ $A_\perp = 80$		[40]
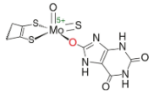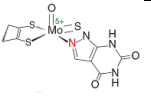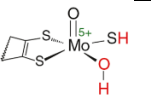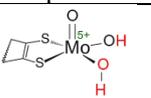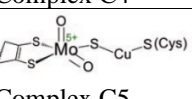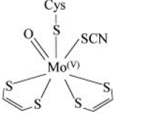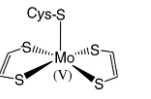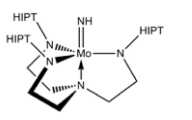
tw: This work; SCN: thiocyanate; NR: Not reported

In order to gain more insight into the nature of complex A and complex B, DFT computations of complexes **4** and **4-Mo^{V}H**, mentioned in Figure 11.1, are performed (Table S11.3).

In order to validate the DFT calculations, the EPR parameters of complex C3 (Table 11.1) were also computed (Table S11.3). Comparison of the DFT-computed values with the experimental values shows an overestimation of g_{iso} and g-anisotropy and an underestimation of the isotropic Mo hyperfine interaction and related anisotropy. Although the computed isotropic ^{1}H hyperfine coupling of $^-$OH matches that observed experimentally, its anisotropy is overestimated. The deviation from the experimental values results from a too low level of theory, notably excluding the relativistic effect, which will be needed to model Mo and S atoms.

Hence, at best, we can deduce some info based on comparing trends in the experimental and theoretical data. Of the Mo^V centres identified in Figure 11.1 (**4** and **4-Mo^V-H**), mainly the computed data of complex **4** seem to align with those of complex A. Complex B has a smaller g anisotropy than complex A, which opposes the theoretical trend when comparing complexes **4** and **4-Mo^V-H**.
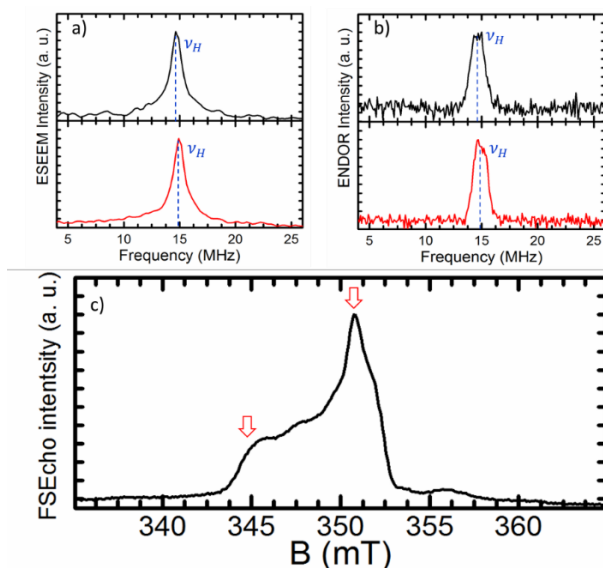

Figure 11.13 *a) 3P-ESEEM and b) Mims ENDOR experiments at the field positions 345mT (black) and 350.9 mT (red) at 10 K, and c) the field sweep echo detected spectrum of the Mo-Cu complex electrolysed at -1.6 V. The red arrows in c indicate the field positions that ESEEM and ENDOR experiments were performed.*

In order to get more information about the nuclei localised further from the unpaired electron (Mo ion), pulse EPR techniques were performed on the frozen solution of the Mo-Cu complex electrolysed at -1.6 V. Figure 11.13 a and b show the 3P-ESEEM and ENDOR spectra, respectively, at the magnetic field positions shown by the red arrows on the field sweep echo-detected EPR (FSEcho) (Figure 11.13.c). In 3P-ESEEM spectra, the dominant signal peak is observed around the ^{1}H Larmor frequency, ν_H. Similarly, a narrow signal around ν_H is found in the Mims ENDOR spectra (Figure

11.13), exhibiting maximum hyperfine coupling of 3 MHz. If this hyperfine coupling is dipolar in nature, this agrees with minimal H-Mo distance of 3.7 Å. This is in line with the distance of the Mo ion to the ligand protons. The single point DFT computations on the geometry optimized molecular structures calculate the largest values for the hyperfine tensor A_H = [1.90 4.18 1.79] MHz for complex **4** with a minimal H-Mo distance of 5.1 Å (see Figure S11.5), and A_H = [0.59 -1.33 -1.08] MHz for complex 4-Mo^VH with minimal H-Mo distance of 5.3 Å (see Figure S 11.6).

The HYSCORE spectrum (Figure 11.14) confirms the presence of small ^{1}H hyperfine couplings (width of the ridge is ~ 3 MHz).

All pulsed EPR experiments only show the presence of weakly coupled ^{1}H nuclei. According to the structure of the intermediates proposed in the reaction mechanism, the Cu nuclei are relatively close to the Mo centre. The DFT calculations show hyperfine tensors of A_{Cu} = [-5.96 -4.20 -18.24] MHz for complex **4**, and A_{Cu} = [-3.46 -18.22 -10.98] for complex **4-Mo^{V}H** (see Table S11.3). These hyperfine couplings are in the detectable range of ESEEM or ENDOR. Although we cannot discard that due to a large quadrupole coupling of the Cu nuclei, the cross-peaks appear beyond the frequency window that is detectable by HYSCORE. Also, the line broadening in CW-EPR spectra could be due to the unresolved fine structures from the Cu hyperfine coupling. However, the noise makes it hard to recognise such small sub-structures on the main peaks. Hence, there are still further experiments needed to have a complete set of results.

Moreover, some possible flaws should be considered in terms of sample preparation. Firstly, air may have leaked into the glovebox in which the experiments are performed. The second reason that should be considered is the small space in the EPR tube and the limited distance between CE and WE, which causes the diffusion of the oxidised products created on CE to the WE part. Finally, the effect of the H_2O on the reaction mechanism may be more than the reaction proposed in Figure 11.12. Potentially $Mo^V=O$ instead of Mo^V complexes are formed. The EPR data of complex A align very well with the experimental data of other $Mo^V=O$ complexes (Table 11.1).
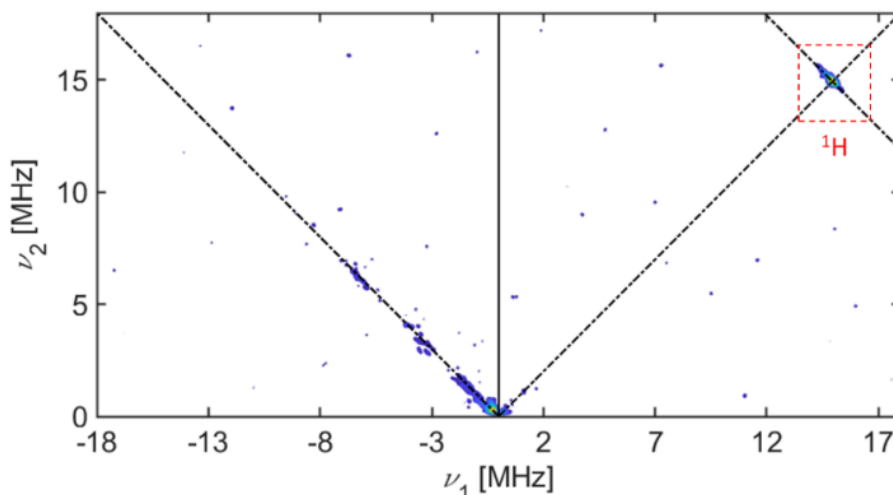

Figure 11.14 The HYSCORE experiment of the Mo-Cu complex electrolysed at -1.6 V at the field positions 350.9 mT at 10 K. The spectrum is the sum of the three spectra recorded at τ = 120, 156 and 192 ns.

11.4 Conclusion

This chapter highlights the use of SEC-EPR in the detection of transition metal paramagnetic centres to provide evidence for the proposed mechanism of the CO_2 reduction via Mo-Cu complexes. Both *ex-situ* and quasi-*in-situ* methods were employed. The *ex-situ* sampling with the vacuum pump was not fast enough to trap the intermediates with the freeze-quenching.

A setup for quasi-*in-situ* SEC-EPR was developed and validated to do the electrochemistry and quench freezing in the EPR tube. The CW and pulse EPR experiments were performed for the quasi-*in-situ* setup. Although the experiments prove the presence of Mo^V paramagnetic centres, there is still some ambiguity. Hence, some improvements need to be made to gain more reliable results. The improvements contain adjusting the geometry of the cell in order to better isolation of CE from WE, Using a more efficient glovebox to prevent oxygen leakage and the presence of water. Furthermore, experiments in the presence of TFE should be performed. Finally, also Davies ENDOR should be performed to probe the presence of Cu hyperfine couplings in the 10-20 MHz range. The DFT computations should also be extended, both improving the level of theory and the inclusion of other models, such as $Mo^V=O$ complexes.
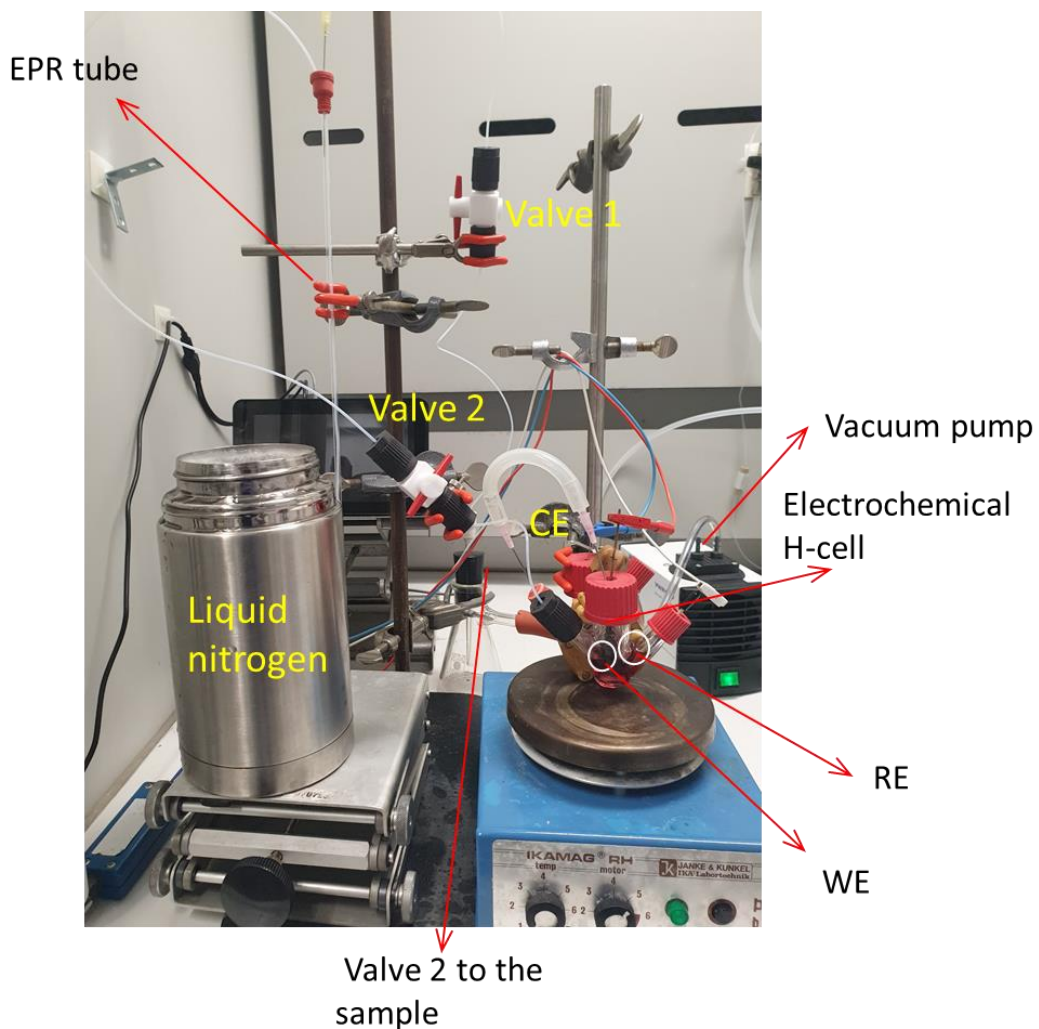
11.5 Supporting information

Figure S11.1 The view of the transferring system, used for the ex-situ experiments.

The amount of Cu(II) species detected in Figure 11.5 (c) was determined by using the below calibration curve for a Cu(II)-bisacetylacetonate complex (Cu(acac)$_2$).

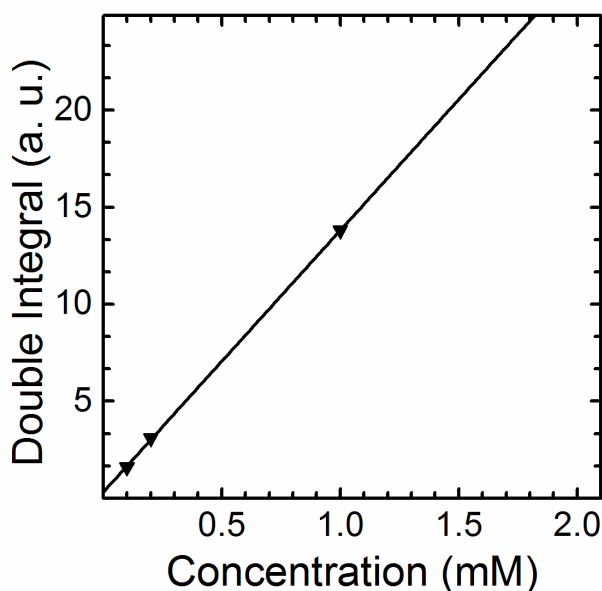*Figure S11.2 The double integral (DI) value of the intensity of the CW-EPR spectrum of the Cu(acac)$_2$ in DMSO vs the concentration of Cu(acac)$_2$. Three experimental data points depicted with solid black triangles were used for the linear fit. The DI values were calculated from the corresponding simulated CW-EPR spectra for different concentrations of Cu(acac)$_2$ solution. The procedure involved the simulation of the spectra and subsequent double integration of the simulated spectrum to avoid noise effect.*

Table S11.1 the DI values and corresponding concentration of the Cu(II) complexes

Double integral (a. u.)	Cu(II) complex concentration (mM)	Cu(II)complex
1.60	0.10	Cu(acac)$_2$
3.08	0.20	Cu(acac)$_2$
13.80	1.00	Cu(acac)$_2$
4.09	0.28	Mo-Cu

Figure S11.3 shows the individual normalised simulated spectra of complexes A and B Figure 11.11. The concentration of all Mo^V centre species differs at the different potential values that electrolysis was performed, as well as the concentration of Complexes A and B. The total EPR spectrum is the sum of these individual spectra with respect to the percentage of each species (Figure S11.4). Table S11.2 shows the percentage of complexes A and B for the samples that are electrolysed at different potential values.
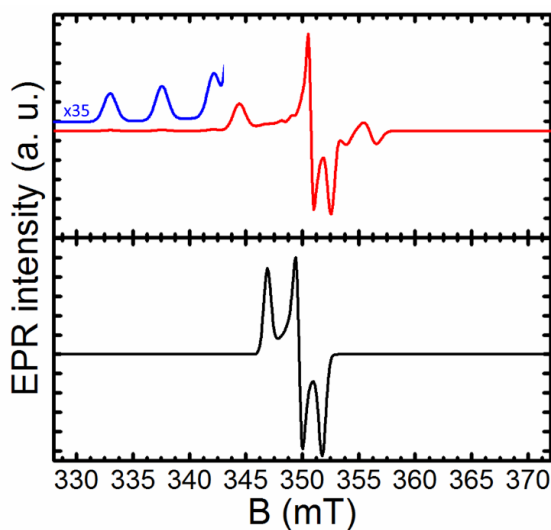

Figure S11.3 The normalised simulated CW-EPR spectra of complex A (red) and complex B (black). (Blue) Blow up of the spectrum in red in the low-field range
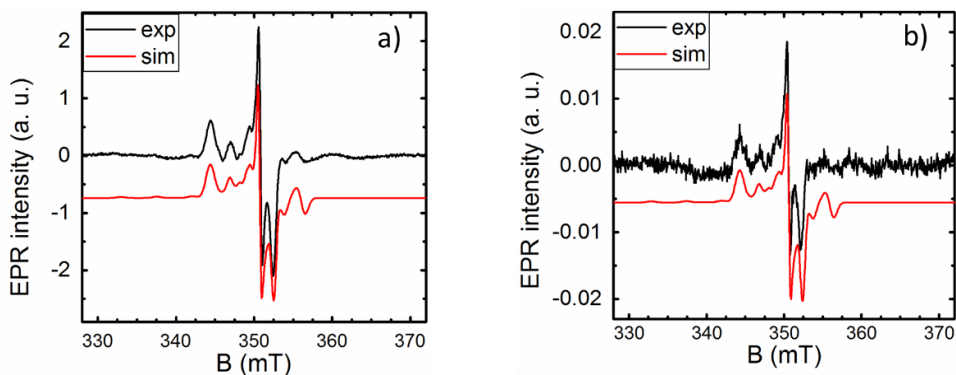

Figure S11.4 The experimental (black) and simulated (red) CW EPR spectra of Mo-Cu complexes electrolysed at a) -1.6 V and b) -2.1 V under CO_2 at 50 K.

Table S11.2 The percentage of the complexes A and B for the samples electrolysed under CO_2 at potential values -1.6 and -2.1 V.

Potential (V)	Complex A percentage (%)	Complex B percentage (%)
-1.6	90	10
-2.1	91	9

This section shows the results of the DFT calculations in detail for the **4** and **4-Mo^{V}H** complexes.
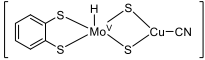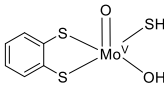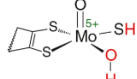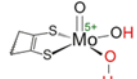
*Table S11.3 DFT calculated EPR values from the geometry optimised structures of complexes **4**, **4-Mo^{V}H** and complex C3 in comparison with the experimental values. The ^{1}H hyperfine values exceeding 5 MHz (in absolute value) are mentioned. The z-axis is along the Mo-O axis in complex C3 and C4 (Mo-H in complex **4-Mo^{V}H**)*

Complex	g-values	A_{Mo} /MHz	A_H / MHz	A_{Cu} /.MHz	ref
4	$g_x = 1.9767$ $g_y = 1.9892$ $g_z = 2.0107$	$A_x = -4.71$ $A_y = -75.37$ $A_z = -97.78$ $A_{iso}=-57.29$	-	$A_x = 4.20$ $A_y = -5.96$ $A_z = 18.24$ $A_{iso} = 5.49$	
4-Mo^{V}H	$g_x = 1.7549$ $g_y = 1.8927$ $g_z = 2.0125$	$A_x = 10.98$ $A_y = 27.201$ $A_z = 101.91$ $A_{iso}= 46.69$	$A_x = -19.04$ $A_y = -49.18$ $A_z = -59.93$ $A_{iso} =-42.72$	$A_x = 3.46$ $A_y = -7.00$ $A_z = -18.22$ $A_{iso} = -7..25$	
Complex C3 computed	$g_x = 1.9256$ $g_y = 1.9760$ $g_z = 2.047$	$A_x = 12.02$ $A_y = 25.30$ $A_z = 104.12$ $A_{iso}= 47.15$	H/OH $A_x = 35.44$ $A_y = 36.23$ $A_z = 51.15$ $A_{iso} = 40.94$ H/SH $A_x = 22.78$ $A_y = 23.39$ $A_z = 31.19$ $A_{iso} = 25.78$	-	
Complex C3 experimental	$g_x = 1.965$ $g_y = 1.969$ $g_z = 1.989$	$A_x = 77.0$ $A_y = 74.0$ $A_z = 184.0$ $A_{iso} = 111.66$	$^HA_x = 38.5$ $^HA_y = 38.3$ $^HA_z = 36.2$	-	[24,32, 34]
Complex C4 experimental	$g_x = 1.955$ $g_y = 1.967$ $g_z = 1.972$	$A_x = 81.24$ $A_y = 78.0$ $A_z = 196.0$ $A_{iso}=118.33$	$^HA_x = 42.6$ $^HA_y = 44.4$ $^HA_z = 44.7$	-	[24,35]
Complex A experimental	$g_x= 1.97350$ $g_y= 1.98290$ $g_z = 2.0196$	$A_x = 27$ $A_y = 26$ $A_z = 128$ $A_{iso} = 60.33$	-	-	tw
Complex B experimental	$g_x = 1.9771$ $g_y = 1.9888$ $g_z = 2.0050$	Not resolved	-		tw

Complex 4

*Figure S11.5 Geometry-optimized configuration of complex **4**. The coordinates of the atoms are reported in Table S 11.4, and the minimal H-Mo atom distance for ligand protons, shown in red.*

*Table S 11.4 The coordinates (in Å) of the geometry-optimized **4** complex*

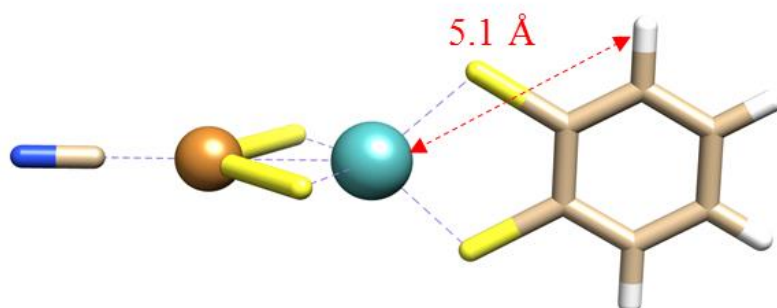|			
C	0.423592	-4.418804	0.063232
C	1.447560	-5.362620	-0.062972
C	2.785720	-4.949024	-0.069283
C	3.099605	-3.591735	0.050893
C	2.077236	-2.637942	0.179460
C	0.730481	-3.054135	0.185451
S	-0.590684	-1.862267	0.349858
S	2.496783	-0.908253	0.337053
Mo	0.445909	0.256647	0.382181
S	0.060578	1.481970	-1.404970
S	0.095637	1.420519	2.216920
Cu	-0.352761	2.863825	0.433616
C	-0.907600	4.696121	0.459511
N	-1.246915	5.814672	0.470409
H	-0.622215	-4.737900	0.066785
H	1.197645	-6.422608	-0.157254
H	3.589344	-5.683348	-0.168716
H	4.143083	-3.265117	0.044824

Complex 4-Mo^{V}H

Figure S 11.6 Geometry-optimized configuration of complex **4-Mo^{V}H.** The coordinates of the atoms are reported in Table S11.5, and the minimal H-Mo atom distance for ligand protons, shown in red

Table S11.5 The coordinates (in Å) of the geometry-optimized **4-Mo^{V}H** complex

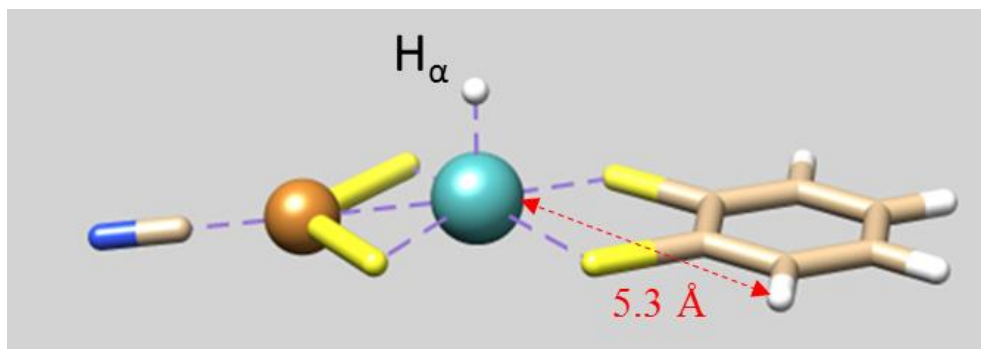|			
C	0.901377	-4.121651	1.387930
C	2.150759	-4.723740	1.616627
C	3.331201	-3.970007	1.461831
C	3.253922	-2.619645	1.079378
C	2.001993	-1.997628	0.848778
C	0.806938	-2.760620	1.005799
S	-0.770033	-2.016879	0.703428
S	1.915988	-0.302559	0.348938
Mo	-0.471347	0.425979	0.281184
S	-2.709121	0.385776	-0.132759
S	0.388585	2.359598	-0.555439
Cu	-1.873046	2.392285	-0.797205
C	-2.875075	3.798688	-1.556321
N	-3.503816	4.680710	-2.032115
H	-0.024937	-4.707429	1.505034
H	2.201342	-5.782875	1.915557
H	4.314930	-4.433356	1.638644
H	4.174390	-2.026313	0.954395
H	-0.565050	0.919666	1.907316

Complex C3
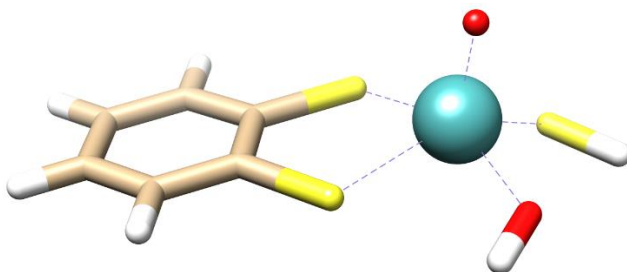
Figure S11.7 Geometry-optimized configuration of complex C3. The coordinates of the atoms are reported in Table S11.6

Table S11.6 The coordinates (in Å) of the geometry-optimized complex C3

C	0.676947	-4.169533	-0.099024
C	-0.513360	-4.859019	-0.343137
C	-1.677016	-4.150322	-0.672925
C	-1.642606	-2.756068	-0.755243
C	-0.448339	-2.051648	-0.513441
C	0.725934	-2.765214	-0.185294
S	2.248081	-1.912629	0.147495
S	-0.436086	-0.278741	-0.586283
Mo	1.892414	0.438532	-0.441016
S	3.714200	0.776293	1.164335
H	1.586645	-4.719456	0.158489
H	-0.531412	-5.950397	-0.277463
H	-2.612355	-4.682613	-0.866441
H	-2.548545	-2.198803	-1.010051
O	1.115585	2.127166	0.148086
H	3.620627	2.129477	1.181891
H	0.152301	2.238856	0.143640
O	2.497985	0.643120	-2.010619

11.6 References

[1]   M. Bourrez, F. Molton, S. Chardon-Noblat, and A. Deronzier, *[Mn(Bipyridyl)(CO)₃Br]: An Abundant Metal Carbonyl Complex as Efficient Electrocatalyst for CO₂ Reduction*, Angew. Chemie **123**, 10077 (2011).

[2]   C. Cometto, L. Chen, P.-K. Lo, Z. Guo, K.-C. Lau, E. Anxolabéhère-Mallart, C. Fave, T.-C. Lau, and M. Robert, *Highly Selective Molecular Catalysts for the CO₂-to-CO Electrochemical Conversion at Very Low Overpotential. Contrasting Fe vs Co Quaterpyridine Complexes upon Mechanistic Studies*, ACS Catal. **8**, 3411 (2018).

[3]   M. D. Rail and L. A. Berben, *Directing the Reactivity of [HFe₄N(CO)₁₂]⁻ toward H⁺ or CO₂ Reduction by Understanding the Electrocatalytic Mechanism*, J. Am. Chem. Soc. **133**, 18577 (2011).

[4]   S. Roy, B. Sharma, J. Pécaut, P. Simon, M. Fontecave, P. D. Tran, E. Derat, and V. Artero, *Molecular Cobalt Complexes with Pendant Amines for Selective Electrocatalytic Reduction of Carbon Dioxide to Formic Acid*, J. Am. Chem. Soc. **139**, 3685 (2017).

[5]   T. Fogeron, P. Retailleau, L. Chamoreau, Y. Li, and M. Fontecave, *Pyranopterin Related Dithiolene Molybdenum Complexes as Homogeneous Catalysts for CO₂ Photoreduction*, Angew. Chemie Int. Ed. **57**, 17033 (2018).

[6]   J. Porcher, T. Fogeron, M. Gomez-Mingot, E. Derat, L. Chamoreau, Y. Li, and M. Fontecave, *A Bioinspired Molybdenum Complex as a Catalyst for the Photo- and Electroreduction of Protons*, Angew. Chemie **127**, 14296 (2015).

[7]   T. Fogeron, J.-P. Porcher, M. Gomez-Mingot, T. K. Todorova, L.-M. Chamoreau, C. Mellot-Draznieks, Y. Li, and M. Fontecave, *A Cobalt Complex with a Bioinspired Molybdopterin-like Ligand: A Catalyst for Hydrogen Evolution*, Dalt. Trans. **45**, 14754 (2016).

[8]   J.-P. Porcher, T. Fogeron, M. Gomez-Mingot, L.-M. Chamoreau, Y. Li, and M. Fontecave, *Synthesis and Reactivity of a Bio-Inspired Dithiolene Ligand and Its Mo Oxo Complex*, Chem. - A Eur. J. **22**, 4447 (2016).

[9]   T. Fogeron, P. Retailleau, L.-M. Chamoreau, M. Fontecave, and Y. Li, *The Unusual Ring Scission of a Quinoxaline-Pyran-Fused Dithiolene System Related to Molybdopterin*, Dalt. Trans. **46**, 4161 (2017).

[10]   A. Mouchfiq, T. K. Todorova, S. Dey, M. Fontecave, and V. Mougel, *A Bioinspired Molybdenum-Copper Molecular Catalyst for CO₂ Electroreduction*, Chem. Sci. **11**, 5503 (2020).

[11]   P. Höfer, A. Grupp, H. Nebenführ, and M. Mehring, *Hyperfine Sublevel Correlation (Hyscore) Spectroscopy: A 2D ESR Investigation of the Squaric Acid Radical*, Chem. Phys. Lett. **132**, 279 (1986).

[12]   S. Stoll and A. Schweiger, *EasySpin, a Comprehensive Software Package for Spectral Simulation and Analysis in EPR*, J. Magn. Reson. **178**, 42 (2006).

[13]   F. Neese, *Prediction of Electron Paramagnetic Resonance g Values Using Coupled Perturbed Hartree–Fock and Kohn–Sham Theory*, J. Chem. Phys. **115**, 11080 (2001).

[14]   F. Neese, *Theoretical Study of Ligand Superhyperfine Structure. Application to Cu(II) Complexes*, J. Phys. Chem. A **105**, 4290 (2001).

[15] F. Neese, *Metal and Ligand Hyperfine Couplings in Transition Metal Complexes: The Effect of Spin–Orbit Coupling as Studied by Coupled Perturbed Kohn–Sham Theory*, J. Chem. Phys. **118**, 3939 (2003).

[16] F. Neese, *Efficient and Accurate Approximations to the Molecular Spin-Orbit Coupling Operator and Their Use in Molecular g-Tensor Calculations*, J. Chem. Phys. **122**, 034107 (2005).

[17] S. Sinnecker, A. Rajendran, A. Klamt, M. Diedenhofen, and F. Neese, *Calculation of Solvent Shifts on Electronic g -Tensors with the Conductor-Like Screening Model (COSMO) and Its Self-Consistent Generalization to Real Solvents (Direct COSMO-RS)*, J. Phys. Chem. A **110**, 2235 (2006).

[18] J. P. Perdew, *Density-Functional Approximation for the Correlation Energy of the Inhomogeneous Electron Gas*, Phys. Rev. B **33**, 8822 (1986).

[19] J. P. Perdew, *Erratum: Density-Functional Approximation for the Correlation Energy of the Inhomogeneous Electron Gas*, Phys. Rev. B **34**, 7406 (1986).

[20] A. D. Becke, *Density-Functional Exchange-Energy Approximation with Correct Asymptotic Behavior*, Phys. Rev. A **38**, 3098 (1988).

[21] A. Schäfer, H. Horn, and R. Ahlrichs, *Fully Optimized Contracted Gaussian Basis Sets for Atoms Li to Kr*, J. Chem. Phys. **97**, 2571 (1992).

[22] W. J. Hehre, R. Ditchfield, and J. A. Pople, *Self—Consistent Molecular Orbital Methods. XII. Further Extensions of Gaussian—Type Basis Sets for Use in Molecular Orbital Studies of Organic Molecules*, J. Chem. Phys. **56**, 2257 (1972).

[23] R. Krishnan, J. S. Binkley, R. Seeger, and J. A. Pople, *Self-consistent Molecular Orbital Methods. XX. A Basis Set for Correlated Wave Functions*, J. Chem. Phys. **72**, 650 (1980).

[24] L. B. Maia, I. Moura, and J. J. G. Moura, *EPR Spectroscopy on Mononuclear Molybdenum-Containing Enzymes*, 55 (2017).

[25] I. K. Dhawan and J. H. Enemark, *EPR Studies of Oxo−Molybdenum(V) Complexes with Sulfur Donor Ligands: Implications for the Molybdenum Center of Sulfite Oxidase*, Inorg. Chem. **35**, 4873 (1996).

[26] E. Carter, K. M. Sharples, J. A. Platts, and D. M. Murphy, *Structure Determination of Bound Nitrogen-Based Adducts with Copper(II) Acetylacetonato; An EPR, ENDOR and DFT Study*, Phys. Chem. Chem. Phys. **17**, 11445 (2015).

[27] P. Nunes, N. V. Nagy, E. C. B. A. Alegria, A. J. L. Pombeiro, and I. Correia, *The Solvation and Electrochemical Behavior of Copper Acetylacetonate Complexes in Ionic Liquids*, J. Mol. Struct. **1060**, 142 (2014).

[28] S. Neukermans, Towards a Targeted Optimization of Electrocatalysts by Combining Electrosynthesis with In-Situ Electron Paramagnetic Resonance, PhD thesis, University of Antwerp, 2021.

[29] M. Knüpling, J. T. Törring, and S. Un, *The Relationship between the Molecular Structure of Semiquinone Radicals and Their G-Values*, Chem. Phys. **219**, 291 (1997).

[30] F. MacMillan, F. Lendzian, and W. Lubitz, *EPR and ENDOR Characterization of Semiquinone Anion Radicals Related to Photosynthesis*, Magn. Reson. Chem. **33**, S81 (1995).

[31] C. S. Butler, J. M. Charnock, C. D. Garner, A. J. Thomson, S. J. Ferguson, B.

C. Berks, and D. J. Richardson, *Thiocyanate Binding to the Molybdenum Centre of the Periplasmic Nitrate Reductase from Paracoccus Pantotrophus*, Biochem. J. **352**, 859 (2000).

[32] G. N. George and R. C. Bray, *Studies by Electron Paramagnetic Resonance Spectroscopy of Xanthine Oxidase Enriched with Molybdenum-95 and with Molybdenum-97*, Biochemistry **27**, 3603 (1988).

[33] T. R. Hawkes, G. N. George, and R. C. Bray, *The Structure of the Inhibitory Complex of Alloxanthine (1 H -Pyrazolo[3,4- d]Pyrimidine-4,6-Diol) with the Molybdenum Centre of Xanthine Oxidase from Electron-Paramagnetic-Resonance Spectroscopy*, Biochem. J. **218**, 961 (1984).

[34] R. C. Bray and S. Gutteridge, *Numbers and Exchangeability with Water of Oxygen-17 Atoms Coupled to Molybdenum(V) in Different Reduced Forms of Xanthine Oxidase*, Biochemistry **21**, 5992 (1982).

[35] G. L. Wilson, R. J. Greenwood, J. R. Pilbrow, J. T. Spence, and A. G. Wedd, *Molybdenum(V) Sites in Xanthine Oxidase and Relevant Analogue Complexes: Comparison of Molybdenum-95 and Sulfur-33 Hyperfine Coupling*, J. Am. Chem. Soc. **113**, 6803 (1991).

[36] B. Zhang, C. F. Hemann, and R. Hille, *Kinetic and Spectroscopic Studies of the Molybdenum-Copper CO Dehydrogenase from Oligotropha Carboxidovorans*, J. Biol. Chem. **285**, 12571 (2010).

[37] C. Gourlay, D. J. Nielsen, J. M. White, S. Z. Knottenbelt, M. L. Kirk, and C. G. Young, *Paramagnetic Active Site Models for the Molybdenum−Copper Carbon Monoxide Dehydrogenase*, J. Am. Chem. Soc. **128**, 2164 (2006).

[38] P. J. González, M. G. Rivas, C. D. Brondino, S. A. Bursakov, I. Moura, and J. J. G. Moura, *EPR and Redox Properties of Periplasmic Nitrate Reductase from Desulfovibrio Desulfuricans ATCC 27774*, JBIC J. Biol. Inorg. Chem. **11**, 609 (2006).

[39] T. Ecclestone, S. H. Laurie, M. C. R. Symons, and F. A. Taiwo, *EPR Studies on Irradiated Group VI Tetrachalconide Ions*, Polyhedron **17**, 1435 (1998).

[40] A. Sharma, M. Roemelt, M. Reithofer, R. R. Schrock, B. M. Hoffman, and F. Neese, *EPR/ENDOR and Theoretical Study of the Jahn–Teller-Active [HIPTN₃ N]Mo ^{V} L Complexes (L = N⁻ , NH)*, Inorg. Chem. **56**, 6906 (2017).

Part V
Conclusions

CHAPTER 12

Conclusions and future perspective

This chapter summarises some of the important conclusions and gives an outlook to future research.

12.1 Conclusions

This thesis shows the strength and versatility of the combination of electrochemistry and EPR. Electrochemistry enables us to make the desired chemical products in a green and environmentally friendly way. The ability of EPR to study paramagnetic species is exploited to detect and identify reaction intermediates and thus to unravel the reaction mechanisms of electrochemical reactions while in turn helps to optimise electrochemical experiment parameters, such as potential control, choice of electrodes, and even the atmosphere under which the reaction occurs. All these factors help in decreasing energy costs.

Despite the advantages that are provided by bringing the world of EPR and electrochemistry together, combining them has so many challenges and requires enough knowledge about physics and (electro)chemistry for data analysis and setting up the experiments. However, with careful experimental design, many of the challenges and sources of error can be overcome or avoided to yield precise information.

The setup design has to meet several requirements to be suitable for *in-situ* SEC-EPR experiments. The challenges related to the experimental setups and an overview of contemporary designs were discussed in review chapter 3. They formed the basics of the newly designed setups that were introduced and used in chapters 5, 9, and 11.

Materials that are used in the electrochemical cell should not contain paramagnetic species that influence the EPR spectrum at the experiment condition. In case their presence is unavoidable, a blank EPR spectrum should be subtracted from each sample's EPR spectra. If the background signal is at field positions that do not interfere with the signals from the sample, it can be neglected. Microwave absorbance by the cell body decreases the Q-factor of the EPR cavity resulting in poor EPR signals, so selecting materials with minimum microwave absorbance is crucial. The choice of electrode materials such as ITO for the experiments in flat-cell setups and as the material for the body of the flow cell in chapter 9, as well as the removal of GC electrode before the EPR measurements in chapter 11, were based on these considerations.

Another point that one should be concerned about is the space limitation due to the small size of the EPR cavities. Finding the best electrode positions in the SEC-EPR cell is crucial to gain the best electrochemical response and EPR experiment efficiency.

Many reaction intermediates in an electrochemical process are radical species known for their high reactivity rate, and they can react very quickly before they can be detected with EPR. Hence spin-trapping is one of the main techniques used in this thesis for stabilising the reactive radical species to be detectable by EPR, which was introduced in Part II and used in Part III.

Spin traps also contain pitfalls and non-innocent side reactions rather than radical detection. In Part II (chapter 4), the non-innocent role of DMPO as a spin trap in copper-catalysed reactions was studied using CW EPR and hyperfine spectroscopy techniques with corroborating DFT computations. An aerobic oxidation reaction of 2-benzylpyridine N-oxide was used as a test case. It was shown that DMPO(-derived)

molecules ligate equatorially to the Cu(II) ion even in the presence of a competing nitrogen base such as pyridine. DMPO showed less competitivity for replacing acac due to its negative charge and bidentate binding mode in [Cu(acac)$_2$]. Overall, chapter 4 showed the importance of validating the spin trapping method in the presence of transition metals before using them. This method of validation should be extended to other spin traps and other transition metal ions.

Part III of this thesis contains the applications of SEC-EPR methods for the analysis of electrochemical reactions by using the spin-trap EPR methods. In this part, four different case studies with different applications were investigated. Using *in-situ* SEC-EPR, the reaction mechanism for electrochemical cyclisation of allyl 2-bromobenzyl ether to 4-methylisochromain (a benzopyran-derivative) as a widely used agent in the pharmaceutical industry was confirmed by detecting and identifying the PBN-trapped intermediates and DFT in chapter 5. The same approach with using DMPO as the spin trap was employed to confirm the reaction mechanisms of the electrochemical self-condensation of acetone to DAA in the presence and absence of O$_2$ in chapter 6. DAA is known for its application in the industry. It was shown that acetone follows different reaction mechanisms under each atmospheric condition towards DAA. Moreover, the presence of O$_2$ caused a significant reduction in overpotential at which the radical intermediates in the acetone reduction are formed. Using DMPO as a spin trap, *ex-situ* SEC-EPR helped to unravel the reaction mechanism of an electrochemical sensor for on-site detection of ecstasy pills and powders in chapter 7. Finally, chapter 8 showed an approach using *ex-situ* experiments to identify and (semi)quantify the oxygen radical species in oxygen reduction reactions from solution using DMPO and DEPMPO spin traps. Overall, part III showed the diversity of applications of spin trap SEC-EPR.

The last part of my thesis (Part IV) focuses on direct SEC-EPR methods without using spin traps. In chapter 9, different novel cells for SEC-EPR experiments were validated. In chapter 10, as part of an ongoing work, the electroreduction of the carbon-halogen bond of 1- and 2-bromonaphthalene was investigated with EPR and DFT were performed. More experiments and analysis is required in future.

The final chapter focuses on understanding the catalytic activity of Mo-Cu complexes for CO$_2$ reduction with low-temperature EPR experiments. A vacuum setup for sample collection and quench freezing was designed and used to perform *ex-situ* experiments. Since the sample collection was not fast enough, a quasi-*in-situ* setup was designed and validated. In this setup, an electrochemical cell is embedded inside an EPR tube that is rapidly frozen during the electrochemical experiment. EPR of this sample and corresponding DFT calculations proved the presence of Mo(V) centres. Improvements in both electrochemistry setups and EPR experiments are still required to remove the ambiguities on data interpretation.

This thesis used the help of different EPR spectroscopy techniques to detect, identify and quantify the molecular structures of the paramagnetic intermediates in electrochemical reactions. CW EPR has been used as the primary technique in all works. Moreover, pulse EPR methods such as ENDOR and ESEEM revealed comprehensive information about the vicinity of the unpaired electron in some of the

studied cases. However, EPR spectroscopy shows its best when it is combined with other complementary techniques. Hence DFT calculations were used throughout this thesis to provide evidence for the EPR observations and identify the molecular structures.

In this thesis, we used different types of spectroelectrochemical approaches, such as *ex-situ, in-situ* and quasi-*in-situ*, depending on the experiment and the reaction and EPR experiments requirements. In order to choose which kinds of approach is preferable, different criteria should be considered. The nature of the intermediate that needs to be analysed determines whether an EPR measurement should be done at room temperature or low temperature. The fast electronic relaxation times of transition metal complexes mean that often low temperature are needed to detect species. This restricts the potential choice to the setups mentioned in chapter 11. Next, the intrinsic lifetimes of the intermediates play a very important role. This lifetime should exceed the EPR detection time, otherwise, spin-trapping is needed, restricting the options to the approaches discussed in Part III of this thesis.

The other point for choosing a setup is the number of paramagnetic species that need to be generated to be detectable by EPR, which should be considered for choosing the shape of the electrodes, such as wire electrodes (*e.g.* Pt wire in chapter 6), metallic surfaces (*e.g.* Ag surface in chapter 6), or large transparent surfaces. In some cases, it is not even feasible to generate enough spin systems inside the flat cell; therefore, the need for a large electrode surface leads to the use of *ex-situ* setups (*e.g.* use of rotating disk electrode in chapter 8). Generally, the most suitable setup is the one that provides a sufficient number of radicals to perform an *in-situ* experiment without decreasing the efficiency of EPR experiments (*e.g.* minimum decreasing of Q-factor). Practically this comes down to having a steady supply of analyte towards the working electrodes while minimising the cell volume and interfering materials.

In the case of choosing *in-situ* methods, in order to perform an efficient *in-situ* SEC-EPR experiment, the electrochemical behaviour of the cell is crucial. First, it should be considered that different electrode materials should be chosen for different reactions, which should be checked with preliminary bulk experiments. Moreover, each setup has a unique electrochemical response due to the shape of the electrode and cell geometry using the same electrode materials. The cell is suitable as long as the electrochemical phenomena can be distinguished in the CV experiment. Furthermore, The electrode surface should be reproducible to enable us to gain a similar electrochemical behaviour when repeating the experiment. Taking into account all these considerations that are mentioned above, every electrochemical reaction needs specific adaptations to the electrode or cell. The first choice can be wire electrodes since they are very straightforward to construct and availability of different materials as wires which are thin enough to fit in the flat cell. Their drawbacks, such as not being reproducibly polishable and preventing electrocatalyst deposition, often make them just suitable to get an idea of the measurability of a specific intermediate by EPR. An improvement is exchanging the wire electrode with substrate-deposited electrodes in which the electrode material is deposited on a substrate. These electrodes show a better electrochemical response in the flat cell due to their reproducible flat surface.

Overall, this thesis showed the strength and diversity of applications of SEC-EPR. Different novel cells were introduced that can be used for many case studies. The application of spin traps and the pitfall of using them can be considered for similar studies. However, this approach still has much potential that can be employed in the future. I hope this thesis and our approach can help other scientists to develop their research.

12.2 Future perspective

After investigating the advantages, pitfalls, and challenges of the SEC-EPR methods and showing some applications, the method and SEC-EPR cells that were employed are ready to be used in a more systematic way for a broader range of applications. Many exciting materials and reactions can be investigated by selecting the most suitable setup and techniques. The first step will be to extend the investigations on the C-X electroreduction and CO_2 reduction started in this work.

The use of spin trap EPR experiments and their drawbacks was discussed in this thesis. It can be extended by focusing on other spin traps to find the most suitable spin trap-transition metal combination for various reactions.

All the setups that have been introduced or employed in this thesis have been developed for X-band experiments. The next important step can be to develop a setup to perform EPR measurements at the higher MW frequencies, such as Q-band and W-band. The significantly smaller resonators for these spectrometers increase the challenges caused by the space limitation. Furthermore, employing the rapid scan EPR technique due to a shorter detection time increases the chance of unravelling the information from short-lived intermediates.

Moreover, we need to improve the quench-freezing technique in combination with the quasi-*in-situ* and *ex-situ* SEC-EPR for low-temperature experiments. This will be beneficial to study the intermediates containing transition-metal ions. Miniaturisation is another promising area for the SEC-EPR approach. The EPR on a chip technology may enable us to think about the *in-situ* EPR measurements without concerns about space limitations in the typical EPR resonators.

Acknowledgements

In these years that I have spent in Belgium, I was lucky to meet fantastic people that made the moments more beautiful than I was expecting. Here I would like to thank all of them.

First, I would like to thank Sabine for trusting me and giving me the opportunity to work and grow as a researcher in the fantastic BIMEF lab.

Vincent, Thanks for being such a patient co-promoter, teaching me, answering all my questions and helping me during these five years.

I'd, also like to acknowledge my committee members for reading my thesis and their highly appreciated remarks.

I was not the only person who was involved in this project. Two other PhD students were involved. I'd like to thank Stephane and Sander for being such nice colleagues.

I'd also thank all the groups and people whom I collaborated with them. Prof. Tom Breugelmans, Prof. Annick Hubin, Prof. Bert Maes, Prof. Karolien De Wael, Jon, Danny, Sara, Nora, Tamas and Tamas.

Finally, I'd like to thank my fantastic colleagues in building N and the friends that I made here. I can not imagine my life without you here. Miles, Salome, Mons De Geneve, Shabab, ZaiZai, KevKev, Anto, Ari, Vini, Joeri, Melissa, Guidetti, Ilenia, Sudakov, Banafshe, Amir, Miguelito, Niels, Fardokht, Kave, Mina, Maksiem, Maruan, Alexander, Paul, Federico, Ivan, Leonora, Ming, Lore, Robine, Dima, Aina, Wouter, Denys, Pari, Marina, Arne, Miguel angel, Alejandro, Etienne, Wim, Valentina, Sashi, Alice, Domenico, Michele, Tanya, Pascale, Pedrito, Lorenzo, Aref, Amin, Mina,Yaser, Aida, Ali, Maryam and Parisa.

In the end, I would like to thank my family, especially my mother and my father, for always being supportive.

Mohammad

<h1 style="text-align: center;">Curriculum Vitae</h1>

Education

Master of Science in Physics
Institute for Advanced Studies in Basic Sciences (IASBS), Zanjan, Iran 2011-014

Bachelor of Science in Physics
Kharazmi University of Tehran, Iran, 2007-011

Publications in peer-reviewed journals

- D. Pauwels, H. Y. Vincent Ching, **M. Samanipour**,S. Neukermans, J. Hereijgers, S. Van Doorslaer, K. De Wael, and T. Breugelmans, Identifying Intermediates in the Reductive Intramolecular Cyclisation of allyl 2-bromobenzyl Ether by an Improved Electron Paramagnetic Resonance Spectroelectrochemical Electrode Design Combined with Density Functional Theory Calculations, *Electrochimica Acta* 271, 10 (2018).

- Sander Neukermans, Jonas Hereijgers, H.Y. Vincent Ching, **Mohammad Samanipour,** Sabine Van Doorslaer, Annick Hubin, Tom Breugelmans, A continuous *in-situ* EPR electrochemical reactor as a rapid in-depth mechanistic screening tool for electrocatalysis, *Electrochemistry Communications*, **97,** 42, (2018)

- **M. Samanipour**, H. Y. V. Ching, H. Streckx, B. U. W. Maes, S. Van Doorslaer, The non-innocent role of spin traps in monitoring radical formation in copper-catalyzed reactions, *Appl. Magn. Reson*., **51**, 1523-1542 (2020).

- Sander Neukermans, **Mohammad Samanipour**, H. Y. Vincent Ching, Jonas Hereijgers, Sabine Van Doorslaer, Annick Hubin, and Tom Breugelmans, A Versatile In-Situ Electron Paramagnetic Resonance Spectro-electrochemical Approach for Electrocatalyst Research, *ChemElectroChem*, **7**, 4578, (2020)

- Morad Biagooi, **Mohammad Samanipour**, S Alireza Ghasemi, SeyedEhsan Nedaaee Oskoee, CAVIAR: A simulation package for charged particles in environments surrounded by conductive boundaries, *AIP Advances,* **10**, 035310, (2020)

- Stephan den Hartog, **Mohammad Samanipour**, H.Y. Vincent Ching, Sabine Van Doorslaer, Tom Breugelmans, Annick Hubin & Jon Ustarroz, Reactive oxygen species formation at Pt nanoparticles revisited by electron paramagnetic resonance and electrochemical analysis, *Electrochemistry Communications*, 122, 106878, (2021)

- Saranya Thiruvottriyur Shanmugam, Robin Van Echelpoel, Griet Boeye, Joy Eliaerts, **Mohammad Samanipour**, H. Y. Vincent Ching, Anca Florea, Sabine Van Doorslaer, Filip Van Durme, Nele Samyn, Marc Parrilla, Karolien De Wael, Towards Developing a Screening Strategy for Ecstasy: Revealing the Electrochemical Profile, *ChemElectroChem*, **8**, 4826 (2021)

- Szilvia Bunda, Nóra V May, Dora Bonczidai-Kelemen, Antal Udvardy, HY Vincent Ching, Kevin Nys, **Mohammad Samanipour**, Sabine Van Doorslaer, Ferenc Joo, Norbert Lihi, Copper(II) Complexes of Sulfonated Salan Ligands: Thermodynamic and Spectroscopic Features and Applications for Catalysis of the Henry Reaction, *Inorganic Chemistry,* **60**, 11259 (2021)

- Stephan den Hartog, Sander Neukermans, **Mohammad Samanipour**, H.Y. Vincent Ching, Tom Breugelmans, Annick Hubin & Jon Ustarroz in "Electrocatalysis under a magnetic lens: a combined electrochemistry and electron paramagnetic resonance review", *Electrochimica Acta*, **407**,139704 2022

- **M. Samanipour,** S. Neukermans, **,** H.Y.V. Ching, J. Hereijgers, T. Breugelmans, S. Van Doorslaer, Re-evaluating the electrochemical self-condensation of acetone by *in-situ* EPR and DFT calculations. *Manuscript in preparation*

Oral presentations

Mohammad Samanipour , Vincent Ching, Sander Neukermans, Danny Pauwles, Tom Breugelmans Sabine Van Doorslaer, Studying electrocatalysis by Electron paramagnetic resonance, *28th meeting of the Benelux EPR society*, June, 2021, Leiden-Gent. The Netherlands-Belgium (Online)